Towards a Hydrobromic Acid Splitting Device Using Earth-Abundant Materials

Thesis by
Christopher W. Roske

In Partial Fulfillment of the Requirements for the
degree of
Doctor of Philosophy

CALIFORNIA INSTITUTE OF TECHNOLOGY
Pasadena, California

2017
Defended August 31, 2016

© 2017

Christopher W. Roske

All rights reserved except where otherwise noted

Acknowledgements

This thesis would not have been possible without the tremendous support of my mentors, collaborators, peers, and friends. The National Science Foundation and Link Energy Foundation are thanked for generous graduate research fellowships. The NSF CCI Solar is thanked for research supplies. Forgive me for those missed below, I am short on time.

Harry Gray, Nate Lewis, Bruce Brunschwig, and (most recently) Jay Winkler have served as my staunch advisors, encouraging and supporting me in every way possible even while I have doubted myself. Harry's positive perspective on life and science brings light to the darkest of days. Nate's confidence in solving the hardest problems inspires scaling the tallest of scientific mountains. Bruce's practical thinking and advice has kept me from falling too hard. I hope, one day, to reach a quarter of Jay's breadth of knowledge. In addition, my committee has been enriched by the valuable insights of Theo Agapie and Bill Goddard.

My advisers have given me the freedom to make plenty of mistakes. Chief among those was trying to be a "One Man Army." After years of failed ideas and projects, it took Shane Ardo's sheer tenacity to convince me to stay, and for that I am extremely grateful. James Blakemore also left an impression on me, as is reflective of his exquisite style. I am convinced that both Shane and James will make excellent professors and I look forward to their continued success. No doubt in my mind, Wes and Aaron Sattler are busy being awesome right now.

Of labmates, Adam Nielander and Noah Plymale are my pals, and I will closely follow their progress. I really regret not getting to know Oliver Shafaat sooner, and I am excited for his future. Brian Sanders has been a welcome addition to the sub-basement crew as of late, and I hope his dreams reach fruition. Additionally, I look forward to following the progress of past and present people who have impacted my career (in the order I saw them last): Astrid Mueller (I imagine her hard efforts will yield continued success), Annelise Thompson, Jonathan Thompson, Anne Davis, James McKone, Leslie O'Leary, Donatella Bellone, and Rocio Mercado. Additionally, the help of Rick Jackson, Barbara Miralles, and Kimberly Papadantonakis has been greatly appreciated in all matters big and small.

My friends and family have always supported me, helping me live a fulfilling life full of adventure and stories, thank you in particular (in order of appearance): Jaime Whitney, Thomas Bitterwolf, Brett Walter, Michael Sasala, Justin Brown, Kyle Rucker, Seth Williams, Frank Cheng, Harmen Zijlstra, Peter Griffiths, Melissa Yeung, Sid Creutz, Amanda Shing, Chris Marotta, and last (but not least) Genie Luzwick.

Abstract

This thesis disembarks from the traditional approach of tailoring a system to the water splitting reaction. As detailed in Chapter 2, this thesis predicts that two silicon photoelectrons connected in parallel are ideally suited to electricity storage in an integrated light collector and chemical storage device driving the splitting of hydrobromic acid ($2\,HBr \longrightarrow H_2 + Br_2$). The predicted dual photoelectrode system could potentially obtain high solar-to-hydrogen conversion efficiencies of up to an $\eta_{STH,\,HBr}$ of 12 %, whereas an equivalent water splitting system is not possible due to the small band gap of silicon. Unfortunately, silicon possesses low catalytic activity for both the hydrogen evolution half-reaction and the bromide oxidation half-reaction. In the past, the electrocatalysis of silicon has been aided by using Pt/Ir alloys to act as both a protective and electrocatalytic layer. Herein, efforts are detailed to replace these precious metals, where possible, by using only earth-abundant materials to decrease the cost of a module. Our hope is that efforts along this path will aid the field of artificial photosynthesis as a whole.

We begin by further testing a chemical insight previously noted within our group and discover a surprisingly high activity electrocatalyst for the hydrogen evolution reaction by cobalt phosphide (CoP) nanoparticles, detailed in Chapter 3. Falling on a traditional technique of increasing the surface area of particular facets, we nanostructured our crystalline CoP to increase its surface area of exposed (111) facets and hoped it would increase our catalytic activity; however, we found that simple structuring resulted in poor adhesion of nanostructures and poorer activity than our multi-faceted CoP nanocrystals (see the appendix to find out more). Our original catalysis efforts spurred a flurry of activity in the literature, and consequently, alternative devices that are more scalable arose. We detail the developments occurring since our work in the last appendix.

Now, with a potential catalyst in hand, comes the difficulty of balancing the delicate interplay between light absorption and catalysis, as detailed in Chapter 4. While CoP is active for HER, our particles possess a relatively low turnover frequency compared to hydrogenase or platinum, and thus require high mass loadings of material ($2\,mg/cm^2$) to obtain competitive extrinsic performance. Planar electrodes are incompatible with our particles because of substantial light absorption by the thick catalyst overlayer. By structuring our photoelectrode, we abnegate our catalyst limitations by exploiting the properties of microwires. High-aspect ratio microwires

have shown promise as potentially low-cost materials for future photovoltaic applications as well as photocathodes functioning as part of an energy storage device. We discuss how to integrate our materials with silicon microwires (the wires were grown by an unscalable process to serve in place of functional CVD wires with radial emitters) to prototype a candidate photocathode. While a parasitic resistance limited the overall efficiency of the photocathode candidate, it still had promising stability. The parasitic resistance was addressed by electrodepositing the cobalt phosphide, thereby giving us a promising efficiency limited by the quality of the p-n junction.

While high-catalytic activity for the HER in acidic solutions using earth-abundant materials represents a significant advance, the photocathode is just one component of what is necessary for a complex system of splitting hydrobromic acid. Silicon, by its virtue of being a small band gap material, is easily passivated in aqueous solutions by the formation of a silicon oxide. In the past, our colleagues had shown that a monolayer of graphene could occasionally provide protection in a test solution, but batch-to-batch variability provided a considerable challenge. The putative hypothesis offered for the degradation argued defects in the crystalline graphene at grain-boundaries were the culprit. In Chapter 5 we present a method to passivate defects in the graphene crystal by light fluorination and observe a considerable enhancement in stability relative to typical graphene-protected silicon photoanodes. We had hoped that catalysis for bromide oxidation would be aided by the near-perfect graphene liquid junction, but electrodeposited Pt was required to effect photoxidation. A cursory stability test shows promising stability for one-half of an hour, but we would like to avoid using Pt. Finally, we also turned our attention to protecting silicon surfaces from oxidation by exploiting covalent silicon surface chemistry, accessible via a two-step chlorination/alkylation procedure, and explored the deposition of potentially protective thin-film metal oxides (see the appendix).

Published Content and Contributions

(1) J. Callejas, C. G. Read, C. W. Roske, N. S. Lewis and R. E. Schaak, *Chem. Mater.*, 2016, **99**, 99,
(used in Appendix K) CWR wrote section on integration.

(2) C. W. Roske, J. W. Lefler and A. M. Muller, *J. Colloid Interface Sci.*, 2016, **00**, 00,
(used in Appendix I) CWR participated in the characterization and writing of the manuscript.

(3) A. C. Nielander, A. C. Thompson, C. W. Roske, J. A. Maslyn, Y. Hao, N. T. Plymale, J. Hone and N. S. Lewis, *Nano Lett.*, 2016, **16**, 4082–6,
(used in Chapter 5) CWR participated in the conception of the project and performed experiments relating to hydrobromic acid.

(4) C. W. Roske, E. J. Popczun, B. Seger, C. G. Read, T. Pedersen, O. Hansen, P. C. Vesborg, B. S. Brunschwig, R. E. Schaak, I. Chorkendorff, H. B. Gray and N. S. Lewis, *J. Phys. Chem. Lett.*, 2015, **6**, 1679–83,
(used in Chapter 4) CWR conceptualized the project, performed all the major experiments, and wrote the manuscript.

(5) E. J. Popczun, C. W. Roske, C. G. Read, J. C. Crompton, J. M. McEnaney, J. F. Callejas, N. S. Lewis and R. E. Schaak, *J. Mater. Chem. A*, 2015, **3**, 5420–5425,
(used in Appendix E) CWR participated in the characterization of electrocatalytic behavior and editing of the manuscript.

(6) L. E. O'Leary, N. C. Strandwitz, C. W. Roske, S. Pyo, B. S. Brunschwig and N. S. Lewis, *J. Phys. Chem. Lett.*, 2015, **6**, 722–726,
(used in Appendix G) CWR participated in surface synthesis, characterization, and editing of the manuscript.

(7) E. J. Popczun, C. G. Read, C. W. Roske, N. S. Lewis and R. E. Schaak, *Angew. Chem.*, 2014, **126**, 5531–5534,
(used in Chapter 3) CWR performed the electrocatalysis characterization.

Table of Contents

List of Illustrations

List of Tables

Chapter 1

Introduction

1.1 Motivation

The world population increased from 3 billion in 1959 to 6 billion in 1999.[1] Projections indicate that we can expect 9 billion souls by 2044.[1] Prominent among the challenges we will face is elevating their standard of living — one key way to do this is by energy equality. Today the average American demands energy at a rate of 9.5 kW per capita, whereas for other rapidly growing countries, such as an India national, 0.74 kW per capita is more typical.[2] The world rate of primary energy consumption is about 17.5 TW, totaling 5.52×10^2 EJ per year, with the United States accounting for about 17 % of the demand despite having 4.4 % of the world population.[2] If every living person today consumed at comparable levels, then worldwide energy consumption would soar to 2.2×10^3 EJ per year today and 2.8×10^3 EJ per year by 2044. If we aim to elevate our fellow (wo)man with energy equality, then there are massive resource challenges along the path ahead.

Today, the world's primary energy production portfolio consists of oil (32.9 %), natural gas (23.8 %), coal (29.2 %), nuclear (4.44 %), hydro (6.79 %), and renewables (2.78 %).[2] We convert approximately two-thirds of this supply to usable energy, while the other third is lost to entropy.[3] This supply includes all transportation (27.6 %), industrial (29.1 %), residential and commercial (34.6 %), and raw material (8.83 %) consumption of primary energy.[4] Fossil fuels, constituting more than 85 % of the supply,[2] fundamentally originate from plants and animals that lived hundreds of millions of years ago.

Photosynthetic organisms captured energy from sunlight and stored it in chemical

bonds that were, occasionally, prevented from oxidizing back to CO_2 after becoming trapped in anaerobic conditions, thereby leaving a finite supply through geological processes. While the same formation processes exist today, their slow rates are unhurried compared with our rapid rate of extraction.[†] This fossil fuel supply is used in two ways: chiefly as an energy carrier and secondly as a chemical feedstock. After the discovery and extraction of crude materials, refining occurs on a massive scale (Figure 1.1). As stewards of this planet, it is our responsibility to carefully consider the benefits and costs to extraction at elevated rates. This first chapter is dedicated to the larger picture of the energy landscape, and motivated the rest of this thesis work. First, an estimate of reduced carbon is taken from Wurfel.[5] Hubbert's model is used to show an estimate of the time left until resource exhaustion.[6] Third, a toy model reflecting the physical mechanism by which fossil fuel emissions can change the temperature of a planet as inspired by others is presented and then energy sources are compared as discussed by others.[7] Finally, a technical solution is argued so as to mitigate climate change as adopted by our cohort (including Lewis[8] and Gray[9]).

Figure 1.1: Featuring (left-to-right) K. Wong, C. Roske, J. Velazuez, J. John, N. Plymale, J. Wiensch, N. Lewis visiting the BP Whiting Oil Refinery converting energy at a rate of 0.028 TW.

[†]Consider that if the total stored reduced carbon energy is 1.60×10^{25} J and this has formed since the great oxygenation event 2.3 billion years ago, then the rate of formation is an estimated: $\frac{1.60\times10^{25} J}{7.25\times10^{16} \mathrm{s}} = 220 \times 10^{6}\,\mathrm{W} = 220\,\mathrm{MW}$.

1.2 Limits of Fossil Fuels

It is instructive to estimate the total stored solar energy in terms of reduced carbon and then frame the present trajectory of resource depletion. We begin by determining the mass of carbon created by life,* then we calculate the total energy stored and consider our extraction progress in the best possible recovery case. Finally, we incorporate estimates from the energy industry to make a projection using proven reserves.

Mass of Carbon Reserves

Free oxygen, making up 21 % of today's atmosphere, is considered biogenic in origin as a product of photosynthesis. Otherwise, photolysis of water to O_2 and H_2 with gaseous escape is the expected abiotic process slowly leading to, for example, the oxidized surface of Mars.[10] However, this inorganic process contributes negligibly compared to photosynthesis because of UV protection afforded by our atmosphere. We are estimating carbon reserves as dictated by the photosynthetic reaction, which produces reduced carbon from carbon dioxide and water:

$$6\,CO_2 + 6\,H_2O \xrightarrow{\text{Light}} C_6H_{12}O_6 + 6\,O_2\,.$$

Therefore, the mass of carbon, m_C, can be estimated from the mass of oxygen, m_{O_2}, in the air:

$$m_C = \frac{12}{32} m_{O_2}.$$

Using a simplified atmospheric makeup (79 % N_2 and 21 % O_2) we infer m_{O_2} from

*We assume that materials not properly stored revert back to CO_2 or are returning at a slow rate.

the mass of air, m_{air}:

$$m_{\text{O}_2} = \frac{21}{100} m_{\text{air}}$$

We determine m_{air} as the product of air pressure ($P_{\text{atm}} = 101325\text{kg} \cdot \text{m}/\text{m}^2$), the reciprocal of the gravitational acceleration constant ($g^{-1} = \frac{\text{s}^2}{9.8\text{m}}$), and the surface area of earth ($4\pi R_{\text{earth}}^2$, where $R_{\text{earth}} = 6371 \times 10^3\text{m}$):

$$m_{\text{air}} = P_{\text{atm}} \times g^{-1} \times 4\pi R_{\text{earth}}^2.$$

Thus, m_{C} is computed:

$$\begin{aligned} m_{\text{C}} &= \frac{12}{32} \times \frac{21}{100} P_{\text{atm}} \times g^{-1} \times 4\pi R_{\text{earth}}^2 \\ &= \frac{12}{32} \times \frac{21}{100} (101325\text{kg} \cdot \text{m}/\text{m}^2) \times \frac{\text{s}^2}{9.8\text{m}} \times 4\pi (6371 \times 10^3\text{m})^2 \\ &= 4.2 \times 10^7 \text{ kg of carbon.} \end{aligned}$$

Total Chemical Energy of Stored Carbon

Determining the total stored energy requires finding the estimated mass of fossil fuels, then using an approximate specific energy[‡] to obtain an energy reserve total. The specific chemical makeup will vary substantially from one resource to another (even site to site), and hence the H/C molar ratio will vary between 1 (for coal) to 4 (for natural gas). Assuming the average H/C ratio is 3 (giving CH_3 with $15\,\text{g}\,\text{mol}^{-1}$) the mass of fossil fuels, m_{ff}, can be calculated as

$$m_{\text{ff}} = \frac{15}{12} m_{\text{C}}.$$

[‡]Specific energy is $\text{J}\,\text{kg}^{-1}$.

Obtaining the specific energy requires calculating the enthalpy of combustion for:

$$4\,CH_3 + 7\,O_2 \xrightarrow{\Delta} 4\,CO_2 + 6\,H_2O.$$

As defined, there is a half C – C bond with a bond dissociation energy (BDE) of approximately $\frac{337}{2}\frac{\text{kJ}}{\text{mol}}$ and three C – H bonds with a BDE of $430\frac{\text{kJ}}{\text{mol}}$. The enthalpy of the reaction is calculated by Σ(energy of bonds broken) $-$ Σ(energy of bonds formed), which in this case results in:

$$\Delta H = \frac{1}{4}(4(\frac{337}{2}+3\times430)+7\times500)-\frac{1}{4}(4\times2\times749+6\times2\times428) = -448.5\,\text{kJ}\,\text{mol}^{-1}.$$

Our desired expression of specific energy, ρ_{E}, is best represented as:

$$\rho_E = 448.5\frac{\text{kJ}}{\text{mol}} \times \frac{1\text{mol}}{15\text{g}} \times \frac{1000\text{mol}}{1\text{kg}} \times \frac{10^3\text{J}}{1\text{kJ}} \times \frac{1\text{MJ}}{10^6\text{J}} = 30\,\text{MJ}\,\text{kg}^{-1}.$$

Now we can calculate an upper-bound of the available energy, Q_{max}, from reduced carbon with:

$$Q_{\text{max}} = \rho_{\text{E}}\times m_{\text{ff}} = \rho_{\text{E}}\times\frac{15}{12}m_{\text{C}} = 30\frac{10^6\text{J}}{\text{kg}}\times\frac{15}{12}\times4.2\times10^{17}\text{kg} = 1.6\times10^7\,\text{EJ} = 16\,\text{YJ}.$$

Progress in Logistic Consumption of Fossil Fuels

We are in a position to make a comparison of our historical fossil fuel extraction with the total reserves as well as track our progress along a relevant model. In light of exponential growth of consumption in the face of finite resources, the logistic growth function is aptly invoked:

$$Q(t) = \frac{Q_{\max}}{1 + ae^{-bt}},$$

where $Q(t)$ denotes the cumulative production at some time, a controls the peak production time, b controls the rates of depletion, and $Q_{\max}$ is the the maximum supply reserve. While this nonlinear function is useful for producing a familiar result used in ecology models, the derivative ($\frac{dQ}{dt}$) is exploited for our purposes in tracking peak production:

$$\frac{dQ}{dt} = \frac{abQ_{\max}e^{bt}}{(a + be^{bt})^2}.$$

A toy model incorporating historical consumption and projecting total supply exhaustion is depicted in Figure 1.2. At a glance these fuels are seemingly inexhaustible, but a large proportion of this total stored energy is in the form of kerogen, which may require expending more energy retrieving the fuel than it produces in combustion. Therefore, this model does not reflect total recoverable fossil fuel energy because that depends on economical and technological considerations.

There is a large abundance of reduced carbon on Earth, but it is impractical to burn the entire reserve because many of these reservoirs are difficult to discover, extract, and refine. As such, predictions of imminent resource exhaustion refer not to the total possible reduced carbon energy supply, but to conventionally proven sources that are more readily recovered and converted into usable energy. Table 1.1 illustrates the proven potential reserve energies. The results from a model reflecting proven reserves and their consumption are shown in Figure 1.3. This estimate only accounts for known geological repositories that can be mined and processed using standard industrial techniques, but history shows (beyond the discovery of new reserves) innovation and demand will turn some unconventional sources to

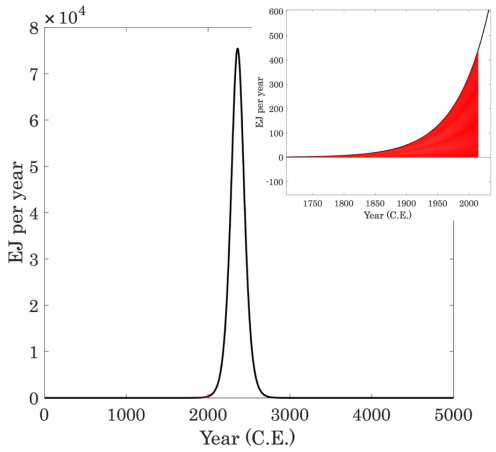

Figure 1.2: Historical data on total world fossil fuel energy supply obtained from BP[11] are fitted using $Q_{\max} = 1.6 \times 10^7$ EJ to give $a = 2.167 \times 10^{19}$ and $b = 1.886 \times 10^{-2}$. The shaded area under the curve is our progress in extraction to date, $Q_{\text{used}} = \int_0^{2016} \frac{abQ_{\max}e^{bt}}{(a+e^{bt})^2}\,dt = 24\,002.1$ EJ.

economical ones. It is unclear when the cost of production will exceed demand. As Figure 1.3 reflects by 2044 (when the world population reaches 9 billion) we will either have: (1) delayed the inevitable exhaustion or (2) significantly modified our energy portfolio. In any case, known reserves are unable to solely provide energy equality either today (2.2×10^3 EJ per year) or by 2044 (2.8×10^3 EJ per year) without substantially decreasing our energy consumption per capita.

Resource Type	Potential Energy (EJ)
Oil	1.0×10^4
Natural Gas	3.9×10^2
Coal	2.2×10^4
Total	3.2×10^4

Table 1.1: Potential energy of fossil fuel resources from proven reserves.[2]

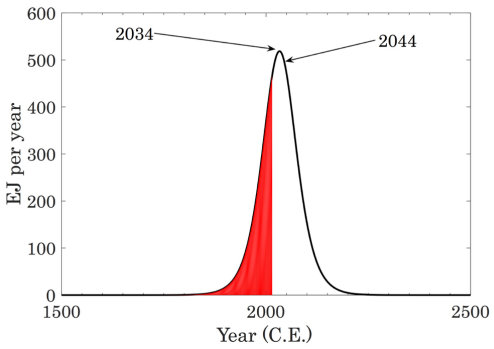

Figure 1.3: Using a more realistic projection based on the data in Table 1.1, we assume that all energy from fossil used to date is 2.4×10^4 EJ and that total proven reserves reach 3.2×10^4 EJ. Thus, $Q_{\max} = 5.7 \times 10^4$ EJ. Nonlinear fitting resulted in $a = 1.37 \times 10^{32}$ and $b = 3.64 \times 10^{-2}$ for the logistic growth model. The red area under the curve reflects our progress of exhaustion to date. This model predicts that by 2034 we will have peaked in production per year and that by 2044 declining performance can be expected.

1.3 Greenhouse Gas Effects

Fossil fuels are poised to meet our current prosaic energy demands for the next 18 years using known geological repositories and standard techniques, although they are insufficient as the sole provider for a world with energy equality. While further geological discoveries or high demands may open additional avenues for extraction, an important penalty to fossil fuel combustion is worth mentioning: we appear to be changing the atmospheric composition as a result of our emission products. We weakly justify the mechanism of the greenhouse effect with simple models to demonstrate the magnitude of the effect at the scale of a planet as presented by others.[7] More exhaustive efforts are found elsewhere.[12]

Black Body Surface Temperature

The surface temperature of a planet, T_{p}, is determined by an equilibrium between the power entering and exiting a planet, $P_{\text{in}} = P_{\text{out}}$. Of course, the power entering a planet from a sun is determined by a simple modification to the Stefan-Boltzmann law that incorporates the surface area of the sun ($4\pi R_{\text{sun}}^2$), the distribution of power

over a sphere with a radius from the sun to a given planet ($4\pi R_{\mathrm{d}}^2$), the cross-sectional area of the planet (πR_{p}^2), and the imperfect absorption of radiation by the planet as represented by the albedo ($1-\alpha$),

$$P_{\mathrm{in}} = \frac{\sigma T_{\mathrm{sun}} \times 4\pi R_{\mathrm{sun}}^2}{4\pi R_{\mathrm{d}}} \times \pi R_{\mathrm{p}}^2 (1-\alpha),$$

where σ is the Stefan-Boltzmann constant, T_{sun} is the temperature of the sun, R_{sun} is the radius of the sun, R_{d} is the average distance between a planet and sun, R_{p} is the radius of a planet, and α is the surface albedo of a planet.

Likewise, black body emissions from a planet are predicted by,

$$P_{\mathrm{out}} = \sigma T_{\mathrm{p}}^4 \times 4\pi R_{\mathrm{p}}.$$

Finally, setting $P_{\mathrm{in}} = P_{\mathrm{out}}$ and rearranging the equality furnishes the desired result:

$$\frac{\sigma T_{\mathrm{sun}} \times 4\pi R_{\mathrm{sun}}^2}{4\pi R_{\mathrm{d}}} \times \pi R_{\mathrm{p}}^2 (1-\alpha) = \sigma T_{\mathrm{p}}^4 \times 4\pi R_{\mathrm{p}}$$

$$T_{\mathrm{p}} = T_{\mathrm{sun}} (1-\alpha)^{1/4} \sqrt{\frac{R_{\mathrm{sun}}}{2R_{\mathrm{d}}}}.$$

Table 1.2 shows the tabulated parameters, results, and a comparison between observed surface temperatures and atmospheric pressures for Mercury, Venus, Earth, and Mars. A cursory glance reveals that this simple relationship reliably estimates the temperatures of Mercury and Mars (both have low atmospheric pressures), but the model grossly fails to predict the average temperatures of Venus and Earth (both planets have considerably higher atmospheric pressures). We ascribe the difference in errors to the greenhouse effect, because we hypothesize atmospheric species introduce additional corrections to our simple model. Below, we incorporate infrared

gas absorptions into an improved model.

Planet	α	R_{d} (m)	T_{p} (K)	T_{obs} (K)	$\frac{\Delta T}{T_{\mathrm{obs}}}$ (%)	P (atm)
Mercury	0.119	5.91×10^{10}	430	440	2.3	10^{-15}
Venus	0.750	1.08×10^{11}	232	735	68	92
Earth	0.306	1.50×10^{11}	254	288	12	1
Mars	0.250	2.29×10^{11}	210	215	2.5	0.007

Table 1.2: Data obtained from NASA.[13] The planet bond albedo, α, and distance from sun to planet, R_{d}, are used in conjunction with sun temperature ($T_{\mathrm{sun}} = 5870\,\mathrm{K}$) and radius ($R_{\mathrm{sun}} = 6.96 \times 10^{8}\,\mathrm{m}$) to predict equilibrium temperatures, $T_{\mathrm{p}} = T_{\mathrm{sun}}(1-\alpha)^{1/4}\sqrt{\frac{R_{\mathrm{sun}}}{2R_{\mathrm{d}}}}$. The observed surface temperature, T_{obs}, is compared with the predicted temperature, T_{p}, and the atmospheric pressure for each planet is noted, P.

Hot-House Effect on Surface Temperature

At the surface, incoming power from the sun, $P_{\mathrm{in,\,sun}}$, will heat the surface and the energy will be re-emitted by the surface, $P_{\mathrm{out,\,sun}} = \sigma T_{\mathrm{surf}}^4 4\pi R_{\mathrm{p}}^2$, back into the atmosphere. Now we consider an atmospheric layer that imperfectly (ϵ) absorbs power, $P_{\mathrm{in,\,atm}}$, isotropically emitting power back to the planet surface ($\epsilon\sigma T_{\mathrm{atm}}^4 4\pi R_{\mathrm{p}}^2$) and into space, $(1-\epsilon)\sigma T_{\mathrm{surf}}^4 4\pi R_{\mathrm{p}}^2 + \epsilon\sigma T_{\mathrm{atm}}^4 4\pi R_{\mathrm{p}}^2$. Balancing this flux requires distinguishing between the atmospheric and black body emissions. Let $P_{\mathrm{in,\,sun}} = \frac{\sigma T_{\mathrm{sun}} \times 4\pi R_{\mathrm{sun}}^2}{4\pi R_{\mathrm{d}}} \times \pi R_{\mathrm{p}}^2(1-\alpha)$ represent the absolute incoming power reaching a planet's surface from a sun. A planet surface will have a temperature, T_{surf}, and the atmosphere will have another temperature, T_{atm}, with an imperfect emissivity of ϵ (note that $\epsilon = 1$ for a perfect black body, while $\epsilon = 0$ for a perfect white body). Thus for the planet's surface,

$$P_{\mathrm{in,\,surf}} = P_{\mathrm{out,\,surf}}$$

$$P_{\mathrm{in,\,sun}} + \epsilon\sigma T_{\mathrm{atm}}^4(4\pi R_{\mathrm{p}}^2) = (1-\epsilon)\sigma T_{\mathrm{surf}}^4(4\pi R_p^2).$$

Correspondingly for the atmosphere,

$$P_{\text{in, atm}} = P_{\text{out, atm}}$$

$$P_{\text{in, sun}} - \epsilon\sigma T_{\text{atm}}^4(4\pi R_{\text{p}}^2) = (1\epsilon)\sigma T_{\text{surf}}^4(4\pi R_{\text{p}}).$$

By the addition method, the relations for the surface and atmosphere are combined and solved for T_{surf}:

$$2P_{\text{in, sun}} = (1-\epsilon)\sigma T_{\text{surf}}^4(4\pi R_p^2)$$

$$2\left(\frac{\sigma T_{\text{sun}} \times 4\pi R_{\text{sun}}^2}{4\pi R_{\text{d}}} \times \pi R_{\text{p}}^2(1-\alpha)\right) = (2-\epsilon)\sigma T_{\text{surf}}^4(4\pi R_{\text{p}}^2)$$

$$T_{\text{surf}} = \sqrt[4]{\frac{2\left(\frac{\sigma T_{\text{sun}} \times 4\pi R_{\text{sun}}^2}{4\pi R_{\text{d}}} \times \pi R_{\text{p}}^2(1-\alpha)\right)}{(2-\epsilon)\sigma}(4\pi R_{\text{p}}^2)}$$

$$T_{\text{surf}} = T_{\text{sun}}\sqrt{\frac{R_{\text{sun}}}{R_{\text{d}}}}\sqrt[4]{\frac{1-\alpha}{2(2-\epsilon)}}.$$

Using values for Earth and $\epsilon = 0, 1.00, 0.780$, we get $T_{\text{surf}} = 254, 302, 288$ K, which accounts well for the surface temperatures on Earth with or without an atmosphere full of heat-absorbing gases.[‡]

Estimates on the Effect of Atmospheric Gases on Surface Temperature of Earth

Early on (1896) the potential effects of heat-absorbing gases in the atmosphere on the surface temperature of the planet were recognized.[14] We use Planck's law to estimate the black body emissions of Earth, and then demonstrate the effect of gas absorptions by either water or CO_2 on the emissivity of a planetary atmosphere.

[‡]An astute reader might test this model against Venus, obtaining $T_{\text{surf}} = 232$ and 276 K for $\epsilon = 0$ and 1.0, which fails to account for $T_{\text{obs}} = 735$ K. Our previous model relies on a simple atmosphere surrounding a planet with sunlight arriving at the surface, but the Venusian atmosphere is more complex owing to the higher pressure at its surface and as a result little sunlight directly reaches the surface, hence model failure. A refined approach would consider several layers of atmosphere, each with coupled radiative energy balances and absorptions. We will also not succeed at predicting the temperature of gaseous giant planets, such as Saturn and Jupiter, because of internal heating from gravitational compression or being unable to define the "surface" of a gas giant.

Planck's law readily calculates spectral irradiance of a black body:

$$B(\lambda(\mathrm{m}), T(\mathrm{K}))(\mathrm{Wm}^{-2}\mathrm{nm}^{-1}) = \frac{2\pi hc^2}{10^9 \lambda^5 (\exp(\frac{hc}{k_\mathrm{B}\lambda T_\mathrm{surf}}) - 1)},$$

where h is the Planck constant, c is the speed of light, λ is the wavelength, k_B is the Boltzmann constant, and $B(\lambda, T)$ is the spectral irradiance. A plot of the wavelength (nm) versus the spectral irradiance for Earth is depicted in Figure 1.4 with colored areas under the emission curve representing infrared transitions of water and carbon dioxide. (The profile for the sun as seen outside the atmosphere is obtained by appropriate scaling and temperature, $B(\lambda, T) \times (\frac{R_\mathrm{s}}{R_\mathrm{d}})^2$.)

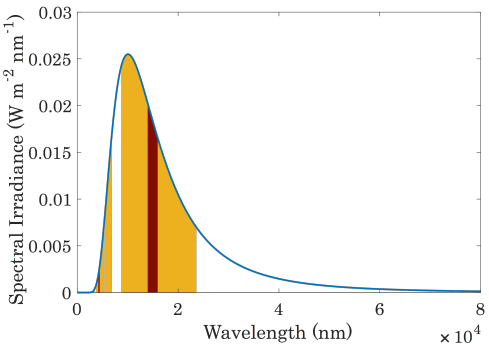

Figure 1.4: Black body emissions of Earth with $T = 288$ K is the curve in blue. Yellow area under the curve reflects water infrared transitions and the red area is from CO_2 transitions. $\int_0^\infty B(\lambda, T)\, d\lambda = 388$ Wm^{-2}. The area corresponding to water vapor totals 265 Wm^{-2} and the area for CO_2 equals 37.1 Wm^{-2}.

In Figure 1.4, a perfectly behaving black body atmosphere would be represented, $\epsilon = 1$, with an area completely filling an entire emission curve area; in this way, our ϵ is a ratio of the power adsorbed relative to the total emission of a planet, therefore to crudely estimate[§] the planetary emissivity we sum contributions for

[§]Indeed, this approximation is rough since we do not capture the full shape of each vibrational transition at each pressure and temperature in the atmosphere; account for the variation in the concentration of these gases at different altitudes; avoid double-counting shared areas between H_2O and CO_2 transitions (we argue it is fair because of underestimates elsewhere); regard different oscillator strengths; include considering other species such as ozone and methane; or use a litany of other factors considered in a full treatment.

each component relative to the total area and obtain

$$\epsilon = \frac{\int (\text{area } H_2O \text{ transitions}) + \int (\text{area } CO_2 \text{ transitions})}{\int_0^\infty B(\lambda, T)\, d\lambda} = \frac{265 \frac{\text{W}}{\text{m}^2} + 37.1 \frac{\text{W}}{\text{m}^2}}{388 \frac{\text{W}}{\text{m}^2}} = 0.779.$$

Our estimated value of $\epsilon = 0.78$ matches our earlier estimate, but most importantly this toy model captures the core behavior of the natural system. Accounting for vibrational features of gases in the atmosphere roughly explains the atmospheric emissivity. Granted that water is the most potent greenhouse gas, but CO_2 should not be undervalued ($\epsilon = 0.68$ without CO_2 or $T_{\text{surf}} = 282$ K).

Estimates on Radiative Forcing of CO_2

One of the last considerations is the effect of CO_2 concentration on the emissivity. We do not fully detail a derivation of the simplified expression used, but the general sense of the relationship between $[CO_2]$ and the area under the curve (called the radiative forcing) is developed in Figure 1.5. Briefly, at low concentrations, the concentration and radiative forcing are linearly related; at intermediate concentrations, they are related by the square root; and at high concentrations the relationship becomes logarithmic.

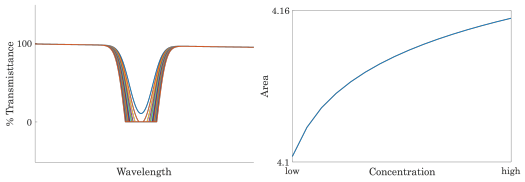

Figure 1.5: (Left) Depicts different concentrations of a gaseous species, at high enough concentrations saturation occurs when transmittance is 0 %. Further gains in the integrated area of a peak occur in the "wings" of a peak. (Right) Shows how the relation between the area and concentration changes dependence on the regime. Low concentrations are fit well to a linear equation; intermediate concentrations have a square-root dependence; and at high concentrations the relationship is logarithmic.

The IPCC estimates that the CO_2 forcing is best represented as,[12]

$$F = 5.35 \ln(\frac{[CO_2]}{[CO_2]_0}),$$

where $[CO_2]$ represents the current concentration of CO_2 (402 ppmv) and $[CO_2]_0$, represents an initial concentration, typically taken as the pre-industrial era value of 280 ppmv.[12]

We should then roughly expect the influence of human combustion of reduced carbon to give an emissivity of:

$$\epsilon = \frac{\int (\text{area } H_2O \text{ transitions}) + \int (\text{area } CO_2 \text{ transitions}) + 5.35 \ln(\frac{[CO_2]}{[CO_2]_0})}{\int_0^\infty B(\lambda, T)\, d\lambda}$$

$$= \frac{265 \frac{W}{m^2} + 37.1 \frac{W}{m^2} + 5.35 \ln(\frac{402\text{ppmv}}{280\text{ppmv}}) \frac{W}{m^2}}{388 \frac{W}{m^2}} = 0.784.$$

Accordingly, the difference in temperature from pre-industrial levels to today's concentrations should be on the order of 0.30 K, which is only a factor of three from IPCC's prediction of 0.85 K. Nonetheless, IPCC's value incorporates the effects of CO_2, methane, N_2O, among feedback systems, whereas ours only roughly accounts for CO_2.[12] This means our rather simple discussion here demonstrates some of the essential principles of the formidable work undertaken by IPCC. In particular, it highlights how human-made emissions are occurring at a scale large enough to shift the surface temperature of the planet. As a final note on this particular discussion, the amount of shift our civilization can tolerate is uncertain because we depend on past climate behavior as part of our risk management strategy. So, seemingly small changes move us into uncharted territory. As such, there is considerable interest in developing energy systems that do not contribute to climate change and can simultaneously help make a world with energy equality possible.

Emissions of CO_2 from Anthropogenic Sources

Now we estimate the magnitude in change of CO_2 concentration in the atmosphere, $\Delta[CO_2]$, from emissions relative to the total air to see if anthropogenic sources can account for the magnitude of change observed from the pre-industrial era level (280 ppmv) to now (402 ppmv). First we calculate the total volume of CO_2 produced by humans and then ratio to the total volume of air in the atmosphere.

Figure 1.2 used 2.4×10^4 EJ as the total fossil fuel energy spent; if we further assumed the entire resource was burnt then this means that the total volume of CO_2 is obtained as:

$$V_{CO_2} = 2.4 \times 10^4 10^{18} \text{J} \left(\frac{1\text{kg}}{30 \times 10^6 \text{J}}\right) \times \frac{44}{15} \times \frac{1\text{m}^3}{1.98\text{kg}} = 1.2 \times 10^{15} \text{m}^3.$$

Similarly, the total volume of the atmosphere is determined:

$$V_{\text{air}} = 101325 \frac{\text{kg} \cdot \text{m}}{\text{m}^2} \times \frac{1\text{s}^2}{9.8\text{m}} \times 4\pi (6471 \times 10^3 \text{m})^2 \times \frac{1\text{m}^3}{1.225\text{kg}} = 4.3 \times 10^{18} \text{m}^3.$$

Thus,

$$\Delta[CO_2] = \frac{V_{CO_2}}{V_{\text{air}}} 10^6 = \frac{1.2 \times 10^{15} \text{m}^3}{4.3 \times 10^{18} \text{m}^3} = 280\text{ppmv}.$$

Our estimated $\Delta[CO_2]$ is approximately double than what is measured because CO_2 becomes trapped in the carbon cycle, with about half the CO_2 ending up in photosynthetic organisms or the ocean. In the ocean, one of the largest reservoirs in the carbon cycle, the formation of carbonic acid from equilibration with CO_2 vapor has led to ocean acidification and detrimental effects seen on the growth of corals.

1.4 Low CO_2 Emission Energy Systems

Any future where humanity expels less CO_2 as part of the operation of modern life will require a mixed portfolio of energy sources, each with positive and negative attributes, tailored to the region of generation and consumption. This future economy will also leverage fossil fuels strictly as a chemical feedstock instead of wasting precious materials on thermal energy. Among the many choices that will be available, a select few are highlighted below due to their immense promise and potential. We will also mention some of their undesirable properties. While it may be obvious fusion and fission rely on the energetic balance of nuclear forces, it is less intuitive that many other sources of energy (including wind and solar) indirectly rely on the sun, a natural nuclear reactor; for this reason, we distinguish between direct and indirect nuclear sources.

Direct Nuclear

Both nuclear options make clear the large difference in specific energy available from nuclear reactions compared to less energetic chemical transformations. Fusion remains a technical challenge ever out of reach, while fission reactors have been available for decades but struggle to gain relevance to electrical companies who would build more power stations. Unlike other renewable options, nuclear systems appear well suited to supplying baseload power, but the economics of fission seem to demonstrate that these power stations are not amenable to a distributed power generation scenario. Instead, these options appear to work best in a centralized power scheme.

Fusion

The oft dreamed future energy source is fusion. A challenging criteria for this brand of energy conversion is the so-called ignition point, which is when the nuclear

reactions become self-sustaining. Humans have transiently achieved ignition in the D-T reaction used by thermonuclear weapons:

$$^{2}\mathrm{H} + {}^{3}\mathrm{H} \longrightarrow {}^{4}\mathrm{He} + {}^{1}\mathrm{n}\,.$$

We can estimate the energy released by Einstein's mass-energy equivalence relationship, $E = mc^2$:

$$E = (\Delta m)c^2$$

$$= (m_{^{2}\mathrm{H}} + m_{^{3}\mathrm{H}} - m_{^{4}\mathrm{He}} - m_{^{1}\mathrm{n}})c^2$$

$$= (3.34 + 5.01 - 6.65 - 1.67)10^{-27}\mathrm{kg}(3.00 \times 10^{8}\mathrm{m/s})^2$$

$$E = \frac{2.70 \times 10^{-12}\mathrm{J}}{2\ \mathrm{atoms}}.$$

A more useful metric of comparison requires converting to the specific energy of an equimolar mixture of deuterium and tritium gas, the fuel, to:

$$\rho_E = \frac{1\mathrm{kg}}{1\mathrm{kg}} \times \frac{1000\mathrm{g}}{1\mathrm{kg}} \times \frac{4\mathrm{mol}}{(4.03 + 6.03)\mathrm{g}} \times \frac{6.02 \times 10^{23}\ \mathrm{atoms}}{1\mathrm{mol}} \times \frac{2.70 \times 10^{-12}\mathrm{J}}{2\ \mathrm{atoms}} = 3.23{\times}10^{14}\,\frac{\mathrm{J}}{\mathrm{kg}}$$

$$= 32.3 \times 10^{7}\,\frac{\mathrm{MJ}}{\mathrm{kg}}.$$

Recall that the specific energy of all reduced carbon on Earth works out to be about $30\frac{\mathrm{MJ}}{\mathrm{kg}}$ which pales in comparison to $32 \times 10^{7}\frac{\mathrm{MJ}}{\mathrm{kg}}$, reflecting the enormous potential of fusion. Unfortunately, we have never harnessed this reaction aside from displays of destruction or laboratory experiments.* Overcoming electrostatic repulsion, material compatibility with high neutron fluxes, and generating sufficient tritium are some of the major challenges facing development of the D-T reactor. We

*To frame the challenge, consider that the "spark" required to "ignite" is a fission explosion in a thermonuclear weapon.

are unlikely to achieve fusion by the same pathway as the Sun, the p-p pathway, because of a considerably lower (10^{-24}) nuclear cross section,[†] but there are other fusion reactions available with different properties.

Fission

Fission accounts for 4.44 % of all energy converted today. Natural uranium ore is 99.3 % ^{238}U and 0.7 % ^{235}U. Of the naturally occurring isotopes, only ^{235}U is fissile, meaning a nuclear reaction with a thermal neutron can lead to fission chain reactions. Typically, isotopic enrichment is performed to increase the ratio of ^{235}U/ ^{238}U for use as a fuel in a light water nuclear reactor, while heavy water reactors can use natural abundance uranium. Among the many different fission reaction pathways that occur, here is an example of a reaction representing the average fission fragment masses and energy:

$$^{235}\mathrm{U} + {}^{1}\mathrm{n} \longrightarrow {}^{236}\mathrm{U} \longrightarrow {}^{140}\mathrm{Xe} + {}^{94}\mathrm{Sr} + 2\,{}^{1}\mathrm{n}\,.$$

The specific energy for pure natural abundance uranium is calculated similarly to our fusion example above,

$$\rho_E = \frac{1\mathrm{kg}}{1\mathrm{kg}} \times \frac{0.7}{100} \times \frac{1000\mathrm{g}}{1\mathrm{kg}} \times \frac{1\mathrm{mol}}{235\mathrm{g}} \times \frac{6.02\times10^{23}\mathrm{atoms}}{1\mathrm{mol}} \times \frac{3.12\times10^{-11}\mathrm{J}}{1\mathrm{atom}} = 56{\times}10^{6}\frac{\mathrm{MJ}}{\mathrm{kg}}.$$

The specific energy of this fission reaction is poorer than our fusion example by a factor of ten but greater than that obtained from fossil fuels by about two million. The energy conversion of a nuclear power plant is limited by Carnot efficiency. As an aside, there is an example of a natural nuclear reactor that occurred in the Oklo region of central Africa millions of years ago when ^{235}U natural abundance was considerably higher, thereby allowing natural water to serve as a neutron moderator

[†]The nuclear cross section is the probability of nuclear fusion reaction rather than scattering.

for a system that released about 0.4 EJ over thousands of years![15]

Fission power plants have a capacity factor of around 0.90. The availability of uranium is of no immediate concern and a plethora of positive attributes of fission energy plants can be found detailed elsewhere,[16] but there are significant hurdles that prevent increased adoption in the US, such as high capital cost, construction delays, uncompetitive electricity pricing, engineering failures that erode the public's trust, no long-term storage of waste, and concerns about the proliferation of nuclear weapons. It is our opinion that additional reactors will be built in a free market when investors believe there is a profit to be made, which seldom appears to have been the case in recent memory, even with substantial government subsidies in place, such as the Price-Anderson Nuclear Industries Indemnity Act.

Indirect Nuclear

Power from wind has been practiced for more than a century, recently undergoing a renaissance and quickly gaining relevance as major player in electricity generation. Whereas, solar energy transformation with the use of photovoltaics has steadily accumulated momentum, and as a result, it is moving toward becoming a competitor with traditional electricity sources. One major problem with both options is their inherent intermittency, but they are not capitally intensive to construct at a small scale; this naturally lends to possible inclusion in distributed power generation scenarios. The advantage of a decentralized grid is that small pieces can be brought together over a wide area (lowering transmission losses and hour-by-hour intermittency), but distributed power will encounter power conversion losses on the order of < 10 %. Centralized power, on the other hand, will suffer from transmission losses likely on the order of < 10 %. Without storage, there are concerns the stability of the grid will be negatively impacted by large scale integration of intermittent power stations.[17]

Wind

As sunlight unevenly heats the surface of Earth, mass transfer through convective processes creates wind. Wind electricity generation depends on wind with a density, ρ, a velocity, v, passing through a turbine with a radius, r, and cross-sectional area, πr^2. The product of the kinetic energy and wind velocity gives the power:

$$P_{\text{wind}} = \frac{1}{2}\pi r^2 \rho v^3.$$

The power conversion is fundamentally limited by Betz's law to $\eta = 16/27$ but more practically reaches $\eta = 0.30$. Wind power complements raw solar energy because it peaks at night while solar peaks during the day. The altitude, blade size, and location all change the characteristics of the wind power that can be collected. Generally speaking, the capacity factor ($C_{\text{f}} = P_{\text{average}}/P_{\text{maximum}}$) is around 0.30. Another constraint is that wind turbines need to be spaced approximately $3 \times (2r)$ from one windmill to another. Among renewable energy sources, wind is one of the fastest growing in number of installations because it has already reached cost parity with natural gas in a variety of locations. Currently wind contributes to 4.7 % of total electricity generation within the United States.[18]

We can calculate the energy intensity of wind per day by,

$$\frac{E_{\text{daily, wind}}}{\text{area day}} = \frac{P_{\text{wind}} \times \eta \times C_{\text{f}} \times t}{\pi(3 \times (2r))^2} = \frac{\rho v^3 \eta C_{\text{f}} \times t}{72}.$$

For instance, in north-eastern Montana an average wind velocity, v, of 7.00 m/s at a height of 30 m can be assumed,[19] giving:

$$\frac{E_{\text{daily, wind}}}{\text{area day}} = \frac{(1.23\text{kg/m}^3)(7.00\text{m/s})^3 \times 0.30 \times 0.30 \times (60^2 \times 24)\text{s}}{72} = 4.56{\times}10^4 \frac{\text{J}}{\text{m}^2\text{day}}.$$

Solar Photovoltaics

Figure 1.6 compares the black body emission of the sun (attenuated by distance) and an AM0 spectrum. As we might expect, the irradiance reaching the Earth fairly matches a black body emission. Integration of AM0 tells us that $1.37\times10^3\,\frac{\mathrm{W}}{\mathrm{m}^2}$ travels to the planet; therefore, for our surface-area illuminated we must receive:

$$P_{\text{arriving}} = (\int \text{AM0})\times 2\pi R_{\text{earth}}^2 = (1.37\times10^3\frac{\mathrm{W}}{\mathrm{m}^2})2\pi(6.37\times10^6\mathrm{m})^2 = 5.56\times10^{16}\ \mathrm{W}$$

$$= 3.49\times10^5\ \mathrm{TW}.$$

As such, in about half an hour we receive all the energy the world demands in a year at current rates (552 EJ) and in about two hours we would have enough for a world with energy equality (2.2×10^3 EJ). There are additional constraints on a real-world system. More specifically, the power available per unit area is limited by the abledo; therefore, $((1-0.306)(1.37\times10^3\frac{\mathrm{W}}{\mathrm{m}^2})) = 951\frac{\mathrm{W}}{\mathrm{m}^2}$ is roughly what we expect at the surface.

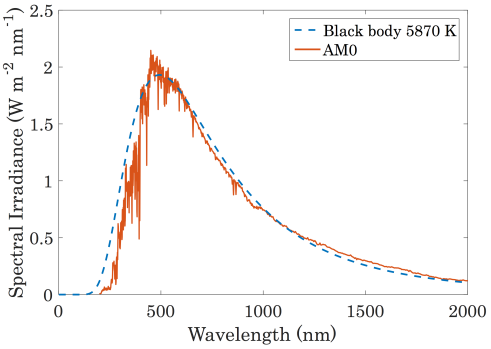

Figure 1.6: The black body emission is calculated as mentioned earlier, $B(\lambda,T)\times(\frac{R_\mathrm{s}}{R_\mathrm{d}})^2$. The AM0 spectrum is provided by NREL.[20] $\int_0^{10000}\mathrm{AM0}(\lambda)\,d\lambda = 1.37\times10^3\frac{\mathrm{W}}{\mathrm{m}^2}$.

Naturally, we do not expect to cover the entire surface of our planet with solar cells,

but some fraction could prove to be an important addition to our future energy portfolio. We will more closely examine the thermodynamic limits of photovoltaics (PV) in the next chapter, although commercial panels can reach $\eta = 0.20$ today and advanced multijunction cells are approaching $\eta = 0.50$.[21] One of the largest drawbacks hampering deployment of photovoltaics is the capacity factor for these power systems, which is about 0.30 for excellent installations using a single-axis tracking system. Considering these factors, the real energy intensity that can be converted on a daily basis is easily calculated from,

$$\frac{E_{\text{daily}}}{\text{area day}} = P_{\text{sun}} \times \eta_{PV} \times C_{\text{p}} \times t,$$

where E_{daily} is the daily energy converted per unit area, P_{sun} is the power of sunlight at the Earth's surface, η_{PV} is the efficiency of a solar cell, C_{p} is the capacity factor, and t is the number of seconds in a day. Now we can use values available today to estimate modern, $\frac{E_{\text{modern, PV, daily}}}{\text{area day}}$, and future, $\frac{E_{\text{future, PV, daily}}}{\text{area day}}$, energy intensities for PV:

$$\frac{E_{\text{modern, PV, daily}}}{\text{m}^2\text{day}} = 951\frac{\text{W}}{\text{m}^2} \times 0.20 \times 0.30 \times (60^2 \times 24)\text{s} = 4.93 \times 10^6 \frac{\text{J}}{\text{m}^2\text{day}},$$

$$\frac{E_{\text{future, PV, daily}}}{\text{m}^2\text{day}} = 951\frac{\text{W}}{\text{m}^2} \times 0.50 \times 0.30 \times (60^2 \times 24)\text{s} = 1.23 \times 10^7 \frac{\text{J}}{\text{m}^2\text{day}}.$$

As a point of comparison, the Palo Verde Nuclear Generating Station, the largest operating complex in these United States, harnesses 3.94 GW with $C_{\text{f}} = 0.98$ over 1.53×10^7 m^2 or

$$\frac{E_{\text{nuclear, daily}}}{\text{m}^2\text{day}} = \frac{3.94 \times 10^9 \times 0.98 \times (60^2 \times 24)}{1.53 \times 10^7 \text{m}^2} = 2.18 \times 10^7 \frac{\text{J}}{\text{m}^2\text{day}}.$$

Thus, the energy intensity of nuclear is a factor of four better than modern high-

density PV and only a factor of two better than future PV, which suggests that in certain regions with proper solar insolation PV may be viable under a number of different scenarios, such as when land is low cost or the area is on a rooftop. Not surprisingly, PV must cover this area cheaply in order to compete economically. As a consequence, the components must also be affordable to make the economics favorable. Within a short period of time, solar's total share has crept up to 0.6 % of the total US electricity generation total.[18]

An essential hypothesis is that no single source will necessarily dominate the immediate future energy landscape (aside from fossil fuels), but cooperation among different systems could enable a shift in energy holdings before our untimely exhaustion of these valuable supplies. In light of the massive potential of solar energy, in terms of what is available from the sun and its relatively high energy intensity, we focus the rest of this thesis on advancing PV.

1.5 Theme of Thesis: Intermittent Energy Storage

The architecture of traditional electrical grids relies on large dispatchable centralized power stations with high capacity factors. These grids have virtually no storage, and their supply is synchronized in tune with demand. Intermittent supplies, such as solar and wind, are a key challenge facing large-scale integration of renewable energy sources.[17,22] Consquently, there is considerable interest in storing this energy. There are some promising methods of electrical storage, such as pumped hydro or compressed air, but they rely on relatively specific geological features. Thermal and chemical energy storage are largely location insensitive, but chemical storage takes the center stage of our focus.

Among the chemical storage options are traditional batteries, such as lead-acid or lithium-ion; unconventional batteries, such as redox-flow; and chemical fuels, by means of water splitting or carbon dioxide reduction.

Chemical storage largely falls within the field of electrochemistry. The specific properties of a battery depend on the chemistry involved, and some chemistries are better suited for specific applications than others. Lead-acid batteries offer cheap storage with a specific energy around 9×10^4 J/kg. This makes them great for small applications (as in a car starter), but as weight becomes important, larger densities as in electric cars are required. For that reason, expensive lithium-ion batteries, offering 4.5×10^5 J/kg, become more attractive.

The key properties for grid-level electricity storage are high-cycle lifetimes (both Pb-acid and Li-ion suffer in this regard), the speed of charging or discharging, scalability (instead of depending on modules, tanks can be easily fitted to change the volumes in a reservoir), and low cost. Redox-flow batteries are promising systems to use in this application.

More broadly, energy storage has more stringent requirements than the chemistry used in electrical storage. This is where the field of artificial photosynthesis sits. In the best case, we could reduce CO_2 to liquid fuels, such as methanol, with renewable power plants, and then, use existing infrastructure to transport stored energy for use in a traditional combustion engine. Unfortunately, the chemistries are fiendishly difficult. From a chemical point of view, water splitting is more tractable, and as a chemical fuel, H_2, has attractive qualities.

The principal focus of this thesis sits at the boundary between redox-flow batteries and artificial photosynthesis. We argue that electrical storage is a goal we are closer to realizing, but we hope that advancements made toward our goal will also simultaneously benefit the field of artificial photosynthesis as a whole.

Our goal of supplanting fossil fuels with alternative energy sources is challenging. Solar PVs are capable as supplemental sources during peak hours of sunlight, and large installations are already being deployed across the globe, but we must move

faster and a way to do this may be by enabling the storage of intermittent electricity.

Specifically, we (in Chapter 1) explore the limits of fossil fuels as a sole provider of energy in a world with energy equality; show how human emissions of CO_2 occur at a large enough scale to shift the temperature of the planet; explore the landscape of renewable energy sources while focusing our attention on solar photovoltaics due to its immense potential; and explain why we are focused on using redox-flow chemistry to store solar energy for electricity consumption. After understanding our broad goal, we outline our specific device goals (in Chapter 2) for our system with a photocathode and photoanode and we model device efficiencies for different configurations of our system. By Chapter 3 we introduce a cathode catalyst, which displays promising activity. We integrated this newly developed material with silicon microwire arrays in Chapter 4. Chapter 5 details efforts towards a photoanode. Inside Chapter 6, we provide an overview of where we have come, where we have fell short, and what still needs to be done. Additionaly there is also an exploration of our catalyst (in Appendix B), another strategy to protect silicon (Appendix C), the synthesis of complex nanominerals by PLAL (Appendix D), and the academic impact our work has had (Appendix E).

1.6 References

(1) Census, *International Data Base World Population: 1950-2050*, 2015, http://www.census.gov/population/international/data/idb/worldpopgraph.php (visited on 08/6/2016).

(2) *BP Statistical Review of World Energy*, 2016, http://www.bp.com/en/global/corporate/energy-economics/statistical-review-of-world-energy.html (visited on 08/6/2016).

(3) NAP, *Energy in Transition, 1985-2010: Final Report of the Committee on Nuclear and Alternative Energy Systems*, 2010, http://www.nap.edu/catalog/11771.html (visited on 08/6/2016).

(4) IEA, *Final World Energy Consumption by Sector (2013)*, 2015, http://www.iea.org/Sankey/#?c=World&s=Final%20consumption (visited on 08/6/2016).

(5) P. Wurfel and U. Wurfel, *Physics of Solar Cells*, Wiley-VCH, Weinheim, 2nd edn., 2009.

(6) A. A. Bartlett, *Math. Geol.*, 2000, **32**, 1–17.

(7) D. Hafemeister, *Renewable Energy*, Springer New York, New York, NY, 2014.

(8) N. S. Lewis and D. G. Nocera, *Proc. Natl. Acad. Sci. U.S.A.*, 2006, **103**, 15729–35.

(9) H. B. Gray, *Nat. Chem.*, 2009, **1**, 7.

(10) H. Hartman and C. P. McKay, *Planet. Space Sci.*, 1995, **43**, 123–128.

(11) *BP Workbook of historical statistical data from 1965-2015 Systems*, 2015, http://www.bp.com/content/dam/bp/pdf/energy-economics/statistical-review-2016/bp-statistical-review-of-world-energy-2016-full-report.pdf (visited on 08/6/2016).

(12) IPCC, *Climate Change 2013: The Physical Science Basis. Contribution of Working Group I to the Fifth Assessment Report of the Intergovernmental Panel on Climate Change*, Cambridge University Press, Cambridge, United Kingdom and New York, NY, USA, 2013, p. 1535.

(13) NASA, *Planetary Fact Sheet - Metric*, 2015, http://nssdc.gsfc.nasa.gov/planetary/factsheet/index.html (visited on 08/6/2016).

(14) S. Arrhenius, *Philosophical Magazine Series 5*, 2009, **41**, 237–276.

(15) F. Gauthier-Lafaye, P. Holliger and P. L. Blanc, *Geochim. Cosmochim. Acta*, 1996, **60**, 4831–4852.

(16) D. McKay, *Energy Without the Hot Air: Chapter 24 Nuclear?*, 2015, https://www.withouthotair.com/c24/page_161.shtml (visited on 08/6/2016).

(17) B. Sovacool, *Util Policy*, 2009, **17**.

(18) *EIA:What is U.S. electricity generation by energy source?*, 2016, https://www.eia.gov/tools/faqs/faq.cfm?id=427&t=3 (visited on 08/6/2016).

(19) NREL, *NREL WindExchange: Montana 30-Meter Wind Map*, 2015, http://apps2.eere.energy.gov/wind/windexchange/windmaps/residential_scale_states.asp?stateab=mt (visited on 08/6/2016).

(20) *NREL: Reference Solar Spectral Irradiance: Air Mass 1.5*, 2000, http://rredc.nrel.gov/solar/spectra/am1.5/ (visited on 08/6/2016).

(21) *NREL: Best Research-Cell Efficiencies*, 2016, http://www.nrel.gov/ncpv/images/efficiency_chart.jpg (visited on 08/6/2016).

(22) M. Z. Jacobson, M. A. Delucchi, M. A. Cameron and B. A. Frew, *Proc Natl Acad Sci*, 2015, **112**, 15060–5.

Chapter 2

System Concept

A prominent role for solar energy in the future requires technical solutions to its intermittent nature and cost. An integrated light collector and storage system could rise to the challenge if it takes advantage of the distributed nature of solar energy. Widespread adoption requires covering a large area with cheap components, which must have reversible chemical reactions, affordable light absorbing materials with high quantum yields, and utilization of abundant electrocatalysts with high activities. What differs from many strategies herein is that we propose using redox-flow chemistry to store the electricity. Instead of splitting water, as would be needed for energy storage, we will split hydrobromic acid for distributed electricity storage by using only light provided by the sun as an input into an integrated device. We begin by reviewing historical efforts on this path, and then, estimate device thermodynamic limits. Finally, we outline our idealized device construction, and describe specific challenges facing our path towards efficient HBr splitting.

2.1 Project Illinois

Among factors that precipitated the 1970s energy crisis, declining oil production within the United States in 1970 made her particularly susceptible to the effects of the OPEC oil embargo of 1973. As a result of the change in trade, prices of oil rapidly increased throughout the country with significant effects. The fact that oil was limitless had been taken for granted, and so this shock initiated a surge of interest in developing alternatives to fossil fuels, culminating in the installation of rooftop thermal solar panels on the White House in 1979 by President Jimmy Carter.

During this time period, rationing of retail gasoline was commonplace,* in addition to federal measures, such as a mandated maximum speed limit of 55 mph that was meant to curb consumption.[1]

Simultaneously, Jack Kilby — co-inventor of the integrated circuit — took a leave of absence from Texas Instruments (TI) in 1970 to pursue independent inventing.[2] Perhaps sensing an opportunity in the growing energy crisis, Kilby initiated conceptual work on a solar electricity storage system using hydrogen iodide in 1973. By 1975 he had refined his idea with Jay Lathrop (former researcher at TI and then professor of electrical engineering) and Arthur Porter (former researcher at TI and then professor at nearby Texas A&M), resulting in a series of patents they filed on the concept.[3–5] They extended earlier efforts within TI and made high-quality spherical solar cells from cheap polysilicon.

Initial experimental work occurred at Texas A&M, but then TI brought this work into their Central Research Laboratory under the code name "Project Illinois" (for Kilby's undergraduate alma mater) in 1976. Scientists within the company characterized the project as risky, but technically sound. By 1978, TI had further refined the concept to include a roof-top residential installation with spherical, hydrogen-bromide-splitting solar cells, which were internally equipped with a fuel cell to generate electricity. To make this idea a reality, TI sought outside funding from the Department of Energy (DOE) because of significant investments elsewhere in the company, such as in personal computing. John Deutch, then Director of Energy Research at the DOE, immediately recognized the significance of the program and supported the formation of a cooperative agreement between TI and the DOE in 1978.

The terms of the agreement were unusual for the time but necessary in light of the significant energy crisis. Over four years, TI would supply $4 million (14.8 million

*An even/odd number of a leading digit on license plate indicated on what days (even/odd) the consumer could purchase automobile fuel.

inflation adjusted 2016 dollars), and the DOE would provide $14 million (51.8 million) for the development of an economical system. In the event a commercial product was brought to market, the $14 million would have been repaid as a portion of the proceeds. With this agreement in hand, the TI Solar Energy System (TISES) development was underway. By 1980, the first TISES development module was completed; in 1981 the first prototype system module was demonstrated.

TISES used four components: the solar chemical converter (SCC), a metal-based hydrogen storage unit, a fuel cell to produce electricity from the stored chemical potential, and a heat exchanger. After exposing the system with solar energy, both electrical and thermal energy would be available for output to a residence. We focus only on the component relevant to this thesis, the SCC. The solar-to-hydrogen efficiency ($\eta_{\mathrm{STH,HBr}}$) achieved by their highest functional cell was $\eta_{\mathrm{STH,HBr}} = 9.5$ %.[6] We begin ascertaining the limits of this value in the next section.

The SCC array consisted of spherical silicon micro-sized crystals embedded in a glass matrix and immersed in the aqueous electrolyte. These microcrystals were chosen to bring down the costs of the light absorber. The spheres were either n^+-on-p or p^+-on-n type for the cathode and anode, respectively. The sphere tops, when exposed to the solution, were coated by a Pt/Ir alloy acting as a protective and electrocatalytic film, while ohmic back-contact was provided by a thin metal film (see Figure 2.1 for a cross-sectional diagram of the component). Another important piece was the membrane, Nafion, that separated the anode and cathode half-reactions and prevented self-discharge. The fuel cell subsystem releases electricity by running the reverse reaction of the SCC. The chemistry of the SCC is straightforward and facile.

As light hits the photoanode, oxidation of bromide to bromine takes place:

$$2\,\mathrm{HBr} + \mathrm{Light} \longrightarrow \mathrm{Br_2} + 2\,\mathrm{H^+} + 2\,\mathrm{e^-}\cdot$$

And at the photocathode, reduction of protons occurs with light:

$$2\,\mathrm{H^+} + 2\,\mathrm{e^-} + \mathrm{Light} \longrightarrow \mathrm{H_2}\cdot$$

These two half-reactions contribute to an overall reaction of

$$2\,\mathrm{HBr} + \mathrm{Light} \longrightarrow \mathrm{Br_2} + \mathrm{H_2}\cdot$$

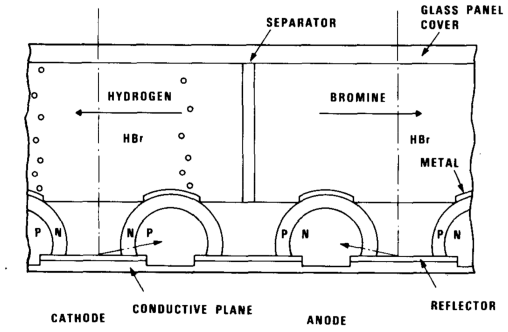

Figure 2.1: Cross section of TISES Solar Chemical Converter. (Used with permission from W. McKee, *IEEE* Transactions on Components, Hybrids, and Manufacturing, **1982**, *5*(4), pp 336-341. Copyright 1982 IEEE.

By 1981, an oil glut appeared under the first term of President Ronald Reagan.[7] This signaled the end of the 1970s energy crisis.[7] The Reagan Administration substantially reduced energy research outlays by 50 %.[7] As a result, the DOE had to revisit the TI cooperative agreement for the 1981 and 1982 fiscal years; instead, the DOE provided $5.3 million, and TI provided $12.5 million for Project Illinois, totaling $17.8 million (65.3 million, factoring in inflation). By the end of the project (1983), the team had succeeded in all technical aspects, and the system was ready for

further development at the pilot-plant level. Due to declining interest in alternative energy, from the uncertainties in the economics and marketability, TI divested from this project by 1985, although spherical solar cells were pursued for some time thereafter. Symbolically marking the end of a chapter in our history, the Reagan administration removed solar panels from the White House in 1986.

Among commercial endeavors, TISES was one of the largest industrial research projects using semiconducting components for electrical storage. Another smaller effort was made between 2009 and 2014 by a start-up called Sun Catalytix, which raised a total of $14.5 million. As a part of a pivot from unsuccessful water splitting, Sun Catalytix briefly investigated electricity storage using haloacids, such as HBr, before the company was acquired by Lockheed Martin for their patented technology on redox-flow batteries using metal-ligand coordination compounds.[8] Reportedly, they are trying to scale up this technology for grid-level electricity storage applications.

2.2 Limits of Solar Energy Power Generation

This section of the chapter focuses on building a thermodynamic foundation from which to determine the limits of solar-to-chemical power generation. The upper-limit of efficiency observed by TI was $\eta_{\mathrm{STC,\,HBr}} = 0.095$, but we would like to ascertain the theoretical upper-limits to this conversion for different devices to make an informed choice of configuration and materials. In this chapter we perform calculations using theoretical estimates on optimized systems not yet constructed, but that are perhaps within reach in the coming decade. For a single light absorber, the oxidation and reduction reactions happen on the same material, but as we have predicted here efficiencies will be lower than a more complex system using two semiconductors. When using two light absorbers, we can either configure them in series or in parallel. For the parallel system, the efficiency is slightly better than a

single-absorber, although the in series system far exceeds both counterparts.

We borrow a simple theoretical approach, refined by Ross, to our specific case.[9,10] Practically, we would like to understand the factors that control the magnitude of η_{power}, where $\eta_{\text{power}} = \frac{\text{extracted power}}{\text{incoming power}}$. The incoming power, of course, is determined by photons of the correct energy from the sun and passing from space through the atmosphere, ultimately reaching the semiconductor surface — see Figure 2.2 for the photon flux density versus wavelength at the surface, according to a standard used in the testing of solar devices. To determine the maximum power attainable a considerable discussion will follow. We start from values that are out of reach and then subsume different parasitic losses until we have the minimum number of necessary parameters needed to describe efficiencies for a wide range of materials and configurations.

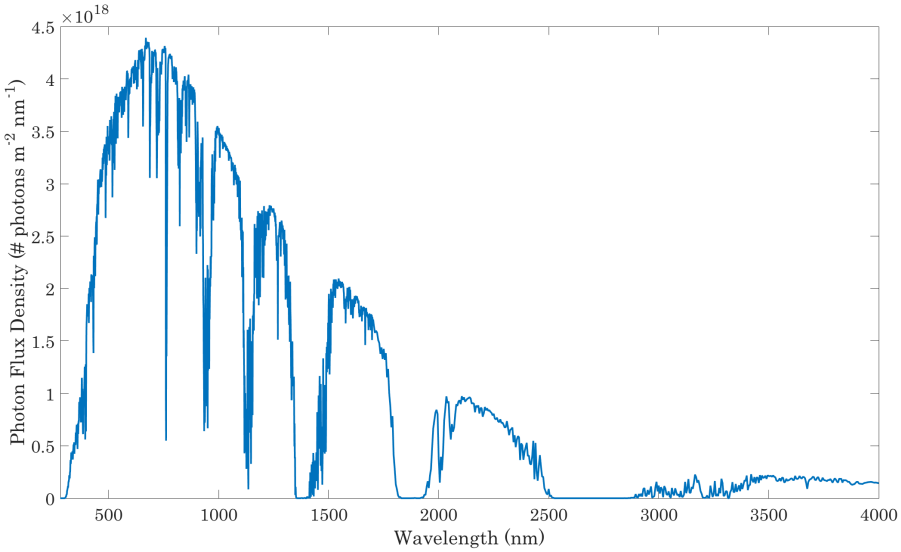

Figure 2.2: Photon flux density of AM1.5D spectrum,[11] which refers to the number of photons arriving at each wavelength that have passed through the atmosphere of Earth when the sun's zenith is 48.2° and the surface is tilted at 37°, representing average conditions, directly illuminating the light absorber.

Apparent Power Yield

The statistical distribution of quasi-particles in a semiconductor is perturbed by incoming photons with an energy greater than the band gap (E_g), that is the difference in energy between the ground state (valence band) and excited state (conduction band) of the semiconductor. Moreover, there is an absorption of light with an energy greater than $E_g = hc/\lambda_g$. It is important to point out that both the valence and conduction bands represent a continuum of states and that we care about both the valence band maximum energy, called the valence band edge, and the conduction band minimum energy, called the conduction band edge. One real key to the operation of a PV solar cell is spatially separating the excited-state electrons from the holes left behind in the valence band before they can recombine; another key is exploiting carefully tuned interfacial energetics so that electrons and holes can be shuttled through an external circuit where power can be extracted.

The rate of excitation, J_e, is calculated by,

$$J_e = \int \sigma I_s \, d\lambda, \tag{2.1}$$

where I_s is the photon flux density of sunlight reaching the installation, and σ is the absorption cross section of the material. Roughly speaking, we say that $\sigma = 1$ for $hc/\lambda > E_g$, and $\sigma = 0$ for $hc/\lambda < E_g$. In a real material a distribution — reflected in the natural line width of absorption spectra — exists at the boundary, but we neglect this to simplify analysis.

The absorption of a photon with sufficient energy results in the excitation of an electron from the valence band to the conduction band. For photons with energies greater than the band gap, energy is lost in the form of phonons (eventually heat) — this process occurs on the timescale of picoseconds (10^{-12}s) until the electron reaches the conduction band edge where it can rest for milliseconds (10^{-3}s).[12] Thus,

any excited-state electrons will have an energy determined by the band gap, hc/λ_g. Naively one might calculate the apparent power yield, P_{yield}, in the vain of obtaining a reasonable estimate on the extractable power. This power yield is calculated as the product of the excitation rate and the associated energy of the band gap:

$$P_{\text{yield}} = J_{\text{e}} \frac{hc}{\lambda_g}.$$

As will soon become clear, this quantity does not represent useful power. The maximum power extractable from the system is governed by thermodynamics and commensurately depends on a detailed balance. Our balance must account for gains and losses; therefore, in our next case, energy is lost through the form of light emission from the semiconductor.[13]

Semiconductor Light Emission

We follow the energy balance by determining the entropy for photons exiting and entering a semiconductor. More importantly, we keep in mind the fact that the entropy change, ΔS, is related to the change in energy, ΔE, at a constant temperature, T, by way of a simple relationship, $\Delta S = \frac{\Delta E}{T}$. In addition, the energy of a photon is related to the wavelength, λ, simply as, $E = \frac{hc}{\lambda}$. Recall that the black body photon flux density is calculated from Planck's law by,[12]

$$I_{BB,SC} = \frac{2hc^2}{\lambda^5} \frac{1}{\exp(\frac{hc}{k_{\text{B}} T_{\text{sc}} \lambda}) - 1} \frac{\lambda}{hc}.$$

Solving for the reciprocal temperature of the semiconductor (T_{sc}^{-1}) gives:

$$T_{\text{sc}}^{-1} = \frac{\lambda k_{\text{B}}}{hc} \ln\left(\frac{2c}{I_{\text{BB, SC}} \lambda^4} + 1\right).$$

To find the entropy for every photon departing the electromagnetic field, the entropy

per photon ($-\partial S/\partial N = (hc/\lambda)/T$) is set equal to the black body intensity of the semiconductor,

$$-\frac{\partial S}{\partial N} = \frac{hc/\lambda}{T} = k_{\mathrm{B}} \ln\Big(\frac{2c}{I_{\mathrm{BB,\,SC}}\lambda^4} + 1\Big).$$

Now we utilize the fact that the chemical potential difference between the band edges, μ, controls the resulting entropy change per absorbed photon within the semiconductor at temperature, T_{sc}, in order to formulate:

$$\frac{\partial S}{\partial N} = \frac{hc/\lambda - \mu}{T_{\mathrm{sc}}}.$$

Equating the entropy changes for the electromagnetic field and the semiconductor, and then solving for $I_{\mathrm{BB,SC},\mu}$ results in:

$$-k_{\mathrm{B}}\Big(\ln(\frac{2c}{I_{\mathrm{BB,SC,mu}}\,\lambda^4} + 1)\Big) = \frac{hc/\lambda - \mu}{T_{\mathrm{sc}}}$$

$$I_{\mathrm{BB,SC},\mu} = \frac{2c}{\lambda^4}\Big[\exp\Big(\frac{hc/\lambda - \mu}{T_{\mathrm{sc}}k_{\mathrm{B}}}\Big) - 1\Big]^{-1}.$$

Now, we use the insight that the term "−1," above, corresponds to stimulated emissions and therefore, is neglected to give:

$$\begin{aligned} I_{\mathrm{BB,SC},\mu} &= \frac{2c}{\lambda^4}\Big[\exp\Big(\frac{hc/\lambda - \mu}{T_{\mathrm{S}}k_{\mathrm{B}}}\Big)\Big]^{-1} \\ &= \frac{2c}{\lambda^4}\exp\Big(\frac{\mu - hc/\lambda}{T_{\mathrm{sc}}k_{\mathrm{B}}}\Big) \\ &= \frac{2c}{\lambda^4}\exp\Big(\frac{\mu}{T_{\mathrm{sc}}k_{\mathrm{B}}}\Big)\exp\Big(\frac{-hc/\lambda}{T_{\mathrm{sc}}k_{\mathrm{B}}}\Big). \end{aligned}$$

Recognizing that the rate of radiative emission, J_{r}, from the semiconductor is the

integrated product of the intensity and surface area results in:

$$\begin{aligned} J_{\mathrm{r}} &= \int \sigma I_{\mathrm{BB,\,SC},\mu}\, d\lambda \\ &= \exp\left(\frac{\mu}{T_{\mathrm{sc}} k_{\mathrm{B}}}\right) \int \sigma \frac{2c}{\lambda^4} \exp\left(\frac{-hc/\lambda}{T_{\mathrm{sc}} k_{\mathrm{B}}}\right) d\lambda \end{aligned}$$

$$\approx \exp\left(\frac{\mu}{T_{\mathrm{sc}} k_{\mathrm{B}}}\right) \int \sigma I_{\mathrm{BB,\,SC}}\, d\lambda\,. \tag{2.2}$$

Maximum Potential Power

We use the expression from 2.2 for the rate of emission from the semiconductor to balance incoming and outgoing fluxes of photons.* The maximum potential, μ_{max}, is less than the apparent band gap due to entropic losses, and it is calculated by letting the flux of photons entering and exiting a semiconductor equal one another ($J_{\mathrm{e}} = J_{\mathrm{r}}$):

$$\mu_{\mathrm{max}} = k_{\mathrm{B}} T_{\mathrm{sc}} \ln\left(\frac{\int_0^{\lambda_0} I_{\mathrm{S}}\, d\lambda}{\int_0^{\lambda_0} I_{\mathrm{BB}}\, d\lambda}\right). \tag{2.3}$$

This has given us the tools required to express a power smaller than the apparent yield, based on the maximum potential:

$$P_{\mathrm{potential}} = J_{\mathrm{e}} \mu_{\mathrm{max}}.$$

This relationship does not capture losses due to the quantum yield of the electronic processes occurring within the material, so it should be unsurprising the that maximum power will be lower still.

*The maximum chemical potential, or Gibbs free energy, is by definition a reversible process: thus an equal rate of excitation and radiative recombination (emission) must occur.

Maximum Power

The maximum extractable power, P_{power}, depends on the product of the chemical potential, rate of excitation, and internal losses (i.e., not contributing to the extracted work in a resistive circuit or a chemical transformation):

$$P_{\text{power}} = \mu_{\text{power}} J_{\text{e}} (1 - \phi_{\text{loss}}),$$

where ϕ_{loss} accounts for both radiative ($J_{\text{r}}/J_{\text{e}}$) and nonradiative losses (α) in the form of

$$\phi_{\text{loss}} = \alpha \frac{J_{\text{r}}}{J_{\text{e}}}. \tag{2.4}$$

Plugging in equation 2.2, expression 2.1, and equality 2.3 into the formula 2.4 results in:

$$\phi_{\text{loss}} = \alpha \exp\left(\mu_{\text{power}}/k_{\text{B}}T_{\text{sc}}\right) \frac{\int \sigma I_{\text{BB}}\, d\lambda}{\int \sigma I_{\text{S}}\, d\lambda}$$

$$\ln\left(\phi_{\text{loss}}\right) = \ln\left(\alpha\right) + \left(\mu_{\text{power}}/k_{\text{B}}T_{\text{sc}}\right) + \ln\left(\frac{\int \sigma I_{\text{BB}}\, d\lambda}{\int \sigma I_{\text{S}}\, d\lambda}\right)$$

$$\mu_{\text{power}} = k_{\text{B}}T_{\text{sc}} \ln\left(\phi_{\text{loss}}\right) - k_{\text{B}}T_{\text{sc}} \ln\left(\alpha\right) + k_{\text{B}}T_{\text{sc}} \ln\left(\frac{\int \sigma I_{\text{S}}\, d\lambda}{\int \sigma I_{\text{BB}}\, d\lambda}\right)$$

recognize that $\mu_{\text{max}} = k_{\text{B}}T_{\text{sc}} \ln\left(\dfrac{\int_0^{\lambda_0} I_{\text{S}}\, d\lambda}{\int_0^{\lambda_0} I_{\text{BB}}\, d\lambda}\right)$

$$\mu_{\text{power}} = \mu_{\text{max}} + k_{\text{B}}T_{\text{sc}} \ln\left(\phi_{\text{loss}}\right) - k_{\text{B}}T_{\text{sc}} \ln\left(\alpha\right).$$

A plot comparing the energy conversion efficiency for the yield ($\eta_{\text{yield}} = \frac{P_{\text{yield}}}{\text{incoming power}}$), potential ($\eta_{\text{potential}} = \frac{P_{\text{potential}}}{\text{incoming power}}$), and extractable power ($\eta_{\text{power}} = \frac{P_{\text{power}}}{\text{incoming power}}$) for different band gap materials is shown in Figure 2.3. Silicon, with $E_{\text{g}} = 1.12$ eV, has an estimated efficiency of around $\eta_{\text{power}} = 0.319$, which is equivalent to the Shockley-Queisser limit.[13] As silicon is perched near the maximum, it is should be

unsurprising to find that silicon solar cells are ubiquitous. The theory just described is used as a foundation for what we call the "μ_{power}" approximation in Appendix A.

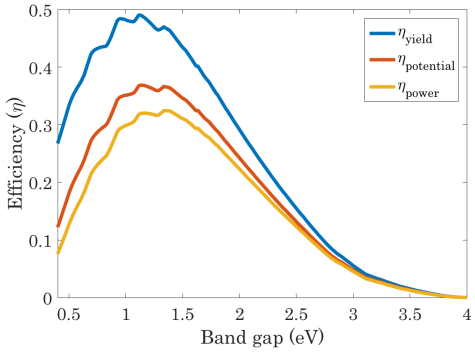

Figure 2.3: Different estimates of the efficiencies depend on the band gap of the semiconductor for the η_{yield} (blue), $\eta_{\text{potential}}$ (red), and η_{power} ($\alpha = 1$, yellow) assuming illumination by AM1.5D.

2.3 Basis Set of Parameters to Model Solar Cells

In this section we discuss the basis set of metrics used for the characterization of a solar cell. An important expression to describe solar cell behavior is the ideal diode equation:

$$J = J_0[\exp(\frac{qV}{nk_{\text{B}}T_{sc}}) - 1] - J_{\text{L}},$$

where J represents net current density flow, J_0 is the dark saturation current density (reflecting recombination occurring within the material), q is the electron charge, n is the ideality factor, V is the applied voltage across the cell, and J_{L} is the photocurrent. Simple demonstrations of this equation reveal important metrics used in performance assessments of solar devices.

Setting $J = 0$ and solving for V reveals:

$$V_{\text{oc}} = \frac{nkT}{q} \ln(\frac{J_{\text{L}}}{J_0} + 1),$$

where we call V_{oc} the open-circuit potential, which represents the maximum potential the system can produce. We use the theory described in the previous section to estimate this value, letting $V_{oc} = \mu_{power}/q$. A plot of the band gap versus the V_{oc} for $\alpha = 1$ or $\alpha = 2$ or $\alpha = 320$,* shown in Figure 2.4, gives a V_{oc} of 0.751 V , 0.733 V, and 0.601 V for silicon solar cells.

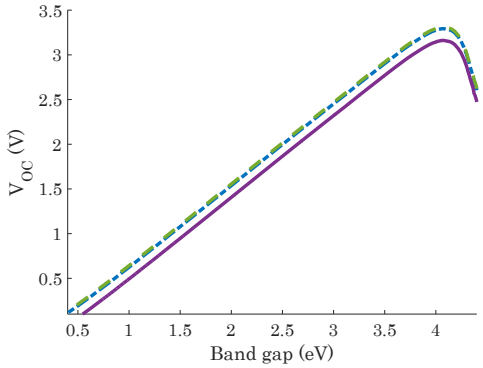

Figure 2.4: Predicted V_{oc} vs band gap for two cases, $\alpha = 1$ (green) and $\alpha = 2$ (blue) to represent idealistic and future values, respectively. Purple reflects obtainable values where $\alpha = 320$.

If we let $V = 0$ in the ideal diode law, then $J = J_{sc} = J_L$. We call J_{sc} the short-circuit current density. The photocurrent, or short-circuit current density, can be calculated from the excitation rate by way of:

$$J_L = J_{sc} = \beta \int_0^{\lambda_0} q J_e \, d\lambda,$$

where β represents (as we define for semi-empircal analysis) the probability of absorbing photons and includes realistic losses such as reflection. In Figure 2.5 we plot the band gap versus J_{sc}. This tells us that for silicon we should be able to reach 43.8, 41.6, and 35.1 mA/cm^2 for $\beta = 1.0$, $\beta = 0.95$, and $\beta = 0.80$.

The J_0 parameter reflects the rate of recombination processes occurring in a solar cell. A full treatment would require a more realistic theory that reflects the micro-

*Recall that we use α as a semi-emprical parameter that reflects losses in a semiconductor.

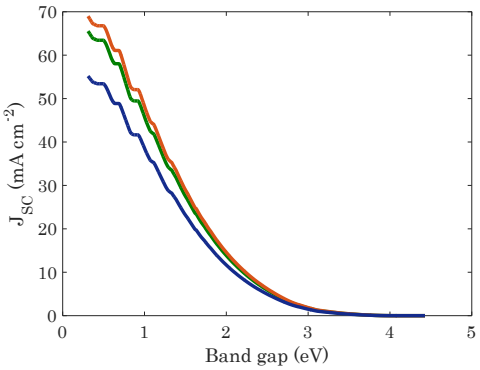

Figure 2.5: Predicted J_{sc} vs band gap for AM1.5D solar illumination with $\beta = 1.0$ (blue), $\beta = 0.95$ (green), and $\beta = 0.80$ (blue).

scopic structure of a photodiode, but in our simpler treatment here we rely on our other parameters to estimate J_0 by:

$$J_0 = \frac{J_L}{\exp(\frac{\mu_{max}}{qnkT}) - 1}.$$

Now we are in a position to simulate a J–V curve for a solar cell (drawn in Figure 2.6 is a silicon solar cell example). This is a natural point to illustrate how to determine another metric. In the Figure 2.6 there is a green box that represents the maximum power obtainable from the system. Graphically, this factor is found by using the maximum power point ($\frac{dP}{dV} = 0$), which has a corresponding voltage (V_{MP}) and power (P_{MP}). The rectangle starts at the origin with its width determined by V_{MP} and its height determined by finding the corresponding current for V_{MP}, which we call the maximum power point current (J_{MP}). This metric is aptly called the fill factor (when ratioed to the total incoming power):

$$\text{ff} = \frac{V_{MP} J_{MP}}{V_{oc} J_{sc}}.$$

Our final value of interest is the solar-to-electricity efficiency (η_{PV}), a value calcu-

lated by way of:

$$\eta_{\mathrm{PV}} = \frac{V_{\mathrm{oc}} J_{\mathrm{sc}} \mathrm{ff}}{P_{\mathrm{in}}}.$$

We demonstrate our simulated metric values for silicon compared to a series of research cells in Table 2.1. Our idealistic simulated silicon solar cell ($\alpha = 2, \beta = 0.95$) is slightly better than demonstrated champion research cells but should be in reach within the decade. The realistic simulated silicon solar cell ($\alpha = 320$ and $\beta = 0.80$) is within reach today.

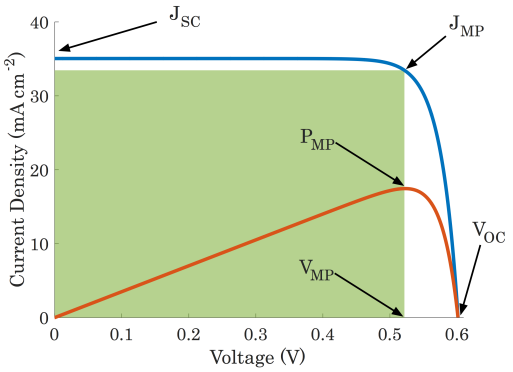

Figure 2.6: Predicted silicon solar cell J–V curve. Blue line represents the solar cell characteristic according to the diode equation. The orange line represents the power ($V \times J$) and at its maximum is the maximum power point, the green rectangle represents the maximum power the solar cell can supply to a resistive load.

Silicon Solar Cell	V_{oc} (V)	J_{sc} (mA/cm^2)	ff (%)	η_{PV} (%)
Simulated (Ideal)	0.733	41.6	87.5	26.7
Simulated (Realistic)	0.601	35.1	82.8	17.5
SunPower	0.737	41.3	82.7	25.2
Kaneka	0.738	40.8	83.5	25.1
Fraunhofer	0.718	42.1	83.2	25.1
UNSW	0.706	42.7	82.8	25.0

Table 2.1: Basis set of solar cell parameters used for the description of performance and comparison of silicon simulated value with high-performing silicon samples.[14]

2.4 Butler–Volmer Kinetic Model Effects on Ideal Diode

Our interest in using the solar cell to directly drive an electrochemical engine means that we must consider parasitic voltage losses from electrocatalysis. A central equation used for electrochemical kinetics is the Butler–Volmer model,[15] *

$$j = j_0(\exp(\frac{\alpha_{\mathrm{CT,a}} F \eta_{\mathrm{op}}}{RT}) - \exp(\frac{-\alpha_{\mathrm{CT,c}} F \eta_{\mathrm{op}}}{RT})),$$

where j is the current density, j_0 is the exchange current density (representing the equilibrium rate of reactions), α_{CT} is the charge-transfer coefficient (which depends on the Tafel slope) for either the anodic or cathodic reaction, F is Faraday's constant, R is the ideal gas constant, T is the temperature, and η_{op} is the overpotential.

A solar cell in isolation will always have better characteristics than a device driving an electrochemical reaction. Since we are not extracting work the easy way, the voltages for our device are coupled in the following way:

$$V_{\mathrm{device}}(J_{\mathrm{d}}) = V_{\mathrm{solar\ cell}}(J_{\mathrm{d}}) + \eta_{\mathrm{catalysis}}(J_{\mathrm{d}}),$$

where $V_{\mathrm{device}}(J_{\mathrm{d}})$ is the voltage of the device and depends on the current of the device (J_{d}), $V_{\mathrm{solar\ cell}}(J_{\mathrm{d}})$ is the voltage of the solar cell, and $\eta_{\mathrm{catalysis}}(J_{\mathrm{d}})$ is overpotential voltage required in the Bulter–Volmer model. J–V curves for a device are calculated by numerically finding, both, their matching currents and their respective voltages, and then, using the voltage relationship above to eventually find a solution where both boundary conditions are satisfied. The effect of the losses encountered during catalysis is illustrated in Figure 2.7. Simply put, real catalysts impose additional voltage requirements on the overall process, in addition to the internal losses we

*You may notice some vague similarities in form of the ideal diode law to this model, and this is no coincidence because it results from the similar underlying physical models used to describe the two phenomena.

account for in the last section.

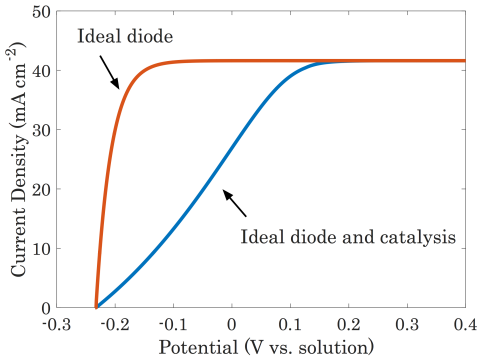

Figure 2.7: Predicted silicon solar cell J–V curve with catalysis. Orange line represents the ideal diode response while the blue line incorporates losses due to the voltage losses from the kinetics of catalysis. In this case we are assuming a single absorber is poorly carrying out both catalysis for the oxidation and reduction half-reactions for HI splitting.

Our model, outlined in the previous sections, captures the core behavior of a semiconductor driving an electrochemical reaction and allows estimations of the magnitude of the effect different parameters have on an overall device efficiency. However, there are several limitations of the simulations used in our discussion below. Among the many factors our model does not include are:

- Light absorption by the solution (this becomes significant as Br_2 concentrations increase);
- Membrane resistance (membranes, such as Nafion, introduce a transport resistance);
- Solution resistance (real liquid electrolytes have a non-zero resistance);
- Internal solar cell resistance (often, real devices have shunt and series resistance components);
- Recombination is being explicitly modeled (explicit modeling of the kinetics for recombination will yield more accurate results);

- Exact device cell geometry is considered for mass transport purposes (the specific construction of a device has a real impact on the resulting performance);
- Mass transport limitations in the Bulter–Volmer model.

2.5 Comparison of Estimated Device Efficiencies for HBr and H_2O Splitting

Now that we are equipped to estimate solar-to-hydrogen efficiency (η_{STH}) for a device, we define this efficiency as:

$$\eta_{\mathrm{STH}} = \frac{J_{\mathrm{MP,\,BV}} \times E_{\mathrm{f}}}{P_{\mathrm{in}}},$$

where $J_{\mathrm{MP,\,BV}}$ is the current density maximum power point for a diode limited by Bulter–Volmer overpotentials, and E_{f} is the difference in the formal potentials between the two-half reactions for either HBr splitting (1.09 V) or H_2O splitting (1.23 V), resulting in either $\eta_{\mathrm{STH,HBr}}$ or $\eta_{\mathrm{STH,H_2O}}$, respectively. We consider three different device configurations and their attributes. The first system uses a single semiconductor while the second system exploits two semiconductors sitting side-by-side, and the third system has two semiconductors in a stacked structure, where the top material absorbs and transmits light to the bottom semiconductor, as determined by the band gap. In Table 2.2 we list the parameters used for devices developed in the future ("idealistic") and for devices that could be made today ("realistic"). Former results are in the next section while the latter results are given in Appendix A.

Reaction	$\alpha_{CT,a}$	$j_{0,a}$	$\alpha_{CT,c}$	$j_{0,c}$	α	β
(Idealistic) H_2O Splitting	0.4402	0.02378	1.66	2.736	2	0.98
(Idealistic) HBr Splitting	1.66	2.736	1.66	2.736	2	0.98
(Realistic) H_2O Splitting	0.4402	0.02378	1.66	2.736	320	0.80
(Realistic) HBr Splitting	1.66	2.736	1.66	2.736	320	0.80

Table 2.2: Parameters used in simulations of efficiency for solar devices driving either water or hydrobromic acid splitting. The "idealistic" values for the PV are obtained from Table 2.1 while the Butler–Volmer parameters come from a fit of experimental data[16] (this same source also documents an excellent analysis of water splitting) for the hydrogen evolution reaction and oxygen evolution reaction (the HBr anode will have similar characteristics to the HER). The "realistic" values for the PV are obtained from a semiemprical fit of α and β to the best values observed in our laboratory.

Single Absorber

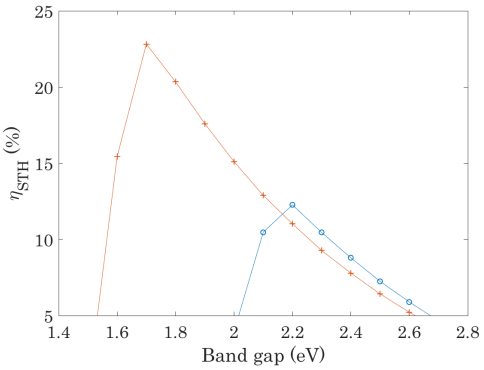

Figure 2.8: The red "+" represents the efficiency for HBr splitting and the blue circles represent H_2O splitting using a single light absorber. Used with permission from C. Roske.

In Figure 2.8, η_{STH} is determined for a range of band gaps driving either HBr or H_2O splitting. Significant voltage losses are encountered for the oxygen-evolving half-reaction due to sluggish kinetics; therefore, a material with a 2.20 eV band gap is required to provide a sufficient driving force for water splitting at η_{STH,H_2O} = 12.3 %. The anodic half-reaction for HBr splitting is considerably more facile and hence higher efficiencies are possible for a 1.80 eV band gap material of $\eta_{STH,HBr}$ = 22.3 %. Cu_2O with a band gap of 2.17 eV might be desirable for water splitting in this scheme. One candidate material for HBr splitting would be CdSe, with a band

gap of 1.74 eV. The results from simulations with realistic parameters are shown in Figure A.1. The beauty of this configuration is that it only requires a single absorber although the sensitivity of the ultimate efficiency highly depends on the quality and band gap of the specific material.

Dual Light Absorbers: Side-by-Side

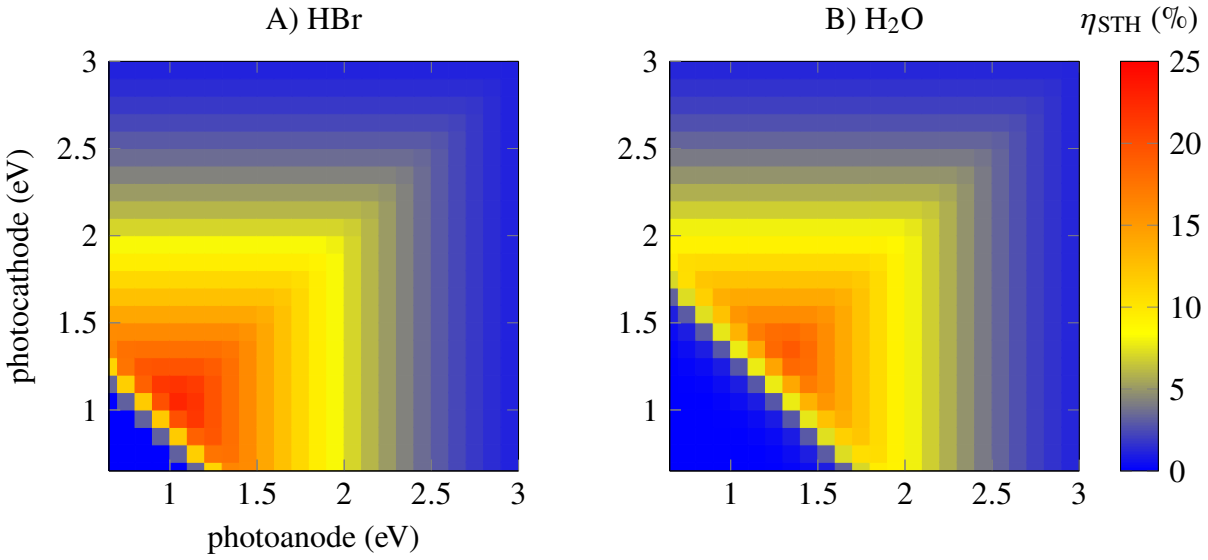

Figure 2.9: This calculation shows the solar-to-hydrogen efficiency (η_{STH}) for two equivalent devices consisting of side-by-side semiconductors connected in parallel using A) HBr splitting and B) H_2O splitting.

In Figure 2.9, we consider two semiconductors sitting side-by-side and connected in parallel at their back-contact. Here, considerably higher efficiencies are possible compared with a single-absorber, especially for water splitting using a wider range of materials. The optimum system for H_2O splitting has two 1.30 eV band gap semiconductors working at η_{STH,H_2O} = 19.5 % while, for HBr splitting the ideal system is two 1.10 eV materials sitting side-by-side producing η_{STH,H_2O} = 22.8 %. For the water splitting system, this might be InP (1.35 eV) or GaAs (1.43 eV) while for hydrobromic acid splitting silicon (1.12 eV) or MoS_2 (1.23 eV) may be optimal. Realistic results are shown in Figure A.2. One of the benefits to the side-by-side

configuration is its wide accommodation of different materials, including those with the same band gap.

Dual Light Absorbers: Tandem

In Figure 2.10, our two systems are configured with a light absorber on top and bottom of a stack. These efficiencies are considerably higher than other competing configurations. For H_2O splitting, a 1.70 eV top and 1.00 eV bottom configuration could give $\eta_{STH,H_2O} = 26.2$ %, and for HBr splitting, a 1.50 eV top and 0.700 eV bottom could give $\eta_{STH,HBr} = 30.0$ %. An example of a system for water electrolysis would be a CdSe top and a Cu_2SnS_3 bottom. While for our haloacid, a Zn_3P_2 top and a Ge bottom could be optimal. Realistic results are shown in Figure A.3. While the tandem, stacked, configuration has the best absolute performance for a well-optimized system, it also has considerable specific challenges, listed below.

1. The band gaps of the two layers must be different for any non-zero efficiency, so in other words, two high-quality semiconductors are needed in a single device.

2. Growing two dissimilar semiconducting materials epitaxially remains a very difficult endeavor, although there are common ways around this.

3. Minimizing mass transport limitations requires careful engineering for tandem structures.

4. Manufacturing complexity increases considerably.

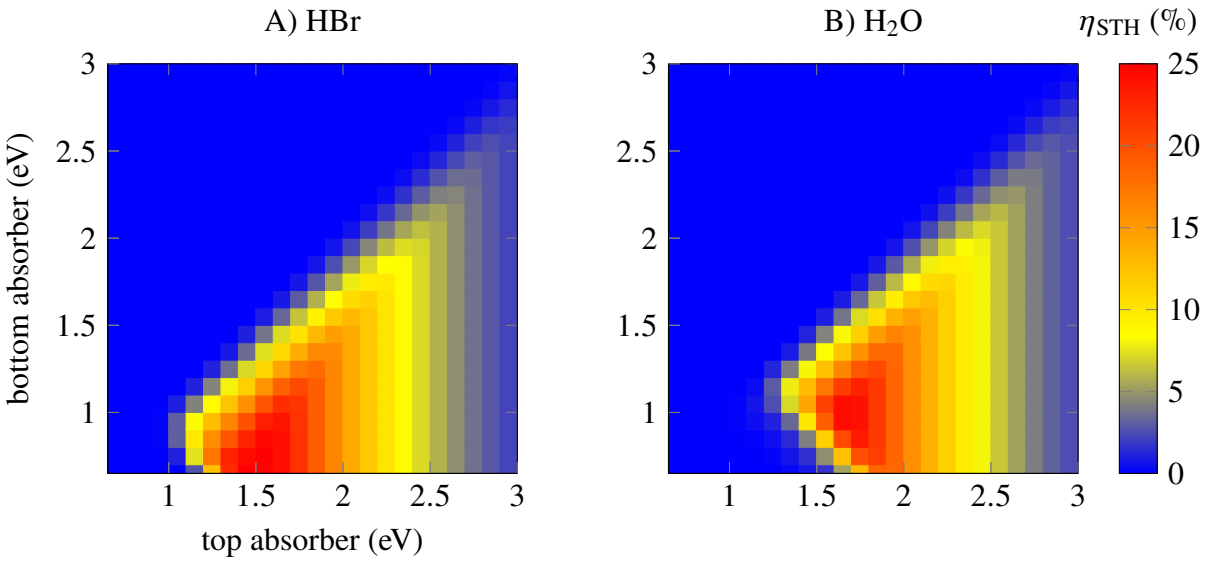

Figure 2.10: This calculation shows the η_{STH} for two equivalent devices consisting of stacked (photoanode on top) semiconductors using A) HBr splitting and B) H_2O splitting.

2.6 Proposed Device Layout

While the tandem structure is the ultimate envisioned device, it has been very hard in practice to build in our laboratories. The single absorber is promising, but we do not have expertise with the materials most suitable for either water or hydrobromic acid splitting. This leaves us with the side-by-side configuration. For HBr splitting, silicon (a material we have a strong understanding of and expertise in handling) would work as both a photocathode and photoanode; therefore, this is the configuration and material we pick. An ultimate efficiency of $\eta_{STH,\,HBr} = 22.8$ % is the theoretical upper-limit, but in our hands $\eta_{STH,\,HBr} = 11.0$ % is more likely to be obtained as reflected by our "realistic" simulation.

In Figure 2.11 the proposed device layout is depicted. It consists of a photoanode and photocathode made of silicon microwires embedded in a glass matrix (to protect the underlying metal back-contact and provide mechanical stability to the wires). Ideally, above the glass matrix is where the electrocatalysts would sit, hopefully avoiding parasitic light absorption by using a reflective layer coating of TiO_2 particles. Above

(I)dealistic (R)ealistic	Configuration	$\eta_{\text{STH, HBR}}$ (%)	$\eta_{\text{STH, H}_2\text{O}}$	E_g HBr (eV)	E_g H_2O
I	S[a]	22.3	12.3	1.80	2.20
I	SBS[b]	22.8	19.5	1.10/1.10	1.30/1.30
I	T[c]	30.0	26.2	1.50/0.70	1.70/1.00
R	S[a]	16.2	8.6	1.80	2.30
R	SBS[b]	17.2	14.2	1.20/1.20	1.70/1.70
R	T[c]	22.2	19.3	1.60/0.900	1.80/1.20
R	SBS[b]	11.0	–	1.10/1.10	–

Table 2.3: This table uses either (I)dealistic or (R)ealistic parameters (defined in Table 2.2). The first six rows represent the maximum efficiencies for those scenarios and the respective band gaps. The realistic value for H_2O splitting compare well with the literature.[16]
[a] S is for (S)ingle light absorber.
[b] SBS is for (S)ide-(B)y-(S)ide configuration.
[c] T is for (T)andem or stacked configuration.

all, the light absorbers are cheap and high-quality silicon microwires. Between the anode and cathode sits a membrane separator, likely Nafion. At the photoanode oxidation occurs, producing bromine, free protons, and electrons (shuttled to the photocathode). At the photocathode, free protons and electrons are consumed to yield H_2(g). In essence, this would be a modern rendition of the TISES, but we would like to lower the costs of the materials even further with earth-abundant materials and microwires more readily manufactured at scale .

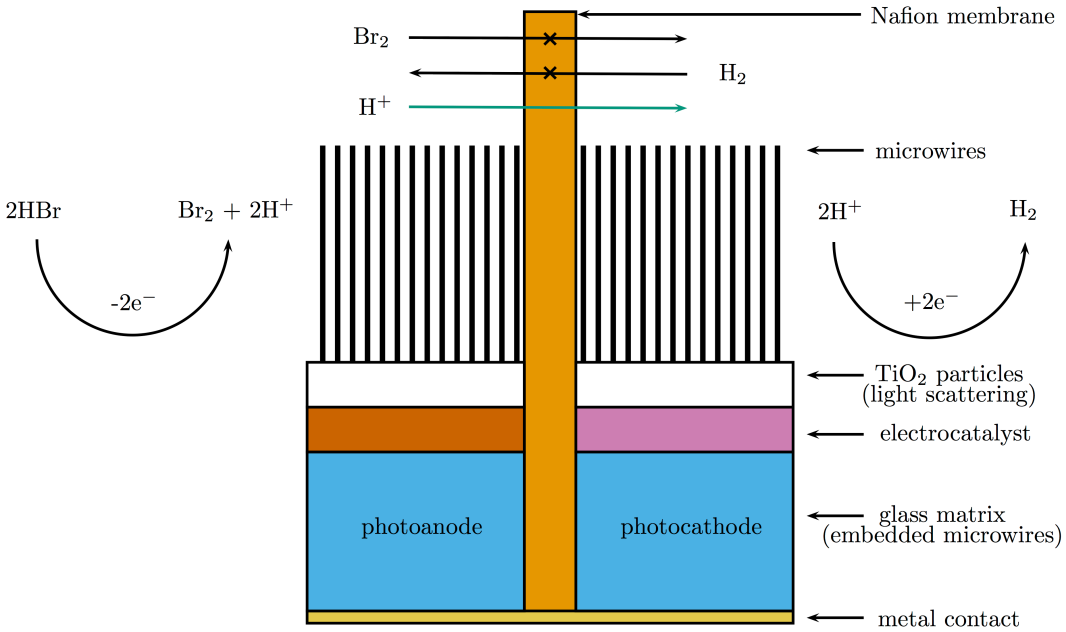

Figure 2.11: In the presence of aqueous hydrobromic acid, hydrogen and bromine will be generated upon irradiation of the integrated photosystem:
$2\,HBr + Light \longrightarrow H_2 + Br_2$.

2.7 Challenges Facing HBr Splitting

The outline of what we must accomplish is as follows:

1. We need high quality microwires of silicon as a light absorber for both a cathode and anode;
2. We must stabilize the photoanode;
3. We must stabilize the photocathode at its resting state;
4. We need an earth-abundant cathode catalyst that has a low overpotential for the hydrogen evolution reaction in acidic media;
5. We need an earth-abundant anode catalyst that has a low overpotential for halide oxidation;
6. We will assess the stabilities of the resulting components;
7. We would need to integrate both components in a complete system.

2.8 Conclusions

One promising strategy to break the world from its dependence on fossil fuels is by massive solar energy conversion. Successful implementation of large-scale solar energy capture may require driving chemical reactions. Semiconductors are suitable materials to capture and convert sunlight into usable power with high efficiency. We suggest that an integrated device capable of collecting solar energy and storing it in chemical potential is a worthwhile goal. In this scheme, a careful choice is required when selecting a compatible combination of materials (for light absorption) and chemical reactions (for storing energy as chemical potential). Silicon has an ideal band gap (1.12 eV) for solar absorption, but silicon cannot drive water splitting ($2\,H_2O \longrightarrow 2\,H_2 + O_2$) because its electronic structure prevents generation of a sufficient photovoltage. Instead, two silicon electrodes connected in parallel can carry out hydrobromic acid splitting ($HBr \longrightarrow H_2 + Br_2$). Modeling with realistic parameters suggests that the ultimate solar to hydrogen conversion η_{STH} is optimized for a device with a band gap of 1.1 eV to 1.2 eV would be ideal for HBr splitting in a side-by-side configuration, with a potential to make between 11 % to 17 %. Silicon, with a band gap of 1.12 eV has the potential to make $\approx$ 12 % in this scenario. Unfortunately, earlier efforts by TI used precious metals to catalyze the two half-reactions and protect the silicon. Our device needs to use earth-abundant materials to both catalyze the relevant half-reactions and protect the underlying silicon electrodes at low cost. In Chapter 3 we introduce a candidate cathode catalyst compatible with strongly acidic solutions. Then, in Chapter 4, we integrate this catalyst with a silicon photocathode. Finally, in Chapter 5 we introduce a method to protect a silicon photoanode from oxidation, but ultimately fail to catalyze the anodic half-reaction without a Pt catalyst.

2.9 References

(1) D. Hafemeister, *Renewable Energy*, Springer New York, New York, NY, 2014.

(2) *Jack Kilby*, 2016, http://www.ti.com/corp/docs/kilbyctr/jackstclair.shtml.

(3) E. L. J. J. S. K. J. W. L. J. S. McFerren and D. J. Meyers, *US Pat.*, 4 173 494, T. Instruments, 1979.

(4) J. S. Kilby, J. W. Lathrop and W. A. Porter, *US Pat.*, 4 021 323, T. Instruments, 1977.

(5) J. S. Kilby, W. R. McKee and W. A. Porter, *US Pat.*, 31 473, T. Instruments, 1983.

(6) J. D. Luttmer and I. Trachtenberg, *J. Electrochem. Soc.*, 1985, **132**, 1312.

(7) J. Skea, *Energy and Environmental Science*, 2014, **7**.

(8) J. Goeltz, D. Amadeo, A. Esswein, T. D. Jarvia, E. R. King, S. Y. Reece and N. Tyagi, *US Pat.*, Patent Pending, Lockheed Martin Advanced Energy Storage, 2013.

(9) R. T. Ross and T.-L. Hsiao, *J. Appl. Phys.*, 1977, **48**, 4783.

(10) R. T. Ross, *The Journal of Chemical Physics*, 1966, **45**, 1–7.

(11) *NREL: Reference Solar Spectral Irradiance: Air Mass 1.5*, 2000, http://rredc.nrel.gov/solar/spectra/am1.5/ (visited on 08/6/2016).

(12) P. Wurfel and U. Wurfel, *Physics of Solar Cells*, Wiley-VCH, Weinheim, 2nd edn., 2009.

(13) W. Shockley and H. J. Queisser, *J. Appl. Phys.*, 1961, **32**, 510.

(14) M. A. Green, K. Emery, Y. Hishikawa, W. Warta and E. D. Dunlop, *Prog. Photovoltaics Res. Appl.*, 2016, **24**, 3–11.

(15) M. G. Walter, E. L. Warren, J. R. McKone, S. W. Boettcher, Q. Mi, E. A. Santori and N. S. Lewis, *Chem. Rev.*, 2010, **110**, 6446–73.

(16) L. C. Seitz, Z. Chen, A. J. Forman, B. A. Pinaud, J. D. Benck and T. F. Jaramillo, *ChemSusChem*, 2014, **7**, 1372–85.

Chapter 3

Highly Active Electrocatalysis of the Hydrogen-Evolution Reaction by Cobalt Phosphide Nanoparticles

Reproduced with permission from E.J. Popczun; C.G. Read*; C.W. Roske*; N.S. Lewis; R.E. Schaak. *Angew. Chem.*, **2014**, *126*, 5531-5534. Copyright 2014 Wiley.

3.1 Abstract

Nanoparticles of cobalt phosphide, CoP, have been prepared and evaluated as electrocatalysts for the hydrogen evolution reaction (HER) under strongly acidic conditions (0.50 M H_2SO_4, pH 0.3). Uniform, multi-faceted CoP nanoparticles were synthesized by reacting Co nanoparticles with trioctylphosphine. Electrodes comprised of CoP nanoparticles on a Ti support (2 mg/cm^2 mass loading) produced a cathodic current density of 20 mA/cm^2 at an overpotential of −85 mV. The CoP/Ti electrodes were stable over 24 h of sustained hydrogen production in 0.50 M H_2SO_4. The activity was essentially unchanged after 400 cyclic voltammetric sweeps, suggesting long-term viability under operating conditions. CoP is therefore amongst the most active, acid-stable, earthabundant HER electrocatalysts reported to date.

3.2 Introduction

The hydrogen-evolution reaction (HER), which generates molecular hydrogen through the electrochemical reduction of water, underpins many clean-energy technologies. Platinum, the most widely used HER catalyst, requires very low overpotentials to generate large cathodic current densities in the highly acidic solutions that are used for water electrolysis in proton-exchange membrane systems.[1–3] However, Pt is expensive and relatively scarce in the Earth's crust, limiting the utility of Pt in

energy systems deployed at global scale. Active, acid-stable alternative HER electrocatalysts include the molybdenum-based MoS_2,[2,4] MoB,[5] Mo_2C,[5,6] $NiMoN_x$,[7] and $Co_{0.6}Mo_{1.4}N_2$ systems,[8] as well as several first-row transition metal dichalcogenides.[9] Alloys of Ni–Mo,[10] Ni–Mo–Zn,[11] Ni–Fe,[12] and Ni–P,[13] along with Ni/NiO/$CoSe_2$ nanocomposites,[14] are active HER electrocatalysts, but are not stable in acidic solutions.

Recently, nanoparticulate films of Ni_2P, comprised of inexpensive and earth-abundant elements, have been reported to show high HER activity, requiring an overpotential of −130 mV to produce cathodic current densities of −20 mA/cm^2 in 0.50 M H_2SO_4.[15] Like MoS_2,[2,16] Ni_2P is also a hydrodesulfurization (HDS) catalyst,[17,18] which suggests that other known HDS catalysts may also be active HER catalysts. We report herein that CoP, a known metal phosphide HDS catalyst that is structurally and compositionally distinct from Ni_2P,[18] is a highly active and acid-stable HER catalyst, exhibiting an overpotential (η) of −85 mV at a current density (j) of −20 mA/cm^2 (at a mass loading of 2 mg/cm^2), as well as stability over 24 h of operation in 0.50 M H_2SO_4.

3.3 Materials and Methods

To synthesize the CoP nanoparticles, 9 ± 1 nm diameter spherical nanoparticles of ϵ-Co (Figure B.1) were prepared by the decomposition of $Co_2(CO)_8$ in 1-octadecene (ODE), oleylamine (OLAM), and nonanoic acid (NA) at 230 °C, followed by addition of oleic acid (OLAC).[19] To form CoP, the ϵ-Co nanoparticles were then reacted for 1 h at 320 °C with trioctylphosphine (TOP) in ODE and OLAM. (See Supporting Information for full experimental details.)

3.4 Results and Discussion

Figures 3.1a and 3.1b show representative transmission electron microscope (TEM) images of the CoP nanoparticles, which were quasi-spherical, multi-faceted, uni-

form, and hollow, with an average diameter of 13 ± 2 nm. The hollow morphology is the result of a nanoscale Kirkendall effect, which often occurs for metal phosphide nanoparticles that have been synthesized by reaction of the metal nanoparticle templates with TOP.[20–24]

Selected-area electron-diffraction (SAED) (Figure 3.1c) showed that the nanoparticles adopted the MnP structure type expected for CoP,[25] whereas energy dispersive X-ray spectroscopy (EDS) (Figure B.2) indicated a 45:55 Co:P ratio, which is consistent within experimental error with the expected 1:1 stoichiometry of CoP. The powder X-ray diffraction (XRD) pattern (Figure 3.2a) confirmed that the bulk sample consisted of high-purity MnP-type CoP. Scherrer analysis of the peak widths of the XRD pattern for the CoP nanoparticles indicated an average grain size of 12 nm, which is consistent with the particle diameters observed by TEM, and suggests that the particles were largely single crystalline. HRTEM (Figure 3.1d) confirmed that the CoP particles were single crystalline, with observed lattice spacings of 2.4 Å that intersected in a manner consistent with expectations for the closely spaced (102) and (111) planes of MnP-type CoP (Figure 3.1e).

The HER electrocatalytic activity of the CoP nanoparticles was evaluated in 0.50 M H_2SO_4. Working electrodes were prepared by applying CoP nanoparticle samples to 0.2 cm^2 titanium supports with CoP loading densities of 0.9 and 2 mg/cm^2, respectively. Ti electrodes were chosen because Ti is not an active HER catalyst and because Ti promoted adhesion of the CoP nanoparticle catalysts, while remaining chemically inert. The Ti/CoP electrodes were heated at 450 °C in H_2/Ar to remove the organic ligands, and the powder XRD pattern (Figure 3.2b) confirmed that the nanocrystalline CoP phase persisted after this treatment. Figure 3.3a shows polarization data for representative Ti/CoP electrodes at two distinct mass loadings, along with polarization data obtained under identical conditions for uncoated Ti foil electrodes as well as for Pt, which is a benchmark HER electrocatalyst. Ten

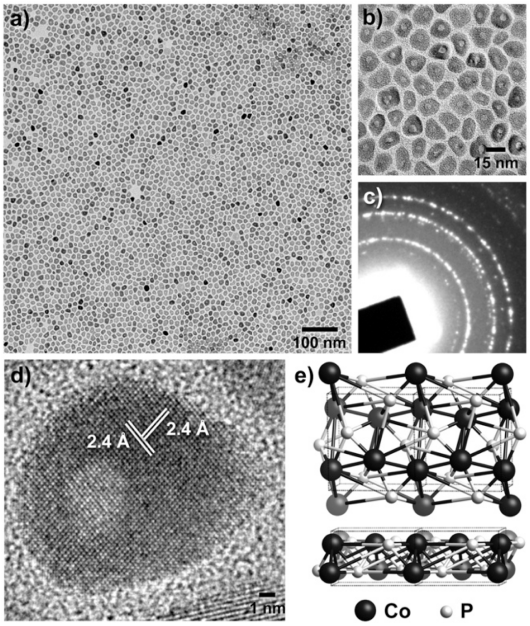

Figure 3.1: (a,b) TEM images, (c) SAED pattern, and (d) HRTEM image of CoP nanoparticles. (e) Two views of the MnP-type crystal structure of CoP.

Ti/CoP electrodes, from several different CoP nanoparticle samples, were tested and showed highly consistent HER activities. The CoP nanoparticles produced a cathodic current density of -20 mA/cm^2 at an overpotential of -95 mV for a mass loading of 0.9 mg/cm^2 (i.e.$\eta_{-20\text{mA/cm}^2} = -95$ mV) and exhibited $\eta_{-20\text{mA/cm}^2} = -85$ mV for a mass loading of 2 mg/cm^2. In contrast, the Ti foil electrode was not an active HER catalyst, as expected, under these conditions.

These overpotentials compare favorably to the values reported at similar current densities and mass loadings for other acid-stable, Earth-abundant HER electrocatalysts, including Ni_2P ($\eta_{-20\text{mA/cm}^2} = -130$ mV),[15] Mo_2C on carbon nanotubes ($\eta_{-10\text{mA/cm}^2} = -152$ mV),[6] and MoS_2 ($\eta_{-20\text{mA/cm}^2} = -175$ mV),[4] and also compare favorably to, but are somewhat larger than, the behavior exhibited by the Pt control electrode ($\eta_{-20\text{mA/cm}^2} = -25$ mV). The overpotentials exhibited by the CoP nanoparticles are also comparable to that of Ni$-$Mo nanopowder ($\eta_{-20\text{mA/cm}^2} = -80$ mV),[10] which is not stable under acidic conditions when Ni^{2+}

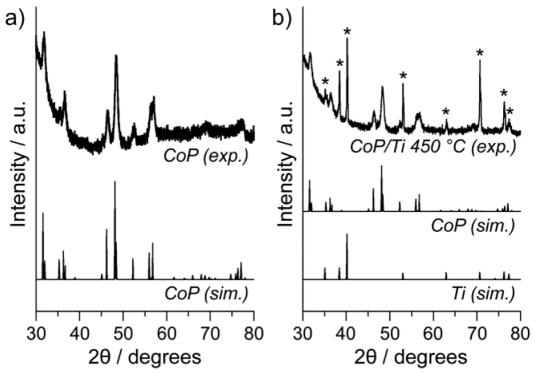

Figure 3.2: Powder XRD patterns for (a) as-synthesized CoP nanoparticles (top, experimental; bottom, simulated) and (b) a CoP/Ti electrode annealed at 450 °C (top, experimental; bottom, simulated for CoP and Ti). In (b), peaks marked with an asterisk (*) correspond to the Ti substrate.

is formed, and the $\eta_{-20\text{mA/cm}^2}$ for CoP is significantly smaller than $\eta_{-20\text{mA/cm}^2}$ for comparable catalytic systems that are unstable in acid, including Ni/NiO/$CoSe_2$ nanocomposites ($\eta_{-20\text{mA/cm}^2} \approx -120$ mV).[14] Porous nanosheets of isostructural FeP have been reported to catalyze the HER, but at significantly higher overpotentials ($\eta_{-20\text{mA/cm}^2} \approx -300$ mV for 0.28 mg/cm^2) than that of CoP, with unknown acid stability.[26] Ni_5P_4, as bulk pellets of nanocrystalline powders, also has been recently reported to be a highly active HER electrocatalyst in both acidic and alkaline solutions.[27]

The slope of the Tafel plot [overpotential vs. log(cathodic current density)] for the Pt control (Figure 3.3b) was ≈ 30 mV/decade, which is consistent with that expected for the known HER mechanism on Pt. In contrast, the Tafel slope for representative CoP/Ti electrodes (Figure 3.3b) was ≈ 50 mV/decade, independent of mass loading. This value does not correspond to one of the standard HER Tafel slopes (29, 38, and 116 mV/decade),[28] indicating that the mechanism of the HER on CoP/Ti is different from that on Pt. However, similar Tafel slopes have been reported for other non noble-metal catalysts, such as MoS_2 (50 mV/decade),[29] Mo_2C (55 mV/decade),[29] and Ni_2P (46 mV/decade).[15] The HER exchange current density of

the CoP nanoparticle catalysts was $\approx 1.4 \times 10^{-4}$ A/cm^2, which is comparable to that exhibited by Ni_2P nanoparticles as HER electrocatalysts under acidic conditions.[15]

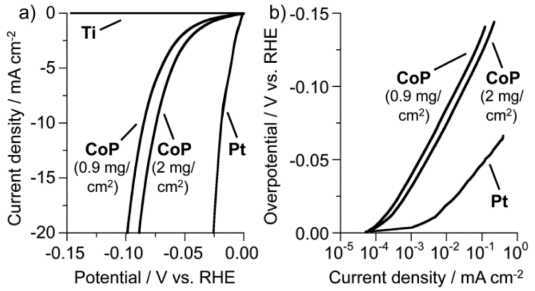

Figure 3.3: (a) Polarization data in 0.50 M H_2SO_4 for CoP nanoparticle electrodes at mass loadings of 0.9 and 2 mg/cm^2, along with a Ti foil and Pt for comparison. (b) Corresponding Tafel plots for the CoP and Pt electrodes

To determine the faradaic yield for hydrogen evolution, a CoP/Ti working electrode was held at -20 mA/cm^2 for 6.94 h. The amount of H_2 collected over 6.94 h was consistent with the amount of charge passed through the system (100 C), indicating essentially 100 % faradaic efficiency for the HER. The amount of hydrogen produced also compared favorably with that produced by a Pt control cathode over the same time period. Complete decomposition of the catalyst would have produced gaseous byproducts that would account for less than 1 % of the gas volume that was observed experimentally. This stable chemical behavior, coupled with the observed long-term acid stability of the material (confirming that significant degradation did not occur), therefore indicates that the CoP nanoparticle catalyst is capable of sustained electrocatalytic H_2 production in acidic media.

The CoP nanoparticles had a measured Brunauer-Emmett-Teller (BET) surface area of 59.1 m^2/g. Using this surface area, the turnover frequency (TOF) was calculated to be 0.046 s^{-1} at $\eta = 100$ mV. As a benchmark, the upper limit of the surface area was estimated based on average particle geometry and size (e.g. 13 nm spheres) to be 71.9 m^2/g, and this procedure yielded a TOF of 0.038 s^{-1}. (See Supporting Information for detailed calculations.) These TOF values are estimates because the

specific active sites are not known and because the calculations do not account for porosity or for surfaces that are inaccessible because of contacts between particles. However, the TOF values estimated based on both the experimental and theoretical surface areas are mutually comparable and compare favorably to the TOF values at $\eta = -100$ mV for Ni_2P nanoparticles (0.015 s^{-1}) and Ni-Mo nanopowder (0.05 s^{-1}).[10,15]

To evaluate the stability of the CoP nanoparticles during repeated cycling in acidic solutions, accelerated degradation studies were performed on representative CoP/Ti electrodes having mass loadings of 0.9 mg/cm^2. As shown in Figure 3.4a, the CoP nanoparticles exhibited no measurable loss of activity after 400 cyclic voltammetry (CV) sweeps between +5 mV and −140 mV (vs. the reversible hydrogen electrode potential, RHE). The production of a current density of −20 mA/cm^2 initially required an overpotential of −95 mV, whereas the overpotential changed to ≈ −90 mV after 400 cycles, demonstrating high stability under strongly acidic conditions. In addition to the accelerated degradation studies, galvanostatic measurements at a current density of −20 mA/cm^2 in a pre-electrolyzed solution indicated that the overpotential increased in magnitude only slightly (25 mV) over 24 h (Figure B.3) of continuous operation. Some particle desorption from the substrate (and therefore a slight decrease in mass loading) is the likely cause of this small increase in overpotential.

X-ray photoelectron spectroscopy (XPS) survey data (Figure B.3) indicated that the surface of the as-prepared CoP/Ti electrode consisted primarily of carbon and oxygen, as expected from the organic surface-stabilizing agents. Co, P, and Ti were also present. After annealing the CoP/Ti electrode at 450 °C, the carbon signal nearly disappeared, consistent with the expected removal of the capping ligands. High-resolution XPS data for the annealed CoP/Ti electrode showed two characteristic Co 2p peaks, with binding energies consistent with those expected for Co(II). Following

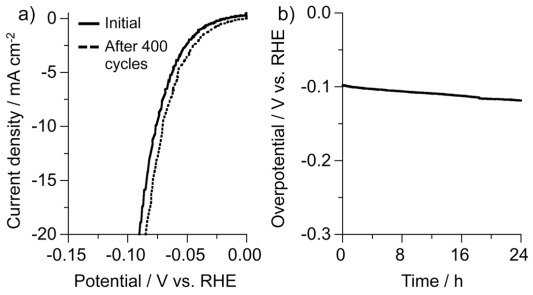

Figure 3.4: (a) Polarization data in 0.50 M H_2SO_4 for a CoP/Ti electrode (0.2 mg/cm^2 mass loading) initially and after 400 CV sweeps between +5 mV and −140 mV vs RHE. (b) Plot of overpotential vs. time for a CoP/Ti electrode (0.2 mg/cm^2 mass loading) at a constant cathodic current density of −20 mA/cm^2.

electrolysis, additional sulfur, carbon, and nitrogen were present, with these signals attributable to the sulfuric acid electrolyte, the graphite rod counter electrode, and epoxy, respectively. Oxygen was present throughout, which was expected due to the handling of samples in air. Importantly, XPS confirmed that the electrode was free of trace Pt, indicating that the observed HER activity was primarily due to the CoP nanoparticles and not to adventitious noble metal impurities.

3.5 Conclusion

In conclusion, nanoparticles of CoP are highly active HER electrocatalysts, with $<$ 100 mV overpotentials at low mass loadings and operationally relevant current densities of −20 mA/cm^2. In addition, CoP nanoparticles are exceptionally stable in acidic solutions, showing no evidence of significant degradation over 24 h of H_2 production in 0.50 M H_2SO_4. These results further establish that HDS electrocatalysts comprised of inexpensive and Earth-abundant elements provide interesting and important candidate materials for obtaining high activity and stability for the HER in acidic media.

3.6 Acknowledgements

This work was supported by the National Science Foundation (NSF) Center for Chemical Innovation on Solar Fuels (CHE-1305124). CWR thanks the NSF for a graduate research fellowship. Research was in part performed at the Beckman Institute Molecular Materials Research Center. TEM and BET data were acquired using facilities in the Materials Characterization Lab of the Penn State Materials Research Institute. EJP and CGR thank Trevor Clark, Ke Wang, and Lymaris Ortiz Rivera for assistance.

3.7 References

(1) H. B. Gray, *Nat. Chem.*, 2009, **1**, 7.

(2) D. Merki and X. L. Hu, *Energy and Environmental Science*, 2011, **4**, 3878–3888.

(3) M. G. Walter, E. L. Warren, J. R. McKone, S. W. Boettcher, Q. Mi, E. A. Santori and N. S. Lewis, *Chem. Rev.*, 2010, **110**, 6446–73.

(4) Y. Li, H. Wang, L. Xie, Y. Liang, G. Hong and H. Dai, *J. Am. Chem. Soc.*, 2011, **133**, 7296–9.

(5) H. Vrubel and X. L. Hu, *Angewandte Chemie-International Edition*, 2012, **51**, 12703–12706.

(6) W. F. Chen, C. H. Wang, K. Sasaki, N. Marinkovic, W. Xu, J. T. Muckerman, Y. Zhu and R. R. Adzic, *Energy and Environmental Science*, 2013, **6**, 943–951.

(7) W. F. Chen, K. Sasaki, C. Ma, A. I. Frenkel, N. Marinkovic, J. T. Muckerman, Y. Zhu and R. R. Adzic, *Angew. Chem. Int. Ed. Engl.*, 2012, **51**, 6131–5.

(8) B. Cao, G. M. Veith, J. C. Neuefeind, R. R. Adzic and P. G. Khalifah, *J. Am. Chem. Soc.*, 2013, **135**, 19186–92.

(9) D. S. Kong, J. J. Cha, H. T. Wang, H. R. Lee and Y. Cui, *Energy and Environmental Science*, 2013, **6**, 3553–3558.

(10) J. R. McKone, B. F. Sadtler, C. A. Werlang, N. S. Lewis and H. B. Gray, *ACS Catal.*, 2013, **3**, 166–169.

(11) D. G. Nocera, *Acc. Chem. Res.*, 2012, **45**, 767–76.

(12) I. A. Raj and K. I. Vasu, *J. Appl. Electrochem.*, 1990, **20**, 32–38.

(13) I. Paseka, *Electrochim. Acta*, 1995, **40**, 1633–1640.

(14) Y. F. Xu, M. R. Gao, Y. R. Zheng, J. Jiang and S. H. Yu, *Angew. Chem. Int. Ed. Engl.*, 2013, **52**, 8546–50.

(15) E. J. Popczun, J. R. McKone, C. G. Read, A. J. Biacchi, A. M. Wiltrout, N. S. Lewis and R. E. Schaak, *J. Am. Chem. Soc.*, 2013, **135**, 9267–70.

(16) R. Prins, V. H. J. Debeer and G. A. Somorjai, *Catalysis Reviews-Science and Engineering*, 1989, **31**, 1–41.

(17) P. Liu, J. A. Rodriguez, T. Asakura, J. Gomes and K. Nakamura, *J. Phys. Chem. B*, 2005, **109**, 4575–83.

(18) S. T. Oyama, *J. Catal.*, 2003, **216**, 343–352.

(19) S. Deka, A. Falqui, G. Bertoni, C. Sangregorio, G. Poneti, G. Morello, M. De Giorgi, C. Giannini, R. Cingolani, L. Manna and P. D. Cozzoli, *J. Am. Chem. Soc.*, 2009, **131**, 12817–28.

(20) D. H. Ha, L. M. Moreau, C. R. Bealing, H. T. Zhang, R. G. Hennig and R. D. Robinson, *J. Mater. Chem.*, 2011, **21**, 11498–11510.

(21) R. K. Chiang and R. T. Chiang, *Inorg. Chem.*, 2007, **46**, 369–71.

(22) J. W. Wang, A. C. Johnston-Peck and J. B. Tracy, *Chem. Mater.*, 2009, **21**, 4462–4467.

(23) A. E. Henkes, Y. Vasquez and R. E. Schaak, *J. Am. Chem. Soc.*, 2007, **129**, 1896–7.

(24) E. Muthuswamy and S. L. Brock, *Chem Commun (Camb)*, 2011, **47**, 12334–6.

(25) S. Rundqvist, L. G. Sillén, D. Timm, K. Motzfeldt, O. Theander and H. Flood, *Acta Chem. Scand.*, 1962, **16**, 287–292.

(26) Y. Xu, R. Wu, J. Zhang, Y. Shi and B. Zhang, *Chem Commun (Camb)*, 2013, **49**, 6656–8.

(27) A. B. Laursen, K. R. Patraju, M. J. Whitaker, M. Retuerto, T. Sarkar, N. Yao, K. V. Ramanujachary, M. Greenblatt and G. C. Dismukes, *Energy Environ. Sci.*, 2015, **8**, 1027–1034.

(28) J. O. Bockris and E. C. Potter, *J. Electrochem. Soc.*, 1952, **99**, 169.

(29) J. Kibsgaard, Z. Chen, B. N. Reinecke and T. F. Jaramillo, *Nat. Mater.*, 2012, **11**, 963–9.

Chapter 4

Comparison of the Performance of CoP-Coated and Pt-Coated Radial Junction n^+p-Silicon Microwire-Array Photocathodes for the Sunlight-Driven Reduction of Water to $H_2(g)$

Adapted with permission from C.W. Roske; E.J. Popczun; B. Seger; C.G. Read; T. Pedersen; O. Hansen; P.C.K. Vesborg; B.S. Brunschwig; R.E. Schaak; I. Chorkendorff; H.B. Gray; N.S. Lewis. *J. Phys. Chem. Lett.*, **2015**, *6*, 1679-1683. Copyright 2014 American Chemical Society.

4.1 Abstract

The electrocatalytic performance for hydrogen evolution has been evaluated for radial-junction n^+p-Si microwire (MW) arrays with Pt or cobalt phosphide, CoP, nanoparticulate catalysts in contact with 0.50 M H_2SO_4(aq). The CoP-coated (2.0 mg/cm^2) n^+p-Si MW photocathodes were stable for over 12 h of continuous operation, and produced an open-circuit photovoltage (V_{oc}) of 0.48 V, a light-limited photocurrent density (J_{ph}) of 17 mA/cm^2, a fill factor (ff) of 0.24, and an ideal regenerative-cell efficiency (η_{IRC}) of 1.9 % under simulated 1-Sun illumination. Pt-coated (0.5 mg/cm^2) n^+p-Si MW array photocathodes produced V_{oc} = 0.44 V, J_{ph} = 14 mA/cm^2, ff = 0.46, and η = 2.9 % under identical conditions. Thus the MW geometry allows the fabrication of photocathodes entirely composed of earth-abundant materials that exhibit performance comparable to that of devices that contain Pt. Increased performance, η = 2.71 %, is obtained upon electrodeposition of CoP onto Si MWs with TiO_2 scattering particles.

4.2 Introduction

One of the challenges to the development of a sustainable and globally scalable solar-driven water-splitting system is the discovery and development of materials and architectures that allow for the replacement or minimal use of scarce elements.[1–4] The most active catalysts for water splitting in an acidic environment are Pt and IrO_2. Pt operates at a very low (< 30 mV) overpotential to catalyze the reduction of H_2O to H_2(g) in acidic or alkaline media at cathodic current densities of > 10 mA/cm^2. Recently, significant progress has been made in the development of earth-abundant catalysts for the hydrogen-evolution reaction (HER) in both acidic and alkaline media. Overpotentials for the HER comparable to those for Pt (albeit at higher mass loadings) have been observed in alkaline media by use of Ni-Mo and related Ni-based alloys,[5–7] whereas transition-metal sulfides and phosphides have emerged as robust, active electrocatalysts for the HER in acidic media,[8–17] with FeP yielding overpotentials as low as 60 mV to produce cathodic current densities of 10 mA/cm^2.[11] Moreover, a sensitivity analysis has shown that further reduction in the HER overpotential from 60 mV to < 50 mV at a cathodic current density of 10 mA/cm^2 would yield little further gain in overall efficiency for an optimally designed solar-driven water-splitting system.[2,18]

The HER activity is, however, only one important factor in assessing whether an electrocatalyst is well-suited for incorporation into a fully integrated solar-driven water-splitting device.[1] At the mass loadings needed to provide low overpotentials under 1 Sun illumination, the catalyst must not significantly absorb incident light, and optimally, any light reflected by the catalyst should be directed toward the photo-electrode to produce additional photocurrent. The electrocatalyst must also remain active when integrated with an appropriate semiconducting photoelectrode, while preserving the photovoltage and photoactivity of the light absorber. In general for a tandem structure in a full solar-driven water-splitting configuration, for at least one

of the photoelectrode/electrocatalyst assemblies the light must be incident through the catalyst. Hence the approach described herein is advantageous when light is incident on such a catalyst-coated wire-array photoelectrode. Herein we examine whether the mass loadings required for HER electrocatalysis at low overpotentials using CoP nanoparticles can be accommodated without adversely affecting the overall performance of a microwire-array photocathode. Specifically, the performance of radial-junction n^+p-Si microwire (MW)-array photocathodes loaded with nanoparticulate CoP is compared to that of otherwise identical photocathodes loaded with smaller amounts of Pt.

4.3 Results and Discussion

Detailed experimental procedures are provided in the Supplementary Information. Briefly, Si microwires (unoptimized in dimensions for light absorption) were fabricated by reactive-ion etching of a (100)-oriented p-Si wafer. The microwires were 4 μm in diameter, 50 μm in length, spaced in a hexagonal grid with an 11 μm pitch, and were nearly completely vertically oriented with respect to the underlying 14.6 ohm-cm resistivity Si(100) substrate. Vapor diffusion of phosphorous at 900 °C for 10 min produced a radial emitter over the surface of the MW array that was estimated to be 100 nm thick at the base of the structure. Similar planar electrodes were also fabricated. The Pt nanoparticles were synthesized by ascorbic acid reduction and were determined to have an average diameter of $\approx$ 3 nm, based on analysis of transmission-electron microscope (TEM) images (See Figure C.1). The CoP nanoparticles were synthesized by the thermal decomposition of octacarbonyl dicobalt(0) to first produce Co nanoparticles, and were then transformed to CoP by reaction with trioctylphosphine.[9] X-ray powder diffraction and TEM data (Figure C.2) confirmed the formation of crystalline CoP nanoparticles having diameters of $\approx$ 13 nm. The Pt and CoP nanoparticles were loaded onto the Si MW arrays using

centrifugation. Figure 4.1 shows SEM images of a bare n^+p-Si MW array and of n^+p-Si MW arrays loaded with either 2.0 mg/cm^2 of CoP nanoparticles or with 0.50 mg/cm^2 of Pt nanoparticles. The CoP particles deposited primarily at the base of the Si MW array and consisted of aggregates of the $\approx$ 13 nm particles. The clusters of CoP completely covered the base of the array, with some of the CoP nanoparticles on the top of the Si microwires and a small amount along the length of each wire. The Pt nanoparticles deposited predominantly at the base of the wire arrays, also aggregated and with some adsorbed particles near the tops of the wires and others sparingly present along the length of the wire, similar to the deposited CoP nanoparticles.

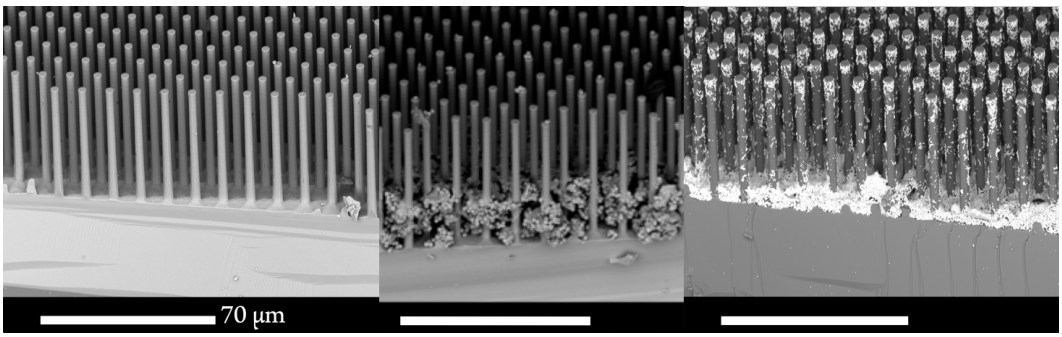

Figure 4.1: Scanning-electron microscopy images of radial-junction n^+p-Si microwire arrays. The microwires were 50 μm in length, 4 μm in diameter, and were spaced on an 11 μm pitch. (Left) A bare microwire array. (Center) A microwire array coated by centrifugation of CoP nanoparticles. The CoP loading was 2.0 mg/cm^2. (Right) A microwire array coated with Pt nanoparticles at a loading of 0.50 mg/cm^2. The scale bars indicated in the images above are each 70 μm.

The photoelectrochemical performance of the n^+p-Si planar and MW-array photocathodes was evaluated in contact with H_2(g)-saturated 0.50 M H_2SO_4(aq). Figure 4.2 shows the current density versus potential (J–E) behavior of n^+p-Si planar, as well as Si MW-array photocathodes with adsorbed Pt or CoP catalysts, and Table C.1 summarizes the relevant J–E parameters for the n^+p-Si electrodes.

Under 1 Sun (100 mW/cm^2) of simulated Air Mass (AM) 1.5G illumination, planar electrodes in the absence of deliberately added catalysts showed a light-limited

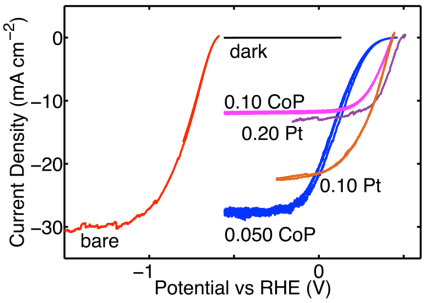

Figure 4.2: Effect of catalyst loading on the current-density versus potential behavior of n^+p-Si planar photocathodes in contact with $H_2(g)$-saturated 0.50 M $H_2SO_4(aq)$ and under 100 mW/cm^2 of AM1.5G simulated solar illumination. The black curve shows a representative scan in the dark. The red curve shows the behavior of a bare, planar n^+p Si sample. The orange and purple curves show the behavior of microwire arrays loaded with 0.10 mg/cm^2 and 0.20 mg/cm^2 of adsorbed Pt, respectively. The blue and magenta curves show the behavior of microwire arrays loaded with 0.050 mg/cm^2 and 0.10 mg/cm^2 of CoP, respectively. These data were collected using a scan rate of 5.0 mV s^{-1}.

current density, J_{ph}, of 30 mA/cm^2. Pt loadings of 0.10 mg/cm^2 on a planar electrode reduced J_{ph} by 24 % (23 mA/cm^2) and gave fill factors (ff) of 0.40. Comparable (0.050 mg/cm^2) mass loadings of CoP on planar electrodes yielded J_{ph} values 20 % higher than for the Pt-coated photocathodes (28 mA/cm^2) but yielded significantly lower fill factors (ff = 0.15), as expected based on the lower HER activity of CoP relative to Pt. Increasing the mass loadings (2.0 mg/cm^2) of CoP on planar Si electrodes increased the fill factor to ff = 0.54, which is comparable to and slightly larger than that observed for Pt at a mass loading of 0.20 mg/cm^2 (ff = 0.49). However, the light-limited photocurrent density produced by the highly loaded CoP-Si planar photocathodes (J_{ph} = 0.19 mA/cm^2) was significantly lower than J_{ph} for 0.20 mg/cm^2 of Pt (J_{ph} = 12 mA/cm^2) or for the bare planar Si photocathode (J_{ph} = 30 mA/cm^2). As such, J_{ph} decreased from that of the bare planar photoelectrode by a factor of $\approx$ 150 due to the increased loadings of CoP, consistent with significant losses associated with the reflection and/or absorption of incident photons by the electrocatalyst.

Figure 4.3 and Table C.1 show the effects of different levels of the light intensity on the J–E behavior of n^+p-Si MW-array photocathodes coated either with Pt or CoP electrocatalysts. For light intensities $\leq$ 100 mW/cm^2 of simulated AM1.5 illumination, the J_{ph} and V_{oc} values observed for deposition of 2.0 mg/cm^2 (of projected electrode area) of CoP were comparable to those obtained for deposition of 0.50 mg/cm^2 of Pt. At 100 mW/cm^2 of simulated sunlight, n^+p-Si MW/Pt photocathodes yielded J_{ph} = 14 mA/cm^2, Voc = 0.44 V, and ff = 0.46, whereas n^+p-Si MW/CoP photocathodes produced J_{ph} = 17 mA/cm^2, Voc = 0.48 V, and ff = 0.24. At higher light intensities, the CoP-loaded Si MW electrodes showed significantly lower ff values than the Pt-loaded Si MW electrodes, reflective of the lower intrinsic HER activity of CoP relative to Pt.

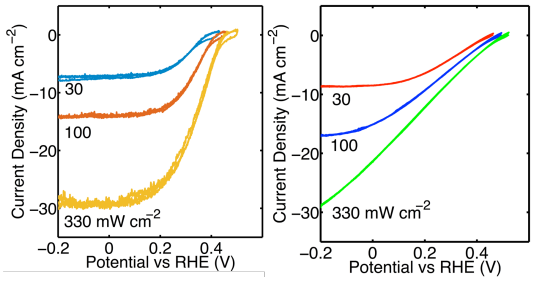

Figure 4.3: Effect of illumination intensity on the current-density versus potential behavior for n^+p-Si microwire-array photocathodes in contact with H_2(g)-saturated 0.50 M H_2SO_4(aq) and loaded with (left) 0.50 mg/cm^2 Pt or (right) 2.0 mg/cm^2 CoP. Data are shown for illumination intensities of 330 (bottom), 100 (middle), and 30 (top) mW/cm^2, respectively of simulated AM1.5G sunlight. Within the potential and current range indicated in the figure, bare n^+p-Si MW cathodes did not show any significant photocurrent.

The open-circuit voltages of all of the photocathodes were similar, as expected for a buried n^+p junction that could be used for construction of a photovoltaic (PV)-biased electrosynthetic water-splitting cell.[19] A significant apparent series resistance was present in the CoP-loaded MW array system (Figure 4.3), which may be indicative of poor electrical contact either between nanoparticles or between the solution and the particles or most likely between the silicon and the nanoparticles. All issues could

presumably be improved by embedding the nanoparticles in a conductive matrix such as Ketjenblack. The CoP mainly was present at the base of the wire arrays, in contrast to the Pt-coated array, which had a significant number of particles along the length of the wires (as seen in the SEMs of Figure 4.1). The resistance of electrons in the radial emitter, calculated assuming the measured doping density of the emitter and the measured emitter thickness is 0.005 Ω (see Supporting Information for details), as compared to the observed resistance of 285 Ω. The longer distance that charge carriers must travel along the wires in the CoP case thus does not contribute significantly to the observed series resistance. Due to the difference in the placement of the catalyst materials, the restricted mass transport of protons from the bulk solution may occur within the internal volume of the microwire structure.[20] The Si microwire array morphology has an 8:1 ratio of its internal surface area relative to its geometric area, and thus a given incident photon flux (per projected electrode area) yields a photogenerated charge-carrier density at the internal surfaces of the Si MW array electrode that is on the order of 8-10-fold lower than that of a planar Si electrode producing the same J_{ph} value. This reduced charge-carrier flux results in a lower overpotential requirement for the electrocatalyst, and thus narrows the difference in the kinetic overpotentials and consequently in the fill factors between the Si MW array photoelectrodes loaded with Pt vs those loaded with CoP.

Figure C.3 shows the external quantum yield, Φ_{ext}, as a function of the wavelength of incident light for the bare and catalyst-coated MW-array photocathodes, respectively, for the same loadings as shown in Figure 4.3. For the Pt-covered Si MW array, the maximum Φ_{ext} value was 0.40, which is comparable to values of Φ_{ext} observed previously on similar chemical-vapor deposition (CVD)-grown Si microwire-array devices of 0.30.[6,21] For the Pt-coated device under 100 mW/cm^2 of simulated AM1.5G illumination, the photocurrent density per wavelength integrated to J_{ph} = 12 mA/cm^2, while the data for the CoP-coated Si MW device integrated to a value

of J_{ph} = 9.2 mA/cm^2. The mutually similar J_{ph} values expected for the CoP-loaded and Pt-loaded Si MW arrays are in accord with observations (Figure 4.3, Table C.1), and the differences in absolute values of J_{ph} between expectation and observation are likely due to spectral mismatch between the ELH-type W-halogen lamp and the solar spectrum.

Figure 4.4 presents the angular dependence of J_{ph} for planar and microwire-array Si photocathodes, respectively, to establish minimal contribution of light absorption by the photoactive substrate in the microwires. The CoP-loaded planar Si and Si MW electrodes exhibited a different dependence of J_{ph} on angle of illumination. For the planar electrodes J_{ph} reached a maximum of 27 mA/cm^2 at an angle of 0° relative to the surface normal, and J_{ph} decreased monotonically with increasing angles of incidence. In contrast, the Si MW array photocathode exhibited a dependence of J_{ph} that peaked at 21.8 mA/cm^2 at an angle of ≈ 35° relative to normal incidence. Microwire arrays show a minimum in photocurrent under standard test conditions with the illumination at normal incidence. Furthermore, Table S1 shows the behavior of a planar Si electrode coated with 2.0 mg/cm^2 CoP, indicating that little photocurrent was observed. Thus J_{ph} for the Si MW array is dominated by light absorption in the Si microwires as opposed to absorption in the underlying p-Si substrate.[22]

Figure 4.4 displays the stability of an n$^+$p-Si MW/CoP electrode during H_2(g) evolution. Over 12 h of continuous operation under potentiostatic control at −0.40 V vs a reversible hydrogen electrode (RHE), the light-limited current density of a n$^+$p-Si MW/CoP (2.0 mg/cm^2) photocathode in 0.50 M H_2SO_4(aq) at 100 mW/cm^2 illumination intensity was stable at 16.3 ± 0.45 mA/cm^2. *J*–*E* data collected at the beginning and end of the experiment showed negligible degradation in the fill factor or J_{ph} over the 12 h period of operation. CoP electrocatalysts deposited on Ti metal supports have been reported to exhibit < 25 mV increase in overpotential during 24 h of continuous operation at cathodic current densities of 20 mA/cm^2,[9] suggesting

that the performance and stability limits of the Si/CoP system were not reached in the experiment shown in Figure 4.4.

Figure 4.5 shows n^+p-Si MWs coated with electrodeposited CoP. At 30, 100, 330 mW/cm^2 the apparent series resistance has disappeared, reflecting improved contact between the catalyst and the light absorber. Correspondingly, markedly improved performance is observed at 100 mW/cm^2 obtaining η_{IRC} of 2.71 %, V_{oc} = 0.472. J_{ph} = 12.6 mA/cm^2. This underscores the importance in obtaining intimate contact between the light absorber and electrocatalyst.

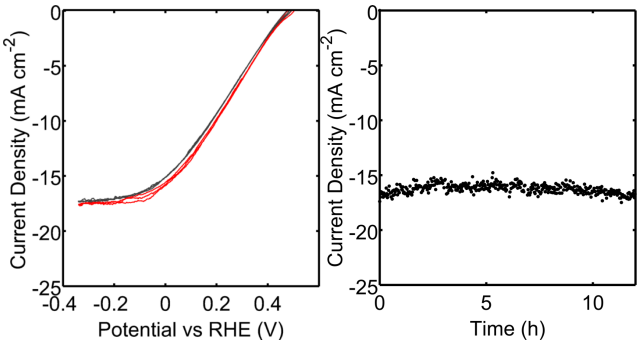

Figure 4.4: Voltammetric sweeps under 100 mW/cm^2 illumination intensity before (black) and after (red) the photocathode was maintained under potentiostatic conditions (left) at −0.40 V vs RHE for 12 h at the same light intensity. The potential for the chronoamperometric experiment was chosen to maintain the light-limited current throughout the experiment in the event of significant degradation within the power-producing region of the sweep. In a tandem structure, the photocathode would presumably be operating at less negative potentials, and thus would produce lower current densities than the light-limited current density at which the stability evaluation was performed. The corresponding chronoamperometric data are displayed on the right under the conditions described for the left panel.

The globally optimized morphology and catalyst placement that simultaneously optimizes optical absorption, carrier collection, reactant access, and product egress while operating during formation of bubbles of H_2(g) requires further investigation. For instance, although the optimum diameter for carrier collection purposes of Si wire arrays is when the wire diameter is approximately equal to the minority-carrier collection length, the exact structure of the material, and whether uniform geometry

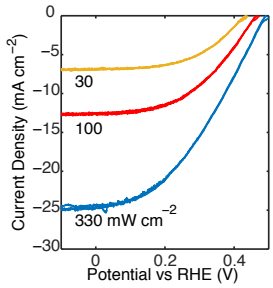

Figure 4.5: 100 mC of CoP were deposited from a known procedure[23]. Several illumination (0, 30, 100, 330 mW/cm^2 intensities illuminate the resulting n$^+$p-Si/MWs coated with a TiO_2 scattering particle underlayer[24] and electrodeposited CoP.

microwires are preferred relative to more branched nanoscale structures or relative to asymmetric structures that will funnel light into the microwires or nucleate bubble formation and growth at the wire tips requires further investigation.

4.4 Conclusion

Due to the lower turnover frequency of CoP relative to Pt,[9] higher mass loadings of CoP are required to produce similar geometric area-based HER activities as those obtained from Pt. Microwire arrays, compared with planar surfaces, therefore can beneficially accommodate the higher CoP mass loadings and provide comparable performance to Pt at 30 mW/cm^2 to 100 mW/cm^2 illumination intensities. Even at < 2 Suns of simulated Air Mass (AM) 1.5 illumination, the J–E behavior of an n$^+$p-Si MW/CoP photocathode was comparable to that observed for an n$^+$p-Si MW/Pt photocathode. Since a photocathode in a tandem water-splitting device would operate at $\approx$ 8 mA/cm^2 for a device having a solar-to-hydrogen energy-conversion efficiency of 10 %,[2,3] earth-abundant CoP is therefore an attractive candidate for use as a catalyst for the HER in a functional, intrinsically safe, integrated solar-driven water-splitting system.[2,3]

4.5 Acknowledgements

This work was supported by the NSF CCI Solar Fuels Program (CHE-1305124) and the Center for Individual Nanoparticle Functionality (CINF) (DNRF54). C.W.R. thanks the National Science Foundation and Link Energy Foundation for a graduate research fellowship. Research was in part carried out at the Molecular Materials Research Center of the Beckman Institute of the California Institute of Technology. N.S.L acknowledges support from the Energy from Sunlight Project funded by the Gordon and Betty Moore Foundation (GBMF1225).

4.6 References

(1) J. C. Stevens and A. Z. Weber, *J. Electrochem. Soc.*, 2016, **163**, H475–H484.

(2) J. R. McKone, N. S. Lewis and H. B. Gray, *Chem. Mater.*, 2014, **26**, 407–414.

(3) M. G. Walter, E. L. Warren, J. R. McKone, S. W. Boettcher, Q. Mi, E. A. Santori and N. S. Lewis, *Chem. Rev.*, 2010, **110**, 6446–6473.

(4) B. A. Pinaud, J. D. Benck, L. C. Seitz, A. J. Forman, Z. Chen, T. G. Deutsch, B. D. James, K. N. Baum, G. N. Baum, S. Ardo, H. Wang, E. Miller and T. F. Jaramillo, *Energy and Environmental Science*, 2013, **6**, 1983.

(5) J. R. McKone, B. F. Sadtler, C. A. Werlang, N. S. Lewis and H. B. Gray, *ACS Catal.*, 2013, **3**, 166–169.

(6) M. D. Kelzenberg, D. B. Turner-Evans, M. C. Putnam, S. W. Boettcher, R. M. Briggs, J. Y. Baek, N. S. Lewis and H. A. Atwater, *Energy and Environmental Science*, 2011, **4**, 866.

(7) C. Maier, *Int. J. Hydrogen Energy*, 1996, **21**, 859–864.

(8) E. J. Popczun, J. R. McKone, C. G. Read, A. J. Biacchi, A. M. Wiltrout, N. S. Lewis and R. E. Schaak, *J. Am. Chem. Soc.*, 2013, **135**, 9267–9270.

(9) E. J. Popczun, C. G. Read, C. W. Roske, N. S. Lewis and R. E. Schaak, *Angew. Chem. Int. Ed.*, 2014, **53**, 5427–5430.

(10) P. Xiao, M. A. Sk, L. Thia, X. Ge, R. J. Lim, J.-Y. Wang, K. H. Lim and X. Wang, *Energy Environ. Sci.*, 2014, **7**, 2624–2629.

(11) J. F. Callejas, J. M. McEnaney, C. G. Read, J. C. Crompton, A. J. Biacchi, E. J. Popczun, T. R. Gordon, N. S. Lewis and R. E. Schaak, *ACS Nano*, 2014, **8**, 11101–11107.

(12) J. M. McEnaney, J. Chance Crompton, J. F. Callejas, E. J. Popczun, C. G. Read, N. S. Lewis and R. E. Schaak, *Chem. Commun.*, 2014, **50**, 11026.

(13) J. M. McEnaney, J. C. Crompton, J. F. Callejas, E. J. Popczun, A. J. Biacchi, N. S. Lewis and R. E. Schaak, *Chem. Mater.*, 2014, **26**, 4826–4831.

(14) B. Seger, A. B. Laursen, P. C. K. Vesborg, T. Pedersen, O. Hansen, S. Dahl and I. Chorkendorff, *Angew. Chem. Int. Ed.*, 2012, **51**, 9128–9131.

(15) A. B. Laursen, T. Pedersen, P. Malacrida, B. Seger, O. Hansen, P. C. K. Vesborg and I. Chorkendorff, *Phys. Chem. Chem. Phys.*, 2013, **15**, 20000.

(16) Y. Hou, B. L. Abrams, P. C. K. Vesborg, M. E. Björketun, K. Herbst, L. Bech, A. M. Setti, C. D. Damsgaard, T. Pedersen, O. Hansen, J. Rossmeisl, S. Dahl, J. K. Nørskov and I. Chorkendorff, *Nat. Mater.*, 2011, **10**, 434–438.

(17) J. D. Benck, S. C. Lee, K. D. Fong, J. Kibsgaard, R. Sinclair and T. F. Jaramillo, *Adv. Energy Mater.*, 2014, **4**, 1400739.

(18) Y. Chen, S. Hu, C. Xiang and N. S. Lewis, *Energy Environ. Sci.*, 2015, **8**, 876–886.

(19) A. C. Nielander, M. R. Shaner, K. M. Papadantonakis, S. A. Francis and N. S. Lewis, *Energy Environ. Sci.*, 2015, **8**, 16–25.

(20) C. Xiang, A. C. Meng and N. S. Lewis, *Proceedings of the National Academy of Sciences*, 2012, **109**, 15622–15627.

(21) E. L. Warren, J. R. McKone, H. A. Atwater, H. B. Gray and N. S. Lewis, *Energy and Environmental Science*, 2012, **5**, 9653.

(22) S. W. Boettcher, J. M. Spurgeon, M. C. Putnam, E. L. Warren, D. B. Turner-Evans, M. D. Kelzenberg, J. R. Maiolo, H. A. Atwater and N. S. Lewis, *Science*, 2010, **327**, 185–187.

(23) F. H. Saadi, A. I. Carim, E. Verlage, J. C. Hemminger, N. S. Lewis and M. P. Soriaga, *J. Phys. Chem. C*, 2014, **118**, 29294–29300.

(24) M. R. Shaner, J. R. McKone, H. B. Gray and N. S. Lewis, *Energy Environ. Sci*, 2015, **8**, 2977–2984.

Chapter 5

Lightly Fluorinated Graphene as a Protective Layer for n-Type Si(111) Photoanodes in Aqueous Electrolytes

Reprinted with permission from Nielander, A.C.; Thompson, A.C.; Roske, C.W.; Maslyn, J.A.; Hao, Y.; Plymale, N.T.; Hone, J.; Lewis, N.S. *Nano Lett.*, **2016**, *16* (7), pp 4082–4086. Copyright 2016 American Chemical Society.

5.1 Abstract

The behavior of n-Si(111) photoanodes covered by monolayer sheets of fluorinated graphene (F–Gr) was investigated under a range of chemical and electrochemical conditions. The electrochemical behavior of n-Si/F–Gr and np^+-Si/F–Gr photoanodes was compared to hydride-terminated n-Si (n-Si–H) and np^+-Si–H electrodes in contact with aqueous $Fe(CN)_6^{3-/4-}$ and Br_2/HBr electrolytes as well as in contact with a series of outer-sphere, one-electron redox couples in nonaqueous electrolytes. Illuminated n-Si/F–Gr and np^+-Si/F–Gr electrodes in contact with an aqueous $K_3(Fe(CN)_6/K_4(Fe(CN)_6$ solutions exhibited stable short-circuit photocurrent densities of $-10\,mA/cm^2$ for 100 000 s (> 24 h), in comparison to bare Si electrodes, which yielded nearly a complete photocurrent decay over ≈ 100 s. X-ray photoelectron spectra collected before and after exposure to aqueous anodic conditions showed that oxide formation at the Si surface was significantly inhibited for Si electrodes coated with F–Gr relative to bare Si electrodes exposed to the same conditions. The variation of the open-circuit potential for n-Si/F–Gr in contact with a series of nonaqueous electrolytes of varying reduction potential indicated that the n-Si/F–Gr did not form a buried junction with respect to the solution contact. Further, illuminated n-Si/F–Gr electrodes in contact with Br_2/HBr(aq) were significantly more electrochemically stable than n-Si–H electrodes, and n-Si/F–Gr

electrodes coupled to a Pt catalyst exhibited ideal regenerative cell efficiencies of up to 5 % for the oxidation of Br^- to Br_2.

5.2 Introduction

Several protective coating strategies have been developed to suppress deleterious surface reactions associated with corrosion or passivation of semiconductor photoanodes in aqueous electrolytes.[1,2] Nickel oxide (NiO_x) films prepared by reactive sputtering or amorphous TiO_2 films in conjunction with a NiO_x based electrocatalyst have produced extended stability for Si photoanodes and allow the electrochemical evolution of O_2(g) from water under alkaline conditions.[3,4] Thin metallic overlayers or transparent conductive metal oxide protective layers often result in relatively low photovoltages due to thermionic emission of majority carriers at Si/overlayer Schottky contacts.[3–10] Insulating metal oxide barriers must be thin enough (a few nm) to permit conduction by tunneling, and such thin layers are difficult to prepare in a pinhole-free manner over macroscopic areas.[5,11,12] Chemical functionalization has led to improved stability of n-Si surfaces, but such methods have not yet yielded stability over extended time periods in aqueous electrolytes.[13–15] An ideal protective coating would be transparent, provide low resistance to charge transfer, allow for maximum energy-conversion efficiency for a range of semiconductor/electrolyte contacts, be applied easily to semiconductor surfaces, be capable of uniformly protecting macroscopic electrode areas, and be chemically and electrochemically stable under the relevant conditions. Monolayer graphene can be prepared in large ($> 100\,cm^2$), pinhole-free layers and transferred to any arbitrary planar surface, and it has been shown to inhibit oxidation of metals both in air and in aqueous solution.[16–21] Graphene is chemically inert, optically transparent, can be deposited onto surfaces at room temperature. Illuminated Si photoanodes coated by polycrystalline, CVD-grown graphene and in contact with neutral pH aqueous electrolytes

have demonstrated stability for over 1000 s while providing desirable photoelectrochemical performance.[22–25] However, the graphene does not completely protect the Si photoanodes from oxidation, and the devices exhibit partial Fermi-level pinning, which limits their energy-conversion efficiency. The incomplete protection and Fermi-level pinning are consistently ascribed to reactive sites near grain boundaries in the polycrystalline graphene produced by chemical-vapor deposition (CVD), and to the presence of mid-gap electronic states introduced at the n-Si/Gr interface as a result of the graphene electronic structure, respectively. Relative to unfluorinated graphene, fluorination of graphene should reduce the density of states near the Fermi level, thus reducing Fermi level pinning effects, and should passivate reactive graphene defect sites via fluorine capping.[26–28] Accordingly, we report herein an investigation of the stability and photoelectrochemical behavior of fluorinated-graphene-coated Si photoanodes in contact with aqueous electrolytes.

5.3 Materials and Methods

Detailed experimental procedures are provided in the Supporting Information. Briefly, monolayer sheets of lightly fluorinated graphene (<10 atom % F) were fabricated by treating CVD-grown graphene on a Cu foil with XeF_2(g).[28] X-ray photoelectron spectroscopy (XPS) of the resulting F–Gr confirmed the fluorination profile, which was consistent with previous reports indicating that low fluorination levels are observed after XeF_2 exposure of CVD grown graphene on copper foil.[27,28] The F–Gr was further characterized by UV/Vis and Raman spectroscopy (see SI). The fluorinated graphene sheets were transferred to n-type Si and np^+-Si (np^+-Si = Si homojunction with moderately doped n region and degenerately doped p region, see SI) electrodes using standard CVD graphene growth and transfer methods.[29,30]

5.4 Results and Discussion

Figure 5.1 shows the current-density vs. time (J–t) and current density vs. potential (J–E) behavior for illuminated ($\approx$ 33 mW/cm^2 ENH-type W-halogen lamp) n-Si/F–Gr photoanodes in contact with aqueous 50 mM $Fe(CN)_6^{3-}$ - 350 mM $Fe(CN)_6^{4-}$(aq). The n-Si/F–Gr electrodes exhibited stable current over 100 s while the current density of n-Si–H electrodes decayed to nearly baseline values over the same time period (Figure 5.1a). Furthermore, the current density of the n-Si/F–Gr electrode decayed by less than 1 mA/cm^2 over 100 000 s of continuous operation (Figure 5.1b). After correcting for fluctuations in the light intensity impinging on the electrode, greater than 97 % of the expected current density of an ideally stable electrode was observed. Similar results were observed for np$^+$-Si/F–Gr electrodes (see SI). Figure 5.1c depicts the J–E behavior before and after exposure to the conditions in Figure 5.1b. The stable open-circuit potential (−0.27 V vs. $E(A/A^-)$) and fill factor (ff, 0.33 before exposure, 0.32 after exposure) attest to the stability of the n-Si/F–Gr interface.

Prior to the stability test, the open-circuit potential (E_{oc}) of the n-Si/F–Gr electrode was −0.27 V vs. $E(A/A^-)$, approximately 70 mV lower than the reported E_{oc} of −0.34 V vs. $E(A/A^-)$ for n-Si coated with a single layer of graphene.[22] Further, exposure of n-Si/F–Gr to a series of non-aqueous electrolytes of varying electrochemical potential showed a dependence of E_{oc} on $E(A/A^-)$, indicating partial Fermi level pinning of the n-Si surface with respect to the solution potential. The mutually similar fill factors of the n-Si/F–Gr to the np$^+$-Si/F–Gr electrodes in aqueous electrolyte, 0.33 and 0.30 respectively, with the non-ideal fill factor for the np$^+$-Si/F–Gr interface attributable to a series resistance imposed by the Si/F–Gr/$Fe(CN)_6^{3-/4-}$ interface (see SI), suggests that the Si/F–Gr/$Fe(CN)_6^{3-/4-}$ may also be the source of the non-ideal fill factor for the n-Si/F–Gr electrode as well.

Figure 5.2 shows a comparison of the XP spectra of methyl-terminated n-Si elec-

trodes (n-Si–Me) with and without a F–Gr protective layer before and after photoelectrochemical testing in an aqueous 50 mM $Fe(CN)_6^{3-}$ - 350 mM $Fe(CN)_6^{4-}$ electrolyte. After passing 1600 mC/cm^2 of anodic charge on an n-Si–Me electrode, the growth of an oxide peak was observed in the Si 2p XPS region and was consistent with formation of multiple layers of oxide. In contrast, no additional growth of the oxide peak was observed after passing twice the number of Coulombs (3200 mC/cm^2) across an n-Si–Me/F–Gr electrode (see SI). As such, F–Gr acts as a physical barrier to oxide formation, preserving the photoelectrochemical behavior of the n-Si–Me/solution interface. Methylated surfaces were used because, in contrast with n-Si–H surfaces, the n-Si–Me surface does not easily oxidize in air nor forms significant oxide upon fabrication of n-Si/F–Gr interfaces, allowing more facile observation of oxide growth in the presence various protective layers, such as F–Gr. F–Gr covered Si surfaces did not form platinum silicide upon evaporation of Pt onto the F–Gr/Si surface, and F–Gr is stable in both aqueous and acidic (pH 0) solutions, suggesting F–Gr also provides as an effective physical barrier to inhibit Pt/Si reactivity and is stable under harsh fabrication and electrolyte conditions (see SI).

Figure 5.3 displays the J–E behavior of n-Si–H and n-Si/F–Gr electrodes under $\approx$ 33 mW/cm^2 illumination intensity in contact with 0.4 M Br_2 - 7.0 M HBr (pH=0), with and without electrochemical deposition of 100 mC/cm^2 of a Pt catalyst, respectively. With the Pt catalyst, the properties of the n-Si/F–Gr/Pt electrode improved to E_{oc} (n-Si/F–Gr/Pt)= 0.26 V, ff = 0.52, and J_{sc} = 8.3 mA/cm^2 from E_{oc} (n-Si/F–Gr)= 0.22 V, ff = 0.16, J_{sc} = 5.14 mA/cm^2. The improved ff can be ascribed to improved catalysis for the Br^- to Br_2 reaction effected by the Pt. The current density of the n-Si–H/Pt electrode under illumination decayed precipitously over two potential sweeps, while the n-Si/F–Gr/Pt electrode showed a stable ff and photocurrent density under the same conditions. The n-Si/F–Gr/Pt electrode had an

ideal regenerative cell efficiency (η_{IRC}) of 3.5 % in contact with the Br_2/HBr (aq) electrolyte.[31] The current density at n-Si/F–Gr/Pt electrodes was stable over 45 min at $E = 0$ V vs. the Nernstian potential of the solution, $E(A/A^-)$ and η_{IRC} increased to 5 % over this time (see SI). The improvement in η_{IRC} indicates a change in the energetics of the n-Si/F–Gr/Pt interface after electrochemical deposition of Pt. Although lightly fluorinated ($C_x F$, $x > 10$) graphene was used herein, these fluorinated polycrystalline graphene sheets provided superior and more consistent protection against corrosion to the underlying Si relative to the protection routinely imparted by polycrystalline monolayer graphene on n-Si(111) photoanodes (see SI).[22] These results are consistent with the hypothesis that light fluorination of graphene induces reaction with high-energy defect sites, such as dangling bonds or missing atoms, effectively passivating defects that otherwise would allow oxide formation at the n-Si surface and further degrade the Gr protective layer (see SI).[28,32] The bonding of a very electronegative atom to the surface may also increase the hydrophobicity of the graphene sheet, which would further reduce deleterious corrosion reactions near pinholes.

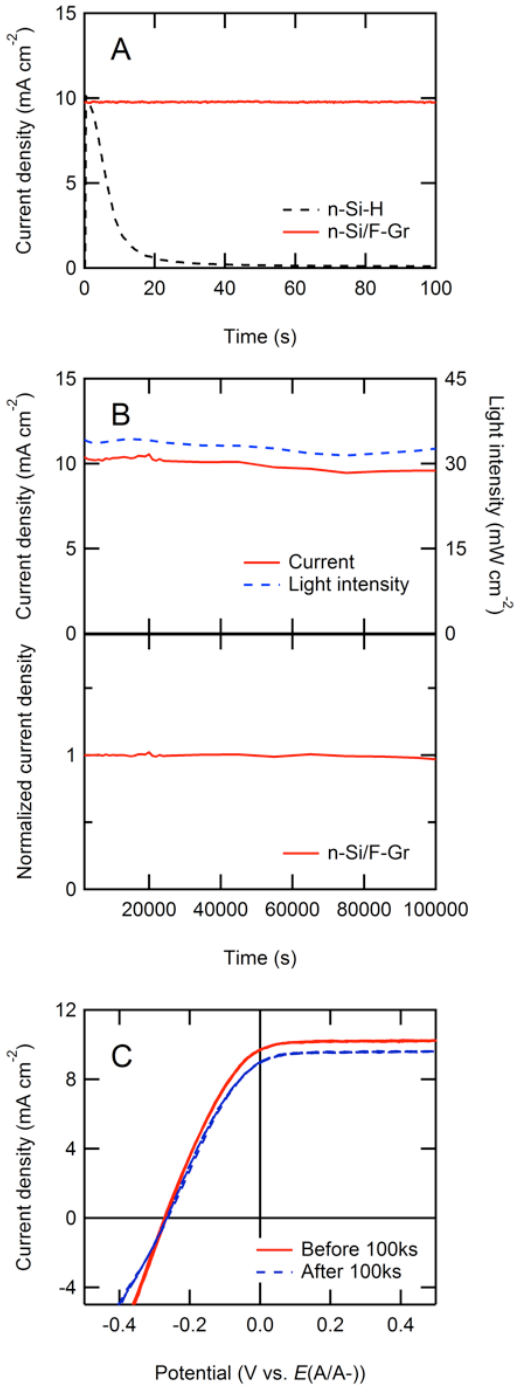

Figure 5.1: Current density-time (J–t) and current density-potential (J–E) behavior of n-Si/F–Gr electrodes in contact with aqueous 50 mM $Fe(CN)_6^{3-}$ - 350 mM $Fe(CN)_6^{4-}$ under $\approx$ 33 mW/cm^2 of ENH-type W-halogen lamp illumination. (A) Comparison of the J–t behavior of bare n-Si–H and n-Si/F–Gr electrodes over 100 s. (B) The J–t behavior of F–Gr covered n-Si at E = 0 V vs. the Nernstian potential of the solution ($E(A/A^-)$) over 100 000 s (> 24 h). The normalized current density is reported to correct for any variation in the intensity of the light source with time. (C) J–E behavior of n-Si/F–Gr (3 scans at 50 mV s^{-1}) before and after exposure to the conditions depicted in (B).

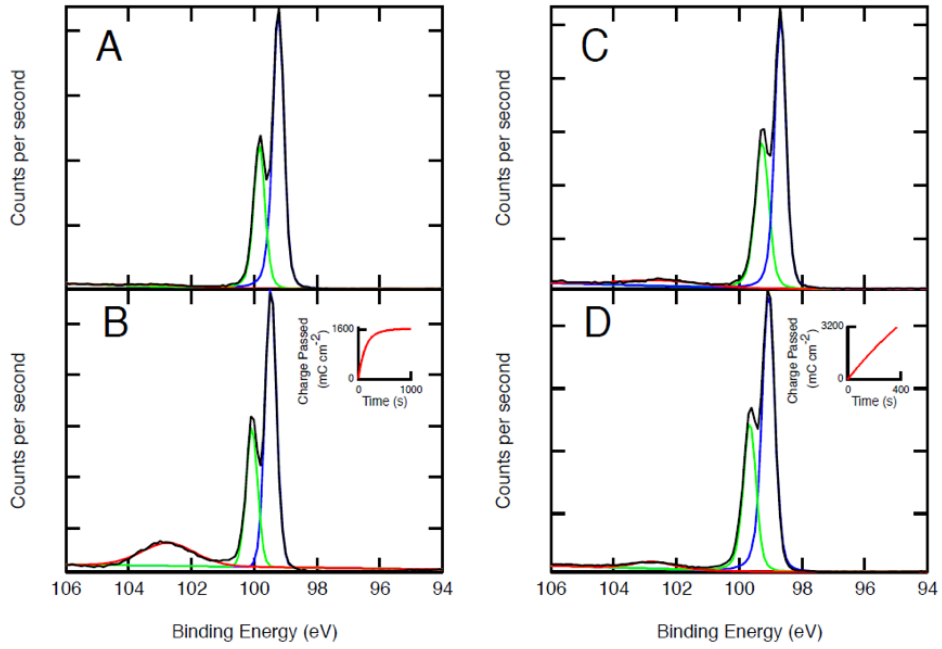

Figure 5.2: XP spectra of n-Si–Me and n-Si–Me/F–Gr electrodes. (A) and (B) show the XP spectra of an n-Si–Me electrode before and after passing 1600 mC/cm^2 (inset) while passing anodic current in contact with an aqueous 50 mM $Fe(CN)_6^{3-}$ - 350 mM $Fe(CN)_6^{4-}$ electrolyte. (C) and (D) show an n-Si–Me/F–Gr electrode before and after passing 3200 mC/cm^2 under similar electrochemical conditions to (A) and (B).

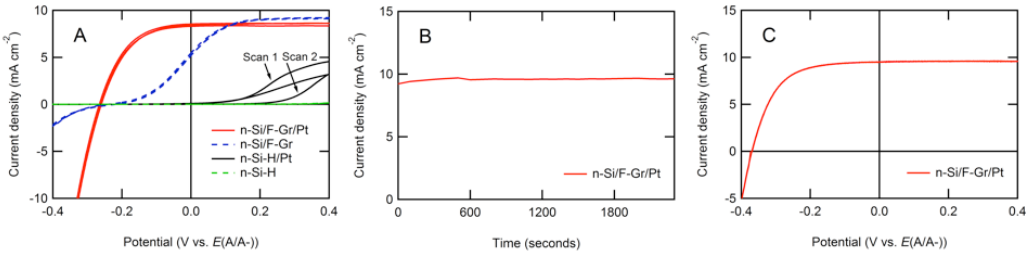

Figure 5.3: Electrochemical behavior of n-Si/F–Gr and n-Si–H electrodes with and without Pt deposition in aqueous 0.4 M Br_2 - 7.0 M HBr (pH = 0) electrolyte under 33 mW/cm^2 from an ELH-type W-halogen lamp). (A) J-E behavior of n-Si/F–Gr and n-Si–H electrodes with and without Pt deposition. Each cyclic voltammogram was started at 0.4 V vs. $E(A/A^-)$ and swept twice to more negative potentials at 50 mV s^{-1}. (B) J–t behavior of an n-Si/F–Gr/Pt electrode over 45 min at E = 0 V vs. $E(A/A^-)$ (C) J–E behavior of an n-Si/F–Gr/Pt electrode after exposure to conditions described in (B).

5.5 Conclusion

In conclusion, fluorinated graphene forms an effective physical barrier between silicon surfaces and a number of contacting phases, including acidic and neutral pH aqueous electrolyte as well as metallic interfaces. Additionally, Si covered by fluorinated graphene exhibits partial Fermi level pinning in contact with non-aqueous electrolytes. Additional work at higher fluorination levels on both p-type and n-type silicon will elucidate whether a reduction in the density of states near the Fermi level can lead to a fully unpinned interface, and will allow elucidation of the effect of the graphene-based surface dipole on the electrochemical behavior of the resultant photoelectrode.

5.6 Acknowledgements

NSL, ACN, and ACT acknowledge NSF, Grant CHE-1214152 for support, and the Beckman Institute Molecular Materials Resource Center and Dr. Bruce S. Brunschwig for facilities and valuable advice. ACN and ACT acknowledge Tom Lee and the UCLA Nanoelectronics Research Facility for valuable advice and access to instrumentation. ACN and NTP acknowledge support from NSF graduate research fellowships. CWR thanks the Link Energy Foundation for a graduate research fellowship. JAM thanks the Amgen Scholars program for a fellowship. This graphene material is based upon work supported by the NSF MRSEC program through Columbia in the Center for Precision Assembly of Superstratic and Superatomic Solids (DMR-1420634) and the Nanoelectronics Research Initiative (NRI) through the Institute for Nanoelectronics Discovery and Exploration (INDEX).

5.7 References

(1) S. Hu, N. S. Lewis, J. W. Ager, J. Yang, J. R. McKone and N. C. Strandwitz, *J. Phys. Chem. C*, 2015, **119**, 24201–24228.

(2) K. Sun, S. Shen, Y. Liang, P. E. Burrows, S. S. Mao and D. Wang, *Chem. Rev.*, 2014, **114**, 8662–8719.

(3) K. Sun, M. T. McDowell, A. C. Nielander, S. Hu, M. R. Shaner, F. Yang, B. S. Brunschwig and N. S. Lewis, *J. Phys. Chem. Lett.*, 2015, **6**, 592–598.

(4) S. Hu, M. R. Shaner, J. A. Beardslee, M. Lichterman, B. S. Brunschwig and N. S. Lewis, *Science*, 2014, **344**, 1005–1009.

(5) N. C. Strandwitz, D. J. Comstock, R. L. Grimm, A. C. Nichols-Nielander, J. Elam and N. S. Lewis, *J. Phys. Chem. C*, 2013, **117**, 4931–4936.

(6) B. A. Lombos, D. Côté, J. P. Dodelet, M. F. Lawrence and J. I. Dickson, *J. Cryst. Growth*, 1986, **79**, 455–462.

(7) A. Q. Contractor and J. O. Bockris, *Electrochim. Acta*, 1984, **29**, 1427–1434.

(8) A. T. Howe, *J. Electrochem. Soc.*, 1986, **133**, 1369.

(9) S. Menezes, *J. Electrochem. Soc.*, 1980, **127**, 1268.

(10) R. P. Pohanish and S. A. Greene, *J. Am. Chem. Soc.*, 2010, **132**, 3230–3230.

(11) Y. W. Chen, J. D. Prange, S. Dühnen, Y. Park, M. Gunji, C. E. D. Chidsey and P. C. McIntyre, *Nat. Mater.*, 2011, **10**, 539–544.

(12) S. J. Fonash, *Solar Cell Device Physics*, Academic Press, Oxford, 2nd edn., 2010.

(13) A. Bansal and N. S. Lewis, *The Journal of Physical Chemistry B*, 1998, **102**, 4058–4060.

(14) A. Bansal and N. S. Lewis, *The Journal of Physical Chemistry B*, 1998, **102**, 1067–1070.

(15) J. M. Bolts, A. B. Bocarsly, M. C. Palazzotto, E. G. Walton, N. S. Lewis and M. S. Wrighton, *J. Am. Chem. Soc.*, 1979, **101**, 1378–1385.

(16) S. Chen, L. Brown, M. Levendorf, W. Cai, S.-Y. Ju, J. Edgeworth, X. Li, C. W. Magnuson, A. Velamakanni, R. D. Piner, J. Kang, J. Park and R. S. Ruoff, *ACS Nano*, 2011, **5**, 1321–1327.

(17) G. W. Flynn, *The Journal of Chemical Physics*, 2011, **135**, 050901.

(18) Y. Lee, S. Bae, H. Jang, S. Jang, S.-E. Zhu, S. H. Sim, Y. I. Song, B. H. Hong and J.-H. Ahn, *Nano Lett.*, 2010, **10**, 490–493.

(19) D. Prasai, J. C. Tuberquia, R. R. Harl, G. K. Jennings and K. I. Bolotin, *ACS Nano*, 2012, **6**, 1102–1108.

(20) J. W. Suk, A. Kitt, C. W. Magnuson, Y. Hao, S. Ahmed, J. An, A. K. Swan, B. B. Goldberg and R. S. Ruoff, *ACS Nano*, 2011, **5**, 6916–6924.

(21) E. Sutter, P. Albrecht, F. E. Camino and P. Sutter, *Carbon*, 2010, **48**, 4414–4420.

(22) A. C. Nielander, M. J. Bierman, N. Petrone, N. C. Strandwitz, S. Ardo, F. Yang, J. Hone and N. S. Lewis, *J. Am. Chem. Soc.*, 2013, **135**, 17246–17249.

(23) S. Dröscher, P. Roulleau, F. Molitor, P. Studerus, C. Stampfer, K. Ensslin and T. Ihn, *Appl. Phys. Lett.*, 2010, **96**, 152104.

(24) L. A. Ponomarenko, R. Yang, R. V. Gorbachev, P. Blake, A. S. Mayorov, K. S. Novoselov, M. I. Katsnelson and A. K. Geim, *Phys. Rev. Lett.*, 2010, **105**, DOI: 10.1103/physrevlett.105.136801.

(25) S. Bae, H. Kim, Y. Lee, X. Xu, J.-S. Park, Y. Zheng, J. Balakrishnan, T. Lei, H. Ri Kim, Y. I. Song, Y.-J. Kim, K. S. Kim, B. Özyilmaz, J.-H. Ahn, B. H. Hong and S. Iijima, *Nature Nanotech*, 2010, **5**, 574–578.

(26) R. R. Nair, W. Ren, R. Jalil, I. Riaz, V. G. Kravets, L. Britnell, P. Blake, F. Schedin, A. S. Mayorov, S. Yuan, M. I. Katsnelson, H.-M. Cheng, W. Strupinski, L. G. Bulusheva, A. V. Okotrub, I. V. Grigorieva, A. N. Grigorenko, K. S. Novoselov and A. K. Geim, *Small*, 2010, **6**, 2877–2884.

(27) J. T. Robinson, J. S. Burgess, C. E. Junkermeier, S. C. Badescu, T. L. Reinecke, F. K. Perkins, M. K. Zalalutdniov, J. W. Baldwin, J. C. Culbertson, P. E. Sheehan and E. S. Snow, *Nano Lett.*, 2010, **10**, 3001–3005.

(28) R. Stine, W.-K. Lee, K. E. Whitener, J. T. Robinson and P. E. Sheehan, *Nano Lett.*, 2013, **13**, 4311–4316.

(29) N. Petrone, C. R. Dean, I. Meric, A. M. van der Zande, P. Y. Huang, L. Wang, D. Muller, K. L. Shepard and J. Hone, *Nano Lett.*, 2012, **12**, 2751–2756.

(30) Y. Hao, M. S. Bharathi, L. Wang, Y. Liu, H. Chen, S. Nie, X. Wang, H. Chou, C. Tan, B. Fallahazad, H. Ramanarayan, C. W. Magnuson, E. Tutuc, B. I. Yakobson, K. F. McCarty, Y. W. Zhang, P. Kim, J. Hone, L. Colombo and R. S. Ruoff, *Science*, 2013, **342**, 720–723.

(31) R. H. Coridan, A. C. Nielander, S. A. Francis, M. T. McDowell, V. Dix, S. M. Chatman and N. S. Lewis, *Energy Environ. Sci.*, 2015, **8**, 2886–2901.

(32) B. Wang, J. Wang and J. Zhu, *ACS Nano*, 2014, **8**, 1862–1870.

Chapter 6

Summary

Considerable interest in diversifying the world energy supply from finite fossil fuels to renewable sources arose in the 1970s as the result of an energy crisis. After the embargo of trade subsided, attention to energy waned until simultaneous concerns of fossil fuel resource exhaustion and anthropogenic climate change reignited a resurgence of interest.

Among renewable energy sources, collecting light from the sun is promising due to its immense potential. Unfortunately, photovoltaic solar cells produce intermittent electricity that is at odds with baseload generation necessary for large-scale adoption. This thesis peers back into the 1970s and examines a failed commercial endeavor by Texas Instruments (TI) to store electricity by splitting hydrobromic acid using silicon photoelectrodes. We try to advance a modern rendition of the TI system by replacing expensive precious metals with earth-abundant materials to further lower the cost of modules. We encounter a wide range of problems spanning from catalysis to semiconductor interfaces.

While water splitting is attractive for fuel storage, hydrobromic acid storage is promising for electricity storage. In this thesis we see, in agreement with predictions by others, that modern oxidation catalysts for water splitting fall short and will always result in lower solar-to-hydrogen (η_{STH}) efficiencies than comparable hydrobromic acid systems. In this thesis, we model different device configurations for the storage of chemical work to tailor the chemical reaction to the material of interest. For a single light absorber, the optimum device converts with an $\eta_{\mathrm{STH,\,HBr}}$ of 16.2 % for a 1.80 eV band gap material and $\eta_{\mathrm{STH,\,H_2O}}$ of 8.60 % for a 2.30 eV band gap material. Two light absorbers sitting side-by-side allow an $\eta_{\mathrm{STH,\,HBr}}$ of 17.8 % for two 1.20 eV

materials and $\eta_{\mathrm{STH,\,H_2O}}$ of 14.2 % for two 1.70 eV absorbers. A tandem system (with the larger band gap material on top of a smaller band gap semiconductor) could produce $\eta_{\mathrm{STH,\,HBr}}$ of 22.2 % for 1.60 eV:0.900 eV and $\eta_{\mathrm{STH,\,H_2O}}$ 19.3 % for 1.80 eV:1.20 eV. In light of the strength of our expertise, we elect to use HBr splitting in a side-by-side configuration where two silicon photoelectrodes (E_{g} = 1.12 eV) could give an $\eta_{\mathrm{STH,\,HBr}} \approx 12.0$ %.

In this thesis we develop an acid-compatible proton reduction catalyst for our system. We recognize that due to the similar mechanism between hydrodesulfurization (HDS) and the hydrogen evolution reaction (HER) that a good HDS catalyst may also be an active HER catalyst. We present another such example, cobalt phosphide (CoP) that reduces protons to H_2(g) with an overpotential (η) of −85 mV at a current density of $-20\,\mathrm{mA/cm^2}$ with promising stability over 24 h.

As part of this thesis, we integrate CoP with silicon microwire photocathodes with radial emitters (to simulate cheaper wires produced by CVD) to demonstrate a prototype photocathode, where we obtain an ideal-regenerative efficiency (η_{IRC}) of 1.9 % with promising stability over 12 h. We obtain a higher η_{IRC} of 2.71 % by electrodepositing amorphous CoP thereby improving electrical contact.

Next, a protection strategy for a silicon photoanode is introduced using lightly-fluorinated graphene as an improvement over graphene. With an appropriate catalyst (Pt), we obtain an η_{IRC} of 5 % for Br^- with promising stability over 30 min (we did not continue extended testing because the goal was to use graphene directly, but fluorination appears to have hampered oxidation catalysis).

Then we present an attempt to improve our CoP by increasing the surface area with highly branched crystalline nanoparticles, but find the η to be 117 mV for $-20\,\mathrm{mA/cm^2}$. Unfortunately these nanoparticles did not appear to adhere well to the Ti substrate and stability was therefore lacking.

We present a strategy to protect silicon by using covalent molecular monolayers as a first step to control the interface by seeding the growth of metal oxides during atomic layer deposition. Upon deposition of thin metal oxide layers, we find that the surface recombination velocity (S) remains low while providing enhanced deposition rates for our aldehyde-terminated surfaces.

Then we present an alternative strategy for controlling the composition of nanoparticles by pulsed laser ablation in liquids by adding select metal salts. This adds an additional knob to enable the synthesis of complex materials by kinetic control, allowing for the selection of future desirable materials.

And finally, we present a review of the general academic impact the metal phosphides have had on the community since their introduction and chart their progress in several aspects.

Appendix A

Efficiency Calculation Matlab Program

A.1 Realistic Calculation Results

Single Absorber

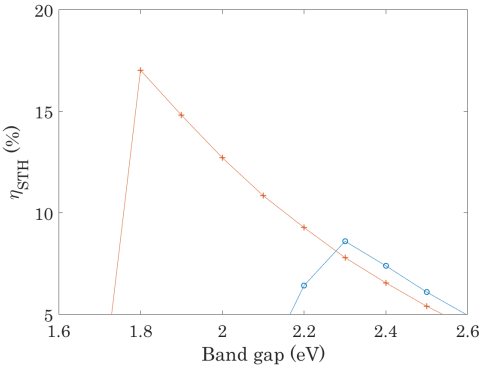

Figure A.1: The "+" (red) represents the efficiency for HBr splitting and the blue circles represents H_2O splitting using a single light absorber.

Dual Light Absorbers: Side-by-Side

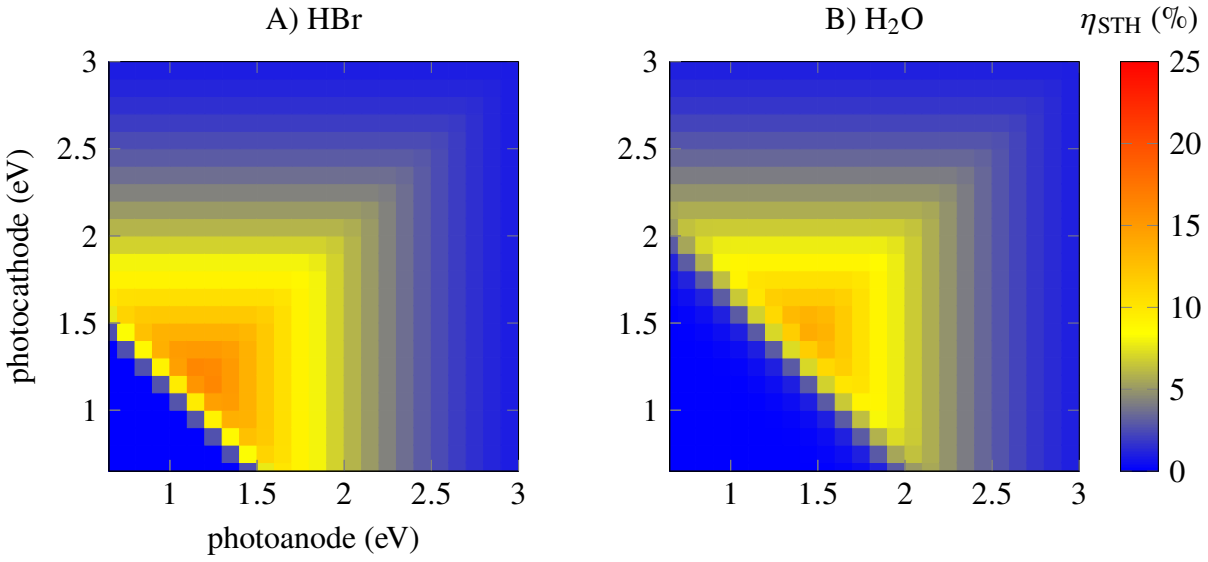

Figure A.2: This calculation shows the solar-to-hydrogen efficiency (η_{STH}) for two equivalent devices consisting of side-by-side semiconductors connected in parallel using A) HBr splitting and B) H_2O splitting.

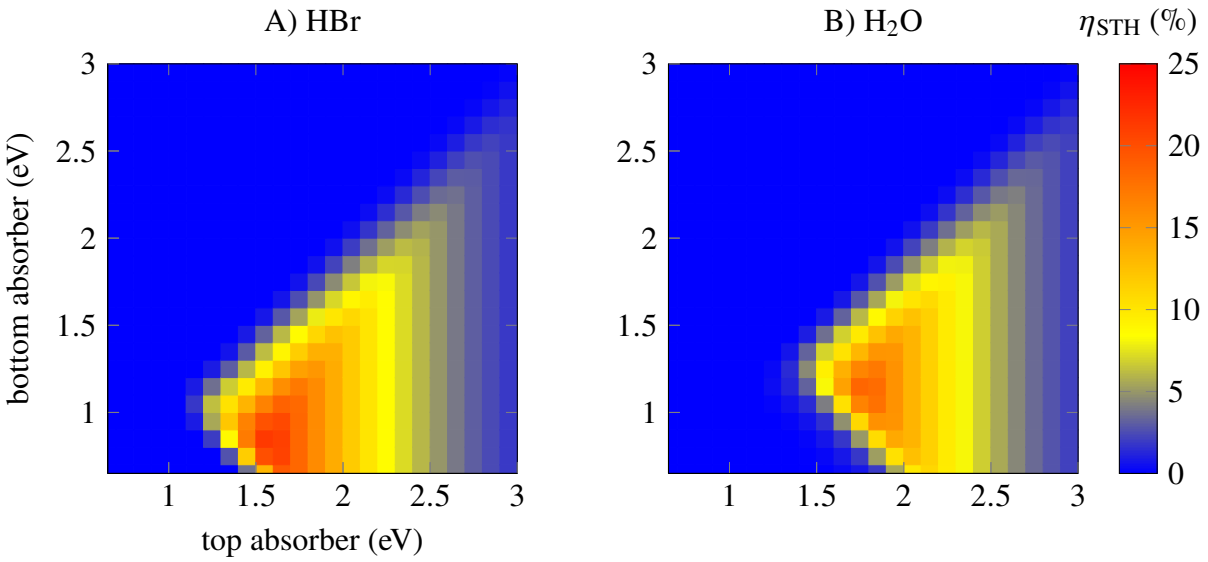

Figure A.3: This calculation shows the η_{STH} for two equivalent devices consisting of stacked (photoanode on top) semiconductors, using A) HBr splitting and B) H_2O splitting.

Dual Light Absorbers: Tandem

A.2 Script Dependencies

The script detailed performs simple calculations on potential device efficiencies for an integrated solar collector and chemical energy converter. It uses the theoretical outline developed in Chapter 2 to calculate efficiency. It works in the MATLAB (R2015b) environment. Dependencies include the `intersections.m` script written by Schwarz on Math Works File Exchange as well as a data file saved as `data.m` which includes a cell called `data` which is merely obtained as `ASTMG173.xls` from NREL stripped of headers.

A.3 Source Code

Listing A.1: Analysis Program for Efficiency Calculation

```
function A
%the purpose of this script is to estimate the efficiencies of certain PEC
%schemes in different solutions.

%dbstop if error %this flag tells the debugger to kick in if there is an error so I may
    investigate.
%dbstop if warning
%Author:
%Christopher W. Roske (CWR)
%Reviewed by:
%Shane Ardo
%James McKone

% v = ver;
% if ~any(strcmp('Parallel Computing Toolbox', {v.Name}));
%     warning('you will have a bad time without parallel computing toolbox, but if you so decide
    to proceed without it then change all parfor to for, good luck!')
% end


```

```
%close all

bg=[1:0.025:3];                          % band gap(s) of interest in eV%
%bg=[0.5:0.1:3];
%bg=[1.4,1.5,1.6];
a_SEP_V=1.09;                           % Volts: standard electrode potential for anodic reaction per 2 photons
c_SEP_V=0;                               % Volts: for cathodic reaction per 2 photons

no_photons=1;                            % no of photons  %no_photons=2 is S4, no_photons=1 is S2
betal = 0.95;                               %light losses from reflection and etc.

%BV parms for anodic reaction
a_ecd_c_mA_cm2=10^(-3)*10^3;             % anodic mA/cm^2 this is the exchange current density for a catalyst to be used in Butler-Volmer calculations
a_ctc_a=0.5;                            % anodic charge tranfer coefficient for anodic reaction for BV
a_ctc_c=0.5;                             % anodic charge transfer coefficient for cathodic reaction for BV

%BV parms for cathodic reaction
c_ecd_c_mA_cm2=10^(-3)*10^3;
c_ctc_a=0.5;
c_ctc_c=0.5;


num_photoabsorbers=2;                    % Dual=2 or single=1 photoabsorber?

sidebyside = 1;                          % 1 means they are side-by-side, 0 means stacked




no_e=1;                                   % no. of electrons transfered in
%desired reaction for BV (we just assume this is =1 for simplicity b/c
%BV is actually written for the 1 e- case.)


%the instructions below with the different cases of a) single light
%absorber doing two half reactions b) two light absorbers side-by-side
%doing two half reactions and c) two stacked light absorbers...



TOP{1,1} = 't';
TOP{1,2} = num2str( bg(1) );
TOP{2,1} = 'b';
TOP{2,2} = num2str( bg(1) );

top_or_bottom = TOP;                    %not important for you the user to set, only important for stacked calculations

if num_photoabsorbers == 1
    %if one photoabsorber is carrying out two half-reactions

    majority_doping_type='n';             % this may be 'p' for photocathode or 'n' for photoanode.


    EFF_A = zeros(1, length(bg));
    EFF_B = zeros(1, length(bg));
    count = 1;
    for i=bg
        display(['i ' num2str(count) ' of ' num2str( length(bg) ) ])
        [EFF_A(count), EFF_B(count)]=B(i, num_photoabsorbers, sidebyside, majority_doping_type, a_SEP_V, c_SEP_V, a_ecd_c_mA_cm2, a_ctc_a, a_ctc_c, c_ecd_c_mA_cm2, c_ctc_a, c_ctc_c, no_e, no_photons, top_or_bottom, betal);
        count=count+1;
```

```
    end

    figure
    plot(bg, EFF_A)
    hold on;
    plot(bg, EFF_B, 'r')

elseif num_photoabsorbers == 2
    %if two photoabsorbers are carrying out two half-reactions

    %they can be either 1) side by side
    %                   2) stacked

    if sidebyside == 1
        %if they are side by side

        %first we compute the photoanode efficiency


        %then we compute the photocathode efficiency


        %the max efficiency is obtained via 1/2 * ( eta_A + eta_C )

        %otherwise we can take the intersection of the J-V curves for the
        %photoanode + BV_a and the photocathode + BV_c and take that
        %intersection to be the operating point for the device.

        %let's do the latter...

        %the best use of resources would save the J-V curve for each
        %photoanode/photocathode + OP and then to the
        %intersection/efficiency calculations after that
%         if any(strcmp('Parallel Computing Toolbox', {v.Name}));
%             s = matlabpool('size');
%             if s ~= 0 %is the matlabpool open?
%                 matlabpool close; %then close it, we are done with it!
%             end
%
%         end
        if  ~( exist('TheData_temp.mat', 'file') == 2 ) %we save files for long computations, in
             the future we will generate these for each particular simulation


            a_EFF_A = zeros(1, length(bg)); %preallocating memory
            a_EFF_B = zeros(1, length(bg));
            c_EFF_A = zeros(1, length(bg));
            c_EFF_B = zeros(1, length(bg));

            TheData={}; %this is a cell


%             defaultProfile = parallel.defaultClusterProfile; %here we take advantage of multi-
     cores, if the computer has them
%             myCluster = parcluster(defaultProfile);
%             matlabpool(myCluster, 'open');

            for i = 1 : length(bg) %again, this loop is special in that is it for parallel
                 processing so its limitations/uses are a bit weird compared with a standard for
                 loop

                %photoanode

                disp([ num2str(bg(i)) ' and ' num2str(i) ]); %this is really just helpful for
                     diagnostic purposes in case something gets stuck or is abnormal

                majority_doping_type = 'n'; %first we compute for the photoanode
```

```
141                 [a_EFF_A_temp(i), a_EFF_B_temp(i), Gibbsoutput_a, Overpotential_a, J_a, SEP_V_a,
                        SEP_V_c, S_temp(i)]=B(bg(i), num_photoabsorbers, sidebyside,
                        majority_doping_type, a_SEP_V, c_SEP_V, a_ecd_c_mA_cm2, a_ctc_a, a_ctc_c,
                        c_ecd_c_mA_cm2, c_ctc_a, c_ctc_c, no_e, no_photons, top_or_bottom, betal);
142                 TheData_temp(i).bandgap_n = bg(i); %now we save the outputs to our cells, you'll
                        notice I am using TheData_temp. We can't save directly to TheData (defined
                        above) for two reasons 1) it is a cell 2) it was not created within the
                        parfor loop
143                 TheData_temp(i).doping_n ='n';
144                 TheData_temp(i).GibbsIncorp_n = Gibbsoutput_a;
145                 TheData_temp(i).Overpotential_n = Overpotential_a;
146                 TheData_temp(i).J_n = J_a;
147                 %photocathode
148
149                 majority_doping_type = 'p'; %now we run the photocathode
150
151                 %you will notice that the output of B is variable, i.e.,
152                 %more vars are saved from the photoanode case than for this
153                 %photocathode case: this is programmed behavior
154                 [c_EFF_A_temp(i), c_EFF_B_temp(i), Gibbsoutput_c, Overpotential_c, J_c]=B(bg(i),
                        num_photoabsorbers, sidebyside, majority_doping_type, a_SEP_V, c_SEP_V,
                        a_ecd_c_mA_cm2, a_ctc_a, a_ctc_c, c_ecd_c_mA_cm2, c_ctc_a, c_ctc_c, no_e,
                        no_photons, top_or_bottom, betal);
155                 TheData_temp(i).bandgap_p = bg(i); %again, we save the output for the
                        photocathode in a temp variable
156                 TheData_temp(i).doping_p = 'p';
157                 TheData_temp(i).GibbsIncorp_p = Gibbsoutput_c;
158                 TheData_temp(i).Overpotential_p = Overpotential_c;
159                 TheData_temp(i).J_p = J_c;
160
161             end
162
163             S=S_temp(1); %we need to save the solar irradiance
164
165             save('TheData_temp', 'TheData_temp', 'a_EFF_A_temp', 'a_EFF_B_temp', 'c_EFF_A_temp',
                        'c_EFF_B_temp', 'S') %here we are temporarily saving simulation results,
166             %these contain the raw J-V curves, but next we need do
167             %load-line analysis to obtain efficiencies
168         end
169
170         if (exist('TheData_temp.mat', 'file') == 2) && (~(exist('Temp.mat', 'file') == 2) )
171
172             %This is actually the computationally intensive process because we must
173             %first generate all the combinations of bandgap materials, draw their J-V
174             %curves and find their intersection to find the operating point of the
175             %device
176             load('TheData_temp') %here we load the temporarily saved file from the parfor loop
                        above
177             a_EFF_A = a_EFF_A_temp; %this contains the individual efficiencies... in this case
                        they are not STH but power
178             a_EFF_B = a_EFF_B_temp;
179             c_EFF_A = c_EFF_A_temp;
180             c_EFF_B = c_EFF_B_temp;
181             TheData = TheData_temp; %this contain the J-V curves
182             S=S(1); %solar irradiance
183             %now when we calculate these values for a side-by-side, their
184             %J-V curves are saved and we can now load them and calculate
185             %the different combinations to find interesections
186
187             %load J-V curves
188
189             %all possible combinations
190
191             %for i = 1 : length(bg)
192
193             TheEff_temp = cell(length(bg), length(bg) );    %preallocating memory
194             TheEff_eff_wBV=zeros(length(bg), length(bg), 1 );
195             TheEff_eff_woBV=zeros(length(bg), length(bg), 1);
```

```
196             clear i
197             for i = 1 : length(bg) %here again we use parallel processing to split up these jobs
                     and enable faster computation on multi-core systems
198
199                 TheEff_temp_eff_wBV = zeros(length(bg),1 ); %unfortunately these variables must
                         be redeclared each time
200                 TheEff_temp_eff_woBV = zeros(length(bg),1 );
201
202                 for v = 1 : length(bg) %this insures we are computing all possible combinations
203
204                     %display([ num2str(i) ' ' num2str(v) ]) %this is used for diagnostic purposes
                           during a run
205
206                     %here we do the load-line analysis for the photoanode plotted on the RHE
207                     %scale and the photocathode plotted on the RHE scale all happening in the
208                     %same current magnitude and determine at what voltage and current they
209                     %intersect at
210                     [a,c_wBV] = intersections(TheData(i).GibbsIncorp_n+TheData(i).Overpotential_n
                             , TheData(i).J_n , TheData(v).GibbsIncorp_p-TheData(v).Overpotential_p,
                             TheData(v).J_p);
211
212                     %the outputs in this case are:
213
214                     %a     is the Voltage where they intersect at vs RHE
215                     %c_wBV     is the current in mA/cm^2 they intersect at
216                     %for the BV case
217
218
219
220                     %for b) w/o BV case
221                     [a,c_woBV] = intersections(TheData(i).GibbsIncorp_n, TheData(i).J_n , TheData
                             (v).GibbsIncorp_p, TheData(v).J_p);
222                     %find efficiencies
223                     %    display(['SBS Efficiency for bandgaps (eV): ' num2str(bg(i)) ' and '
                             num2str(bg(v)) ])
224
225
226                     %there are several possible cases to deal with for the
227                     %output of c_wBV & c_woBV... those are dealt with here.
228
229                     if any(c_woBV) %if the without BV case has any non-zero elements then
                           continue
230                         %find max idx of woBV
231                         IndexWOBV = [];
232                         IndexWOBV = find(c_woBV); %find the index of the non-zero elements
233                         %now see if multiple indicies
234
235                         if length(IndexWOBV) > 1 %if there is more than one non-zero element then
                                we want the one which has the largest current
236                             MJ = c_woBV(IndexWOBV(1) ); %first value
237                             win=IndexWOBV(1); %at presesnt, the first value is the winner
238                             for JK = IndexWOBV
239                                 if abs(c_woBV(JK) ) > abs(MJ) %if any of the other values have a
                                       higher current than the first one then they are elected to
                                       be the winner
240                                     MJ = c_woBV(IndexWOBV(JK) );
241                                     win=JK;
242                                 end
243                             end
244                             IndexWOBV = win; %This is the index for the value of the highest
                                   current
245                         end
246
247                         if any(c_wBV) %now that we know c_woBV is non-zero it is time to find out
                                if w/BV is non-zero as well
248
249                             IndexWBV = find(c_wBV);
250
```

```
                if length(IndexWBV) > 1
                    MJ = c_wBV(IndexWBV(1) );
                    win=IndexWOBV(1);
                    for JK = IndexWBV
                        if abs(c_wBV(JK)) > abs(MJ)
                            MJ= c_wBV(IndexWBV(JK));
                            win=JK;
                        end
                    end
                    IndexWBV = win;
                end


            else %if sadly c_wBV is zero then we must empty that variable

                c_wBV = [];
            end


        else
            %if no nonzero's in the w/o BV case then
            %isempty or is nan

            c_woBV =[];
            c_wBV =[];

        end

        %The folowing actually computes the STH (%):

        if ~isempty(c_wBV) %there are two cases, w/BV is empty or it is not empty...
             if it is not empty then the efficiency can be calculated with that
             current

            TheEff_temp_eff_wBV(v) = abs((a_SEP_V - c_SEP_V)/no_e * c_wBV(IndexWBV)
                 / (2*S) *10 * 100);
        else %if it is empty then the efficiency is zero
            TheEff_temp_eff_wBV(v) = 0;
        end

        if ~isempty(c_woBV)

            TheEff_temp_eff_woBV(v) = abs(( (a_SEP_V - c_SEP_V)/no_e * c_woBV(
                 IndexWOBV) / (2* S) *10 * 100));

        else
            TheEff_temp_eff_woBV(v) = 0;
        end



        plot(TheData(i).GibbsIncorp_n+TheData(i).Overpotential_n, TheData(i).J_n, '
             displayname', num2str(i) )
        hold on;
        plot(TheData(v).GibbsIncorp_p-TheData(v).Overpotential_p, TheData(v).J_p, 'r'
             , 'displayname', num2str(v) )
        hold off;
        filename = 'Slice.gif';
        title(['BG PA: ' num2str(TheData(i).bandgap_n) ' and BG PC: ' num2str(TheData
             (v).bandgap_p) ' STH%: ' num2str( TheEff_temp_eff_wBV(v) ) ] )
        ylim([-60 0]);
        drawnow
        frame = getframe(1);
        im = frame2im(frame);
        [imind,cm] = rgb2ind(im,256);
        if i == 1 && v == 1;
            imwrite(imind,cm,filename,'gif', 'Loopcount',inf);
        else
```

```
312                         imwrite(imind,cm,filename,'gif','WriteMode','append');
313                     end
314
315                 end
316                 display( [ num2str(i) ' of ' num2str(length(bg)) ] ) %this allows the user to
                        keep up with the progress
317
318                 TheEff_eff_wBV(i,:)=TheEff_temp_eff_wBV;
319                 TheEff_eff_woBV(i,:)=TheEff_temp_eff_woBV;
320
321
322             end
323             %  plot( TheData(i).GibbsIncorp_n+TheData(i).Overpotential_n, TheData(i).J_n )
324             %  hold on;
325             %  plot( TheData(j).GibbsIncorp_p-TheData(j).Overpotential_p, TheData(j).J_p, 'p')
326
327
328             TheEff.eff_wBV=zeros(length(bg), length(bg));
329
330             TheEff.eff_woBV=zeros(length(bg), length(bg));
331
332             for R = 1 : length(bg)
333                 for a = 1 : length(bg)
334
335                     TheEff.eff_wBV(R,a)=TheEff_eff_wBV(R,a); %we store the variables like this
                            because it is convinent to debug with
336                     TheEff.eff_woBV(R,a)=TheEff_eff_woBV(R,a );
337
338                 end
339
340
341             end
342
343             save('Temp')
344
345         end
346
347
348         if (exist('Temp.mat', 'file') == 2 )
349             load('Temp.mat')
350             %put in a nice 3D plot! (well, bg by bg by color)
351             for i = 1 : length(bg)
352                 for d = 1 : length(bg)
353                     X(i,d) = bg(i);
354                     Y(i,d) = bg(d);
355                     if isempty(TheEff.eff_wBV(i,d) )
356                         TheEff.eff_wBV(i,d) = 0;
357                     end
358                     PlotHeatEff_wBV(i,d) = TheEff.eff_wBV(d,i);
359                 end
360             end
361             imagesc( bg, bg, PlotHeatEff_wBV, [0 25]);
362             axis xy; %this sets the origin
363             colorbar;
364             set(gcf, 'color', 'white');
365             xlabel('band gap (photoanode) eV')
366             ylabel('band gap (photocathode) eV')
367             title('Side by Side')
368         end
369
370     elseif sidebyside == 0
371         %if they are stacked
372
373         %first we compute the photoanode efficiency
374
375         %then we compute the photocathode efficiency
376
377         %the max efficiency is obtained via eta_A + eta_C
```

```
378
379         %otherwise we can take the J-V curves for the photoanode + BV_a and
380         %photocathode + BV_c and take the intersection to be the operating
381         %point for the device.
382
383         %let's do the latter
384
385         %unlike in the side-by-side case, it does little for us to save
386         %each J-V curve and then calculate efficiencies because the light
387         %absorption by the top semiconductor changes the J-V curves, so we
388         %do not have that luxury here
389
390
391 %         if any(strcmp('Parallel Computing Toolbox', {v.Name}));
392 %             s = matlabpool('size');
393 %             if s ~= 0 %is the matlabpool open?
394 %                 matlabpool close; %then close it, we are done with it!
395 %             end
396 %
397 %         end
398
399         if  ~( exist('TheData_temp.mat', 'file') == 2 ) %we save files for long computations, in
                 the future we will generate these for each particular simulation
400
401
402             a_EFF_A = zeros(1, length(bg)); %preallocating memory
403             a_EFF_B = zeros(1, length(bg));
404             c_EFF_A = zeros(1, length(bg));
405             c_EFF_B = zeros(1, length(bg));
406
407             TheData={}; %this is a cell
408
409 %
410 %             defaultProfile = parallel.defaultClusterProfile; %here we take advantage of multi-
        cores, if the computer has them
411 %             myCluster = parcluster(defaultProfile);
412 %             matlabpool(myCluster, 'open');
413
414             for i = 1 : length(bg) %again, this loop is special in that is it for parallel
                     processing so its limitations/uses are a bit weird compared with a standard for
                     loop
415
416                 %photoanode
417
418                 disp([ num2str(bg(i)) ' and ' num2str(i) ]); %this is really just helpful for
                         diagnostic purposes in case something gets stuck or is abnormal
419
420                 majority_doping_type = 'n'; %first we compute for the photoanode
421                 TOP=cell(2,2);
422                 TOP{1,1} = 't';
423                 TOP{1,2} = num2str( bg(i) );
424                 TOP{2,1} = 'b';
425                 TOP{2,2} = num2str( bg(i) );
426
427                 top_or_bottom = TOP;
428                 [a_EFF_A_temp(i), a_EFF_B_temp(i), Gibbsoutput_a, Overpotential_a, J_a, SEP_V_a,
                         SEP_V_c, S_temp(i)]=B(bg(i), num_photoabsorbers, sidebyside,
                         majority_doping_type, a_SEP_V, c_SEP_V, a_ecd_c_mA_cm2, a_ctc_a, a_ctc_c,
                         c_ecd_c_mA_cm2, c_ctc_a, c_ctc_c, no_e, no_photons, top_or_bottom, betal);
429                 TheData_temp(i).bandgap_n = bg(i); %now we save the outputs to our cells, you'll
                         notice I am using TheData_temp. We can't save directly to TheData (defined
                         above) for two reasons 1) it is a cell 2) it was not created within the
                         parfor loop
430                 TheData_temp(i).doping_n ='n';
431                 TheData_temp(i).GibbsIncorp_n = Gibbsoutput_a;
432                 TheData_temp(i).Overpotential_n = Overpotential_a;
433                 TheData_temp(i).J_n = J_a;
434                 c_EFF_A_temp_bottom = zeros(1, length(bg));
```

```
435                 c_EFF_B_temp_bottom = zeros(1, length(bg));
436                 a_EFF_A_temp_bottom = zeros(1, length(bg));
437                 a_EFF_B_temp_bottom = zeros(1, length(bg));
438                 TheData_temp_bottom={};
439                 %photocathode
440                 for v = 1 : length(bg)
441
442
443                     TOP{1,1} = 'b';
444                     TOP{1,2} = num2str( bg(v) );
445                     TOP{2,1} = 't';
446                     TOP{2,2} = num2str( bg(i) );
447
448                     top_or_bottom = TOP;
449                     majority_doping_type = 'p'; %now we run the photocathode
450
451                     %you will notice that the output of B is variable, i.e.,
452                     %more vars are saved from the photoanode case than for this
453                     %photocathode case: this is programmed behavior
454                     [c_EFF_A_temp_bottom(v), c_EFF_B_temp_bottom(v), Gibbsoutput_c,
                            Overpotential_c, J_c]=B(bg(v), num_photoabsorbers, sidebyside,
                            majority_doping_type, a_SEP_V, c_SEP_V, a_ecd_c_mA_cm2, a_ctc_a, a_ctc_c
                            , c_ecd_c_mA_cm2, c_ctc_a, c_ctc_c, no_e, no_photons, top_or_bottom,
                            betal);
455                     TheData_temp_bottom(v).bandgap_p = bg(i); %again, we save the output for the
                            photocathode in a temp variable
456                     TheData_temp_bottom(v).doping_p = 'p';
457                     TheData_temp_bottom(v).GibbsIncorp_p = Gibbsoutput_c;
458                     TheData_temp_bottom(v).Overpotential_p = Overpotential_c;
459                     TheData_temp_bottom(v).J_p = J_c;
460
461                 end
462                 c_EFF_B_temp_Bottom(i,:)=c_EFF_B_temp_bottom;
463                 c_EFF_A_temp_Bottom(i,:)=c_EFF_A_temp_bottom;
464                 TheData_temp_Bottom(i,:)=TheData_temp_bottom;
465
466             end
467
468             S=S_temp(1); %we need to save the solar irradiance
469
470             save('TheData_temp', 'TheData_temp', 'a_EFF_A_temp', 'a_EFF_B_temp', 'S', '
                    c_EFF_B_temp_Bottom', 'c_EFF_A_temp_Bottom', 'TheData_temp_Bottom') %here we are
                     temporarily saving simulation results,
471             %these contain the raw J-V curves, but next we need do
472             %load-line analysis to obtain efficiencies
473         end
474
475         if (exist('TheData_temp.mat', 'file') == 2) && (~(exist('Temp.mat', 'file') == 2) )
476
477             %This is actually the computationally intensive process because we must
478             %first generate all the combinations of bandgap materials, draw their J-V
479             %curves and find their intersection to find the operating point of the
480             %device
481             load('TheData_temp') %here we load the temporarily saved file from the parfor loop
                    above
482             a_EFF_A = a_EFF_A_temp; %this contains the individual efficiencies... in this case
                    they are not STH but in fact power
483             a_EFF_B = a_EFF_B_temp;
484             %             c_EFF_A = c_EFF_A_temp;
485             %             c_EFF_B = c_EFF_B_temp;
486             TheData = TheData_temp; %this contain the J-V curves for the top case
487             c_EFF_B_B = c_EFF_B_temp_Bottom;
488             c_EFF_A_B = c_EFF_A_temp_Bottom;
489             TheData_B = TheData_temp_Bottom;
490
491
492             S=S(1); %solar irradiance
493             %now when we calculate these values for a side-by-side, their
```

```
494             %J-V curves are saved and we can now load them and calculate
495             %the different combinations to find interesections
496
497             %load J-V curves
498
499             %all possible combinations
500
501             %for i = 1 : length(bg)
502
503             TheEff_temp = cell(length(bg), length(bg) );    %preallocating memory
504             TheEff_eff_wBV=zeros(length(bg), length(bg), 1 );
505             TheEff_eff_woBV=zeros(length(bg), length(bg), 1);
506             clear i
507             for i = 1 : length(bg) %here again we use parallel processing to split up these jobs
                     and enable faster computation on multi-core systems
508
509                 TheEff_temp_eff_wBV = zeros(length(bg),1 ); %unfortunately these variables must
                         be redeclared each time
510                 TheEff_temp_eff_woBV = zeros(length(bg),1 );
511
512                 for v = 1 : length(bg) %this insures we are computing all possible combinations
513                     display([ num2str(i) ' ' num2str(v) ]) %this is used for diagnostic purposes
                             during a run
514
515                     %here we do the load-line analysis for the photoanode plotted on the RHE
516                     %scale and the photocathode plotted on the RHE scale all happening in the
517                     %same current magnitude and determine at what voltage and current they
518                     %intersect at
519                      if any( TheData_B(i,v).J_p(:) )
520                         [a,c_wBV] = intersections(TheData(i).GibbsIncorp_n+TheData(i).
                                 Overpotential_n, TheData(i).J_n , TheData_B(i,v).GibbsIncorp_p-
                                 TheData_B(i,v).Overpotential_p, TheData_B(i,v).J_p(:) );
521                      else
522                          c_wBV =[];
523                      end
524                     %the outputs in this case are:
525
526                     %a     is the Voltage where they intersect at vs RHE
527                     %c_wBV     is the current in mA/cm^2 they intersect at
528                     %for the BV case
529
530
531
532                     %for b) w/o BV case
533                     if any(TheData_B(i,v).J_p(:) )
534                         [a,c_woBV] = intersections(TheData(i).GibbsIncorp_n, TheData(i).J_n ,
                                 TheData_B(i, v).GibbsIncorp_p, TheData_B(i,v).J_p(:) );
535                      else
536                          c_woBV = [];
537                      end
538                     %find efficiencies
539                     %    display(['SBS Efficiency for bandgaps (eV): ' num2str(bg(i)) ' and '
                             num2str(bg(v)) ])
540
541
542                     %there are several possible cases to deal with for the
543                     %output of c_wBV & c_woBV... those are dealt with here.
544
545                     if any(c_woBV) %if the without BV case has any non-zero elements then
                             continue
546                         %find max idx of woBV
547
548                         IndexWOBV = find(c_woBV); %find the index of the non-zero elements
549                         %now see if multiple indicies
550
551                         if length(IndexWOBV) > 1 %if there is more than one non-zero element then
                                 we want the one which has the largest current
552                             MJ = c_woBV(IndexWOBV(1) ); %first value
```

```
553                         win=IndexWOBV(1); %at presesnt, the first value is the winner
554                         for JK = IndexWOBV
555                             if abs(c_woBV(JK) ) > abs(MJ) %if any of the other values have a
                                     higher current than the first one then they are elected to
                                     be the winner
556                                 MJ = c_woBV(IndexWOBV(JK) );
557                                 win=JK;
558                             end
559                         end
560                         IndexWOBV = win; %This is the index for the value of the highest
                                 current
561                     end
562
563                     if any(c_wBV) %now that we know c_woBV is non-zero it is time to find out
                            if w/BV is non-zero as well
564
565                         IndexWBV = find(c_wBV);
566
567                         if length(IndexWBV) > 1
568                             MJ = c_wBV(IndexWBV(1) );
569                             win=IndexWOBV(1);
570                             for JK = IndexWBV
571                                 if abs(c_wBV(JK)) > abs(MJ)
572                                     MJ= c_wBV(IndexWBV(JK));
573                                     win=JK;
574                                 end
575                             end
576                             IndexWBV = win;
577                         end
578
579
580                     else %if sadly c_wBV is zero then we must empty that variable
581
582                         c_wBV = [];
583                     end
584
585
586                 else
587                     %if no nonzero's in the w/o BV case then
588                     %isempty or is nan
589
590                     c_woBV =[];
591                     c_wBV =[];
592
593                 end
594
595                 %The folowing actually computes the STH (%):
596
597                 if ~isempty(c_wBV) %there are two cases, w/BV is empty or it is not empty...
                         if it is not empty then the efficiency can be calculated with that
                         current
598
599                     TheEff_temp_eff_wBV(v) = abs((a_SEP_V - c_SEP_V)/no_e * c_wBV(IndexWBV)
                             / (S) *10 * 100);
600                 else %if it is empty then the efficiency is zero
601                     TheEff_temp_eff_wBV(v) = 0;
602                 end
603
604                 if ~isempty(c_woBV)
605
606                     TheEff_temp_eff_woBV(v) = abs(( (a_SEP_V - c_SEP_V)/no_e * c_woBV(
                             IndexWOBV) / (S) *10 * 100));
607
608                 else
609                     TheEff_temp_eff_woBV(v) = 0;
610                 end
611
612
```

```
                end
                display( [ num2str(i) ' of ' num2str(length(bg)) ] ) %this allows the user to keep up with the progress

                TheEff_eff_wBV(i,:)=TheEff_temp_eff_wBV;
                TheEff_eff_woBV(i,:)=TheEff_temp_eff_woBV;

            end
            %  plot( TheData(i).GibbsIncorp_n+TheData(i).Overpotential_n, TheData(i).J_n )
            %  hold on;
            %  plot( TheData(j).GibbsIncorp_p-TheData(j).Overpotential_p, TheData(j).J_p, 'p')


            TheEff.eff_wBV=zeros(length(bg), length(bg));

            TheEff.eff_woBV=zeros(length(bg), length(bg));

            for R = 1 : length(bg)
                for a = 1 : length(bg)

                    TheEff.eff_wBV(R,a)=TheEff_eff_wBV(R,a); %we store the variables like this because it is convinent to debug with
                    TheEff.eff_woBV(R,a)=TheEff_eff_woBV(R,a );

                end


            end

            save('Temp')

        end


        if (exist('Temp.mat', 'file') == 2 )
            load('Temp.mat')
            %put in a nice 3D plot! (well, bg by bg by color)
            for i = 1 : length(bg)
                for d = 1 : length(bg)
                    X(i,d) = bg(i);
                    Y(i,d) = bg(d);
                    if isempty(TheEff.eff_wBV(i,d) )
                        TheEff.eff_wBV(i,d) = 0;
                    end
                    PlotHeatEff_wBV(i,d) = TheEff.eff_wBV(d,i); %this flip is to make sure the photoanode is on the x-axis and photocathode is on the y-axis
                end
            end
            imagesc( bg, bg, PlotHeatEff_wBV, [0 25]);
            axis xy; %this sets the origin
            colorbar;
            set(gcf, 'color', 'white');
            xlabel('band gap (photoanode) eV')
            ylabel('band gap (photocathode) eV')
            title('Stacked')
        end
    end
end

end

function [OUTPUT_A, OUTPUT_B, varargout] = B(band_gap_eV, num_photoabsorbers, sidebyside, majority_doping_type, a_SEP_V, c_SEP_V, a_ecd_c_mA_cm2, a_ctc_a, a_ctc_c, c_ecd_c_mA_cm2, c_ctc_a, c_ctc_c, no_e, no_photons, top_or_bottom, betal)

%note this may be unusual to you for outputs, but 'varargout' gives
%variables length for the output so I can pass J-V curves to the primary
%function
```

```
676
677
678 %H2O -> H2 + 1/2 O2 has E^0 = 1.229 V per electron... assume two electron
679 %process so 1.229 * 2 is SEP_V... so an S2 will require 1.229 eV per
680 %photon! (as bolton says)
681
682
683 AM='1.5';                           % may be set as 'i' for imaginary sun, '0' for AM 0 data or
        '1.5' for AM 1.5 data
684 Voc_approx='mu_power';                   % There are multiple estimates available for Voc, the '
        mu_power' approach or 'mindiosat' or 'Sze'
685 %stp_size=0.0005;                      % step size for J-V curve calculations...
686 stp_size=0.001;
687 %CONSTANTS
688
689 hc_eV_micron = 1.23984193;          % in eV * micron
690
691 band_gap_micron= hc_eV_micron/band_gap_eV;  %The bandgap internally is computed in microns. Deal
        with it.
692
693 Avocado=6.02214129*10^(23);
694
695 e_C=1.60217646*10^(-19);            % Coulombs
696 c_m_s = 2.99792458e8;               % speed of light m/s
697 h_Js = 6.62608e-34;                 % Planck constant J * s
698 kB_J_K = 1.38066e-23;               % Boltzmann constant J K^-1
699
700 R_J_molK=kB_J_K*Avocado;            % gas constant with units of J/(mol K)
701 F=e_C * Avocado;                    % Faraday constant
702 hc_J_um = 1.986446*10^(-19);        % J * um
703 n_refractive = 1;                   % refractive index of semiconductor for BB calcs
704 n_idealityfactor=1;                 % ideality factor for semiconductor for J_0, Voc, J calcs
705 alpha = 2;                          % internal conversion coefficient for calculating P curve
706 T_K = 300;                          % Kelvin of semiconductor for BB calcs
707 T_sun_K=5800;                       % Kelvin of the calculated sun
708 radius_sun_m=6.955 *10^8;           % radius of sun in meters
709 distance_earth_m=1.484*10^11;       % distance of earth to sun in meters (on avg)
710 A_mA_cm2_K2=1.20*10^5;              % free electron value, 120 A cm^-2 K-2... Richardson constant
711 %COMPUTATIONS
712
713 load reqd.mat %This contains NREL data for AM 1.5 spectrum, AM 0 and AMG 1.5
714 %This loads data, a variable that is important for calculations involving
715 %AM 1.5
716
717 lambda=data(1:end,1)*1/10^3;        % this puts the internal data in terms of microns... Why my
        obsession with um? Made it easier to compare with literature while writing this.
718 [nn, index_of_interest]= (min(abs(lambda - band_gap_micron ))); %calculates index of the band gap
         we are interested in
719
720 %%%%%%%%%%%%%%%%%%%%%%%%%%%%%%%%%%%%%%%%%%%%%%%
721 %%%%%%%%%%%%%%Calculate BB %%%%%%%%%%%%%%%%%%%%
722 %%%%%%%%%%%%%%%%%%%%%%%%%%%%%%%%%%%%%%%%%%%%%%%
723
724 %disp('Calculating BB');
725
726
727 ratio=radius_sun_m^2/distance_earth_m^2; %recall that light intensity from a pt source follows
        the inverse square law
728
729 sun=zeros(length(lambda),1);
730 for i=2:length(lambda)
731     sun(i)=2 * pi * h_Js * c_m_s^2/lambda(i)^5 * ( 1 / ( exp( h_Js * c_m_s/ ( lambda(i)*10^(-6) *
            kB_J_K * T_sun_K ) )-1 )) * 10^(24) * ratio;
732 end
733
734 %This means sun(i) is in units of W/m^2/microns and lambda is in units of
735 %microns
736
```

```
737
738
739 %%%%%%%%%%%%%%%%%%%%%%%%%%%%%%%%%%%%%%%%%%%%
740 %%%%%%%%%%%%%%%Calculate E %%%%%%%%%%%%%%%%%
741 %%%%%%%%%%%%%%%%%%%%%%%%%%%%%%%%%%%%%%%%%%%%
742
743 %disp('Calculating E')
744
745 %The next three if statements are optional swtiches to make it easy to pick
746 %between the different scenarios for incoming light flux.
747 if strcmp(AM, 'i')
748     Spectral_Irradiance=sun; %in units of W/m^2/microns from generated BB sun.
749 end
750
751 if strcmp(AM, '0')
752     Spectral_Irradiance=data(1:end,2) * 1000; %in units of W/m^2/microns AM 0
753 end
754
755 if strcmp(AM, '1.5')
756     Spectral_Irradiance=data(1:end,3) * 1000; %in units of W/m^2/microns AM 1.5
757 end
758
759
760 S = trapz( lambda, Spectral_Irradiance )*no_photons; %integrated AM 1.5 in W m^-2, of course
      ~1000 W/m^2
761
762 if sidebyside == 0
763     if strcmp( top_or_bottom{1,1}, 't') % if top
764         % do nothing
765     elseif strcmp(top_or_bottom{1,1}, 'b')
766         %remove lambda corresponding to the top, to account for its
767         %complete light absorption
768         bg_t_eV = str2num( top_or_bottom{2,2} ); %bg of top light absorber to remove
769
770         bg_t_microns = ( bg_t_eV ./ hc_eV_micron )^(-1); %bg of top in microns
771
772         %find index of bg corresponding to bg_t_microns in lambda
773         [aa, idx] = min(abs( lambda - bg_t_microns ) );
774         lance = length([1:idx]);
775         Spectral_Irradiance(1:idx) = zeros( lance,1 );
776     end
777
778 end
779
780
781
782 I_s = (Spectral_Irradiance./hc_J_um).*lambda; %This converts from spectral irradiance to photon
      flux... should be ~ 5 * 10^21 photons/(s * micron * m^2) around max
783
784 J_e = zeros(length(lambda),1); %preallocate memory
785
786 sigma = zeros(length(lambda),1); %prealocate memory
787
788 for i=1:length(sigma) %This is a temporary placeholder until we decide to incorporate sigma data
      aka absorption spectrum for the semiconductor
789     sigma(i) = 1;
790 end
791
792
793 for i = 2 : length(J_e)
794
795     J_e(i) = trapz( lambda(1:i) , I_s(1:i) * sigma(i) ); % \int I_s(lambda) * sigma(lambda) d(
          lambda)
796     %This is eqn 1 in Ross 1977.
797
798 end
799
800
```

```
%We define the energy yield as being the rate of excitation times the
%band-gap energy, E = J_e * (hc/lambda_0)

E = zeros(length(lambda),1); %preallocate memory

for i = 2: length(E)

    E(i) = J_e(i) * (hc_J_um/lambda(i)); %eqn 2 in Ross 1977

end


%this is also called the total incident solar power.

%At this point one may plot the 'E' in Fig. 1 of Ross 1977 by the
%following:

%Sanity check:

%ylabel(gca, 'Yield (W/m^2)')
%xlabel(gca, 'Band gap (nm)')
%plotyy(lambda*1000, E, lambda*1000, E./S) %Y-axis 1 is YIELD, 2 is
%efficiency


%%%%%%%%%%%%%%%%%%%%%%%%%%%%%%%%%%%%%%%%%%%%%%%%
%%%%%%%%%%%%%%%Calculate Y %%%%%%%%%%%%%%%%%%%%%
%%%%%%%%%%%%%%%%%%%%%%%%%%%%%%%%%%%%%%%%%%%%%%%%

%disp('Calculating Y')

%Now to calculate the open-circuit yield, Y, which is defined as the
%product of the maximum flux and the maximum potential difference.
%This is defined as Y = J_e and \mu_max


%we know mu_max is equal to kT * ln (int I_s/ int I_BB)

%Calculate I_BB
I_BB=zeros(length(lambda),1);
for i=1:length(lambda)
    I_BB(i) = 8 * pi * n_refractive^2 * c_m_s/lambda(i).^4 * (1 / ( exp(h_Js*c_m_s/(kB_J_K .*
        lambda(i).*10^(-6) * T_K) ) -1 ) ) * 10^(18);
end

%Now we need to integrate I_BB over d lambda from 0 microns to band gap
%microns to obtain the rate of photons absorbed per area per micron

for i = 2:length(lambda)
    clear indexofinterest
    [m,indexofinterest] = min(abs(lambda-lambda(i)));
    int_I_BB(i) = trapz(lambda(1:indexofinterest), I_BB(1:indexofinterest) );
end


%mu_max calculation

mu_max=zeros(length(lambda),1); %preallocate memory

for i=1: length(mu_max)
    mu_max(i) = kB_J_K*T_K*log( J_e(i) /int_I_BB(i) );   %as defined in eqn 8 of Ross 1977
end

%what we do here is take total number of absorbed photons then convert it
%to moles of photons then times by mu_max which is in terms of J/mol so
%that we get the total J per micron per unit area
Y = zeros(length(lambda),1);
for i = 2:length(lambda)
```

```
868     Y(i) = J_e(i) .* mu_max(i); %eqn 10 Ross 1977
869 end
870
871 %At this point one may plot the 'Y' and 'E' in Fig. 1 of Ross 1977 by the
872 %following:
873
874 %ylabel(gca, 'Yield (W/m^2)')
875 %xlabel(gca, 'Band gap (nm)')
876 %plotyy(lambda*1000, Y, lambda*1000, Y./S)
877 %plot(lambda*1000, E, 'displayname', 'E')
878 %hold on;
879 %plot(lambda*1000, Y, 'displayname', 'Y')
880
881
882 %%%%%%%%%%%%%%%%%%%%%%%%%%%%%%%%%%%%%%%%%%%%
883 %%%%%%%%%%%%%%%Calculate P %%%%%%%%%%%%%%%%
884 %%%%%%%%%%%%%%%%%%%%%%%%%%%%%%%%%%%%%%%%%%%%
885
886 %disp('Calculating P')
887
888 %in order to get the net production of photoproduct, it is necessary to
889 %lower the potential difference below mu_max. In most photochemical
890 %systems, this is achieved by reducing the fraction of absorber molecules
891 %that are in the upper electronic state at any instant. The total power
892 %production is P = J_e ( 1 - phi_loss) mu
893 %where phi_loss is the fraction of absorbed quanta that are lost from the
894 %excited state without yielding a photoproduct.
895 %phi_loss ~= kT/mu_max
896
897 mu=zeros(length(lambda),1); %preallocate memory
898
899 for i=1:length(lambda)
900     mu_P(i) = mu_max(i) - kB_J_K * T_K * log( mu_max(i)./ (kB_J_K * T_K) ) - kB_J_K * T_K * log(
          alpha); %eqn 15 Ross 1977
901 end
902
903
904 J_r=zeros(length(lambda),1); %preallocate memory
905
906 for i=1:length(lambda)
907     J_r(i) = exp( mu_P(i) / (kB_J_K * T_K) ) .* int_I_BB(i); %eqn 3 Ross 1977
908 end
909
910 phi_loss=zeros(length(lambda),1); %preallocate memory
911
912 for i=1:length(lambda)
913
914     phi_loss(i) = alpha * J_r(i) ./ J_e(i); %eqn 12 Ross 1977
915
916 end
917
918 P = zeros(length(lambda),1);
919
920 for i = 2:length(lambda)
921     P(i) = J_e(i) .* mu_P(i).*(1 - phi_loss(i) ); %eqn 11 Ross 1977
922 end
923 %sanity check:
924
925 %ylabel(gca, 'Yield (W/m^2)')
926 %xlabel(gca, 'Band gap (nm)')
927 %plotyy(lambda*1000, Y, lambda*1000, Y./S)
928 %plot(lambda*1000, E, 'displayname', 'E')
929 %hold on;
930 %plot(lambda*1000, Y, 'displayname', 'Y')
931 %plot(lambda*1000, P, 'displayname', 'P')
932
933 %or as efficiency
934 %
```

```
%  figure('Color', [1 1 1])
%  plot(lambda*1000, E./S, 'displayname', 'E', 'LineWidth', 4)
%  hold all;
%  plot(lambda*1000, Y./S, 'displayname', 'Y', 'LineWidth', 4)
%  plot(lambda*1000, P./S, 'displayname', 'P', 'LineWidth', 4)
%  ylabel(gca, 'Efficiency (%)')
%  xlabel(gca, 'Band gap (nm)')
%  legend('toggle')
%  set(gca, 'FontSize', 33)
%  ylim([0 0.5]);
%  set(findall(gca,'type','text'),'fontSize',33)
%  set(findall(gca,'type','LineWidth'),'LineWidth',4)
%
%


%%%%%%%%%%%%%%%%%%%%%%%%%%%%%%%%%%%%%%%%%%%%%%%%
%%%%%%%%%%%%%%Calculate Jsc %%%%%%%%%%%%
%%%%%%%%%%%%%%%%%%%%%%%%%%%%%%%%%%%%%%%%%%%%%%%%

%disp('Calculating J_sc')

%the implicit assumption is that J_L and J_sc are equal AND J_L is voltage
%independent.
%The following is for finding the short-circuit current density under E
%conditions and then P conditions
%figure
%hold all;

photon_flux_E=E./hc_J_um .*lambda; %takes spectral irradiance of E and turns it into photoflux
     and then we make it into current
for i = 2: length(lambda)
    current_E(i) = photon_flux_E(i).*e_C/10.*betal;
end
J_sc = current_E;


%%%%%%%%%%%%%%%%%%%%%%%%%%%%%%%%%%%%%%%%%%%%%%%%
%%%%%%%%%%%%%%Calculate J_0 %%%%%%%%%%%%
%%%%%%%%%%%%%%%%%%%%%%%%%%%%%%%%%%%%%%%%%%%%%%%%

%There are two possible ways and switches to reflect these different
%assumptions. The first method does not depend on Ross' method, whilst the
%second method does use Ross' method involving mu. The first method gives
%more realistic/conservative estimates and the second method gives more
%ideal estimates.

%disp('Calculating J_0')



%%%%%%%%%% Conservative estimate mindiosat %%%%%%%%%%

%the minimum value of the diode saturation current is
%J_0 = q/k ( 15 * SBC / pi^4) * T^3 * int from u to infty x^2/(e^x -1) dx
%where u = E_g/kT

%more information on this assumption can be found at Solar Energy Materials
%and Solar Cells. 36 (1995) pp 201-222.

%unfortunately evaluation of this intergral is very complex and numerical
%integration may suffer in the lim x--> infty due to build up of errors
%over the course of this improper integral... one could pick infinity to be
%something like 6 eV or put this in terms of the Rieman Zeta
%series for convergence, however, numericaly 4 eV is easier, which I have
%defined to be the infinite variable.

%infinite= 4;                 % eV for calculation of J_0 in slow algorithm (disabled now)
```

```
1002
1003 %SBC is the Stefan-Boltzman constant or 2 * pi^5 * k_B^4/(15 * h^3 * c^2)
1004 SBC= 2 * pi^5 * kB_J_K^4/(15 * h_Js^3 * c_m_s^2);
1005
1006
1007 %The problem with the algorithm below, while it works and is simple to
1008 %impelment or understand, is that it is very slow to converge and takes 2 hrs on my
1009 %processor to process all of lambda. Either I can save it as a text-file and load it on demand or
1010 %utilize a more sophisticated method so that it can change whenever a user
1011 %inputs a different variable.
1012 %
1013 %  for i = 1 : length(lambda)
1014 kB_eV_K = kB_J_K /(1.602176565*10^(-19)); %kB in terms of eV
1015 %
1016 % % 1 electronvolt = 1.602E+19 J
1017 %
1018 %     u = (hc/(lambda(i) *e ))/(kB_eV*T); %it's very important kB here is in
1019 % %    terms of eV/K not J/K, otherwise the math explodes due to incompatible
1020 % %    units.
1021 %
1022 %      x=[u:1:infinite/kB_eV*T];
1023 %
1024 %     J_0(i) = e / kB * (15 * SBC /pi^4) * T^3 * trapz( x ,x.^2./(exp(x) -1) );
1025 %     disp([num2str(i) ' of ' num2str(length(lambda)) ] )
1026 %  end
1027 %
1028 %  To check sanity:
1029
1030 %  semilogy(hc./(lambda.*e), J_0)
1031 %  xlabel(gca, 'Band gap (eV)')
1032 %  ylabel(gca, 'diode saturation current (A/m^2)') %should show a linear line from ~10^0 down to
       10^-70 A/m^2 at 4 eV
1033
1034 % the basic problem is to compute the integral int_x^\infty \frac{t^n}{e^{t}-1} dt
1035 % This integral is not trivial to solve.
1036 % its expansion is:
1037 % \sum_k=1^{\infty} exp(-k * x} * [ x^n/k + n * x^{n-1}/k^2 +
1038 % (n)(n-1)x^(n-2)/k^3 + ... + n!/k^{n+1}
1039 % courtesy of Abramowitz and Stegun: Handbook of Mathematical Functions
1040 %
1041 % pp 998, Misc functions. Debye Integral. 27.1.2 (tenth printing, 1972)
1042 % our case is n=2.
1043
1044 J_0 = zeros(length(lambda),1);
1045
1046 if strcmp(Voc_approx,'mindiosat')     %Voc may be calculated from mu_max or mindiosat
1047
1048     CONST_h=e_C / kB_J_K * (15 * SBC /pi^4) * T_K^3;
1049
1050     %This for loop is merely a fininte truncation of the infinite series mentioned above.
1051     for i=1:length(lambda)
1052         x=(hc_J_um/(lambda(i) * e_C))/(kB_eV_K * T_K);
1053         % x= (hc_J_um/lambda(i)) * e_C / (kB_J_K * T_K) ;
1054         J_0_int=0;
1055         k=1;
1056         M= exp(-k * x) * ( x^2 / 2 + 2 * x^1 /k^2 + 2/k^3 ); % new term
1057         while M > ( 10^(-100)) %check if new term is larger than some arb. small value. A test
               for convergence. The smallest value here is 10^(-70) so this precision is justified.
1058             J_0_int = J_0_int + M;
1059             M= exp(-k * x) * ( x^2 / 2 + 2 * x^1 /k^2 + 2/k^3 );
1060             k=k+1;
1061         end
1062         J_0(i) = CONST_h * J_0_int;
1063     end
1064
1065 end
1066
1067
```

```
%sanity check:

%semilogy(hc./(lambda.*e), J_0)
%xlabel(gca, 'Band gap (eV)')
%ylabel(gca, 'diode saturation current (A/m^2)') %should show a linear line from ~10^0 down to
     ~10^-70 A/m^2 at 4 eV


%The above is one way. Another way is to use the diode eqn to calculate it:
% I = I_0 * (exp(q * V/(nkt) -1 ) - I_L
% at Voc we have I, q, Voc, nkt and I_L, all we need to do is rearrange to
% solve.

% (I+I_L)/(exp(q*V/(nkT)) -1) = I_0


%%%%%%%%%% Liberal Estimate Based on mu_max %%%%%%%%%%

if strcmp(Voc_approx,'mu_power')    %Voc may be calculated from mu_max or mindiosat
    for i = 1 : length(lambda)
        J_0(i) = J_sc(i)/ ( ( exp( ( 1 * mu_P(i)/e_C ) / (n_idealityfactor * kB_eV_K * T_K) )-1 )
             *100 );
    end

end

if strcmp(Voc_approx, 'Sze')

    for i = 1 : length(lambda)
        bH=hc_J_um./(lambda(i).*e_C); %barrier height (eV)
        J_0(i) = A_mA_cm2_K2 * T_K^2 * exp( - bH / (kB_eV_K * T_K)); %pg 156 of Sze
    end


end

if strcmp(Voc_approx, 'IEEE')
    % from http://ieeexplore.ieee.org/stamp/stamp.jsp?arnumber=01486627
    C=17.90;% mA/cm^2 K^3
    for i = 1 : length(lambda)
        E_g = hc_J_um./(lambda(i).*e_C);
        J_0(i) = C * T_K^3 * exp( - E_g / (kB_eV_K * T_K) );

    end

end



%%%%%%%%%%%%%%%%%%%%%%%%%%%%%%%%%%%%%%%%%%%%
%%%%%%%%%%%%%Calculate Voc %%%%%%%%%%%%
%%%%%%%%%%%%%%%%%%%%%%%%%%%%%%%%%%%%%%%%%%%%

%Voc may be determined by either the mindiosat method or the mu_max method.
%One is more conservative/realistic than the other.

%disp('Calculating V_oc')

%given as Voc = (n * k * T/ q) * ln ( I_L/ I_0 + 1)

Voc=zeros(length(lambda),1);

%The method below is one method.

if strcmp(Voc_approx,'mindiosat')
    for i = 1:length(lambda)
        Voc(i) = n_idealityfactor * kB_J_K * T_K/ e_C * log( J_sc(i)/J_0(i) + 1);
    end
```

```
1134 end
1135
1136
1137
1138 %The method below is another method.
1139 if strcmp(Voc_approx,'mu_power')
1140     for i = 1:length(lambda)
1141
1142         Voc(i) = mu_P(i)./e_C;
1143
1144     end
1145 end
1146
1147
1148 if strcmp(Voc_approx, 'Sze') || strcmp(Voc_approx, 'IEEE')
1149     for i = 1:length(lambda)
1150         Voc(i) = n_idealityfactor * kB_J_K * T_K/ e_C * log( J_sc(i)/(J_0(i)) + 1);
1151     end
1152 end
1153 % %%sanity check:VOC
1154 %  plot(hc_J_um./(lambda.*e_C), Voc)
1155 %  xlabel(gca, 'Band gap (eV)')
1156 %  ylabel(gca, 'Voc (Volts)')
1157 % %
1158 % %
1159 % % %
1160
1161 %unrelated to the methods above are these variables:
1162 V_max_u = max(Voc);
1163 V_max_l = -max(Voc);
1164
1165 % V_max_u=Voc(index_of_interest);
1166 % V_max_l=-Voc(index_of_interest);
1167
1168 %they are used to set bounds on the size of later arrays to aid in speeding
1169 %up computations.
1170 %
1171
1172
1173
1174
1175 %%%%%%%%%%%%%%%%%%%%%%%%%%%%%%%%%%%%%%%%%%%%%%%
1176 %%%%%%%%%%Calculate J-V curves %%%%%%%%
1177 %%%%%%%%%%%%%%%%%%%%%%%%%%%%%%%%%%%%%%%%%%%%%%%
1178
1179 %disp('Calculating J-V curves')
1180
1181 %IV curve in the first quadrant is given by:
1182
1183 % I = I_L - I_0 [ exp ( q V/ (n k T ) - 1) ]
1184
1185
1186
1187
1188 %Voltage=[V_max_l:stp_size:V_max_u];
1189
1190 Voltage=[V_max_l:stp_size:V_max_u];
1191
1192 J = zeros(1, length(Voltage) );
1193
1194
1195 %the structure of the following statements may not be very intuitive, but
1196 %it was written this way to increase throughput
1197
1198 if strcmp(majority_doping_type, 'p')
1199
1200     for i = index_of_interest %this is written this way so that we may scan just one lambda of
          interest or all of them
```

```
1201
1202        [nn, stopV] = min(abs(Voltage-Voc(i))); %we find the Voc
1203
1204        startV = 1;
1205
1206
1207        for j= startV : stopV %we use startV:stopV to limit the number of calls required
1208            if ((Voltage(j) < Voc(i) ) && (Voltage(j) > V_max_l ))
1209                J(1,j) = J_0(i) * ( exp( 1 * Voltage(j) / (n_idealityfactor * kB_eV_K * T_K) )-1
                        )*100 - J_sc(i);
1210
1211                if J(1,j) > 0  %when the exponential takes over we don't really care what those
                        currents are and so they are ignored.
1212                    J(1,j) = 0;
1213                end
1214            end
1215
1216        end
1217
1218
1219    end
1220 else
1221    for i = index_of_interest
1222        [nn, stopV] = min(abs(Voltage-Voc(i)));
1223        startV  = length(Voltage) - stopV;
1224        %[nn, stopV] = min(abs(Voltage));
1225        if startV == 0
1226            startV = 1;
1227        end
1228        %for j= startV : stopV
1229        for j = startV: length(Voltage)
1230
1231            if ((Voltage(j) < V_max_u) && (Voltage(j) > -Voc(i) ))
1232                J(1,j) = J_0(i) * -( exp( -1 * Voltage(j) / (n_idealityfactor * kB_eV_K * T_K) )
                        -1 )*100 + J_sc(i);
1233                if J(1,j) < 1
1234                    J(1,j) = 0;
1235                end
1236
1237            end
1238        end
1239
1240
1241    end
1242
1243 end
1244
1245
1246 %%%%%%%%%%%%%%%%%%%%%%%%%%%%%%%%%%%%%%%%%%%%
1247 %%%%%Incorporate Butler-Volmer Curves %
1248 %%%%%%%%%%%%%%%%%%%%%%%%%%%%%%%%%%%%%%%%%%%%
1249
1250 disp('Calculating B-V')
1251
1252
1253 if majority_doping_type == 'p'
1254    GibbsIncorp_a = Voltage - a_SEP_V/no_photons; %these are corrections necessary to put all our
          plots on the same x-axis
1255    GibbsIncorp_c = Voltage - c_SEP_V/no_photons;
1256 end
1257
1258 %
1259
1260 if majority_doping_type == 'n'
1261    GibbsIncorp_a = Voltage/no_photons + a_SEP_V/no_photons;
1262    GibbsIncorp_c = Voltage/no_photons + c_SEP_V/no_photons;
1263
1264 end
```

```
1265
1266 %calculate BV
1267 %ecd_c is the exchange current density for a catalyst
1268 %ctc_a is the charge transfer coefficient for anodic reaction
1269 %ctc_c is the charge transfer coefficient for cathodic reaction
1270 %eta is the activation overpotential
1271
1272 %j = ecd_c * ( exp(  (ctc_a * no_e * F * eta)/RT) - exp( (ctc_c * no_e * F* eta)/RT);
1273
1274 J_BV_a = zeros( length(Voltage), 1);
1275 J_BV_c = zeros( length(Voltage), 1);
1276 if majority_doping_type == 'n'
1277     for i = 1: length(Voltage)
1278
1279         J_BV_a(i) = (a_ecd_c_mA_cm2 * ( exp( ( a_ctc_a * no_e * F *Voltage(i) )/(R_J_molK*T_K) )
                 - exp( -(a_ctc_c * no_e * F * Voltage(i)/ (R_J_molK*T_K) ) ) ));
1280         J_BV_c(i) = (c_ecd_c_mA_cm2 * ( exp( ( c_ctc_a * no_e * F *Voltage(i) )/(R_J_molK*T_K) )
                 - exp( -(c_ctc_c * no_e * F * Voltage(i)/ (R_J_molK*T_K) ) ) ));
1281
1282         J(1,i) = -J(1,i);
1283     end
1284 end
1285 if majority_doping_type == 'p'
1286     for i = 1: length(Voltage)
1287
1288         J_BV_a(i) = (a_ecd_c_mA_cm2 * ( exp( ( a_ctc_a * no_e * F *Voltage(i) )/(R_J_molK*T_K) )
                 - exp( -(a_ctc_c * no_e * F * Voltage(i)/ (R_J_molK*T_K) ) ) ));
1289         J_BV_c(i) = (c_ecd_c_mA_cm2 * ( exp( ( c_ctc_a * no_e * F *Voltage(i) )/(R_J_molK*T_K) )
                 - exp( -(c_ctc_a * no_e * F * Voltage(i)/ (R_J_molK*T_K) ) ) ));
1290
1291         J(1,i) = J(1,i);
1292     end
1293 end
1294
1295 % plot(Voltage, J_BV)
1296 % hold on;
1297 % plot(GibbsIncorp, J)
1298 % ylim([-45 1])
1299 % xlim([-1 0])
1300
1301
1302
1303 %%%%%%%%%%%%%%%%%%%%%%%%%%%%%%%%%%%%%%%%%%%%
1304 %%%%%%%%%%Calculate Efficiency %%%%%%%
1305 %%%%%%%%%%%%%%%%%%%%%%%%%%%%%%%%%%%%%%%%%%%%
1306
1307
1308
1309 %an important constraint is that overpotentials should only be calculated
1310 %when the efficiency w/o BV effects incorporated is above 0
1311
1312
1313
1314 %%%%%%%%%%%%%%%%%%%%%%%%%%%%%%%%%%%%%%%%%%%%
1315 %%%%%%%%%%Single Light Absorber %%%%%%
1316 %%%%%%%%%%%%%%%%%%%%%%%%%%%%%%%%%%%%%%%%%%%%
1317
1318
1319
1320 if  ( num_photoabsorbers == 1 )
1321     %this is only necessary for the single photoabsorber carrying out two
1322     %different half-reactions because there is no graphical solution
1323
1324     %essentially solve the B-V equation for overpotential at each point
1325     %along the ideal-diode equation (this is computationally expensive)
1326     %then make a new B-V corrected diode plot that we can then perform a
1327     %load-line analysis on
1328
```

```
    if ( majority_doping_type == 'n' ) %photoanode case


                    [a, idx] = min(abs(GibbsIncorp_a));
            [V_M, I_M, Power]=MaxPPT(GibbsIncorp_a(1:idx) , J(1:idx) );

%         [a, idx] = min(abs(GibbsIncorp_a)); %find V=0 for plot w/o BV

      %  if ( abs(( (a_SEP_V - c_SEP_V)/no_e * J(1, round(idx))  / (S) *10 * 100)) >0.1 )

      if abs(V_M*I_M/(S)*1000) > 0.01
            %this saves us time because if w/o BF efficiency is 0, then why
            %calculate an overpotential?

            %Calculate the B-V overpotential at each point along the diode
            %equation

            %we actually want to limit the number of expensive computations
            %we need to do. There are two ways to do this: 1) limit the
            %voltage range of interest 2) stop calculating OP after its
            %change reaches a minima

            %We shall try 2) for the time being. We will look at the OP
            %calculated for the previous value, although recall that that
            %they start as NaN or near 0 for a few values initially, change
            %for a bit and then reach a plateu
            Whereabout = Voc(index_of_interest);
            [aa, V_Start] = min( abs(Voltage+Whereabout) );

            Output_a = zeros(1, length(Voltage));

            for i = V_Start : length (Voltage)
                if ( i < V_Start+400 )
                    Output_a(i) = OP(majority_doping_type,Voltage(i), J(i), a_ecd_c_mA_cm2, no_e,
                          a_ctc_a, a_ctc_c, F, R_J_molK, T_K, J_0(index_of_interest),
                         n_idealityfactor, kB_eV_K, J_sc(index_of_interest) );

                elseif ( i > V_Start+400) && (  abs(Output_a(i-2)-Output_a(i-1))/abs(Output_a(i
                     -2))*100 > 10^-2 ) %this implements the
                    %test to see if the prv two values for OP changed much,
                    %if they do then great calculate new OP

                    Output_a(i) = OP(majority_doping_type, Voltage(i), J(i), a_ecd_c_mA_cm2, no_e
                         , a_ctc_a, a_ctc_c, F, R_J_molK, T_K, J_0(index_of_interest),
                         n_idealityfactor, kB_eV_K, J_sc(index_of_interest) );
                else %if they do not change much, do not calculate and just
                    %use prv. value
                    Output_a(i) = Output_a(i-1);
                end
            end

            Output_c = zeros(1, length(Voltage));
            for i = V_Start : length(Voltage)
                if (i < V_Start+400 )

                    Output_c(i)=OP( majority_doping_type, Voltage(i), -J(i), c_ecd_c_mA_cm2, no_e
                         , c_ctc_c, c_ctc_a, F, R_J_molK, T_K, J_0(index_of_interest),
                         n_idealityfactor, kB_eV_K, J_sc(index_of_interest) );
                    %note the distinct difference here is that the BV transfer
                    %coefficients are reversed
                elseif (i > V_Start+400) && ( abs(Output_c(i-2) - Output_c(i-1))/abs(Output_c(i
                     -2))*100 > 10^(-2) )
                    Output_c(i)=OP( majority_doping_type, Voltage(i), -J(i), c_ecd_c_mA_cm2, no_e
                         , c_ctc_c, c_ctc_a, F, R_J_molK, T_K, J_0(index_of_interest),
                         n_idealityfactor, kB_eV_K, J_sc(index_of_interest) );
                else
                    Output_c(i) = Output_c(i-1);
                end
```

```
1387            end
1388
1389            %sanity check
1390            %plot(GibbsIncorp_a+Output_a+Output_c, -J) %check for photoanode case
1391
1392            display(['Efficiency for band gap (eV): ' num2str(band_gap_eV) ])
1393
1394            %w/ BV
1395            [a, idx] = min(abs(GibbsIncorp_a+Output_a+Output_c ));
1396            if abs(( GibbsIncorp_a(idx)+Output_a(idx)+Output_c(idx) )) < 10^(-2) %what if the
                     curve isn't anywhere near 0 or exactly zero? Then check to see if value is above
                      zero. i.e., required an external bias to work, within some error
1397                OUTPUT_A=abs(( (a_SEP_V )/no_e * J(1, round(idx))  / (S) *10 * 100));
1398                display(['w/ BV Efficiency: ' num2str(OUTPUT_A) ' %'])
1399
1400            else %clearly this is for when the curve is shifted to the right (non power producing
                      region for photoanode)
1401                OUTPUT_A=0;
1402                display(['w/ BV Efficiency: ' num2str(OUTPUT_A) ' %'])
1403            end
1404
1405            %w/o BV
1406            [a, idx] = min(abs(GibbsIncorp_a));
1407
1408            OUTPUT_B=abs(( (a_SEP_V)/no_e * J(1, round(idx))  / (S) *10 * 100));
1409            display(['w/o BV Efficiency: ' num2str(OUTPUT_B) ' %'])
1410
1411
1412        elseif abs(V_M*I_M/(S)*1000) < 0.01
1413            %this is the no-efficiency case, do not calculate B-V
1414            %overpotential
1415            display(['Efficiency for band gap (eV): ' num2str(band_gap_eV) ])
1416            display(['w/o BV Efficiency: 0 %'])
1417            OUTPUT_A = 0;
1418            OUTPUT_B = 0;
1419        end
1420
1421    elseif ( majority_doping_type == 'p' )
1422
1423                    [a, idx] = min(abs(GibbsIncorp_a));
1424            [V_M, I_M, Power]=MaxPPT(GibbsIncorp_a(1:idx) , J(1:idx) );
1425
1426
1427        if abs(V_M*I_M/(S)*1000) > 0.01
1428            %this saves us time because if w/o BF efficiency is 0, then why
1429            %calculate an overpotential?
1430
1431            %Calculate the B-V overpotential at each point along the diode
1432            %equation
1433
1434            %we actually want to limit the number of expensive computations
1435            %we need to do. There are two ways to do this: 1) limit the
1436            %voltage range of interest 2) stop calculating OP after its
1437            %change reaches a minima
1438
1439            %We shall try 2) for the time being. We will look at the OP
1440            %calculated for the previous value, although recall that that
1441            %they start as NaN or near 0 for a few values initially, change
1442            %for a bit and then reach a plateu
1443            Output_a = zeros(1, length(Voltage));
1444                        Whereabout = Voc(index_of_interest);
1445            [aa, V_Start] = min( abs(Voltage-Whereabout) );
1446
1447            for i = V_Start: -1: 1 %we do we start by going in reverse? This is because
1448                %our exit command depends on reaching a plateu, this plateu
1449                %only happens on the trail toward the end (starting from 1
1450                %-> end wastes our computations and our exit condition
1451                %isn't compatible
```

```
1452                if ( i > ( V_Start - 400 ) )
1453                    Output_a(i) = OP(majority_doping_type, Voltage(i), J(i), a_ecd_c_mA_cm2, no_e
                            , a_ctc_a, a_ctc_c, F, R_J_molK, T_K, J_0(index_of_interest),
                            n_idealityfactor, kB_eV_K, J_sc(index_of_interest) );
1454
1455                elseif ( i < ( V_Start - 400 ) ) && (  abs(Output_a(i+2)-Output_a(i+1))/abs(
                         Output_a(i+2))*100 > 10^-2 ) %this implements the
1456                    %test to see if the prv two values for OP changed much,
1457                    %if they do then great calculate new OP
1458
1459                    Output_a(i) = OP(majority_doping_type, Voltage(i), J(i), a_ecd_c_mA_cm2, no_e
                            , a_ctc_a, a_ctc_c, F, R_J_molK, T_K, J_0(index_of_interest),
                            n_idealityfactor, kB_eV_K, J_sc(index_of_interest) );
1460                else %if they do not change much, do not calculate and just
1461                    %use prv. value
1462                    Output_a(i) = Output_a(i+1);
1463                end
1464            end
1465
1466            Output_c = zeros(1, length(Voltage));
1467            for i = V_Start : -1: 1
1468                if (i > ( V_Start - 400 ) )
1469                    Output_c(i)=OP( majority_doping_type, Voltage(i), J(i), c_ecd_c_mA_cm2, no_e,
                             c_ctc_c, c_ctc_a, F, R_J_molK, T_K, J_0(index_of_interest),
                            n_idealityfactor, kB_eV_K, J_sc(index_of_interest) );
1470                    %note the distinct difference here is that the BV transfer
1471                    %coefficients are reversed
1472                elseif (i < ( V_Start - 400) ) && ( abs(Output_c(i+2) - Output_c(i+1))/abs(
                         Output_c(i+2))*100 > 10^(-2) )
1473                    Output_c(i)=OP( majority_doping_type, Voltage(i), J(i), c_ecd_c_mA_cm2, no_e,
                             c_ctc_c, c_ctc_a, F, R_J_molK, T_K, J_0(index_of_interest),
                            n_idealityfactor, kB_eV_K, J_sc(index_of_interest) );
1474                else
1475                    Output_c(i) = Output_c(i+1);
1476                end
1477            end
1478
1479            %sanity check
1480  %           plot(GibbsIncorp_a, -J)
1481  %           hold on;
1482  %           plot(GibbsIncorp_a-Output_a-Output_c, -J, 'r') %check for photoanode case
1483  %           hold off;
1484            Output_c = fliplr(Output_c);
1485            Output_a = fliplr(Output_a);
1486            display(['Efficiency for band gap (eV): ' num2str(band_gap_eV) ])
1487
1488            %w/ BV
1489            %GibbsIncorp_a-Output_a
1490            [a, idx] = min(abs(GibbsIncorp_c-Output_a-Output_c ));
1491            if abs(( GibbsIncorp_c(idx)-Output_a(idx)-Output_c(idx) )) < 10^(-2) %what if the
                     curve isn't anywhere near 0 or exactly zero? Then check to see if value is above
                      zero. i.e., required an external bias to work, within some error
1492                OUTPUT_A=abs(( (a_SEP_V - c_SEP_V)/no_e * J(1, round(idx))  / (S) *10 * 100));
1493                display(['w/ BV Efficiency: ' num2str(OUTPUT_A) ' %'])
1494
1495            else %clearly this is for when the curve is shifted to the right (non power producing
                      region for photoanode)
1496                OUTPUT_A=0;
1497                display(['w/ BV Efficiency: ' num2str(OUTPUT_A) ' %'])
1498            end
1499
1500            %w/o BV
1501            [a, idx] = min(abs(GibbsIncorp_c));
1502
1503            OUTPUT_B=abs(( (a_SEP_V - c_SEP_V)/no_e * J(1, round(idx))  / (S) *10 * 100));
1504            display(['w/o BV Efficiency: ' num2str(OUTPUT_B) ' %'])
1505
1506
```

```
1507        elseif abs(V_M*I_M/(S)*1000) < 0.01
1508            %this is the no-efficiency case, do not calculate B-V
1509            %overpotential
1510            display(['Efficiency for band gap (eV): ' num2str(band_gap_eV) ])
1511            display(['w/o BV Efficiency: 0 %'])
1512            OUTPUT_A = 0;
1513            OUTPUT_B = 0;
1514        end
1515
1516
1517    end
1518
1519
1520
1521 end
1522
1523
1524
1525 %%%%%%%%%%%%%%%%%%%%%%%%%%%%%%%%%%%%%%%%%%%%
1526 %%%%%%%%%% Dual Light Absorber %%%%%%%%%
1527 %%%%%%%%%%%%%%%%%%%%%%%%%%%%%%%%%%%%%%%%%%%%
1528
1529
1530 if (num_photoabsorbers == 2)
1531
1532     %we have the stacked and side-by-side cases to deal with
1533
1534     if (sidebyside == 1) || (sidebyside == 0)
1535         %yes, it is side by side
1536
1537         %remember, in a side-by-side case we save each J-V curve so that it
1538         %may be loaded for analysis later.
1539
1540         if (majority_doping_type == 'n')
1541             %is it the photoanode?
1542             %compute J-V + OP curve
1543
1544             %before computing OP, we must ask if that is even necessary?
1545             %i.e., is the w/o BV > 0 % efficiency
1546             %   [a, idx] = min(abs(GibbsIncorp_a)); %find V=0 for plot w/o BV
1547
1548
1549             %[V_M, I_M, Power]=MaxPPT(GibbsIncorp_a, J);
1550             [a, idx] = min(abs(GibbsIncorp_a));
1551             [V_M, I_M, Power]=MaxPPT(GibbsIncorp_a(1:idx) , J(1:idx) );
1552
1553
1554             % if ( abs(( (a_SEP_V - c_SEP_V)/no_e * J(1, round(idx))  / (S*no_photons) *10 * 100)
                      ) > 0.1 )
1555
1556            % if abs(V_M*I_M/(S)*1000) > 0.01 %verify we are producing some power
1557
1558
1559                 %this is necessary before OP calc if non-negligble
1560                 %efficiency for w/o BV curve
1561
1562                 %now we have to ask about whether or not we have already
1563                 %reached a plateu in OP
1564                 Output_a = zeros(1, length(Voltage));
1565                             Whereabout = Voc(index_of_interest);
1566             [aa, V_Start] = min( abs(Voltage+Whereabout) );
1567
1568                 for i = V_Start : length(Voltage)
1569
1570                     if (i < 400+V_Start ) %of course, just compute OP
1571
1572                         Output_a(i) = OP(majority_doping_type,Voltage(i), -J(i), a_ecd_c_mA_cm2,
                                 no_e, a_ctc_a, a_ctc_c, F, R_J_molK, T_K, J_0(index_of_interest),
```

```
                            n_idealityfactor, kB_eV_K, J_sc(index_of_interest) );
1573
1574                    elseif (i > 400+V_Start ) && (  abs(Output_a(i-2)-Output_a(i-1))/abs(Output_a
                             (i-2))*100 > 10^-2 ) %this implements the
1575                        %test to see if the prv two values for OP changed much,
1576                        %if they do then great calculate new OP
1577                        Output_a(i) = OP(majority_doping_type, Voltage(i), -J(i), a_ecd_c_mA_cm2,
                                 no_e, a_ctc_a, a_ctc_c, F, R_J_molK, T_K, J_0(index_of_interest),
                                n_idealityfactor, kB_eV_K, J_sc(index_of_interest) );
1578
1579                    else %if they do not change much, do not calculate and just
1580                        %use prv. value
1581                        Output_a(i) = Output_a(i-1);
1582
1583                    end
1584
1585                end
1586
1587
1588                display(['Photoanode Efficiency for band gap (eV): ' num2str(band_gap_eV) ])
1589                %w/ BV
1590                % [a, idx] = min(abs(GibbsIncorp_a+Output_a));
1591
1592                %[V_M, I_M, Power] = MaxPPT(GibbsIncorp_a+Output_a, J);
1593                [a, idx] = min(abs(GibbsIncorp_a+Output_a));
1594                [V_M, I_M, Power] = MaxPPT(GibbsIncorp_a(1:idx) + Output_a(1:idx), J(1:idx));
1595
1596                if abs(( GibbsIncorp_a(idx)+Output_a(idx) )) < 10^(-2) %what if the curve isn't
                         anywhere near 0 or exactly zero? Then check to see if value is above zero. i
                         .e., required an external bias to work, within some error
1597                    OUTPUT_A=abs(( V_M(end) * I_M(end)/ (S)*1000));
1598                    display(['w/ BV Efficiency: ' num2str(OUTPUT_A) ' %'])
1599
1600                else %clearly this is for when the curve is shifted to the right (non power
                         producing region for photoanode)
1601                    OUTPUT_A=0;
1602                    display(['w/ BV Efficiency: ' num2str(OUTPUT_A) ' %'])
1603                end
1604
1605                %w/o BV
1606                % [V_M, I_M, Power] = MaxPPT(GibbsIncorp_a);
1607                [a, idx] = min(abs(GibbsIncorp_a));
1608                [V_M, I_M, Power] = MaxPPT(GibbsIncorp_a(1:idx), J(1:idx) );
1609
1610                OUTPUT_B=abs(( (V_M(end) * I_M(end) / (S)*1000)));
1611                display(['w/o BV Efficiency: ' num2str(OUTPUT_B) ' %'])
1612
1613
1614 %              elseif (( V_M(end) * I_M(end)/ (S)*1000) < 0.01 )
1615 %
1616 %                  %this is the no-efficiency case
1617 %                  display(['Photoanode Efficiency for band gap (eV): ' num2str(band_gap_eV) ])
1618 %                  display(['w/o BV Efficiency: 0 %'])
1619 %                  OUTPUT_A = 0;
1620 %                  OUTPUT_B = 0;
1621 %                  Output_a = zeros(1, length(Voltage));
1622 %              end
1623
1624
1625
1626         elseif (majority_doping_type == 'p')
1627             %is it the photocathode?
1628             %before computing OP, we must ask if that is even necessary?
1629             %i.e., is the w/o BV > 0 % efficiency
1630             [a, idx] = min(abs(GibbsIncorp_c)); %find V=0 for plot w/o BV
1631             [V_M, I_M, Power]=MaxPPT(GibbsIncorp_c(idx:end), J(idx:end) );
1632
1633 %
```

```
%             if ( abs(( V_M(1) * I_M(1)  / (S)*1000 )) > 0.01 )
                %this is necessary before OP calc if non-negligble
                %efficiency for w/o BV curve

                %now we have to ask about whether or not we have already
                %reached a plateu in OP
                Output_c = zeros(1, length(Voltage));
            Whereabout = Voc(index_of_interest);
            [aa, V_Start] = min( abs(Voltage-Whereabout) );

                for i = V_Start : -1 : 1

                    if (i > ( V_Start - 400) ) %of course, just compute OP

                        Output_c(i)=OP( majority_doping_type, Voltage(i), J(i), c_ecd_c_mA_cm2,
                             no_e, c_ctc_a, c_ctc_c, F, R_J_molK, T_K, J_0(index_of_interest),
                             n_idealityfactor, kB_eV_K, J_sc(index_of_interest) );

                    elseif (i < ( V_Start - 400 ))  && (  abs(Output_c(i+2)-Output_c(i+1))/abs(
                         Output_c(i+2))*100 > 10^-2 ) %this implements the
                        %test to see if the prv two values for OP changed much,
                        %if they do then great calculate new OP
                        Output_c(i)=OP( majority_doping_type, Voltage(i), J(i), c_ecd_c_mA_cm2,
                             no_e, c_ctc_a, c_ctc_c, F, R_J_molK, T_K, J_0(index_of_interest),
                             n_idealityfactor, kB_eV_K, J_sc(index_of_interest) );

                    else %if they do not change much, do not calculate and just
                        %use prv. values
                        Output_c(i) = Output_c(i+1);

                    end

                end

                Output_c = fliplr(Output_c);

                display(['Photocathode Efficiency for band gap (eV): ' num2str(band_gap_eV) ])
                %w/ BV
                [a, idx] = min(abs(GibbsIncorp_c-Output_c));
                [V_M, I_M, Power]=MaxPPT(GibbsIncorp_c(idx:end)-Output_c(idx:end), J(idx:end) );


                if abs(( GibbsIncorp_c(idx)-Output_c(idx) )) < 10^(-2) %what if the curve isn't
                     anywhere near 0 or exactly zero? Then check to see if value is above zero. i
                     .e., required an external bias to work, within some error
                    OUTPUT_A=abs((V_M(1) * I_M(1)  / (S)*1000 ));
                    display(['w/ BV Efficiency: ' num2str(OUTPUT_A) ' %'])

                else %clearly this is for when the curve is shifted to the right (non power
                     producing region for photoanode)
                    OUTPUT_A=0;
                    display(['w/ BV Efficiency: ' num2str(OUTPUT_A) ' %'])
                end

                %w/o BV
                [a, idx] = min(abs(GibbsIncorp_c));

                [V_M, I_M, Power]=MaxPPT(GibbsIncorp_c(idx:end), J(idx:end) );


                OUTPUT_B=abs(( V_M(1) * I_M(1) / (S)*1000 ));
                display(['w/o BV Efficiency: ' num2str(OUTPUT_B) ' %'])



%
%
%             elseif ( abs(( V_M(1) * I_M(1) / (S)*1000)) < 0.01 )
```

```
%
%                 %this is the no-efficiency case
%                 display(['Photocathode Efficiency for band gap (eV): ' num2str(band_gap_eV) ])
%                 display(['w/o BV Efficiency: 0 %'])
%                 OUTPUT_A = 0;
%                 OUTPUT_B = 0;
%                 Output_c = zeros(1, length(Voltage));
%             end
%
        end

        %output
        %output parms

        if (majority_doping_type == 'n')
            varargout{1}= GibbsIncorp_a;
            varargout{2} = Output_a;
            varargout{3} = J;
            varargout{4} = a_SEP_V;
            varargout{5} = c_SEP_V;
            varargout{6} = S;

        elseif (majority_doping_type == 'p')
            varargout{1} = GibbsIncorp_c;
            varargout{2} = Output_c;
            varargout{3} = J;
        end

        %compute J-V curve + OP curve
        %save to file
    end
end
end


%%%%%%%%%%%%%%%%%%%%%%%%%%%%%%%%%%%%%%%%%%%%
%%%%%%%%%%%Overpotential %%%%%%%%%%%%%%%%%%
%%%%%%%%%%%%%%%%%%%%%%%%%%%%%%%%%%%%%%%%%%%%


function Overpotential=OP(majority_doping_type, V, J, ecd_c, no_e, ctc_a, ctc_c, F, R, T, J_0,
     n_idealityfactor, kB_eV_K, J_sc)


%now the current densities must be matched up to allow incorporation of
%Butler-Volmer eqn.

%this will go through each point from the diode eqn and find the
%relevant current density from the BV.

%will generate new voltage that takes into overpotential from BV then plot
%diode currents on top of that range.

% we have some J(i,j) and we need to solve the Butler-Volmer eqn
% for that current and obtain the overpotential


%B-V is of the form A = B*( exp(C * x) - exp(-D * x) )
%there is no closed form solution for x given A,B,C,D

%can numerically calculate answer using Newton-Raphson Method
%where x_{n+1} = x_n - f(x_n)/f'(x_n)
%f(x) = B * ( exp(C*x) - exp(-D*x ) )
```

```
%f'(x) = B * ( C * exp(C*x) + D * exp(-D * x) )
% FYI:
% f(x) in terms of our equation is
% f(x) = ecd_c * ( exp( ( ctc_a * no_e * F *Voltage(j) )/(R*T) ) - exp( -(ctc_c * no_e * F * Voltage(j)/ (R*T) ) ) );
% f_x(x) = ecd_c * ( exp( ( ctc_a * no_e * F *Voltage(j) )/(R*T) ) - exp( -(ctc_c * no_e * F * Voltage(j)/ (R*T) ) ) );


B = ecd_c;
C = ctc_a * no_e * F/(R*T);
D = ctc_c * no_e * F/(R*T);


%what is x_0?
%answer: a first estimate.

%assume both C and D are equal:
%then the answer is given by
%x_0 = ( (R * T) / ( ctc_a * no_e * F ) ) * sinh( J(i,j)/ (2 * ecd_c) )^(-1);

%f(i,j) = B * ( exp(C*x_0) - exp(-D*x_0 ) ) - J(i,j); % why - J(i,j)? Remember N-R Method only works for finding r when f(r) = 0
%f_x(i,j) = B * ( C * exp(C*x_0) + D * exp(-D * x_0) );

%the probem with the method just mentioned is that sinh explodes
%very quickly, therefore very high numerical precision is required
%and therefore a better method must be sought.

%alternatively we can assume that | overpotential | > 118 mV/no_e
% in which case overpotential = - RT/
% (alpha_c * no_e * F) * ln ( - j/ j_0,cat )

x_0 = real( -(R*T / (ctc_a * no_e * F)) * log( - J/ecd_c )); %initial guess
%     clear x
%     f_=@(x)B*( exp(C*(x) ) - exp(-D*(x)) ) - J(1,j);
%
%     if isinf(x_0)
%         x_0=0;
%     end
%     options=optimset('TolX', 1*10^(-1));
%
%     Overpotential(1,j) = fzero( f_, x_0, options);
%
%     waitbar(j/ length(Voltage) )
%
%

if ~isinf(x_0) %x_0 will equal zero when J=0 because log(J) is in approximation
    if majority_doping_type == 'n'
        G_=@(x)J_0* -(exp(-V/(n_idealityfactor * kB_eV_K * T) ) -1)*100+ J_sc - B*(exp(C*x) - exp(-D*x)) ;
    elseif majority_doping_type == 'p'
        G_=@(x)J_0* (exp(V/(n_idealityfactor * kB_eV_K * T) ) -1)*100- J_sc + B*(exp(C*x) - exp(-D*x)) ;
    end
    options=optimset('MaxFunEvals', 10^6,'Diagnostics','off','Display','off');
    [Overpotential, fval, exitflag]=fsolve(G_, x_0, options);
elseif isinf(x_0)
    Overpotential = 0;
end

end



%%%%%%%%%%%%%%%%%%%%%%%%%%%%%%%%%%%%%%%%%%%%
%%%%%%%%%% Max Power Point %%%%%%%%%%%%%%
```

```
%%%%%%%%%%%%%%%%%%%%%%%%%%%%%%%%%%%%%%%%


function [MaxPPT_V, MaxPPT_J, Power]=MaxPPT(V, J)


Power = zeros(1, length(V));
for i = 1 : length(V)

    Power(i) = abs( V(i) * J(i));

end

[MaxPPT_J, idx] = max(Power);

MaxPPT_V = V(idx);


end
```

Appendix B

Supplementary Information for Highly Active Electrocatalysis of the Hydrogen-Evolution by Cobalt Phosphide Nanoparticles

Reproduced with permission from E.J. Popczun; C.G. Read*; C.W. Roske*; N.S. Lewis; R.E. Schaak. *Angew. Chem.*, **2014**, *126*, 5531-5534. Copyright 2014 Wiley.

B.1 Materials and Methods

Chemicals and Materials

Octacarbonyl dicobalt [stabilized with 1-5 % hexane, $Co_2(CO)_8$], oleic acid [tech. 90 %, $C_{18}H_{34}O_2$], and nonanoic acid [97 %, $C_9H_{18}O_2$] (Alfa-Aesar), as well as 1-octadecene [tech. 90 %, $C_{18}H_{36}$], oleylamine [tech. 70 %, $C_{18}H_{37}N$], trioctylphosphine [97 %, $(C_8H_{17})_3P$], titanium foil [99.7 %, 0.25 mm thickness], and sulfuric acid [99.999 %] (Sigma-Aldrich) were used as received. Ag paint was purchased from SPI supplies, and two-part epoxy [HYSOL 9460] was purchased from McMaster-Carr.

Synthesis of ϵ-Co nanoparticles

Using an adaptation of a previously reported protocol,[1] 1-octadecene (10 mL, 31.3 mmol), oleylamine (6 mL, 18.2 mmol), and nonanoic acid (2 mL, 11.3 mmol) were added to a 100 mL three-necked round bottom flask containing a polytetrafluoroethylene-coated magnetic stir bar. The flask was then placed in a heating mantle. A thermometer adapter, thermometer, Liebig condenser, and rubber septum were also connected to the flask. The reaction mixture was vigorously stirred and heated to 120 °C for 1 h under vacuum, to remove residual low-boiling solvents, including water. Following degassing, the mixture was heated to 230 °C under Ar. Meanwhile, in an Ar-filled septum-capped vial, octacarbonyl dicobalt (100 mg, 0.29 mmol) was suspended in 1-octadecene (4.5 mL, 14.1 mmol). Following solvation via sonication, the cobalt solution was slowly injected into the reaction flask. After injection of the Co solution, the reaction was held at ≈230 °C for 10 min, followed by rapid injection of degassed oleic acid (2 mL, 6.3 mmol). The reaction was maintained at ≈230 °C for 10 additional min until the contents were allowed to cool by removal of the heating mantle. The resulting cobalt nanoparticle sample was cleaned by adding isopropyl alcohol to the reaction mixture, followed by

centrifugation at 9000 rpm for 5 min. Following centrifugation, the precipitate was resuspended in hexanes, followed by addition of isopropyl alcohol and subsequent centrifugation. The resulting pellet was suspended in hexanes, for characterization purposes, or was suspended trioctylphosphine, for conversion to CoP.

Synthesis of CoP hollow nanoparticles

1-octadecene (5 mL, 15.7 mmol), oleylamine (5 mL, 15.2 mmol), and trioctylphosphine (5 mL, 11.2 mmol) were added to a 100 mL three-necked round-bottom flask that contained a borosilicate stir bar. The flask was also equipped with a thermometer adapter, thermometer, Liebig condenser, and rubber septum and placed in a heating mantle. The reaction mixture was degassed at 120 °C for 1 h under vacuum to remove water and other low boiling impurities from the system. The reaction mixture was then heated to ≈320 °C, and allowed to equilibrate for 10 min. Following temperature equilibration, a pre-made suspension of cobalt nanoparticles in degassed trioctylphosphine (2 mL, 4.5 mmol) was slowly injected into the reaction mixture. The resulting mixture was held at 320 °C for 1 h. The reaction mixture was allowed to cool to room temperature by removal of the heating mantle. The resulting CoP nanoparticles were cleaned by addition of the isopropyl alcohol to the reaction mixture. Precipitation of the CoP nanoparticles was performed via centrifugation at 9000 rpm for 5 min. The precipitate was resuspended using hexanes, followed by ethanol to promote flocculation and then centrifugation. This process was then repeated, and for later use the resulting CoP nanoparticles were suspended in hexanes.

Preparation of Working Electrodes

To make working electrodes, a stock solution of CoP nanoparticles at 5 mg mL^{-1} in hexanes was prepared. In 5-10 µL increments, 36 µL of the nanoparticle stock solution was deposited onto 0.2 cm^2 samples of Ti foil to achieve 0.9 mg/cm^2 mass loading, or 80 µL was deposited to achieve the 2 mg/cm^2 mass loading. Following deposition of CoP and drying, the CoP-coated Ti foils were annealed at 450 °C under 5 % H_2/Ar (Air Liquide). The foils were affixed with Ag paint to a polyvinylchloride-coated copper wire that had been threaded through a 6 mm diameter glass capillary. Two-part epoxy was used to cover all surfaces except the CoP-coated side of the Ti electrode.

Electrochemical Measurements

All electrochemical measurements were obtained using a Gamry Instruments Reference 600 potentiostat. All measurements were performed in high-purity 0.50 M sulfuric acid, unless otherwise noted. Data were collected using a three-electrode single-compartment cell that contained a mercury/mercury sulfate (Hg/Hg_2SO_4) reference electrode and a graphite rod counter electrode.

Polarization data were collected at a sweep rate of 5 mV s^{-1}, and rapid stirring from a magnetic stir bar was used to agitate the solution. The current-interrupt method was used to account for any uncompensated resistance (R = 2 ohms, leading to an iR correction of about 8 mV at 20 mg/cm^2). Constant bubbling of research-grade H_2 at $\approx$ 1 atm was used to maintain a constant potential for the RHE, with the RHE potential determined by measuring the open-circuit potential of a platinum electrode that was tested following investigation of the behavior of the CoP nanoparticle-coated electrode. Short-term electrochemical stability was measured without correcting for uncompensated resistance by galvanostatically maintaining for 24 h a current density of -20 mg/cm^2. Long-term electrochemical stability measurements were performed by cyclic voltammetric cycling from +0.005 V to -0.140 V without accounting for any uncompensated resistance.

Quantitative Hydrogen Yield Measurements

Quantitative measurements of the faradaic H_2 yield were performed in 0.50 M sulfuric acid using a two-electrode cell which had two compartments that were separated by a Nafion membrane (Fuelcellstore.com). The working electrode and counter electrode were identical to those used in the three-electrode measurements described above. An inverted solution-containing graduated cylinder was positioned around the working electrode, and collected the volume of H_2 that was produced by a constant cathodic current density of 20 mA/cm^2 on an electrode having a projected area of 0.2 cm^2. This current density was maintained for 6.94 h, after which the volume of H_2 was recorded and compared to the ideal gas volume expected from the total faradaic charge passed in conjunction with the ideal gas law.

Materials Characterization

Powder X-ray diffraction (XRD) patterns were acquired using a Bruker-AXS D8 Advance diffractometer with Cu Kα radiation and a LynxEye 1-D detector operating at room temperature. The CrystalMaker/Crystal Diffract software package was used to simulate the XRD patterns, using published crystallographic parameters for

MnP-type CoP.[2] Transmission electron microscopy (TEM) images were collected using a Phillips 420 microscope operating at an accelerating voltage of 120 kV. A JEOL EM-2010F was used to collect high-resolution bright-field TEM images as well as to obtain energy dispersive X-ray spectroscopy (EDX) measurements at an accelerating voltage of 200 kV. Gatan Digital Micrograph(TM) software was used to measure the lattice spacings from the fast-Fourier transform (FFT) of the HRTEM images. These values, and the corresponding FFT diffraction pattern, were compared to single-crystal diffraction patterns simulated using the CrystalMaker/Single Crystal software. Brunauer-Emmett-Teller (BET) surface area measurements were performed using a Micromeretics ASAP 2020 at liquid nitrogen temperatures, and the data were analyzed using the ASAP 2020 software version 4.0. X-ray photoelectron spectroscopy was performed using a Kratos Ultra XPS with a delay-line detector and a resolution of 0.27 eV as determined by the full-width at half-maximum of the Ag 3d peak on a calibration sample.

Estimation of turnover frequencies

To calculate the turnover frequency (TOF), the density of the sample was first calculated using the CoP unit cell, via the CrystalMaker software suite. Theoretical surface areas were estimated using 13 nm spherical, solid CoP nanoparticles. The measured BET surface areas were used as the "actual" surface area values in the calculations. As was done for Ni_2P and Ni–Mo,[3,4] the turnover frequencies are reported as turnovers per second per surface atom. Co and P surface atoms were counted separately, as opposed to per hydrogen binding site. An example of the procedure used to perform these calculations is provided below:

The molar mass (89.907 g mol^{-1}), density (6.416 g/cm^3), molar volume (14.01 mL mol^{-1}), volume of a 13 nm sphere (1.15×10^{-18} cm^3), surface area of a 13 nm sphere (5.31×10^{-12} cm^2), and current density at $\eta = -100$ mV (for 0.032 mg/cm^2 $\eta = -5.04 \times 10^{-4}$ A/cm^2, for 0.9 mg/cm^2 $\eta = -2.53 \times 10^{-2}$ A/cm^2, and for 2.02 mg/cm^2 $\eta = -4.30 \times 10^{-2}$ A/cm^2. The surface area per gram of a 13 nm sphere (BET value = 595 cm^2/g) is calculated as:

$$\frac{5.31 \times 10^{-12}\,\text{cm}^2}{1\ \text{particle}} \times \frac{1\ \text{particle}}{1.15 \times 10^{-18}\,\text{cm}^3} \times \frac{1\,\text{cm}^3}{6.416\,\text{g}} = 719\,\text{cm}^2/\text{mg}.$$

The average surface atoms per 1 square centimeter (used for BET-based calculations

also) is found by:

$$\left(\frac{2 \times 6.022 \times 10^{23}\ \text{atoms}}{1\ \text{mol}} \times \frac{1\ \text{mol}}{14.0\ \text{cm}^3}\right)^{2/3} = 2.45 \times 10^{15} \frac{\text{atoms}}{\text{cm}^2}.$$

Using the surface atoms per tested area at $0.9\ \text{mg/cm}^2$ (BET value = 1.31×10^{18} atoms/foil):

$$\frac{0.9\ \text{mg}}{1\ \text{cm}^2} \times \frac{7.19 \times 10^2\ \text{cm}^2}{\text{mg}} \times \frac{2.45 \times 10^{15}\ \text{atoms}}{1\ \text{cm}^2} = 1.65 \times 10^{18} \frac{\text{atoms}}{\text{test}}.$$

Values calculated for the $0.032\ \text{mg/cm}^2$ loading for theory is 5.65×10^{16} atoms/foil and a BET value of 4.67×10^{16} atoms/foil. At $2.02\ \text{mg/cm}^2$ loading the values for theory give 3.57×10^{18} atoms/foil with a BET value of 2.95×10^{18} atoms/foil.

Finally, the turnover frequency at 100 mV overpotential is calculated (per surface atom) as:

$$\frac{1\text{turnover}}{2\text{e}^-} \times \frac{2.53 \times 10^{-2}\ \text{A}}{1\ \text{cm}^2} \times \frac{1\ \text{mol}}{96\,485\ \text{C}} \times \frac{6.022 \times 10^{23}\text{e}^-}{1\ \text{mol}} \times \frac{1\ \text{text}}{1.65 \times 10^{18}\ \text{atoms}} = 0.048\text{s}^{-1}\text{atom}^{-1}.$$

For $0.032\ \text{mg/cm}^2$, the theoretical value gives $0.028\ \text{s}^{-1}\ \text{atom}^{-1}$ with a BET value of $0.034\ \text{s}^{-1}\ \text{atom}^{-1}$. For $0.9\ \text{mg/cm}^2$, the theoretical value gives $0.048\ \text{s}^{-1}\ \text{atom}^{-1}$ with a BET value of $0.060\ \text{s}^{-1}\ \text{atom}^{-1}$. For $2.02\ \text{mg/cm}^2$, the theoretical value gives $0.038\ \text{s}^{-1}\ \text{atom}^{-1}$ with a BET value of $0.045\ \text{s}^{-1}\ \text{atom}^{-1}$.

B.2 Supporting Data

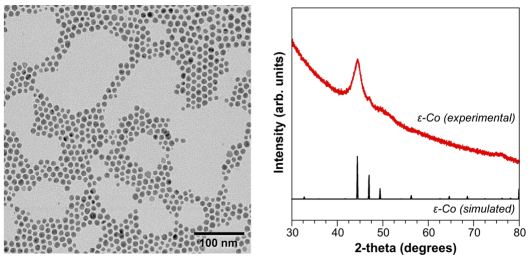

Figure B.1: TEM and powder XRD data for ϵ-Co nanoparticles.

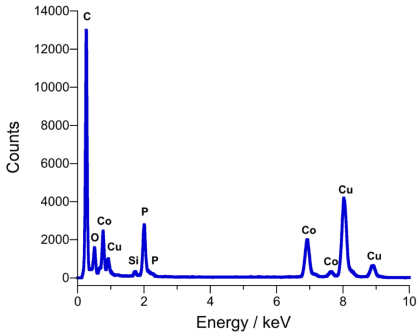

Figure B.2: EDS data for CoP nanoparticles. The Cu is from the TEM grid and the Si is present in the background samples, originating from the column.

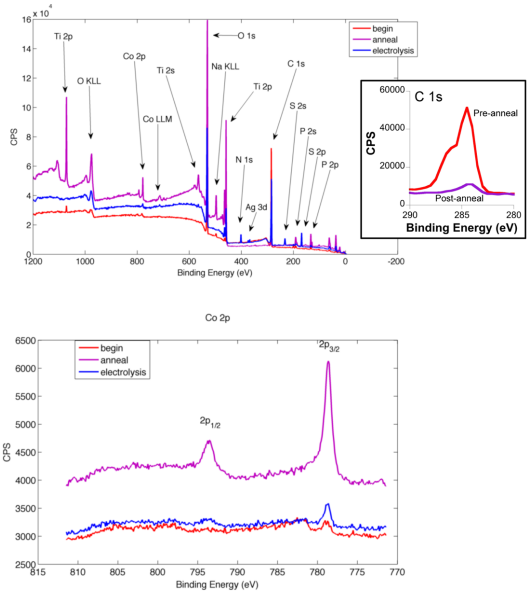

Figure B.3: XPS data for a CoP/Ti electrode: (top) survey scans showing spectra obtained pre-anneal, post-anneal, and after electrolysis (inset: enlarged C 1s region pre-anneal and post-anneal) and (bottom) high-resolution scan of the Co 2p region, also showing spectra obtained pre-anneal, post-anneal, and after electrolysis.

B.3 References

(1) S. Deka, A. Falqui, G. Bertoni, C. Sangregorio, G. Poneti, G. Morello, M. De Giorgi, C. Giannini, R. Cingolani, L. Manna and P. D. Cozzoli, *J. Am. Chem. Soc.*, 2009, **131**, 12817–28.

(2) S. Rundqvist, L. G. Sillén, D. Timm, K. Motzfeldt, O. Theander and H. Flood, *Acta Chem. Scand.*, 1962, **16**, 287–292.

(3) J. R. McKone, B. F. Sadtler, C. A. Werlang, N. S. Lewis and H. B. Gray, *ACS Catal.*, 2013, **3**, 166–169.

(4) E. J. Popczun, J. R. McKone, C. G. Read, A. J. Biacchi, A. M. Wiltrout, N. S. Lewis and R. E. Schaak, *J. Am. Chem. Soc.*, 2013, **135**, 9267–70.

Appendix C

Supplementary Information for Comparison of the Performance of CoP-Coated and Pt-Coated Radial Junction n^+p-Silicon Microwire-Array Photocathodes for the Sunlight-Driven Reduction of Water to $H_2(g)$

Reprinted with permission from C.W. Roske; E.J. Popczun; B. Seger; C.G. Read; T. Pedersen; O. Hansen; P.C.K. Vesborg; B.S. Brunschwig; R.E. Schaak; I. Chorkendorff; H.B. Gray; N.S. Lewis. *J. Phys. Chem. Lett.*, **2015**, *6* (9), pp 1679 – 1683.
Copyright 2015 American Chemical Society.

C.1 Methods

Electrode Preparation

Reactive ion etching of Si(100) substrate (B-doped, resistivity of 14.6 ohm-cm) was used to form 4 μm diameter Si microwires (MWs) at an 11 μm pitch, with the wires being 50 μm in length. Radial n^+ junctions on the p-Si microwires were formed by vapor-phase P diffusion from phosphoryl chloride ($POCl_3$) at 900 °C. Ohmic contacts to the back of the Si(100) substrates were made by electron-beam evaporation of 150 nm of Al, followed by a 5 min anneal at 800 °C under forming gas (5 % $H_2(g)$ in $N_2(g)$). The Si MW arrays were etched for 10 s in 0.5 M HF(aq) (Transene, Inc.) and were dried under a stream of Ar(g). Centrifugation was then promptly performed in 25 mL falcon tubes in a swinging-head centrifuge, with the tubes filled with ≈ 15 mL of polydimethylsiloxane (PDMS, Dupont). The PDMS was cured overnight while centrifuging at 3000 rpm. Si MW arrays were then loaded into the bottom of the falcon tubes and centrifugation of the particles was performed at 3000 rpm with a suspension of the CoP nanoparticles (0.2 mg mL^{-1}) in hexane for 5 min (the suspension was sonicated immediately prior to application of 15 μL for a 0.1 cm^2 sample). A Cahn microbalance was used to determine the geometric mass loading (mg/cm^2) by weighing samples before and after deposition of particles. After deposition of the particles, the catalyst was activated by annealing at 450 °C for 30 min under forming gas. Ga-In eutectic was scratched onto the back side of the wire arrays, and Ag paint (SPI) was then applied to the back side of the arrays. A Cu wire was affixed to the array using Ag paint. The Cu wire was then threaded through a glass tube. Hysol 9460 epoxy was used to adhere the glass tube

to the back side of the electrode and to seal the back and sides of the electrode. The epoxy was cured overnight. Synthesis of Pt nanoparticles: A solution of 0.10 mM H_2PtCl_6 (Sigma, ACS Reagent), 0.10 mM sodium polyacrylate (M_w 2100, Aldrich), and 0.50 mM ascorbic acid (Sigma, ACS Reagent) was prepared in 250 mL of degassed, deionized H_2O with a resistivity of $\approx$ 18.2 MΩ – cm obtained from a Barnsted Nanopure column. The solution was stirred for 1 h under N_2(g), prior to cooling overnight with the subsequent addition of 2.0 g of NaOH. The suspension was left overnight, centrifuged, and then washed with deionized H_2O three times before suspending the particles in isopropanol. Synthesis of CoP nanoparticles: synthesized and characterized as previously reported.[1]

Electrochemical Measurements

Photoelectrochemical measurements were performed in 0.50 M H_2SO_4(aq). Experiments were performed in a Pyrex electrochemical cell in a conventional three-electrode configuration, with a Ag/AgCl reference electrode (BASi) in saturated KCl(aq) and a high-purity carbon cloth counter electrode (FuelCellStore). During a typical acquisition with a Gamry Reference 600 potentiostat, H_2(g) was constantly purged into the solution (except for the H_2 determination case), to maintain a constant, reversible (H^+/H_2) Nernstian potential in the solution. The solution was rapidly stirred with a magnetic stir bar, to minimize mass-transport limitations and to minimize any effects due to bubble formation. Potentially detrimental oxidative processes were minimized by limiting the scans to potentials that were negative of the open-circuit potential. The cell was illuminated with an ELH-type W-halogen lamp equipped with a dichroic rear reflector. The light intensity was calibrated using a Si photodiode (Thorlabs UDT UV-005) that had been mounted in the same orientation as the Si working electrodes. The Si photodiode was calibrated, in turn, against a NIST-traceable secondary standard Si cell that had been calibrated and produced a specified short-circuit current density under 100 mW/cm^2 of illumination by Air Mass 1.5 G sunlight. Prior to data collection, trace metal impurities were removed by soaking the cell overnight in aqua regia, then thoroughly rinsing the cell with 18 MΩ – cm resistivity H_2O. After each set of experiments, a Pt electrode was used to determine the reversible hydrogen potential, and thereby to calibrate the reference electrode. We have not extended the measurement time nor have we compared the stability of the Si/Pt system to that of the Si/CoP system for extended time periods.

Spectral Response

Photoelectrochemical spectral response measurements were performed using illumination from a 150 W Xe lamp that was passed through an Oriel monochromator (0.50 mm slits), then chopped at 30 Hz, and focused to a beam spot that illuminated a portion of the electrode area in solution. A calibrated Si photodiode (Thorlabs UDT UV-050) was used to measure the light intensity incident on the electrode. Another Si photodiode was used to measure the beam-split portion of the illumination, with this Si photodiode providing a continuous calibration of the light intensity from the monochromator. A Gamry G 300 potentiostat was used to maintain the potential of the Si working electrode at −0.20 V vs RHE and to record the current produced by the sample. The signal components were measured by use of independent lock-in detection of the sample channel and the calibration channel.

Characterization

Scanning-electron microscopy (SEM) was performed using a Phenom Pro (Phenom World) electron microscope. The substrate was affixed to the sample chuck using Cu tape. A FEI model TF30ST transmission-electron microscope with 300 kV field emission, equipped with a HAADF STEM detector and a CCD camera, was used to image Pt nanoparticles that were dispersed on a copper mesh supported by a Cu grid. Although the images in Figure 4.1 are displayed with different tilt angles for convenience of viewing, when these images were loaded into software such as ImageJ, with the appropriate calibration indicated by the scale bar, the diameters and lengths of the wires were found to be the same in all three cases. The CoP nanoparticles were monodisperse (Figure C.2), whereas the Pt nanoparticles (Figure C.1) were dispersed in a carbonaceous conductive matrix that may more readily adhere to a hydrophobic Si–H surface than the CoP. These factors may contribute to the differences in the distributions of the Pt and CoP nanoparticle on the MW arrays (Figure 4.1).

In some cases, i.e. with a highly resistive radial emitter or with no emitter present, a more uniform distribution of catalyst on the tops, sides, and bottoms of the wire arrays would be more optimal than deposition only at the bottoms of the wire arrays as described herein. Electrodeposition could be used to obtain a more uniform placement of the electrocatalyst onto microwire arrays.[2]

H_2 Faradaic Yield

H_2(g) generation was determined by quantitative volumetric collection of the gas

evolved in the catholyte chamber in a two-electrode setup consisting of an H-tube made from volumetric burets. The gas formed at the cathode was collected after passage of −100 °C with the electrode held at a current density of −10 mA/cm^2. The electrode area was 0.050 cm^2. The volume of the collected gas was in excellent agreement with the amount of H_2(g) expected assuming 100 % Faradaic efficiency for H_2(g) production. The counter electrode was an IrO_x-coated Ti wire.

Calculation of Photocathode Efficiency

The ideal regenerative-cell efficiency was calculated by using the measured three-electrode characteristics of the photoelectrode in conjunction with an ideally non-polarizable counterelectrode operating at the Nernstian potential E(O_2/H_2O). As such, $\eta_{\mathrm{IRC}} = \frac{\mathrm{ff} V_{\mathrm{oc}} J_{\mathrm{sc}}}{P_{\mathrm{in}}}$, where P_{in} is the input solar power, V_{oc} is the difference between the open-circuit potential and $E(O_2/H_2O)$, J_{sc} is the current density observed at E(O_2/H_2O), and the fill factor is calculated as fractional maximum power with respect to the quantity $V_{\mathrm{oc}} \cdot J_{\mathrm{sc}}$.

Comparison Between Calculated Resistance and Measured Series Resistance

The sheet resistance of 100 Ω □$^{-1}$ for a 100 nm (t) thick emitter yields a calculated resistivity of 0.001 Ω cm (ρ). The resistance for a single wire of radius 2 μm (r) along the radial emitter on a 50 μm (L) tall wire is 398 Ω ($R_{\mathrm{wire}} \frac{\rho L}{2\pi r t}$). For an entire wire array, the total resistance decreases by the number of parallel resistors ($R_{\mathrm{array}} = \frac{R_{\mathrm{wire}}}{N_{\mathrm{wires}}}$). A 0.1 cm^2 geometric array on an 11 μm pitch (8.26×10^5 wire cm^{-2}) therefore produces a total calculated emitter-based resistance of 0.0048 Ω. The measured series resistance was determined by the measurement of the area ($A = \int_0^{J_{\mathrm{sc}}} V\, dJ$) under the J–E data,[3] yielding ($R_{\mathrm{S},\int} = 2(\frac{V_{\mathrm{oc}}}{J_{\mathrm{sc}}} - \frac{A}{{J_{\mathrm{sc}}}^2} - \frac{n k_{\mathrm{b}} T}{q} \times \frac{1}{J_{\mathrm{sc}}})$) a value of 285 Ω.

C.2 Supplementary Data

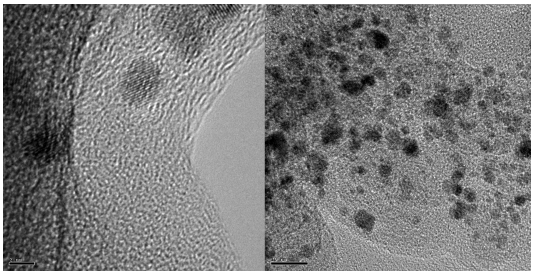

Figure C.1: Transmission-electron micrographs of ≈ 3 nm mean diameter crystalline Pt nanoparticles, with diameters ranging from 1 to 8 nm. The scale bar on the left image is 2 nm, whereas the bar on the right indicates 10 nm.

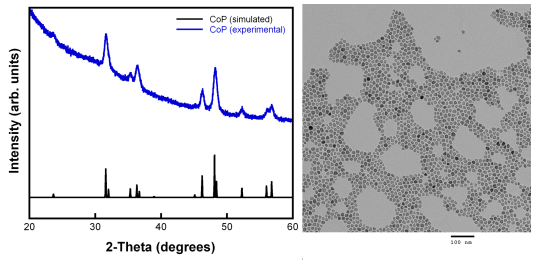

Figure C.2: Powder x-ray diffraction (left) and transmission-electron micrograph (right) of ≈ 13 nm diameter crystalline CoP nanoparticles. The scale bar indicates 100 nm.

Catalyst	Loading (mg/cm^2)	J_{ph} (mA/cm^2)	ff	V_{oc} (V vs. RHE)	Illumination (mW/cm^2)
Bare (planar)	0	30	-	0.44	100
Pt (planar)	0.10	23	0.40	0.43	100
Pt (planar)	0.20	12	0.49	0.48	100
Pt (MW)	0.50	7.8	0.49	0.37	30
Pt (MW)	0.50	14	0.46	0.44	100
Pt (MW)	0.50	30	0.43	0.46	330
CoP (planar)	0.050	28	0.15	0.41	100
CoP (planar)	0.20	12	0.52	0.49	100
CoP (planar)	2.0	0.19	0.54	0.29	100
CoP (MW)	2.0	8.5	0.35	0.45	30
CoP (MW)	2.0	17	0.24	0.48	100
CoP (MW)	2.0	21	0.23	0.52	330

Table C.1: J–E parameters for n$^+$p-Si planar and microwire photocathodes.

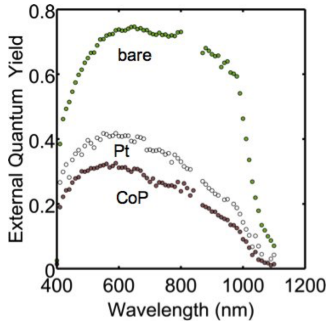

Figure C.3: Spectral response for bare (top), Pt-coated (middle), and CoP-coated (bottom) n^+p Si MW arrays in contact with $H_2(g)$-saturated 0.50 M H_2SO_4. The data points that were acquired near complex Xe arc-lamp spectral features were omitted due to artifacts.

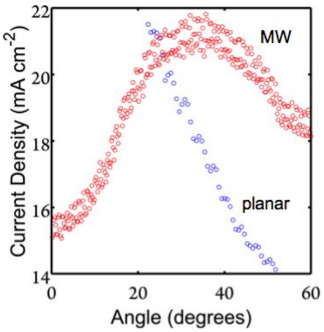

Figure C.4: Dependence of photocurrent on the angle of illumination. The blue data were obtained using a CoP-coated planar n^+p Si photocathode (0.050 mg/cm^2 mass loading), whereas the red data were obtained using a CoP-coated n^+p Si microwire-array photocathode (2.0 mg/cm^2 mass loading), both at 1 Sun of simulated AM1.5G solar illumination in 0.50 M H_2SO_4.

C.3 References

(1) E. J. Popczun, C. G. Read, C. W. Roske, N. S. Lewis and R. E. Schaak, *Angew. Chem. Int. Ed.*, 2014, **53**, 5427–5430.

(2) D. Pysch, A. Mette and S. W. Glunz, *Sol. Energy Mater. Sol. Cells*, 2007, **91**, 1698–1706.

(3) F. H. Saadi, A. I. Carim, E. Verlage, J. C. Hemminger, N. S. Lewis and M. P. Soriaga, *J. Phys. Chem. C*, 2014, **118**, 29294–29300.

Appendix D

Supplementary Information for Lightly Fluorinated Graphene as a Protective Layer for n-Type Si(111) Photoanodes in Aqueous Electrolytes

Reprinted with permission from Nielander, A.C.; Thompson, A.C.; Roske, C.W.; Maslyn, J.A.; Hao, Y.; Plymale, N.T.; Hone, J.; Lewis, N.S. *Nano Lett.*, **2016**, *16* (7), pp 4082–4086. Copyright 2016 American Chemical Society.

D.1 Methods

Materials

Single-crystalline, Czochralski grown, (111)-oriented, planar, 380 µm thick, phosphorus doped, 1.1 Ω – cm resistivity (doping density, $N_D \approx 5 \times 10^{15}$ /cm^3) single-side polished n-type silicon wafers were obtained from University Wafer, Inc. Single-crystalline, (100)-oriented, planar, 380 µm thick, boron doped, 1 Ω – cm to 10 Ω – cm resistivity single-side polished p-type silicon with 300 nm thermal oxide (SiO_2 on Si substrate) were also obtained from University Wafer, Inc. Silicon wafers with an np^+ homojunction (np^+-Si) was fabricated using a previously reported procedure (Yang et. al) via room temperature ion implantation on n-Si at a 7° incident angle using ^{11}B accelerated to 45 keV with a dose of 1×10^{14} /cm^2, and then at 32 keV with a dose of 5×10^{14} /cm^2.[1] To reduce the contact resistance, the back sides of the wafers were implanted with ^{31}P at 140 keV with a dose of 1×10^{14} /cm^2, and then at 75 keV with a dose of 5×10^{14} /cm^2. Dopant activation, both for the junction p^+ layer and the back-surface field (BSF) n^+ layer, was achieved via rapid thermal annealing at 1000 °C for 15 s under a flow of N_2(g). Water was obtained from a Barnstead Nanopure system and had a resistivity ≥ 18.0 MΩ – cm. Copper Etch Type CE - 100 ($FeCl_3$-based, Transene Company, Inc., Danvers, MA), and buffered HF improved (aq) (semiconductor grade, Transene Company, Inc., Danvers, MA) were used as received. Acetone (HPLC grade, Sigma-Aldrich) was used as received. Acetonitrile (99.8 % anhydrous, Sigma-Aldrich) used in electrochemical measurements was dried over Al_2O_3 prior to use. Ferrocene (Fc, bis(cyclopentadienyl)iron(II), 99 %, Strem), cobaltocene ($CoCp_2$, bis(cyclopentadienyl)cobalt(II), 98 %, Strem), and acetylferrocene (AcFc, (acetylcyclopentadienyl)-cyclopentadienyl iron(II), 99.5 %, Strem) were purified via sublimation. Ferrocenium tetrafluoroborate ($Fc^+[BF_4]^-$,

bis(cyclopentadienyl)iron(III) tetrafluoroborate, technical grade, Sigma-Aldrich) was recrystallized from a mixture of diethyl ether (ACS grade, EMD) and acetonitrile (ACS grade, EMD) and dried under vacuum. Cobaltocenium hexafluorophosphate ($CoCp^{2+}$, bis(cyclopentadienyl)cobalt(III) hexafluorophosphate, 98 %, Sigma-Aldrich) was recrystallized from a mixture of ethanol (ACS grade, EMD) and acetonitrile (ACS grade, EMD) and dried under vacuum. Acetylferrocenium ($AcFc^{+}$) was generated in situ via electrochemical oxidation of $AcFc^{0}$ with the concomitant reduction reaction occurring in a compartment that was separated by a Vycor frit from the working electrode compartment. Potassium ferricyanide ($K_3[Fe(CN)_6]$, 99.2 %, Sigma-Aldrich) and potassium ferrocyanide ($K_4[Fe(CN)_6]$ trihydrate, ACS Certified, Fisher Scientific) were used as received. $LiClO_4$ (battery grade, Sigma-Aldrich) was used as received. Petri dishes used were Falcon Optilux(TM) branded and were cleaned with water prior to use. All other chemicals were used as received unless otherwise noted.

Electrode/Sample fabrication

Monolayer graphene was grown by chemical vapor deposition (CVD) of carbon on Cu.[2] Additional CVD-grown monolayer graphene on Cu was purchased from Advanced Chemical Supplier Materials (Medford, MA). A 2.5 cm × 1 cm piece of monolayer graphene on Cu (from either source) was fluorinated using a home-built XeF_2 pulse chamber, with one pulse of XeF_2(g) at 2 torr for 90 s with a base pressure of < 1 mtorr. The fluorinated graphene samples on Cu were then coated with 495K A4 polymethyl methacrylate (PMMA, MicroChem) by spinning at 2000 rpm (500 rpm s^{-1} acceleration) for 60 s, followed by a 5 min bake at 185 °C. This procedure was repeated twice to increase the PMMA thickness. This process yielded a PMMA/F–Gr/Cu stack. PMMA/Gr/Cu stacks were obtained using nominally the same spin coating method but without graphene exposure to XeF_2.

Smaller pieces were cut from the PMMA/F–Gr/Cu and floated in $FeCl_3$ solution until complete removal of the Cu (≈ 1 h) was observed. To remove the etchant residue, each stack was transferred between five consecutive ≥18 MΩ − cm resistivity water baths. N-type Si was etched for 30 s in buffered HF improved to yield n-Si–H surfaces . SiO_2 on Si substrates were cleaned using a modified SC1/SC2 cleaning method. SC-1 consisted of soaking the Si wafers in a 5:1:1 (by volume) solution of H_2O, NH_4OH (≈30 wt. %, J.T. Baker) and H_2O_2 (≈35 wt. %, Sigma) for 10 min at 75 °C. After washing with H_2O, SC-1 cleaned wafers were exposed to SC-2 conditions, which consisted of soaking the Si wafers in a 5:1:1 (by volume)

solution of H_2O, HCl (11.1 M, Sigma) and H_2O_2 (≈35 wt. %, Sigma) for 10 min at 75 °C. A clean PMMA/F–Gr stack was then transferred gently onto the appropriately prepared Si wafer (HF etched Si for electrode fabrication, SC1/SC2 cleaned SiO_2 on Si substrate for chemical stability interrogation via Raman spectroscopy) from the water bath and dried with a stream of N_2(g) to remove any remaining water between the Si wafer and the graphene sheet. The final PMMA/F–Gr/wafer stack was baked at 80 °C for 10 min in air. The majority of the PMMA was detached with a 10 min acetone soak and the remaining PMMA residue was removed by an anneal (H_2:Ar v:v 5:95) for 2 h at 350 °C, leaving an F–Gr/Si stack.[3] Gr/Si stacks were prepared by nominally identical procedures using pristine graphene. Generally, 5-10 electrodes were made at the same time from the same PMMA/F–Gr/Cu or PMMA/Gr/Cu stack, respectively.

N-Si/F–Gr electrodes were fabricated using Ga:In (75:25) eutectic as an ohmic back contact. The wafers were attached to a Cu wire with Ag paint (high purity, SPI Supplies). All surfaces except the F–Gr layer were covered with insulating epoxy (Loctite Hysol 9460). Monolayer graphene-covered Si(111) electrodes were fabricated using an analogous procedure in which all of the above steps were executed with the exception that the graphene was not exposed to the XeF_2 (g). CH_3-terminated Si(111) wafers were prepared using a previously reported procedure and were not etched with HF prior to use in electrode fabrication.[4] Graphene-free, H-terminated Si(111) electrodes were etched with HF(aq) immediately before use.

Instrumentation

X-ray photoelectron spectroscopic (XPS) data were collected at $\approx 5 \times 10^{-9}$ torr using a Kratos AXIS Ultra DLD with a magnetic immersion lens that consisted of a spherical mirror and concentric hemispherical analyzers with a delay-line detector (DLD). An Al Kα (1.486 keV) monochromatic source was used for X-ray excitation. Ejected electrons were collected at a 90° angle from the horizontal. The CASA XPS software package v 2.3.16 was used to analyze the collected data. Raman spectra were collected with a Renishaw Raman microscope at λ =532 nm through an objective with numerical aperture=0.75. The laser power was ≈ 3 mW.

UV/Vis transmission spectra were collected with a Cary 5000 absorption spectrometer equipped with an external DRA 1800 attachment. The data were automatically zero/baseline corrected by the instrument before any additional processing was performed.

Scanning electron microscope (SEM) images were obtained using a FEI Nova NanoSEM 450 at an accelerating voltage of 10.00 kV with a working distance of 5 mm and an in-lens secondary electron detector. Electrochemical data were obtained using a Princeton Applied Research Model 273, Biologic SP-250, or a Gamry Reference 600 potentiostat. A Pt wire reference electrode (0.5 mm dia., 99.99 % trace metals basis, Sigma-Aldrich) and a Pt mesh counter electrode (100 mesh, 99.9 % trace metals basis, Sigma-Aldrich) were used for the electrochemical measurements. The cell potentials for the nonaqueous redox species were determined using cyclic voltammetry to compare the solution potential to the formal potential of the redox species. The potential difference between cells was calculated using the difference between the solution potentials for each redox couple in conjunction with standard formal reduction potentials from the literature. The CH_3CN-$CoCp^{2+/0}$ solution ($CoCp_2$ [3 mM]/ $CoCp^{2+}$ [50 mM]) was calculated to have a solution potential of $E(A/A^-) = -1.26$ V vs. Fc/Fc^+, the CH_3CN-$Fc^{+/0}$ solution (Fc [55 mM]/ Fc^+ [3 mM]) was calculated to have $E(A/A^-) = -0.10$ V vs. Fc^+/Fc, and the CH_3CN-$AcFc^{+/0}$ solution (pre-electrolysis AcFc concentration = [50 mM]) was calculated to have $E(A/A^-) = 0.40$ V vs. Fc^+/Fc. The nonaqueous electrochemical solutions each contained 1.0 M $LiClO_4$. The aqueous 50 mM $K_3[Fe(CN)_6]$ - 350 mM $K_4[Fe(CN)_6]$ solution contained no additional supporting electrolyte due to the high intrinsic salt concentration. The current under forward bias saturated at much larger values in the $Fe(CN)_6^{3-/4-}$ solution than in the Fc^+/Fc solution due to the increased concentration of electron-accepting species in the $Fe(CN)_6^{3-/4-}$ solution. The electrolyte solution was rapidly stirred with a small, Teflon-covered stir bar. Illumination was provided with an ENH-type tungsten-halogen lamp. Illumination intensities were set to provide $\approx 10\,mA/cm^2 to 11\,mA/cm^2$ of light-limited current density. These intensities corresponded to ≈1/3rd Sun at AM1.5G ($\approx 33\,mW/cm^2$), respectively, as determined through the concurrent use of a Si photodiode (Thor Laboratories) that was calibrated relative to a secondary standard photodetector that was NIST-traceable and calibrated at $100\,mW/cm^2$ of AM1.5G illumination. Nonaqueous electrochemistry was performed anaerobically in an Ar(g)-filled glovebox. Aqueous electrochemistry was performed in air. Electrodes were washed with H_2O and dried prior to transfer between electrolyte solutions. Plots of current density vs. time data were smoothed using a 9 point Savitzky-Golay algorithm via data analysis software (Igor Pro 6). Normalized current density was calculated by multiplying the ratio of the light intensity at a time point of interest to the light intensity at $t = 0$ s by the original current density and dividing the resulting value by the current density

measured at the time point of interest. The current density versus potential data in HBr(aq) were measured using a three-electrode setup with a Si working electrode, a Pt wire pseudo-reference electrode, and a large Pt mesh counter electrode. The electrolyte consisted of aqueous 0.4 M Br_2 - 7.0 M HBr (pH=0) electrolyte under rapid stirring, and $\approx 33\,mW/cm^2$ of simulated solar illumination from an ELH-type W-halogen lamp. Photoelectrochemical deposition of Pt was performed by immersing the electrode into an aqueous solution of 5 mM K_2PtCl_4 (99.9 %, Alfa Aesar) and 200 mM LiCl. Using a three-electrode setup, with a saturated calomel reference electrode and a Pt mesh counter electrode, galvanostatic control was maintained at $-0.1\,mA/cm^2$ in a stirred solution until $-100\,mC/cm^2$ had passed. The samples were then rinsed with deionized water and were dried under a stream of $N_2(g)$.

D.2 Supporting Data

Electrochemical behavior of np^+-Si/F–Gr electrodes in aqueous solution

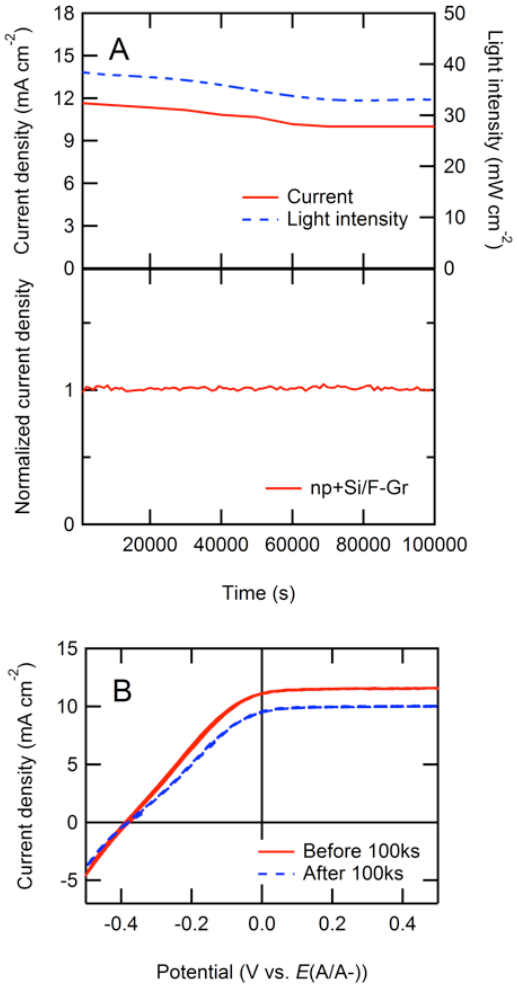

Figure D.1: Current density vs. time (J–t) and current density vs. potential (J–E) behavior of np$^+$-Si/F–Gr electrodes in contact with aqueous 50 mM $Fe(CN)_6^{3-}$ - 350 mM $Fe(CN)_6^{4-}$ electrolyte under $\approx$ 33 mW/cm^2 of ENH-type W-halogen illumination. (A) The J–t behavior of np$^+$-Si/F–Gr at E = 0 V vs. E(A/A$^-$) over 100 000 s (> 24 h). The normalized current density is reported to correct for any variations in the light intensity during the experiment. (B) J–E behavior of np$^+$-Si/F–Gr (3 scans at 50 mV s^{-1}) before and after exposure to the conditions depicted in (A). The current density decay in the original chronoamperograms is consistently ascribed to fluctuations in the light source, as well as to decomposition of the $Fe(CN)_6^{3-/4-}$ under illumination, which produced thin colored film on the electrochemical cell over the course of the experiment depicted in (A).

Comparison of graphene-imparted stability between graphene and fluorinated graphene electrodes

The photoelectrochemical stability of pristine graphene-coated n-Si electrodes and of fluorinated graphene-coated electrodes was tested by collecting J-t data for n-

Si/Gr and n-Si/F–Gr electrodes from four different electrode 'batches' (two Gr/n-Si and two F–Gr/Gr batches) in contact with aqueous 50 mM $Fe(CN)_6^{3-}$ - 350 mM $Fe(CN)_6^{4-}$ under $\approx$ 33 mW/cm^2 of ENH-type W-halogen illumination (Figure D.2). These batches of electrodes each mutually consisted of 5-6 electrodes in which each electrode was fabricated from the same section of a larger sheet of Gr or F–Gr, respectively. However, between batches of electrodes, different PMMA/(F-)Gr/Cu stacks or different regions of the same stack were used. The n-Si/Gr from the first graphene electrode batch (batch GrA) exhibited stable current densities for $>$ 1000 s (Figure D.2A). Among these electrodes fabricated, all five electrodes were photoelectrochemically stable (5/5 stable, where stability was defined as having a current density at t=1000 s of at least 60 % of the current density displayed at t = 0 s. This definition was used because some graphene-covered (and F–Gr covered) electrodes displayed an initial decay of current density followed by a subsequent stabilization, as seen in Figure D.3. This behavior is consistent with the hypothesis that any pinholes in the graphene protective coating led to the oxidation at the exposed Si surface, but that stability is observed when the exposed Si is passivated with SiO_x. However, the other batch (batch GrC, Figure D.2C) yielded only two n-Si/Gr electrodes out of six that exhibited stable current densities for $>$ 1000 s (2/6 stable). The inconsistent behavior in the photoelectrochemical stability imparted by graphene coatings on n-Si electrode was observed over many iterations of graphene growth and electrode fabrication. Conversely, both batches of F–Gr coated n-Si electrodes (batch F–GrB, Figure D.2B and batch F–GrD, Figure D.2D) yielded n-Si/F–Gr electrodes that exhibited stable current densities for $>$ 1000 s (5/5 stable in batch F–GrB and 5/5 stable in batch F–GrD). The improved consistency of the photoelectrochemical stability is one of the key attributes of the fluorinated graphene-coated n-Si electrodes relative to the routinely observed behavior of pristine graphene-coated n-Si electrodes.

We also explored the extended stability behavior of the Gr-coated n-Si electrodes as compared to F–Gr-coated n-Si electrodes. Figure D.4 depicts the J–t behavior of the most stable n-Si/F–Gr and n-Si/Gr electrodes. After both starting at an initial current density of $\approx$ 10 mA/cm^2, the n-Si/F–Gr electrode current density decayed to 9.5 mA/cm^2, whereas the n-Si/Gr electrode decayed to 8 mA/cm^2. The fluorinated graphene-coated electrode was more stable, but the pristine graphene coated electrode also exhibited reasonable stability, particularly between t = 20 000 s and t = 80 000 s. In conjunction with the data depicted in Figure D.2, under ideal conditions for extended (100 000 s) time periods, these observations suggest that

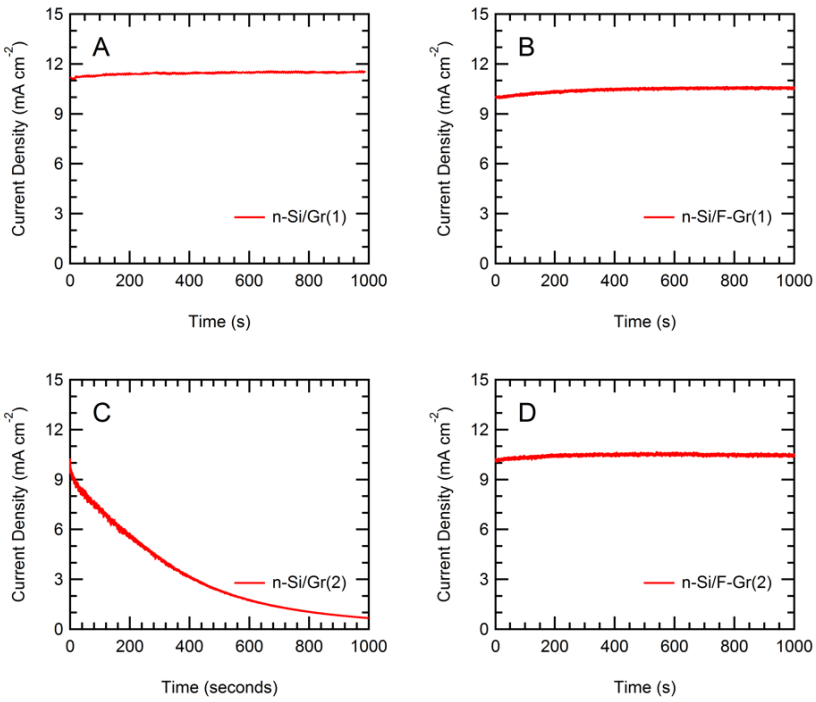

Figure D.2: Representative *J–t* data for n-Si/Gr and n-Si/F–Gr electrodes from four different electrode batches (two Gr/n-Si and two F–Gr/Gr batches, see above) in contact with aqueous 50 mM $Fe(CN)_6^{3-}$ - 350 mM $Fe(CN)_6^{4-}$ under $\approx$ 33 mW/cm$-^2$ of W-halogen illumination. (A) The n-Si/Gr electrodes from the batch GrA exhibited stable current densities for > 1000 s (5/5 stable). (B The n-Si/F–Gr electrodes from batch F–GrB exhibited stable current densities for > 1000 s (5/5 stable). (C) The n-Si/Gr electrodes from batch GrC did not consistently exhibit stable current densities for > 1000 s (2/6 stable). (D) The n-Si/F–Gr electrodes from batch F–GrD exhibited stable current densities for > 1000 s (5/5 stable).

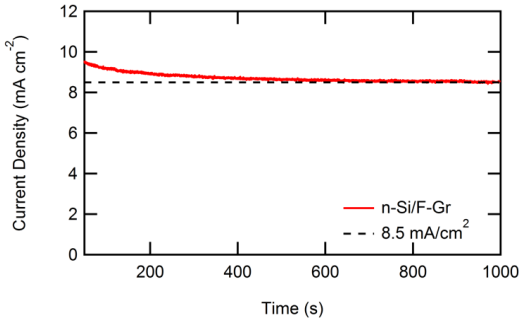

Figure D.3: Representative *J–t* data of an n-Si/F–Gr electrode in contact with aqueous 50 mM $Fe(CN)_6^{3-}$ - 350 mM $Fe(CN)_6^{4-}$ under $\approx$ 33 mW/cm^2 of W-halogen illumination. After an initial decay in current density, the current density stabilized at $\approx$ 8.5 mA/cm^2.

pristine graphene may be able to provide to n-Si electrodes the same level of stability as that provided by F–Gr coatings. However, some difficult-to-control variable in the growth or transfer of graphene limits the routine observation of such extended stability. This hypothesis is consistent with the supposition that grain boundaries and defect sites on the graphene coatings lead to the observed degradation, and that fluorination of such sites passivates them to further loss of integrity. As such, the inconsistency seen in the graphene electrode stability data can be ascribed to the relative preponderance or dearth of defect sites present on an electrode surface, with fluorination greatly decreasing the effect that such sites have on the photoelectrochemical stability of such systems. Future work involving the targeted study of single crystal graphene sheets or single grains in a polycrystalline graphene sheet are underway to further examine this hypothesis.

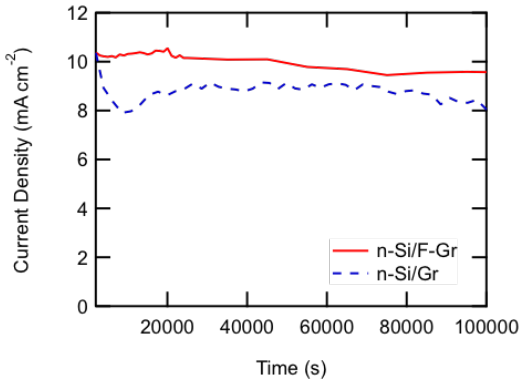

Figure D.4: *J–t* data of the 'champion' n-Si/F–Gr and n-Si/Gr electrodes in contact with aqueous 50 mM $Fe(CN)_6^{3-}$ - 350 mM $Fe(CN)_6^{4-}$ under $\approx$ 33 mW/cm^2 of W-halogen illumination. After both starting at an initial current density of $\approx$ 10 mA/cm^2, the n-Si/F–Gr electrode current density decayed to 9.5 mA/cm^2 compared to the n-Si/Gr electrode which decayed to 8 mA/cm^2.

Stability of fluorinated graphene-covered n-Si electrodes under high light intensity conditions

Fluorinated graphene-coated and pristine graphene-coated n-Si electrodes were tested for photoelectrochemical stability under approximately 1 sun conditions ($\approx$ 100 mW/cm^2 from an ENH -type W-halogen lamp). Figure D.5 depicts the photoelectrochemical stability over 1000 s for n-Si/Gr and n-Si/F–Gr electrodes in contact with aqueous 50 mM $Fe(CN)_6^{3-}$ - 350 mM $Fe(CN)_6^{4-}$ under $\approx$ 100 mW/cm^2 of W-halogen illumination. The current density of the n-Si/F–Gr electrode was effectively constant over this time period, whereas the current density of the n-Si/Gr

electrode decayed from ≈ 25 mA/cm^2 to less than 7 mA/cm^2 over the same time period. This behavior supports the hypothesis that under these conditions fluorinated graphene provides a superior protective layer relative to pristine graphene. Figure D.6 further depicts the photoelectrochemical stability under the same conditions of a F–Gr coated n-Si electrode over 100 000 ks. Although the F–Gr coated electrode was stable over the same time period (100 000 s) under lower light intensity conditions (Figure 5.1), at near 1 sun conditions the current density of the electrode decayed to near baseline conditions over the same time period.

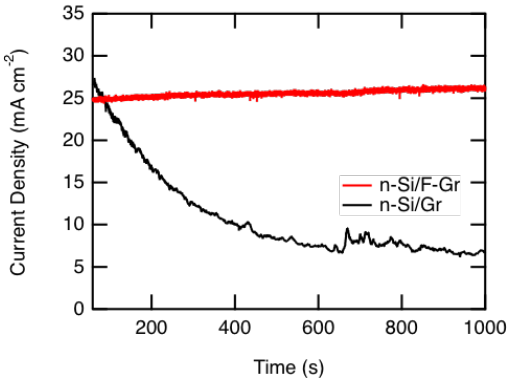

Figure D.5: J-t data for n-Si/Gr and n-Si/F–Gr electrodes in contact with aqueous 50 mM $Fe(CN)_6^{3-}$ - 350 mM $Fe(CN)_6^{4-}$ under ≈ 100 mW/cm^2 of W-halogen illumination over 1000 s.

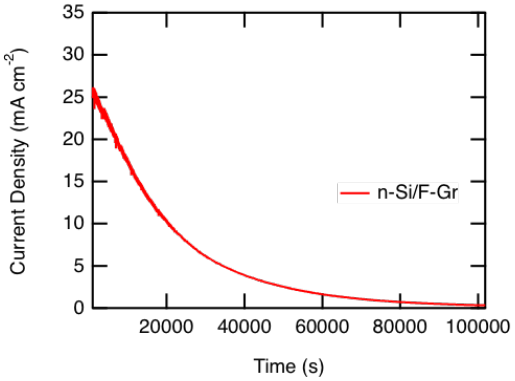

Figure D.6: *J–t* data for n-Si/F–Gr electrodes in contact with aqueous 50 mM $Fe(CN)_6^{3-}$ - 350 mM $Fe(CN)_6^{4-}$ under ≈ 100 mW/cm^2 of W-halogen illumination over 100 000 s.

The stability of the fluorinated graphene was tested under acidic, neutral, and alkaline aqueous solutions, respectively. To insure that the same area was examined before and after testing, a small area on the graphene wafer was outlined with Hysol 9460

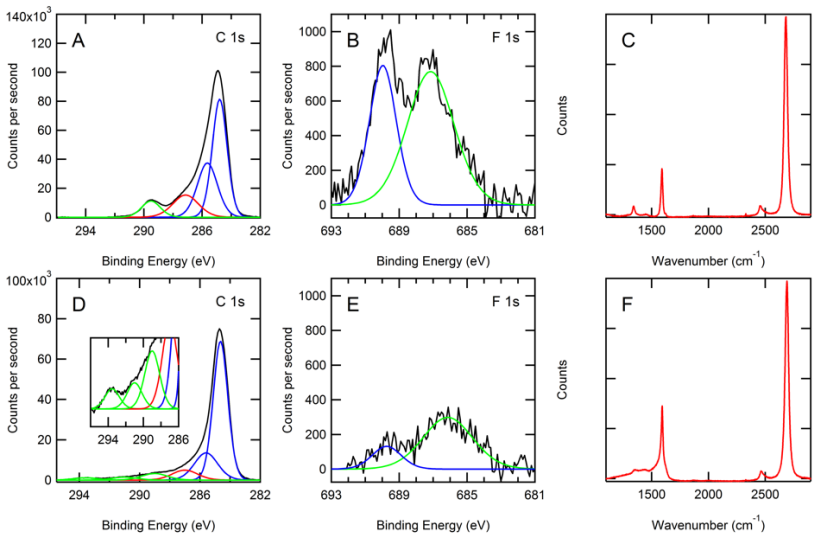

Figure D.7: Raman and X-ray photoelectron (XP) spectra of fluorinated graphene (F–Gr) before and after annealing. (A) The C 1s region before annealing displayed four peaks at binding energies of 284.8 eV, 285.6 eV, 287.2 eV, and 289.5 eV, respectively. Peaks attributed to carbon bound to fluorine are shown in green; peaks attributed to carbon bound to carbon are shown in blue; and peaks attributed to carbon bound to oxygen are shown in red. (B) The F 1s region displayed two peaks at binding energies of 687.1 eV and 690.0 eV, respectively. (C) The Raman spectra before annealing showed a prominent defect peak at 1350 cm^{-1}. (D) Two additional peaks, at 291 eV and 293.5 eV (inset), attributable to CF_2 and CF_3 groups, were observed in the C 1s XP spectra after annealing. (E) The positions of the peaks in the F 1s region were shifted slightly to 686.1 eV and 689.8 eV, respectively, and decreased in size. (F) The defect peak at 1350 cm^{-1} broadened after the anneal. These spectra are consistent with a lightly fluorinated ($C_x F$, x > 10) graphene surface.[5] The change in fluorination profile after annealing is consistent with a reorganization of the fluorine on the surface, and the XPS spectra demonstrate the expected decrease in fluorine content after a two-hour 350 °C anneal under a H_2:Ar (5:95) atmosphere.[6]

epoxy. Optical images along with Raman spectra were acquired, and wafers were then placed for 1 h in aqueous solutions at pH 0, pH 7, and pH 14. After carefully rinsing the samples with > 18 MΩ – cm H_2O and drying the samples with a stream of N_2(g), optical images along with Raman spectra were obtained from the same areas as before testing. The Raman spectra and optical images of the samples soaked in acidic and neutral solutions showed no change after testing (Figure D.8-D.9). The samples tested in alkaline solutions showed a marked decrease in defect density of the remaining sections of fluorinated graphene, closely mimicking the profile of pristine graphene. Repeated tests of fluorinated graphene in 1 M KOH(aq) showed

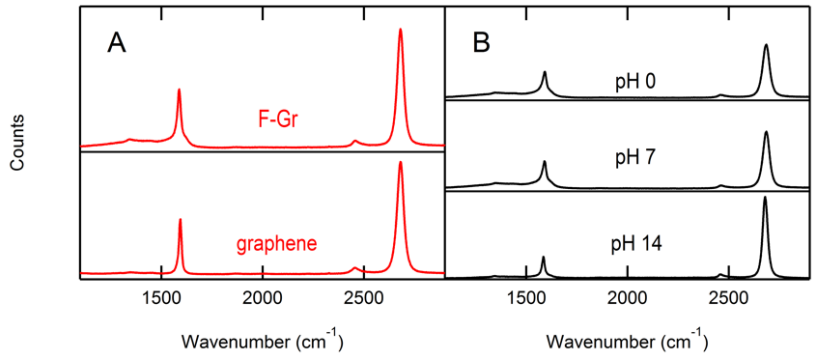

Figure D.8: Stability tests of F–Gr in acidic (1 M HCl), alkaline (1 M KOH), and neutral aqueous conditions. (A) Raman spectra of the pristine graphene sheets before fluorination (top) and after fluorination (bottom) showed an increase in the size of the defect peak at 1350 cm^{-1}. (B) The 1350 cm^{-1} defect peak remained unchanged after 1 h in acidic or neutral aqueous solutions. In contrast, immersion for 1 h in aqueous alkaline media produced a decrease in the intensity of the defect peak. However, in all three spectra the intensity of the G ($\approx$ 1580 cm^{-1}) and 2D ($\approx$ 2680 cm) peaks are consistent with monolayer graphene.

large-scale delamination of the fluorinated graphene sheet, as observed in the images before and after exposure to the aqueous pH 14 solution.

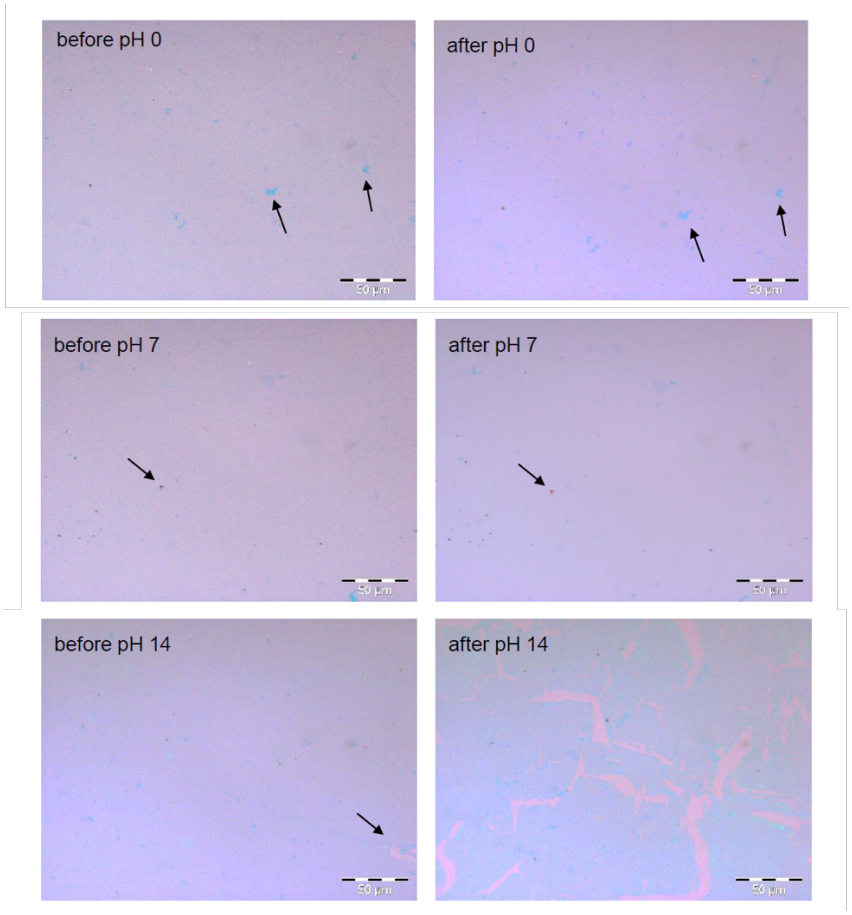

Figure D.9: Optical images of stability tests of F–Gr in acidic (1 M HCl), alkaline (1 M KOH), and neutral (deioninzed water) conditions. Arrows indicate points of reference for the corresponding before and after images.

UV-Vis Spectroscopy of Graphene and Fluorinated Graphene

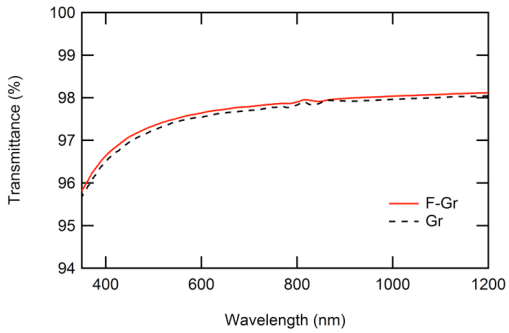

Figure D.10: UV/Vis spectra of Gr and F–Gr on glass. Graphene and fluorinated graphene were transferred to borosilicate glass slides using the standard transfer procedures (vide supra). The slightly increased transmission for F–Gr is consistent with the expectation of decreased visible light absorption upon fluorination of graphene.

Inhibition of platinum silicide formation

XP spectra of Si–Me/F–Gr/Pt and Si–Me/Pt surfaces were obtained to investigate the ability of F–Gr to inhibit platinum silicide formation. Pt was deposited at ≈ 3 nm thickness via electron-beam evaporation on both F–Gr covered and bare Si surfaces. The 3 nm Pt thickness was chosen to allow for interrogation of the sample surface to a depth at which both Si and Pt ware observable by XPS. Methylated Si surfaces were used to inhibit the formation of Si oxide at the Si/Pt interface during sample fabrication, because Si oxide of sufficient thickness is also capable of preventing silicide formation.[8] Figure D.11a shows the XP spectrum of a pure Pt phase. A thicker Pt layer (20 nm) was used to interrogate only the pure Pt phase. Figure D.11b shows the Pt 4f XP spectrum of CH_3-terminated Si with a 3 nm Pt overlayer. The Pt 4f peak shifted to higher binding energy, indicative of platinum silicide formation.[7] The shoulder of the peak at low binding energy is consistent with a pure Pt phase overlayer. Conversely, 3 nm of Pt on F–Gr covered silicon showed essentially no change in the Pt 4f binding energy immediately after fabrication (Figure D.11c or after a 1 h anneal under forming gas at 300 °C (Figure D.11d). The data are thus indicative of little or no platinum silicide formation. Figure D.11e presents an overlay of the spectra in Figure D.11a-D.11d and highlights the difference between the Pt 4f peak positions.

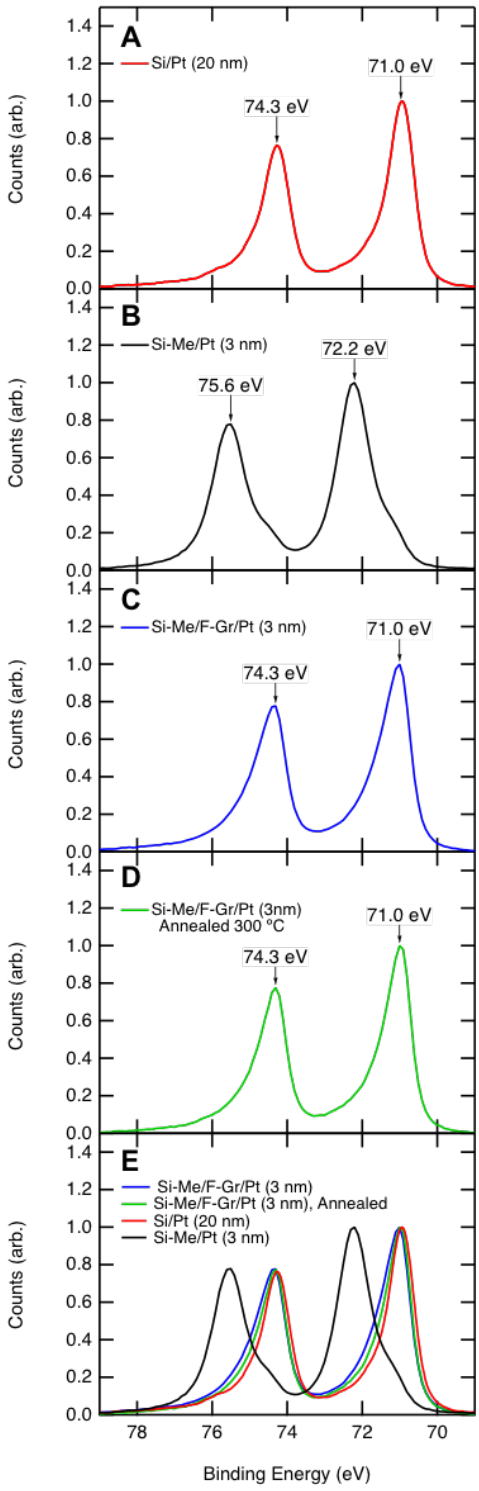

Figure D.11: The Pt 4f XP spectra of Pt on both F–Gr covered and Si surfaces. (A) XP spectrum of a thick (20 nm) layer of Pt on Si. This spectrum is representative of a pure Pt phase. (B) XP spectrum of a 3 nm layer of Pt on Si. The Pt 4f peak shifted to high binding energy (72.2 and 75.6 eV), characteristic of platinum silicide formation.[7] The shoulder to lower binding energy is attributed to a pure Pt phase. (C) XP spectrum of Si–Me/F–Gr/Pt (3 nm). The Pt 4f peak positions (71.0 and 74.3 eV) are consistent with pure Pt. (D) XP spectrum of Si–Me/F–Gr/Pt after annealing at 300 °C under forming gas. (E) Overlay of XP spectra (A)-(D).

n-Si/F–Gr non-aqueous photoelectrochemistry

Sample	$E_{oc,CoCp^{2+/0}}$ (V vs. $E(CoCp_2^{+/0})$)	$E_{oc,Fc^{+/0}}$ (V vs. $E(Fc^{+/0})$)	$E_{oc,AcFc^{+/0}}$ (V vs. $E(AcFc^{+/0})$)
Gr	0	0.26	0.43
FGr	0	0.20	0.30

Table D.1: E_{oc} values for n-Si/Gr and n-Si/F–Gr electrodes in contact with non-aqueous redox couples under $\approx$ 33 mW/cm^2 of W-halogen (ENH) illumination. The Nernstian potential, $E(A/A^-)$, of the contacting non-aqueous electrolytes were measured as follows: $E(CoCp^{2+/0}) = -1.26$ V vs. $E^{\circ\prime}(Fc^{+/0})$, $E(Fc^{+/0}) = -0.1$ V vs. $E^{\circ\prime}(Fc^{0/+})$, $E(AcFc^{+/0}) = 0.4$ V vs. $E^{\circ\prime}(Fc^{+/0})$.

H-Br stability/efficiency over time

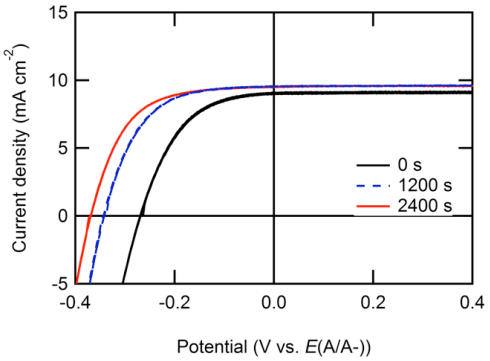

Figure D.12: Current density-potential (J–E) behavior of an n-Si/F–Gr/Pt photoanode before, during, and after 2400 s of photoelectrochemical stability testing in contact with 0.4 M Br_2 - 7.0 M HBr (pH=0) aqueous electrolyte. Photoelectrochemical stability was measured by observing the J–t behavior at an initial current density of 10 mA/cm^2 over the specified time period (see Figure 5.3). The behavior of the n-Si/F–Gr/Pt electrode improved over 2400 s, with improvements in E_{oc} (0.27 V to 0.37 V), J_{sc} (9.0 mA to 9.5 mA), and ff (0.51 to 0.59), resulting in an increase in the ideal regenerative cell conversion efficiency from 3.5 % to $\geq$ 5 %.

XPS Oxide Analysis

XPS analysis was performed in order to determine the effect of electrochemical oxidation at the Si–Me surface on the oxidation state of the Si photoanode surface (Figure 5.2). Silicon oxide detected before and after electrochemical oxidation was quantified using a simple substrate—overlayer model described by equation D.1:[9]

$$d = \lambda_{ov} \sin\theta \{\ln[1 + \frac{I^0_{Si}}{I^0_{ov}} \times \frac{I_{ov}}{I_{Si}}]\}, \tag{D.1}$$

where d is the overlayer thickness, λ_{ov} is the attenuation factor through the oxide overlayer (assumed to be 2.6 nm),[10] the angle from the surface of the sample to the detector (90°), $\frac{I^0_{Si}}{I^0_{ov}}$ is an instrument normalization factor related to the expected signal for a pure Si and a pure SiO_2 sample (taken to be 1.3 for this instrument), I_{ov} is the measured intensity of the silicon, and I_{ov} is the measured intensity of the silicon oxide overlayer. The thickness of a monolayer of oxide was taken to be 0.35 nm.[11] Negligible silicon oxide was detected on the bare methyl-terminated silicon surfaces prior to electrochemical oxidation (Figure D.2a) and an oxide thickness of approximately 0.75 nm, or > 2 monolayers of oxide, was observed after exposure of the Si–Me surface (Figure D.2b) to the electrochemical oxidation conditions described in Figure D.2. An oxide thickness of approximately 0.15 ± 0.05 nm was detected on the Si–Me/F–Gr surfaces prior to electrochemical oxidation (Figure D.2c) and an oxide thickness of approximately 0.17 ± 0.5 nm, was observed after exposure (Figure 5.2d) of the Si–Me/F–Gr surface to the electrochemical oxidation conditions described in Figure 5.2.

np$^+$-Si Solid State Junction Behavior

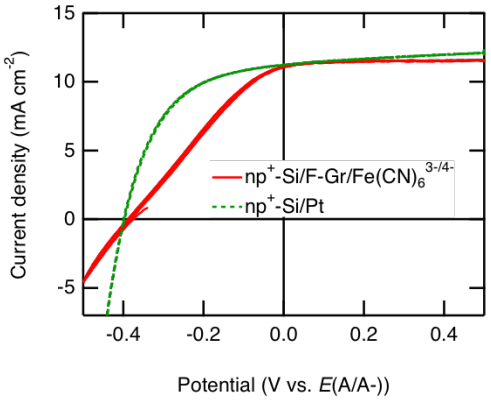

Figure D.13: J–E behavior of an np$^+$-Si/Pt PV cell and an np$^+$-Si/F–Gr/Fe(CN)$_6^{3-/4-}$ photoanode under $\approx$ 33 mW/cm^2 of ENH-type W-halogen illumination. For the np$^+$-Si/Pt PV cell, the following photovoltaic metrics were measured: E_{oc} = −0.40 V, J_{sc} = 11.3 mA/cm^2, ff = 0.50. For the np$^+$-Si/F–Gr/Fe(CN)$_6^{3-/4-}$ cell, the following photovoltaic metrics were measured: E_{oc} = −0.39 V, J_{sc} = 11.1 mA/cm^2, ff = 0.30. The similar E_{oc} values with varying fill factors between these two interfaces suggest that the Si/F–Gr/Fe(CN)$_6^{3-/4-}$ interface is the source of an additional series resistance but that the parallel shunt resistances are similar between the np$^+$-Si/Pt and np$^+$-Si/F–Gr/Fe(CN)$_6^{3-/4}$ interfaces. A similar parallel shunt resistance is also consistent with the use of the same buried photoactive junction at each interface. The np$^+$-Si/Pt PV cell was prepared by evaporating 15 nm of Pt onto the freshly HF etched p$^+$ surface of an np$^+$-Si chip and scribing a Ga:In eutectic onto the backside of an n-doped surface. For the np$^+$-Si/Pt PV cell, the (E(A/A$^-$)) referenced on the x-axis refers to the potential of the Pt contact.

Analysis of fluorine atom concentration relative to defect site carbon concentration

A key hypothesis of this work is that the fluorination of CVD-grown graphene leads to passivation of defect sites present in CVD graphene. Assuming a carbon-carbon bond length of 0.142 nm and the hexagonal structure of graphene, the area of each hexagonal unit in a graphene sheet is 0.052 nm^2 and encompasses two carbon atoms. Therefore, a 1 cm^2 sheet of pristine graphene will include $\approx 1 \times 10^{15}$ carbon atoms. A rigorous evaluation of the density and total number of carbon atoms in a polycrystalline graphene sheet is challenging, due to the presence of a variety of defect types, including point and line defects, with various geometries, and also due to a variable number of defects that may be produced by fabrication of the graphene-covered electrode.[12] For simplicity, we consider only the line defects associated with grain boundaries. These line defects have a variety of geometries and can be composed of alternating 5- and 7-membered carbon rings. Assuming

that the density of carbon atoms at a line defect and in the defect-free graphene sheet are equivalent, and further that the density of carbon atoms in a polycrystalline CVD graphene sheet is equivalent to that in a single crystalline graphene sheet, allows calculation of the percentage of total carbon atoms at defect sites in the graphene sheet. The grain size of the graphene used in this work is 0.2 µm to 5 µm on a side. The grains are generally amorphously shaped, but are approximated herein for simplicity as hexagons for simplicity. Assuming hexagonal grains with side length of 0.2 µm (area of 0.10 µm2) implies $\approx 10^9$ grains in a 1 cm^2 sheet of grapheme, and a total length of 8×10^8 µm of grain boundary area. If the width of these boundaries is equal to the width of a single hexagonal unit of the graphene lattice (≈ 0.28 nm), and assuming that the carbon density is the same as that of a single hexagonal unit, the total number of defect carbon atoms at grain boundary line defects is $\approx 10^5$ C atoms per 1 cm^2 area of graphene. Thus ($10^5/10^{15}$), i.e., 1 defective carbon atom is present for every 10^{10} pristine carbon atoms in the polycrystalline graphene sheet. This ratio is significantly smaller than the ratio of F atoms to C atoms found via XPS analysis ($10 > F/C > 0.01$. In conjunction with the knowledge that the defect sites on a graphene sheet are significantly more reactive than the pristine carbon sites, this XPS F/C ratio suggests that most or all of the defect carbon atoms are capped with fluorine. Further studies using electron microscopy methods are underway to confirm this hypothesis.

SEM of Pt electrodeposition on n-Si/F–Gr surfaces Assuming 100 % faradaic yield for charge transfer to platinum during the photoelectrochemical deposition of Pt from an aqueous solution of 5 mM K_2PtCl_4 and 200 mM LiCl, in conjunction with 2 e^- per Pt atom deposited, and a conformal deposition, a charge density of -100 mC/cm^2 should result in the deposition of an $\approx$ 50 nm thick of Pt layer on the n-Si/F–Gr electrodes. SEM images were obtained on n-Si/F–Gr surfaces before photoelectrochemical deposition and after 10 mC/cm^2 or 100 mC/cm^2 of cathodic charge density was passed during electrodeposition (Figure D.14-D.16). Figure D.15 indicates that the Pt deposited stochastically across the F–Gr surface, in contrast to previous reports of metal deposition via other methods on graphene, which produced preferential metal deposition at grain boundaries.[12] This difference in behavior may be due to passivation of highly reactive grain boundary sites by the XeF_2 treatment. The incomplete electrochemical stability observed in Figure D.3 for the n-Si–H/Pt electrode may be related to imperfect conformal deposition, consistent with the observations of Figure D.16.

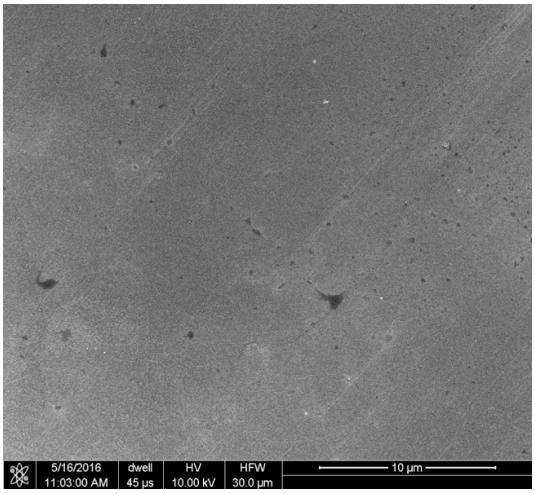

Figure D.14: SEM image of a fluorinated graphene-covered n-Si surface prior to photoelectrochemical deposition of Pt metal from an aqueous solution of 5 mM K_2PtCl_4 (99.9 %, Alfa Aesar) and 200 mM LiCl electrolyte solution.

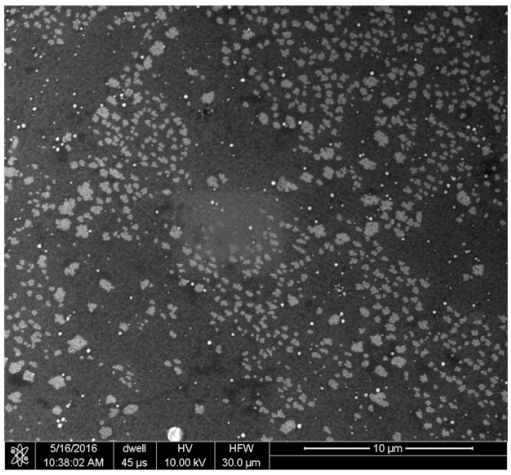

Figure D.15: SEM image of a fluorinated graphene-covered n-Si surface after passing 10 mC/cm^2 charge during photoelectrochemical deposition of Pt metal from an aqueous solution of 5 mM K_2PtCl_4 (99.9 %, Alfa Aesar) and 200 mM LiCl electrolyte solution.

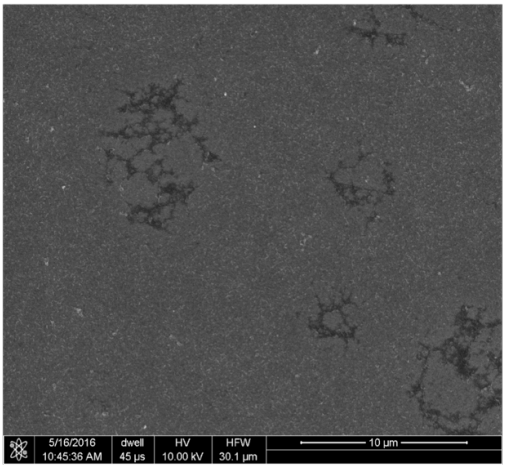

Figure D.16: SEM image of a fluorinated graphene-covered n-Si surface after passing 100 mC/cm^2 charge during photoelectrochemical deposition of Pt metal from an aqueous solution of 5 mM K_2PtCl_4 (99.9 %, Alfa Aesar) and 200 mM LiCl electrolyte solution.

D.3 References

(1) J. Yang, K. Walczak, E. Anzenberg, F. M. Toma, G. Yuan, J. Beeman, A. Schwartzberg, Y. Lin, M. Hettick, A. Javey, J. W. Ager, J. Yano, H. Frei and I. D. Sharp, *J. Am. Chem. Soc.*, 2014, **136**, 6191–6194.

(2) N. Petrone, C. R. Dean, I. Meric, A. M. van der Zande, P. Y. Huang, L. Wang, D. Muller, K. L. Shepard and J. Hone, *Nano Lett.*, 2012, **12**, 2751–2756.

(3) A. Pirkle, J. Chan, A. Venugopal, D. Hinojos, C. W. Magnuson, S. McDonnell, L. Colombo, E. M. Vogel, R. S. Ruoff and R. M. Wallace, *Appl. Phys. Lett.*, 2011, **99**, 122108.

(4) S. Hu, M. R. Shaner, J. A. Beardslee, M. Lichterman, B. S. Brunschwig and N. S. Lewis, *Science*, 2014, **344**, 1005–1009.

(5) R. Stine, W.-K. Lee, K. E. Whitener, J. T. Robinson and P. E. Sheehan, *Nano Lett.*, 2013, **13**, 4311–4316.

(6) N. T. Plymale, Y.-G. Kim, M. P. Soriaga, B. S. Brunschwig and N. S. Lewis, *J. Phys. Chem. C*, 2015, **119**, 19847–19862.

(7) G. Larrieu, E. Dubois, X. Wallart, X. Baie and J. Katcki, *J. Appl. Phys.*, 2003, **94**, 7801.

(8) J. R. Abelson, K. B. Kim, D. E. Mercer, C. R. Helms, R. Sinclair and T. W. Sigmon, *J. Appl. Phys.*, 1988, **63**, 689.

(9) J. E. Castle, *Surf. Interface Anal.*, 1984, **6**, 302–302.

(10) M. F. Hochella and A. H. Carim, *Surf. Sci.*, 1988, **197**, L260–L268.

(11) J. A. Haber and N. S. Lewis, *The Journal of Physical Chemistry B*, 2002, **106**, 3639–3656.

(12) F. Banhart, J. Kotakoski and A. V. Krasheninnikov, *ACS Nano*, 2011, **5**, 26–41.

Appendix E

Highly Branched Cobalt Phosphide Nanostructures for Hydrogen-Evolution Electrocatalysis

Reproduced from E. J. Popczun; C.W. Roske; C.G. Read; J.C. Crompton; J.M. McEnaney; N.S. Lewis; R. E. Schaak. *J. Mater. Chem. A*, **2015**, *3*, 5420-5425..
Copyright 2015 The Royal Society of Chemistry.

E.1 Abstract

CoP nanostructures that exposed predominantly (111) crystal facets were synthesized and evaluated for performance as electrocatalysts for the hydrogen-evolution reaction (HER). The branched CoP nanostructures were synthesized by reacting cobalt(II) acetylacetonate with trioctylphosphine in the presence of trioctylphosphine oxide. Electrodes comprised of the branched CoP nanostructures deposited at a loading density of $\approx 1\,mg/cm^2$ on Ti electrodes required an overpotential of 117 mV to produce a current density of $-20\,mA/cm^2$ in 0.50 M H_2SO_4. Hence the branched CoP nanostructures belong to the growing family of highly active non-noble-metal HER electrocatalysts. Comparisons with related CoP systems have provided insights into the impact that shape-controlled nanoparticles and nanoparticle–electrode interactions have on the activity and stability of nanostructured HER electrocatalysts.

E.2 Introduction

Transition metal phosphides have recently emerged as an important family of highly active electrocatalysts that facilitate the production of molecular hydrogen from acidic aqueous solutions, which is important for clean-energy technologies such as water electrolyzers and solar fuels generators. For example, phosphides of nickel,[1–3] cobalt,[4–12] iron,[13,14] copper,[15] molybdenum,[16–18] and tungsten[19] have been found to electrocatalytically generate H_2(g) with low overpotentials at operationally relevant current densities for solar-driven water splitting systems, while exhibiting high stability under strongly acidic conditions. Metal phosphides therefore offer an Earth-abundant and inexpensive alternative to platinum, which serves as the benchmark catalyst for the hydrogen-evolution reaction (HER). The relationship between the electrocatalytic activity and the exposed crystal face has not yet been elucidated

for the transition metal phosphides, which are generally studied as nanocrystals. The (001) surface of Ni_2P contains proximate phosphorus and nickel sites that are hypothesized to work cooperatively to facilitate moderate binding of the intermediates and products to the catalyst surface.[20] The other metal phosphides that have been identified as HER catalysts have related crystal structures which also contain proximate metal and phosphorus structural motifs on their low-index surfaces. This structural feature suggests that metal phosphide nanostructures that preferentially expose different crystal facets would be expected to exhibit different activities for HER catalysis. The CoP system, which has been studied extensively, exhibits high HER activity across a diverse group of morphologies, characteristic grain sizes, support materials, and synthetic preparations. For example, nominally comparable activity has been observed for multi-faceted single-crystalline hollow CoP nanoparticles on Ti foil,[4] electrochemically deposited CoP films,[9] CoP nanocrystals on carbon nanotube[7] and carbon cloth supports,[10] porous CoP nanowires on carbon cloth5 and Ti substrates,[6] CoP nanosheets on a Ti plate,[8] porous template-grown CoP nanowires,[11] and a collection of morphologically variant CoP nanoparticles on glassy carbon electrodes.[6] The primary methods used to synthesize these CoP nanostructures include reaction of pre-made Co nanoparticles with trioctylphosphine, or phosphidation of cobalt oxide and related nanostructured templates.[4–8] Although these results collectively demonstrate the high inherent HER activity of CoP nanostructures, a direct comparison of the activities and performance is difficult for samples made by different methods and for electrodes prepared in different laboratories, because of unavoidable differences in the electrode preparation methods, mass loadings, and accessible surface areas. Additionally, the HER-active CoP nanostructures reported to date have been polycrystalline or multi-faceted, without statistically relevant differences in the proportions of the different crystal facets that have been exposed and accessible. An important first step toward the goal of better understanding the origin of the high HER activity in CoP and related nanostructured metal phosphide systems is to synthesize and study high quality, morphologically distinct samples. CoP is ideally suited for such an approach, because multi-faceted single-crystalline CoP nanoparticles have amongst the highest activities and acid stabilities of the metal phosphide family of HER catalysts.[4] Also, using closely related chemical strategies, methods exist for synthesizing CoP and related metal phosphide nanostructures to produce materials of the same chemical composition and structure but with different morphologies. Accordingly, we report herein the synthesis of highly branched CoP nanostructures with single-crystal CoP nanorod

protrusions that expose a high density of accessible (111) facets. The electrocatalytic HER performance of the branched CoP nanostructures was evaluated and compared to that of multi-faceted CoP nanocrystals.[4] These observations provide a starting point for the identification of the key parameters that impact the HER performance of morphologically distinct nanostructures in the same materials system.

E.3 Experimental

Chemicals and Materials.

1-Octadecene [tech. 90 %, $C_{18}H_{36}$], oleylamine [70 %, $C_{18}H_{37}N$], trioctylphosphine [TOP, 97 %, $(C_8H_{17})_3P$], trioctylphosphine oxide [TOPO, 99 %, $(C_8H_{17})_3PO$], titanium foil [99.7 %, 0.25 mm thickness], and sulfuric acid [99.999 %] were purchased from Sigma-Aldrich, and cobalt(II) acetylacetonate [$Co(acac)_2$] was purchased from Alfa Aesar. All chemicals were used as received. Silver paint was purchased from SPI supplies, and two-part epoxy [HYSOL 1C] was purchased from McMaster-Carr.

Synthesis of highly branched CoP nanostructures. $Co(acac)_2$ (256 mg, 1 mmoll) was introduced into a three-necked round bottom flask that contained oleylamine (6.4 mL, 19.4 mmol), TOPO (3.8 g, 9.8 mmol), TOP (0.5 mL, 1.1 mmol), and a magnetic borosilicate-coated stir bar. The flask was placed into a heating mantle and was equipped with a mercury thermometer with a thermometer adapter in the first port, a Liebig condenser with gas inlet adapter in the second port, and a glass pennywise stopper in the final port. The reaction mixture was heated to 120 °C for 1 h under vacuum to remove water and other low-boiling impurities. Following degassing, an Ar(g) blanket was introduced to the reaction flask while the temperature was raised to 355 °C to 360 °C and then maintained for 3 h. Following heating, the reaction flask was cooled rapidly by removing the heating mantle. Upon reaching 80 °C, the flask was opened to the atmosphere and ≈10 mL of toluene was added to the reaction to avoid solidification of the TOPO. To isolate the nanoparticles, the reaction solution was separated into centrifuge tubes, with each tube being ≈1/3 full. An equal volume of isopropyl alcohol was added to the centrifuge tubes to promote precipitation. The tubes were sealed and then centrifuged at 7000 rpm for 3 min. The resulting supernatant was discarded and the particles were resuspended by addition of hexanes. The particles were then flocculated by addition of excess isopropyl alcohol and centrifuged again. This entire process was repeated two additional times. The resulting oily residue that contained the nanoparticle precipitate was resuspended in 0.50 M H_2SO_4 and centrifuged to collect the final CoP powder, which was suspended in hexanes for storage.

Preparation of Working Electrodes.

Working electrodes were prepared by first making 10 mL of a CoP nanostructure stock solution in hexanes (10 mg mL^{-1}). To this suspension, ≈5 µL of oleylamine was added to help promote particle adhesion to the electrode surface. To a 0.2 cm^2 piece of titanium foil, 20 µL of the CoP nanostructure stock solution was deposited in 5 µL increments to achieve a loading density of ≈1 mg/cm^2. The resulting CoP-decorated Ti foils were annealed under H_2(5 %)/Ar(95 %) at 450 °C for 30 min. The loading densities were validated experimentally using a microbalance, by taking the difference between the mass of the annealed foils and the mass of the initial foil. The back sides of the nanostructure-loaded Ti foils were attached to polyvinylchloride-coated Cu wires with Ag paint. The wires were placed through a 6 mm-diameter glass capillary and two-part epoxy was used to cover all exposed surfaces except the front of the Ti foil, onto which the CoP nanostructure sample was deposited.

Electrochemical Characterization.

Electrochemical data were collected using a Gamry Instruments Reference 600 potentiostat. All measurements were performed in 0.50 M H_2SO_4, unless otherwise noted. A single-compartment cell was used with a graphite rod counter electrode and mercury-mercury sulfate (Hg/Hg_2SO_4) reference electrode.

Polarization data were collected at a scan rate of 2 mV s^{-1}, with the solution agitated using a magnetic stir bar. The data were corrected for uncompensated resistance (≈6 Ω) using the current-interrupt method that was built into the Reference 600 potentiostat software suite. The reversible hydrogen electrode (RHE) potential was maintained by continuous bubbling of ≈1 atm of research-grade H_2(g) into the electrochemical cell. To determine the RHE potential, the open-circuit potential of a platinum mesh electrode was determined following the completion of any experiments involving CoP, to avoid Pt contamination. To test the short-term stability, the potential was held at a current density of −10 mA/cm^2 for 18 h of continuous galvanostatic testing. To test the long-term stability, accelerated degradation studies were performed using cyclic voltammetry from 5 mV to −160 mV vs. RHE for 500 cycles at a scan rate of 100 mV s^{-1}.

Materials Characterization.

Transmission-electron microscopy (TEM) images were collected using a JEOL 1200 microscope operating at an accelerating voltage of 80 kV. A JEOL JEM-2010F was used to collect high-resolution bright-field TEM images as well as to

obtain energy-dispersive X-ray spectroscopy (EDX) data at an accelerating voltage of 200 kV. Gatan Digital Micrograph software was used to measure the lattice spacings from the fast-Fourier transform (FFT) of the HRTEM images. These values, and the corresponding FFT diffraction patterns, were simulated using the CrystalMaker/SingleCrystal software package. Scanning-electron microscopy (SEM) images were collected using a FEI Nova NanoSEM 630 at a working distance of 1.5 mm and an accelerating voltage of 2.00 kV. Powder X-ray diffraction (XRD) patterns were collected using a Bruker-AXS D8 Advance diffractometer with Cu Kα radiation and a LynxEye 1-D detector operating at room temperature. The CrystalMaker/ CrystalDiffract software package was also used to simulate the XRD patterns, using previously published crystallographic parameters for MnP-type CoP.[21] Brunauer-Emmett-Teller (BET) surface area measurements were performed using a Micromeretics ASAP 2020 at liquid-nitrogen temperatures, and the data were analyzed using the ASAP 2020 software version 4.0.

E.4 Results and Discussion

Figure E.1 shows TEM images for the highly branched CoP nanostructures that formed upon heating $Co(acac)_2$, TOP, TOPO, and OLAM at 360 °C for 3 h. A majority of the CoP nanostructures consisted of a central core with multiple nanorod protrusions that grew outward. The nanorod protrusions had an average diameter of 14 ± 3 nm and the average diameter of the complete nanostructures was 390 ± 70 nm. The SEM image in Figure E.2 confirmed the three-dimensional branched morphology of the CoP nanostructures, as well as their uniformity. HRTEM images of both the core (Figure E.3a) and the branches (Figure E.3b,c,d) indicated that both regions were crystalline and that the branches appeared to be single-crystalline. The majority of the nanorods that protruded from the core predominantly exposed the (111) lattice plane of CoP, with a lattice spacing of 2.4 Å.

Figure E.4 shows powder XRD data for a bulk sample of the CoP branched nanostructures, with a SAED pattern and an EDS spectrum that both correspond to the TEM image shown in Figure E.1a included in Figure E.1c and Figure F.1, respectively. The experimental powder XRD pattern in Figure E.4 matches well with that expected for MnP-type CoP, with no observable crystalline impurities. The agreement between the relative peak intensities that were observed experimentally vs. those that are expected for an isotropic sample indicates that no significant preferred orientation was present in the sample. Strong preferred orientation would be expected for nanorods, but not for the branched nanostructures with three-dimensionally pro-

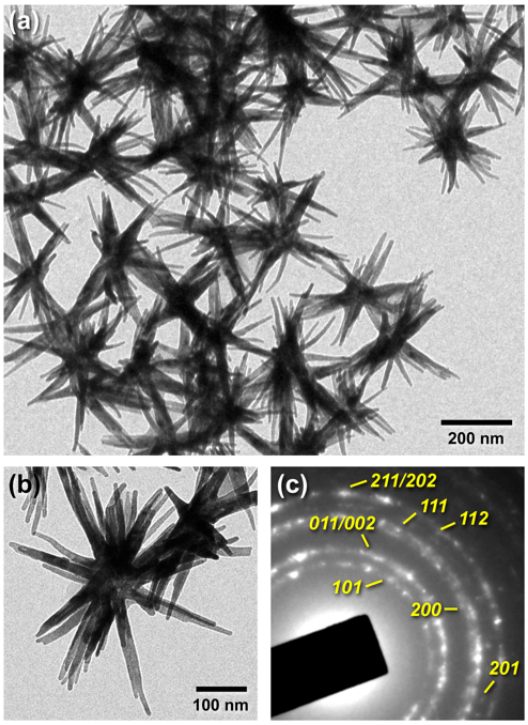

Figure E.1: a,b) TEM images and c) corresponding SAED pattern of a representative sample of highly branched CoP nanostructures. The indexing in (c) corresponds to MnP-type CoP.

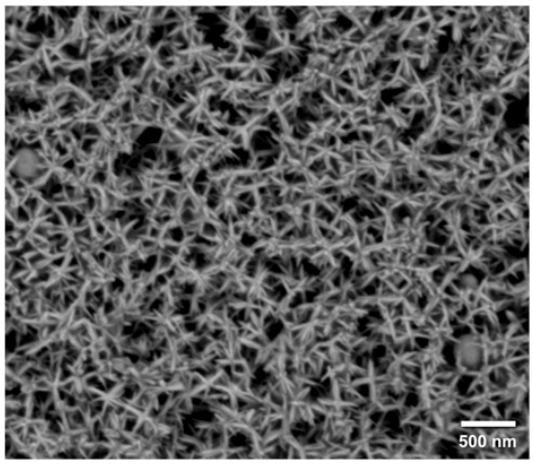

Figure E.2: SEM image of a sample of highly branched CoP nanostructures.

truding nanorods, which cannot align along a preferential crystal direction upon deposition onto a flat substrate. The lack of preferred orientation in the bulk powder XRD sample is therefore consistent with the morphology observed by TEM and SEM. Scherrer analysis of the peak widths indicated an average grain size of 17 nm,

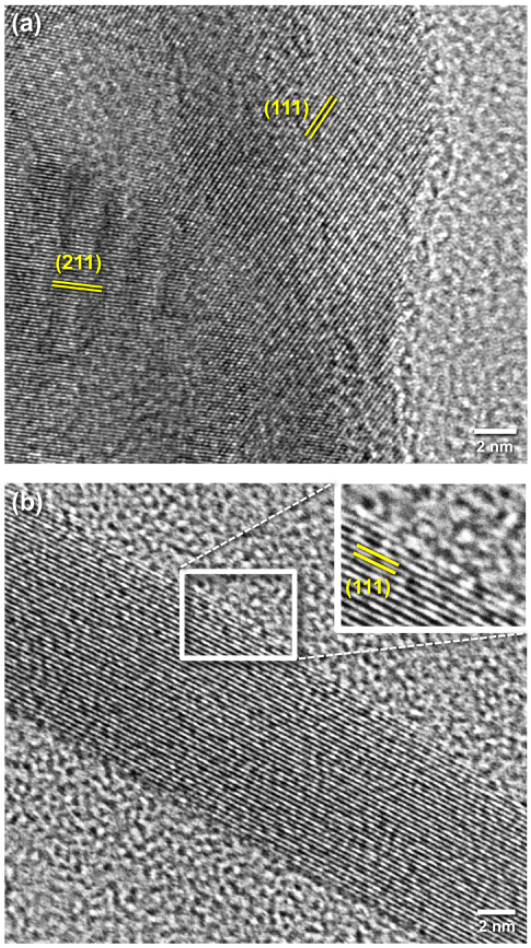

Figure E.3: HRTEM images of (a) the core region and (b) a nanorod branch of a representative CoP nanostructure.

which is, within expected experimental error, consistent with the average diameter of the single-crystalline nanorod protrusions as observed by TEM.

The SAED pattern in Figure E.1c is also consistent with MnP-type CoP, and therefore matches well with that observed for the bulk sample by powder XRD. The EDS spectrum in Figure F.1, acquired for an ensemble of particles, indicated a Co:P ratio of 50:50, which matches with that expected for CoP. Taken together, the XRD, SAED, and EDS data therefore confirm the assigned composition and crystal phase, and indicate that the CoP branched nanostructures formed with high purity. Although highly branched colloidal CoP nanostructures have not apparently been synthesized previously, morphologically similar Co_2P nanostructures have been reported.[22] To access highly branched Co_2P nanostructures, Zhang and Robinson thermally decomposed cobalt (II) oleate in the presence of pure TOPO, which was

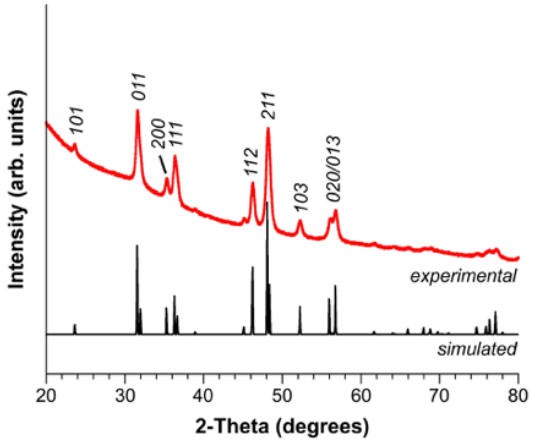

Figure E.4: XRD pattern for the as-synthesized CoP nanostructures. The simulated XRD pattern for MnP-type CoP is shown for comparison.

the lone phosphorus source.[22] Our protocol for synthesizing highly branched CoP nanostructures also used TOPO, but we observed that TOPO alone did not produce CoP. Instead, OLAM and TOP were required to form CoP, suggesting that TOP is the primary phosphorus source under our conditions. TOPO is required to generate the highly branched CoP nanostructures, however, rather than the morphologically distinct pseudo-spherical particles that formed when only TOP was used. When TOPO was used as a co-solvent, the highly branched CoP nanostructures form reproducibly, suggesting that TOPO is involved in directing the growth of the nanorod protrusions and/or stabilizing the predominantly exposed facets.

The branched CoP nanostructures were highly crystalline and exposed predominantly single-crystal (111) facets, as compared to the multi-faceted CoP nanoparticles that have been synthesized previously.[4] Furthermore, the surface areas, as measured by Brunauer, Emmett, and Teller (BET) analysis, are comparable for the two different morphologies, with the branched CoP nanostructures having a BET specific surface area of 66 m^2/g and the multi-faceted CoP nanoparticles having a BET specific surface area of 59 m^2/g.[4]

The similar BET areas for the two different CoP nanostructures provides an opportunity to evaluate the role of morphology on the HER performance of an earth-abundant HER electrocatalyst. Hence electrodes coated with the branched CoP nanostructures were prepared in an analogous manner to the multi-faceted CoP nanoparticles studied previously.[4] Briefly, the highly branched CoP nanostructures were deposited onto $\approx$0.2 cm^2 Ti substrates from a hexanes dispersion that contained $\approx$0.1 vol % oleylamine. The mass loadings were $\approx$ 1 mg/cm^2, and the electrodes

were annealed under H_2(5 %)/Ar(95 %) to remove the surface ligands. The SEM and XRD data in Figure F.2 indicate that both the morphology and crystal phase of the CoP nanostructures remained largely unchanged during the electrode preparation and annealing steps, although a small Co_2P impurity was observed. The Ti electrode containing the branched CoP nanostructures exposed a high density of accessible (111) lattice planes, as shown schematically in Figure E.5.

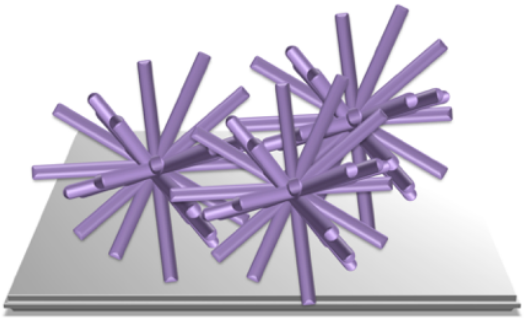

Figure E.5: Schematic highlighting the high density of exposed (111) facets on the Ti electrodes that contain the highly branched CoP nanostructures.

Figure E.6 shows the polarization (current density vs potential, *J*–*E*) data that correspond to the HER activity in 0.50 M H_2SO_4 of the highly branched CoP nanostructures. The HER activity of the branched CoP nanostructures was lower than that of the multi-faceted CoP nanoparticles reported previously (Figure S3),[4] despite the mutually comparable surface areas for the two different CoP electrocatalyst morphologies. The overpotentials required to produce a (cathodic) current density of $-20\,mA/cm^2$ were -117 mV and -100 mV for the branched nanostructures and multi-faceted nanoparticles,[4] respectively, despite their similar loading densities on analogous Ti substrates. Additionally, the material outperforms previously reported Co_2P nanostructures (= -167 mV),[12] suggesting that the small Co_2P impurity does not play a significant role in the observed activity of the branched CoP nanorods. A quantitative Faradaic yield of H_2(g) was observed for both types of CoP catalytic systems (see Supplementary Information). A Tafel analysis, shown in the inset to Figure E.6, revealed Tafel slopes of 29 mV/decade and 123 mV/decade for the Pt mesh and Ti foil controls. Both of these values are consistent with values expected based on literature reports.[1,4,23] The Tafel slope for the branched CoP nanostructures was 48 mV/decade, which is comparable to the 50 mV/decade Tafel slope observed previously for the multi-faceted pseudo-spherical CoP nanoparticles.[4] The comparable values suggest a similar mechanism for the HER on the branched CoP nanostructures and on the CoP nanoparticles.

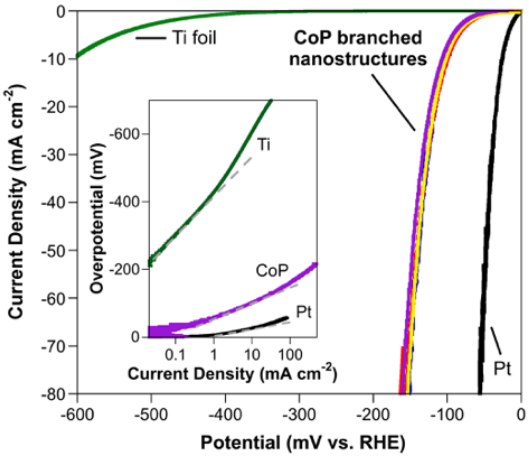

Figure E.6: Polarization data in 0.50 M H_2SO_4 for 6 distinct electrodes of the branched CoP nanostructures on Ti foil substrates at mass loadings of ≈1 mg/cm^2, along with Ti foil and Pt mesh electrodes for comparison. Inset: Tafel plots for the Ti and Pt electrodes, as well as a representative branched CoP/Ti electrode. Tafel slopes, denoted by the grey dashed lines, were calculated using the following linear regions: $-60\,\text{mV} > \eta > -125\,\text{mV}$ for CoP, $-10\,\text{mV} > \eta > -60\,\text{mV}$ for Pt, and $-250\,\text{mV} > \eta > -400\,\text{mV}$ for Ti

Given the different activities of the branched CoP nanostructures vs. the CoP nanoparticles, the turnover frequency (TOF) values are necessarily quite different. (See the Supplementary Information for TOF calculations.) The branched CoP nanostructures exhibited a TOF of 0.019 s^{-1} at an overpotential (η) of −100 mV. This TOF value is lower than that of CoP nanoparticles, which showed a TOF = 0.060 s at η= −100 mV.[4] The branched CoP nanostructures, however, still provided exceptionally high activity for the HER, performing comparably to many other non-noble-metal HER catalysts in acidic solutions, based on evaluation metrics reported in the literature. Examples include MoS_2 ($\eta_{-20\,\text{mA/cm}^2} = -175\,\text{mV}$),[24] Mo_2C ($\eta_{-10\,\text{mA/cm}^2} = -152\,\text{mV}$),[25] CoS_2 ($\eta_{-10\,\text{mA/cm}^2} = -145\,\text{mV}$),[26] $CoSe_2$ ($\eta_{-20\,\text{mA/cm}^2} = \approx -155\,\text{mV}$),[27] MoP ($\eta_{-20\,\text{mA/cm}^2} = -110\,\text{mV}$),[17] WP ($\eta_{-20\,\text{mA/cm}^2} = -140\,\text{mV}$)[19] and Ni_2P ($\eta_{-20\,\text{mA/cm}^2} = -130\,\text{mV}$).[1] However, the long-term stability of the branched CoP nanostructures on a Ti electrode was inferior to that of the CoP nanoparticles, presumably due to poor adhesion of the branched CoP nanostructures to the Ti electrode surface.[4] Specifically, under galvanostatic conditions (holding at $-10\,\text{mA/cm}^2$ for 18 h), the particles physically detached from the electrode surface, and the overpotential increased from −113 mV to −174 mV over this time period (Figure S4a). Likewise, 500 cycles between −160 mV and 5 mV (vs. the relative hydrogen electrode, RHE), which simulated multiple catalytic start/stop cycles, re-

sulted in an increase in overpotential at $-10\,\mathrm{mA/cm^2}$ from $-115\,\mathrm{mV}$ to $-135\,\mathrm{mV}$ (Figure S4b). The instability is therefore attributed to poor adhesion and is not reflective of the behavior of the catalytic CoP nanostructures themselves. Typically, differences in activities among morphologically distinct nanostructures of the same compound are routinely attributed to inherent differences in the activities of the exposed crystal facets. However, the complexity of such nanostructured materials and their electrodes makes it difficult to unambiguously determine the reason(s) for the inferior performance of the branched CoP nanostructures relative to their nanoparticle analogues. Indeed, the (111) surface could inherently be less active for the HER than one or more other surfaces that are simultaneously exposed and accessible on the CoP nanoparticles. However, the lower HER activity of the branched CoP nanostructures could also result from poorer adhesion and/or a lower density of direct CoP-Ti contacts on the electrode surface. Despite this issue, the present study is a first step toward evaluating the relative HER activities of distinct nanostructured catalysts of the same material that are of high morphological quality and uniformity. As such, these results begin to place empirical boundaries on the range of overpotentials that are observed for similarly prepared materials and electrodes. The branched CoP nanostructures nevertheless offer exceptionally high HER activity, exceeding that of most other non-noble-metal systems. These results suggest that nanostructuring to expose specific facets may not be necessary to achieve high HER performance. Indeed, comparable HER activity has been observed by several groups for CoP materials that span a range of morphologies, synthetic protocols, accessible surface areas, and support materials.[4–11] A key finding of this work is that the activities are largely the same, regardless of morphology or preparation method, underscoring the high intrinsic activity of CoP. The intrinsic HER activity of CoP makes it a highly viable candidate for practical applications, regardless of morphological details, and this study reinforces that hypothesis. However, establishing trends in activity that can be correlated to specific crystal facets, surface areas, and electrode materials is still important for furthering the understanding of the origin of the HER activity in these systems, and these results represent a step toward this goal.

E.5 Conclusion

Highly branched nanostructures of CoP, with single-crystal nanorod protrusions that predominantly expose (111) facets act as an active HER electrocatalyst. Moreover, the activity of such samples, while not as high as that of comparable multi-faceted

pseudospherical CoP nanoparticles,[4] is still excellent among the growing family of non-noble-metal nanostructured HER electrocatalysts, producing current densities of $-10\,\mathrm{mA/cm^2}$ and $-20\,\mathrm{mA/cm^2}$ at overpotentials of $-100\,\mathrm{mV}$ and $-117\,\mathrm{mV}$, respectively. These results further establish the high intrinsic activity of CoP as an electrocatalyst for the HER and provide important insights into some of the factors that influence its performance, including exposed crystal facets and nanoparticle-electrode interactions.

E.6 Acknowledgements

The work at PSU was supported by the National Science Foundation (NSF) Center for Chemical Innovation on Solar Fuels (CHE-1305124) and at Caltech by the Joint Center for Artificial Photosynthesis, a DOE Energy Innovation Hub, supported through the Office of Science of the U.S. Department of Energy under Award Number DE-SC0004993, as well as the Gordon and Betty Moore Foundation. TEM was performed in the Penn State Microscopy and Cytometry Facility (University Park, PA) and HRTEM, EDS, SEM, and BET data were acquired at the Materials Characterization Laboratory of the Penn State Materials Research Institute. C.W.R. thanks the NSF for a graduate research fellowship. The authors thank Juan Callejas for helpful discussions.

E.7 References

(1) E. J. Popczun, J. R. McKone, C. G. Read, A. J. Biacchi, A. M. Wiltrout, N. S. Lewis and R. E. Schaak, *J. Am. Chem. Soc.*, 2013, **135**, 9267–9270.

(2) L. Feng, H. Vrubel, M. Bensimon and X. Hu, *Phys. Chem. Chem. Phys.*, 2014, **16**, 5917.

(3) Z. Huang, Z. Chen, Z. Chen, C. Lv, H. Meng and C. Zhang, *ACS Nano*, 2014, **8**, 8121–8129.

(4) E. J. Popczun, C. G. Read, C. W. Roske, N. S. Lewis and R. E. Schaak, *Angew. Chem. Int. Ed.*, 2014, **53**, 5427–5430.

(5) J. Tian, Q. Liu, A. M. Asiri and X. Sun, *J. Am. Chem. Soc.*, 2014, **136**, 7587–7590.

(6) P. Jiang, Q. Liu, C. Ge, W. Cui, Z. Pu, A. M. Asiri and X. Sun, *J. Mater. Chem. A*, 2014, **2**, 14634.

(7) Q. Liu, J. Tian, W. Cui, P. Jiang, N. Cheng, A. M. Asiri and X. Sun, *Angew. Chem. Int. Ed.*, 2014, **53**, 6710–6714.

(8) Z. Pu, Q. Liu, P. Jiang, A. M. Asiri, A. Y. Obaid and X. Sun, *Chem. Mater.*, 2014, **26**, 4326–4329.

(9) F. H. Saadi, A. I. Carim, E. Verlage, J. C. Hemminger, N. S. Lewis and M. P. Soriaga, *J. Phys. Chem. C*, 2014, **118**, 29294–29300.

(10) Q. Li, Z. Xing, A. M. Asiri, P. Jiang and X. Sun, *Int. J. Hydrogen Energy*, 2014, **39**, 16806–16811.

(11) H. Du, Q. Liu, N. Cheng, A. M. Asiri, X. Sun and C. M. Li, *J. Mater. Chem. A*, 2014, **2**, 14812.

(12) Z. Huang, Z. Chen, Z. Chen, C. Lv, M. G. Humphrey and C. Zhang, *Nano Energy*, 2014, **9**, 373–382.

(13) J. F. Callejas, J. M. McEnaney, C. G. Read, J. C. Crompton, A. J. Biacchi, E. J. Popczun, T. R. Gordon, N. S. Lewis and R. E. Schaak, *ACS Nano*, 2014, **8**, 11101–11107.

(14) P. Jiang, Q. Liu, Y. Liang, J. Tian, A. M. Asiri and X. Sun, *Angew. Chem. Int. Ed.*, 2014, **53**, 12855–12859.

(15) J. Tian, Q. Liu, N. Cheng, A. M. Asiri and X. Sun, *Angew. Chem. Int. Ed.*, 2014, **53**, 9577–9581.

(16) P. Xiao, M. A. Sk, L. Thia, X. Ge, R. J. Lim, J.-Y. Wang, K. H. Lim and X. Wang, *Energy Environ. Sci.*, 2014, **7**, 2624–2629.

(17) J. M. McEnaney, J. C. Crompton, J. F. Callejas, E. J. Popczun, A. J. Biacchi, N. S. Lewis and R. E. Schaak, *Chem. Mater.*, 2014, **26**, 4826–4831.

(18) Z. Xing, Q. Liu, A. M. Asiri and X. Sun, *Adv. Mater.*, 2014, **26**, 5702–5707.

(19) J. M. McEnaney, J. Chance Crompton, J. F. Callejas, E. J. Popczun, C. G. Read, N. S. Lewis and R. E. Schaak, *Chem. Commun.*, 2014, **50**, 11026.

(20) P. Liu and J. A. Rodriguez, *J. Am. Chem. Soc.*, 2005, **127**, 14871–14878.

(21) S. Rundqvist, L. G. Sillén, D. Timm, K. Motzfeldt, O. Theander and H. Flood, *Acta Chem. Scand.*, 1962, **16**, 287–292.

(22) H. Zhang, D.-H. Ha, R. Hovden, L. F. Kourkoutis and R. D. Robinson, *Nano Lett.*, 2011, **11**, 188–197.

(23) J. O. Bockris and E. C. Potter, *J. Electrochem. Soc.*, 1952, **99**, 169.

(24) Y. Li, H. Wang, L. Xie, Y. Liang, G. Hong and H. Dai, *J. Am. Chem. Soc.*, 2011, **133**, 7296–7299.

(25) W. F. Chen, C. H. Wang, K. Sasaki, N. Marinkovic, W. Xu, J. T. Muckerman, Y. Zhu and R. R. Adzic, *Energy and Environmental Science*, 2013, **6**, 943.

(26) M. S. Faber, R. Dziedzic, M. A. Lukowski, N. S. Kaiser, Q. Ding and S. Jin, *J. Am. Chem. Soc.*, 2014, **136**, 10053–10061.

(27) D. Kong, H. Wang, Z. Lu and Y. Cui, *J. Am. Chem. Soc.*, 2014, **136**, 4897–4900.

Appendix F

Supplementary Information for Highly Branched Cobalt Phosphide Nanostructures for Hydrogen Evolution Electrocatalysis

Reproduced from E. J. Popczun; C.W. Roske; C.G. Read; J.C. Crompton; J.M. McEnaney; N.S. Lewis; R. E. Schaak. *J. Mater. Chem. A*, **2015**, *3*, 5420-5425..
Copyright 2015 The Royal Society of Chemistry.

F.1 Additional Experimental Details

Quantitative Hydrogen Yield Measurements

Quantitative H_2 yield measurements were performed in 0.50 M H_2SO_4 in a two-electrode experiment using a two-compartment cell. The two compartments, for the working and counter electrode, respectively, were separated by a Nafion(R) membrane (Fuelcellstore.com). A graduated cylinder was inverted above the working electrode to collect the H_2(g) produced during the experiment. A constant (cathodic) current of -10 mA was maintained for 50 min (3000 s) on a $\approx 0.2\,cm^2$ electrode. The amount of H_2(g) produced was 3.92 mL, as compared to the theoretical yield of 3.92 mL, as calculated with Faraday's law, Dalton's law of partial pressures and the ideal gas law. In a control experiment, a platinum electrode produced an identical quantity of H_2(g) when the same amount of charge was passed through the cathode.

Estimation of Turnover Frequencies

The turnover frequency was calculated using an established method.[1–3] First, the density of the sample was calculated using the CoP unit cell. Using the measured BET surface areas, the turnover frequencies are reported as turnovers per second per surface atom, analogous to prior reports for Ni-Mo,[1] N_2P,[2] and CoP hollow nanoparticles.[3] The Co and P surface atoms were counted separately.

Calculation of TOF values

The molar mass (89.907 g mol^{-1}), density (6.416 g/cm^3), molar volume (14.01 mL mol^{-1}), volume of a 13 nm sphere ($1.15 \times 10^{-18}\,cm^3$), surface area of a 13 nm sphere ($5.31 \times 10^{-12}\,cm^2$), and current density at $\eta = -100$ mV (for 1.0 mg/cm^2 $\eta = -1.03 \times 10^{-2}$ A/cm^2. The average surface atoms per 1 square centimeter is found

by:

$$\left(\frac{2 \times 6.022 \times 10^{23}\ \text{atoms}}{1\ \text{mol}} \times \frac{1\ \text{mol}}{14.0\ \text{cm}^3}\right)^{2/3} = 2.45 \times 10^{15} \frac{\text{atoms}}{\text{cm}^2}.$$

Using the surface atoms per tested area at $0.9\ \text{mg/cm}^2$ (BET value = 1.31×10^{18} atoms/foil):

$$\frac{0.9\ \text{mg}}{1\ \text{cm}^2} \times \frac{6.65 \times 10^2\ \text{cm}^2}{\text{mg}} \times \frac{2.45 \times 10^{15}\ \text{atoms}}{1\ \text{cm}^2} = 1.63 \times 10^{18} \frac{\text{atoms}}{\text{test}}.$$

Finally, the turnover frequency at $-100\ \text{mV}$ overpotential is calculated (per surface atom) as:

$$\frac{1\text{turnover}}{2\text{e}^-} \times \frac{1.3 \times 10^{-2}\ \text{A}}{1\ \text{cm}^2} \times \frac{1\ \text{mol}}{96\,485\ \text{C}} \times \frac{6.022 \times 10^{23}\text{e}^-}{1\ \text{mol}} \times \frac{1\ \text{text}}{1.65 \times 10^{18}\ \text{atoms}} = 0.019\ \text{s}^{-1}\text{atom}^{-1}.$$

For $0.032\ \text{mg/cm}^2$, the theoretical value gives $0.028\ \text{s}^{-1}$ atom^{-1} with a BET value of $0.034\ \text{s}^{-1}$ atom^{-1}. For $0.9\ \text{mg/cm}^2$, the theoretical value gives $0.048\ \text{s}^{-1}$ atom^{-1} with a BET value of $0.060\ \text{s}^{-1}$ atom^{-1}. For $2.02\ \text{mg/cm}^2$, the theoretical value gives $0.038\ \text{s}^{-1}$ atom^{-1} with a BET value of $0.045\ \text{s}^{-1}$ atom^{-1}.

F.2 Supplementary Figures

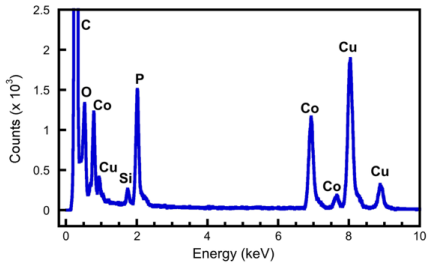

Figure F.1: Representative EDS spectrum of a sample of highly-branched CoP nanostructures. The Co/P ratio was 1/1. The Cu and Si impurities are due to the TEM grid and column, respectively, and were present in control samples of blank TEM grids.

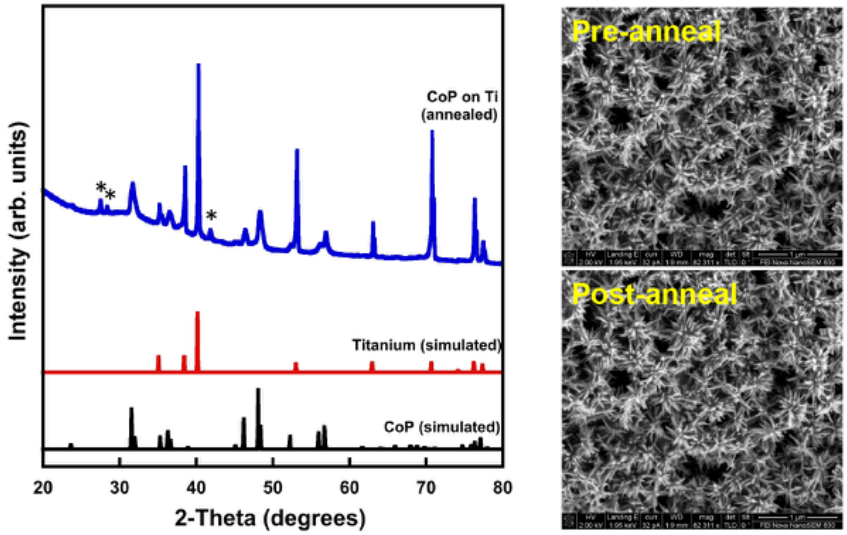

Figure F.2: (Left) Powder X-ray diffraction data for a sample of highly branched CoP nanostructures deposited onto Ti foil then annealed at 450 °C under H_2 (5 %)/Ar(95 %) for 30 min. Simulated XRD patterns for Ti and CoP are shown for comparison. The asterisks indicate a small Co_2P impurity that was observed after annealing. (Right) SEM images of the same sample prior to and after annealing. We did not observe any crystallographic relationships between the interior cores and the branches. It is also difficult to capture the relevant early stages of the reactions that produce the branched CoP nanostructures because of the high temperatures involved.

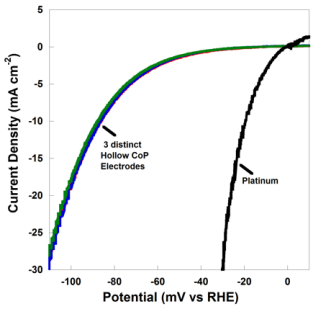

Figure F.3: Three distinct linear sweep voltammograms for hollow, pseudospherical CoP nanoparticles deposited on Ti foil at a loading density of $\approx 0.8\,\mathrm{mg/cm^2}$ in 0.5 M H_2SO_4. The electrodes consistently required an overpotential of -100 mV to produce a current density of $-10\,\mathrm{mA/cm^2}$. This value is lower than the overpotential of -117 mV required for the branched CoP nanostructures.

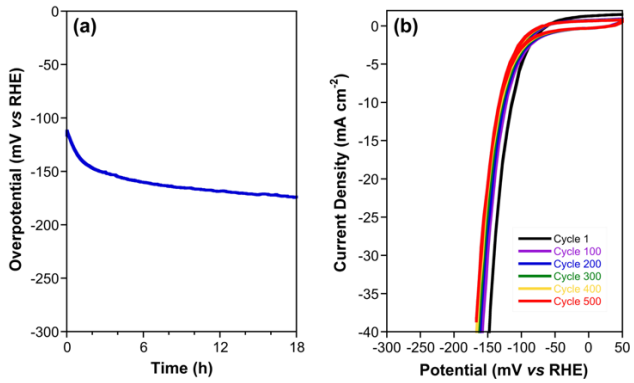

Figure F.4: (a) Plot of overpotential vs. time, held at $-10\,\mathrm{mA/cm^2}$ for 18 h, for a Ti foil electrode containing the highly branched CoP nanostructures. (b) Cyclic voltammetric cycles used to simulate the long-term stability of a comparable CoP/Ti electrode in 0.50 M H_2SO_4 when cycled between 50 mV and -160 mV at a scan rate of $100\,\mathrm{mV\,s^{-1}}$.

F.3 References

(1) J. R. McKone, B. F. Sadtler, C. A. Werlang, N. S. Lewis and H. B. Gray, *ACS Catal.*, Feb. 2013, **3**, 166–169.

(2) E. J. Popczun, J. R. McKone, C. G. Read, A. J. Biacchi, A. M. Wiltrout, N. S. Lewis and R. E. Schaak, *J. Am. Chem. Soc.*, June 2013, **135**, 9267–9270.

(3) E. J. Popczun, C. G. Read, C. W. Roske, N. S. Lewis and R. E. Schaak, *Angew. Chem. Int. Ed.*, Apr. 2014, **53**, 5427–5430.

Appendix G

Use of Mixed CH_3- /$HC(O)CH_2CH_2-$Si(111) Functionality to Control Interfacial Chemical and Electronic Properties During the Atomic Layer Deposition of Ultrathin Oxides on Si(111)

Reprinted with permission from L.E. O'Leary; N.C. Strandwitz; C.W. Roske; S. Pyo; B.S. Brunschwig; N.S. Lewis. *J. Phys. Chem. Lett.*, **2015**, *6*, 722-726.. Cpyright 2014 American Chemical Society.

G.1 Abstract

Silicon surfaces terminated with a mixed monolayer containing both a propyl aldehyde functionality and methyl groups were prepared and used to control the interfacial chemical and electronic properties of Si(111) surfaces during atomic layer deposition (ALD) of Al_2O_3 or MnO. Si(111) surfaces functionalized only with the aldehyde moiety exhibited surface recombination velocities, S, of $2500 \pm 600\ cm\ s^{-1}$ whereas the mixed CH_3-/$HC(O)CH_2CH_2-$Si(111) surfaces displayed $S = 25 \pm 7 cm\ s^{-1}$. During the ALD growth of either Al_2O_3 or MnO, both the $HC(O)CH_2CH_2-$Si(111) and CH_3-/$HC(O)CH_2CH_2-$Si(111) surfaces produced increased metal oxide deposition at low cycle number, relative to H–Si(111) or CH_3-Si(111) surfaces. As detected by X-ray photoelectron spectroscopy after the ALD process, the CH_3- and mixed CH_3-/$HC(O)CH_2CH_2-$ functionalized Si(111) surfaces exhibited less interfacial SiO_x than was observed for ALD of metal oxides on H–Si(111) substrates.

G.2 Introduction

Atomic-layer deposition (ALD) is of interest as a conformal, scalable method for the deposition of ultrathin oxides on semiconductor surfaces.[1–3] For example, ALD has been used to deposit Al_2O_3, ZrO_2, and HfO_2 for high-permittivity gates on Si,[4–6] and is of interest for high-permittivity memory capacitor dielectrics, ferroelectrics, and deposition of metals and nitrides for electrodes and interconnects.[7–9] Very thin, conformal metal oxide films grown by ALD have produced increased stability of Si photoanodes during water oxidation,10 and relatively thick ($\approx$100 nm) films of conductive TiO2 deposited by ALD recently have been shown to stabilize Si, GaAs, and GaP photoanodes for the oxidation of water at pH 14.[10]

ALD precursors are generally transition-metal alkoxides or organometallics that yield initiation and control of film growth by undergoing self-limiting reactions with reactive surface groups. The functionality on the semiconductor surface is thus critical to achieving control over the uniformity of film deposition, the minimization of induction periods, and to provide control over the chemical and electrical properties of the resulting semiconductor/ALD-oxide interfaces.[3,9,11–14] In the case of Si, reaction with the metal precursor oxidizes the hydrogen-terminated Si surface obtained by etching, and is critical to the subsequent growth of the metal oxide layer.[15] Although functionalization of the Si surface via hydrosilylation has been previously demonstrated as a route for initiation of the ALD process that beneficially decreases the amount of silicon oxide (SiO_x) formed during the growth process,[16] hydrosilylation leaves electronically defective interfaces on Si surfaces, and requires functionalization with long-chain alkanes ($> C_{10}$) to produce ordered monolayers.[17] We demonstrate herein that aldehyde groups can be introduced to Si surfaces via a chlorination-alkylation reaction sequence designed to terminate all of the Si surface atoms with Si – C bonds. This approach allows the introduction of ALD-initiating functional groups onto the Si surface while maintaining molecular-level control over the chemical and electronic properties of the silicon/ALD-oxide interface.

G.3 Materials and Methods

Films of Al_2O_3 or MnO were grown by ALD through sequential exposure of Si(111) surfaces to trimethyl aluminum (TMA) or bis(ethylcyclopentadienyl)manganese(II) ($(EtCp)_2Mn$)[14] and water, at 80 °C or 150 °C respectively. The Si(111) samples used for ALD growth were terminated either by: a) H – Si, from etching the Si(111) in NH_4F(aq); b) CH_3 – Si, prepared by a two-step chlorination/alkylation process;[13,18] c) a propyl aldehyde ($HC(O)CH_2CH_2-$) functionality; d) a mixed monolayer consisting of the propyl aldehyde functionality with methyl groups "back-filling" the remaining reactive Si surface sites of a $HC(O)CH_2CH_2$ – Si functionalized surface; or e) etching the Si surface with a "piranha etch" (3:1 H_2SO_4:H_2O_2(aq) v/v) after an NH_4F(aq) etch produced terraces on the Si surface. The aldehyde functionality was obtained by functionalization of Cl – Si(111) with (1,3-dioxan-2-ylethyl)magnesium bromide, with subsequent deprotection of the aldehyde with dilute HCl producing the desired $HC(O)CH_2CH_2$ – Si(111) surface. The mixed CH_3 –/$HC(O)CH_2CH_2$ – Si(111) surface was synthesized by reacting the Cl – Si(111) surface with (1,3-dioxan-2-ylethyl)magnesium bromide, followed by exposure to CH_3MgCl prior to deprotection of the aldehyde with dilute HCl(aq)

(Figure G.1).

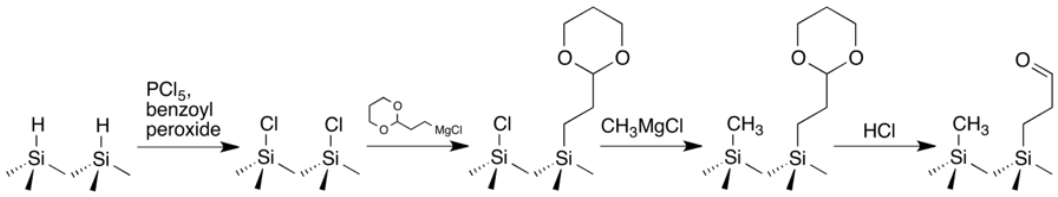

Figure G.1: Synthesis of mixed CH_3-/$HC(O)CH_2CH_2-$Si(111) surfaces through use of a protected aldehyde.

G.4 Results and Discussion

Figure G.2 shows the Al 2p and Si 2p regions of the X-ray photoelectron (XP) spectra obtained after 5 deposition cycles of TMA/H_2O onto these various functionalized Si(111) surfaces at 80 °C. The $HC(O)CH_2CH_2-$Si(111) and mixed CH_3-/$HC(O)CH_2CH_2-$Si(111) surfaces clearly showed greater film growth than the CH_3-Si(111) or H–Si(111) surfaces (Figure G.2A, Table G.4). In addition, the CH_3-Si(111) and mixed CH_3-/$HC(O)CH_2CH_2-$Si(111) surfaces showed small amounts of SiO_x at 102.5 eV (Figure G.2b), whereas significant SiO_x was observed for the H – terminated Si(111) surface. The position of the Si 2p peak was different for surfaces modified with different functional groups due to effects of band banding and dipoles at the surface.[19] Table G.4 presents the estimated coverages of the Al_2O_3 and SiO_x calculated by application of the XPS data to the substrate overlay model.

Surface	0-cycles	5 cycle			20 cycle		
	S $(cm\,s^{-1})^1$	S $(cm\,s^{-1})^1$	Al_2O_3 (ML)	SiO_x (ML)	S $(cm\,s^{-1})^1$	Al_2O_3 (ML)	SiO_x (ML)
H	39	510	0.1 ± 0.1	1.2 ± 0.3	2400	11.5 ± 6.1	1.5 ± 0.3
CH_3	17	19	0.5 ± 0.3	0.1 ± 0.1	160	4.7 ± 2.4	0.1 ± 0.1
CH_3 /$HC(O)CH_2CH_2$	25	73	1.8 ± 0.9	0.4 ± 0.1	27	9.0 ± 4.3	0.5 ± 0.2
$HC(O)CH_2$ CH_2	2500	1700	0.7 ± 0.4	1.3 ± 0.3	2600	16.4 ± 7.8	1.0 ± 0.2
SiO_x	4000	46	3.7 ± 1.7	4.0 ± 0.2	140	19.4 ± 9.1	3.8 ± 0.2

Table G.1: Surface recombination velocity and $Al_2\,O_3$ and SiO_x surface coverage by surface functionality and ALD cycle number.[1] indicates measured in air.

Analogous behavior was observed on these four types of Si(111) surfaces for deposition of MnO. Specifically, the CH_3-/$HC(O)CH_2CH_2-$Si(111) surface showed greater MnO deposition than the H–terminated surface (Figure G.3a), but approximately half of the MnO deposition of the piranha-cleaned surface. The mixed CH_3-/$HC(O)CH_2CH_2-$Si(111) surface contained little interfacial SiO_2, even after

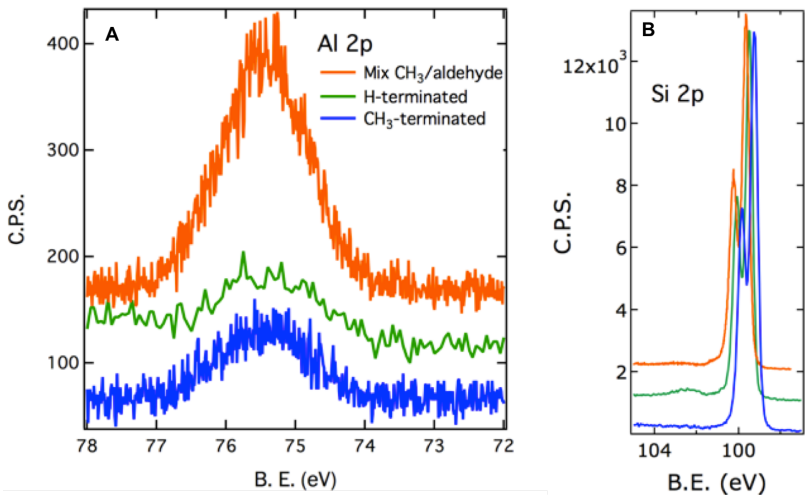

Figure G.2: X-ray photoelectron spectra of CH_3- (blue), H – (green), and $CH_3-/HC(O)CH_2CH_2-Si(111)$ (orange) surfaces after 5 cycles of TMA/H_2O deposition. (A) Al 2p spectral region (offset for clarity). The H^- terminated spectrum was taken at a different scan step size. All other factors are equal, so the comparison of counts per second is valid. (B) Si 2p spectral region (offset for clarity) showing the development of SiOx ($\approx$ 102.5 eV) after 5 cycles of TMA/H_2O deposition on H–Si(111) surfaces.

ALD, as detected by XPS (Figure G.3b). By this method, an abrupt Si/M_xO_y interface was formed, whereas ALD at H–terminated Si or piranha-etched Si results in a Si/SiO_x/M_xO_y interface.

The electrical properties of the metal oxide-coated functionalized surfaces were probed by measurement of the lifetime of photogenerated charge carriers under conditions for which the carrier lifetime was dominated by interfacial rather than bulk recombination. In this process, a high-carrier-lifetime, float-zone grown, double-side polished Si(111) sample (4 kΩ to 8 kΩ) was exposed simultaneously on both sides to all of the wet chemical functionalization and ALD process steps. Time-resolved microwave conductivity methods, described elsewhere,[20,21] were then used to probe the minority-carrier lifetimes of the various samples. The minority-carrier lifetime was related to the surface recombination velocity, S, using conventional relationships.[22] H–Si(111) surfaces have extremely low S values, $< 10 \times 10^{-2}$ cm s^{-1}, when measured in a stabilizing environment such as H_2SO_4,[20] but these values increase substantially upon even brief exposure to air, due to the formation of undesirable Si oxides. In contrast to H–Si(111) surfaces, the CH_3-Si(111) surface retains a low S value for over a month of air exposure, due to essentially

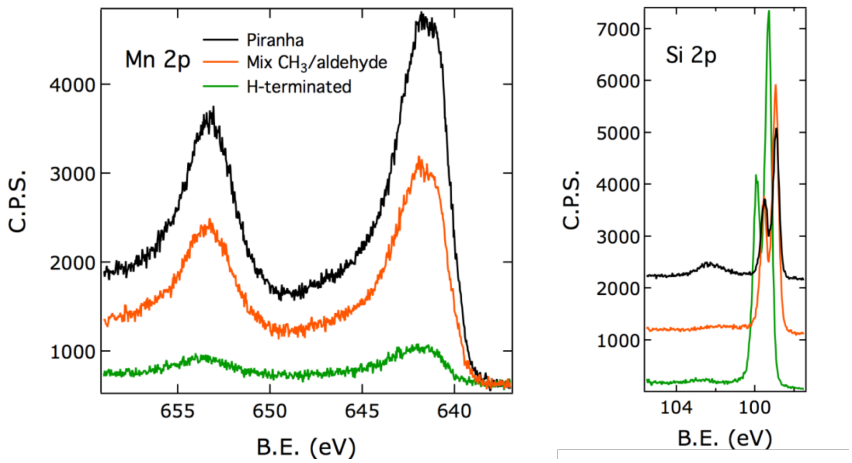

Figure G.3: X-ray photoelectron spectra of H– (green), CH_3–/HC(O)CH_2CH_2–Si(111) (orange), and piranha-etched (black) surfaces after 5 cycles of $(EtCp)_2Mn/H_2O$ deposition. (A) Mn 2p spectral region. (B) Si 2p spectral region showing SiO_x development ($\approx$ 102.5 eV) on H–Si(111) and piranha-etched Si(111) surfaces.

complete termination of Si atop sites by unreactive Si–C bonds. Although pristine H–Si(111) surfaces have very low electronic defect densities, after 1 cycle of TMA/H_2O exposure, the photogenerated carrier lifetime decreased significantly. The HC(O)CH_2CH_2–Si(111) surface exhibited a rapid photogenerated carrier decay, and consequently high S value ($2500 \pm 600 \text{cm s}^{-1}$) as synthesized and at the low ALD cycle numbers investigated herein (Figure G.4). In contrast, the as-synthesized, mixed CH_3–/HC(O)CH_2CH_2–Si(111) surface, had a low S value of $25 \pm 7 \text{cm s}^{-1}$, similar to that of the CH_3–Si(111) surface, in accord with previous reports of mixed monolayer functionalized Si(111) surfaces.[18,22] After 5 cycles of TMA/H_2O deposition, the CH_3– and mixed CH_3–/HC(O)CH_2CH_2–Si(111) surfaces showed little change in their photogenerated carrier decay profiles (Figure G.4b). Previous work has shown that ALD initiation at H–Si(111) proceeds via Si–M formation,[15] which is consistent with the development of electronic defects at the interface, as observed herein on surfaces that were not extensively terminated with Si–C bonding.

Figure G.5 shows the progression of the Al 2p:Si 2p XP intensity ratio and S with the number of TMA/H_2O ALD cycles. Up to $\approx$ 5 cycles, the Al 2p:Si 2p ratio correlated with the presumed density of reactive surface sites, in the order H– $\approx$ CH_3– < mixed CH_3–/HC(O)CH_2CH_2– < HC(O)CH_2CH_2– < piranha cleaned (Figure G.5a). After 5 exposure cycles, deposition at the H–terminated surface increased significantly (with increased variance), therefore exhibiting behavior sim-

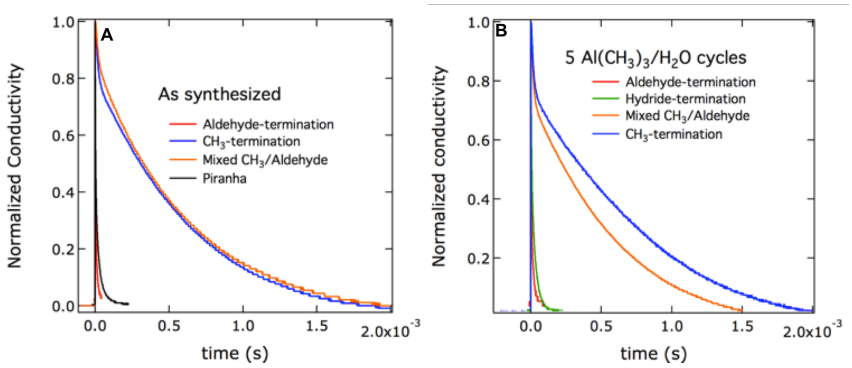

Figure G.4: Photogenerated carrier-decay profiles measured by time-resolved microwave conductivity for H – terminated, piranha-cleaned, and chemically functionalized Si(111) surfaces (A) as synthesized (B) and after 5 cycles of TMA/H_2O deposition. The CH_3 – Si(111) and mixed CH_3 –/HC(O)CH_2CH_2 – Si(111) surfaces retained long carrier lifetimes after the ALD cycles.

ilar to what has previously been described as an "initiation period" due to poor ALD nucleation.[3,13,23–25] As shown in Figure G.5b, the HC(O)CH_2CH_2 – Si(111) surface exhibited a high *S* value even at 20 ALD cycle numbers. For the H-terminated surface, S increased substantially with the first ALD cycle, and then slowly increased as cycle number increased. The behavior is consistent with literature reports of deposition initiation via Si – M formation.[15] The CH_3 – and mixed CH_3 –/HC(O)CH_2CH_2 – Si(111) surfaces, however, exhibited low *S* values at all ALD cycle numbers tested. Interestingly, the piranha-cleaned Si(111) surface showed a decrease in *S* after deposition of Al_2O_3, which may be due to fixed charge generation and consequent development of a surface field, rather than 'repair' of the electronic defects present at the Si/SiO_x interface. However, the thickness of the oxide left after piranha cleaning adds to the overall oxide thickness and to the electrical resistance across the Si interface.

Figure G.6 shows the topography of the Al_2O_3 films formed after 20 TMA/H_2O cycles on the CH_3 – Si(111), CH_3 –/HC(O)CH_2CH_2 – Si(111), HC(O)CH_2CH_2 – Si(111), and piranha cleaned-Si(111) surfaces, respectively. Both the additional Al or Mn in the XP spectra of the Si surfaces, as well as the smoothness of the resulting ALD films, attest to the improved deposition efficiency for the aldehyde-terminated Si(111) surfaces relative to that of the CH_3 – Si(111) or H – Si(111) surfaces. Due to the chemical inertness of the CH_3 – groups, ALD likely initiates at structural defects on the surface and progresses as "island growth" in an inhomogeneous process that leads to the loss of the atomic flatness that is characteristic of the CH_3 – Si(111)

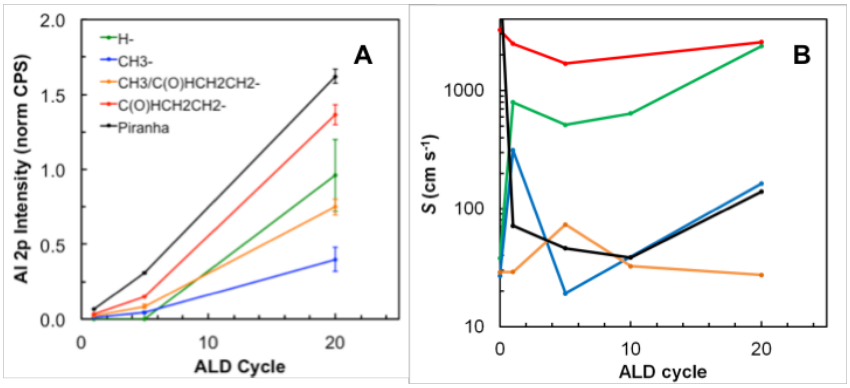

Figure G.5: (A) Al 2p:Si 2p counts per second ratio versus ALD cycle number, indicating a higher deposition efficiency at low cycle number for surfaces with a high density of initiation points (–OH groups at piranha-cleaned surfaces and aldehyde groups at $HC(O)CH_2CH_2-Si(111)$ surfaces). Slow growth was observed at unreactive and stable $CH_3-Si(111)$ surfaces, whereas delayed initiation was observed at $H-Si(111)$ surfaces. (B) High S values were observed at $HC(O)CH_2CH_2-Si(111)$ surfaces, independent of ALD cycle number. Increasing S values were observed with increasing ALD cycle numbers for $H-Si(111)$ surfaces, indicating the formation of electronic defect states as the film growth proceeded.

surface.[26] Initiation is likely to occur more homogeneously at aldehyde-terminated and SiO_x surfaces, which have high densities of surface bound $-OH$ or $-C(O)H$ groups, and therefore produces smooth Al_2O_3 films even at low cycle numbers.

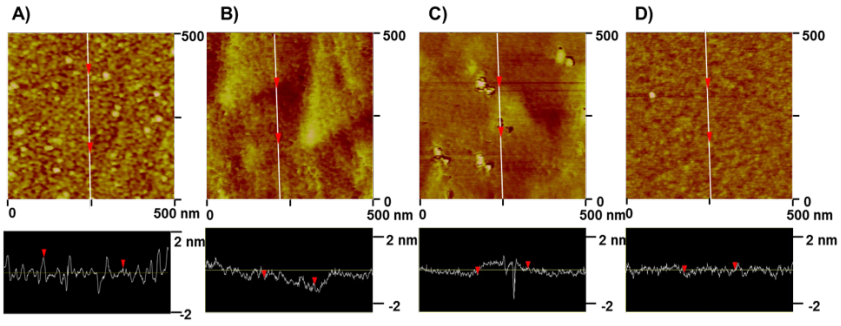

Figure G.6: Tapping-mode AFM images of (A) $CH_3-Si(111)$ (rms roughness = 0.320 nm), (B) mixed $CH_3-/HC(O)CH_2CH_2-Si(111)$ (0.259 nm), (C) $HC(O)CH_2CH_2-Si(111)$ (0.360 nm), and (D) piranha-cleaned SiO_x on Si(111) (0.171 nm) surfaces after ALD 20 cycles of TMA/H_2O exposure. All topographs (Digital Instruments Multi-Mode AFM-2 with a Nanoscope IIIa controller) are 500×500 nm, and the height profile follows the line depicted in the corresponding image. Height scales are 4 nm.

G.5 Conclusion

In summary, mixed monolayer formation and functionalization with a protected aldehyde allowed for the synthesis of a low electronic defect-density, high functionality aldehyde-terminated Si(111) surface. Low surface recombination velocities (41 ± 18 cm s^{-1} for 1-20 cycles) were observed at very low ALD cycle numbers and without subsequent thermal treatment, which is in contrast to reports of surface passivation by the introduction of fixed negative interfacial charge within Al_2O_3 ALD films.[27] No additional thermal annealing step or ozone addition during ALD was required to produce the observed low surface recombination velocities. The ALD growth of Al_2O_3 or MnO proceeded with higher efficacy on the aldehyde-functionalized Si(111) surface than on the low S $CH_3-Si(111)$ surface, with lower interfacial recombination velocities and controlled interfacial chemistry obtained from the aldehyde-terminated surfaces. Furthermore, the resulting Si/M_xO_y interfaces were abrupt and free of detectable interfacial SiO_x. As such, these chemically modified Si surfaces have allowed for molecular level control over the film uniformity as well as for beneficial control over the interfacial chemical and electronic properties of ALD-deposited oxides on Si surfaces.

G.6 Acknowledgements

This work was supported by the National Science Foundation (CHE-1214152) and the Molecular Materials Research Center of the Beckman Institute at the California Institute of Technology. This work was additionally supported by BP and the Gordon and Betty Moore Foundation. The Link Foundation Energy fellowship (L. E. O.), the NSF ACC-F (CHE-1042006, N. C. S.), and the NSF-GRFP (C. W. R.) are gratefully acknowledged for graduate and postdoctoral fellowship support. The authors thank Judith Lattimer for assistance with XPS data, and Ron Grimm for H-terminated silicon data.

G.7 References

(1) S. M. George, O. Sneh, A. C. Dillon, M. L. Wise, A. W. Ott, L. A. Okada and J. D. Way, *Appl. Surf. Sci.*, 1994, **82-83**, 460–467.

(2) M. Leskelä and M. Ritala, *Thin Solid Films*, 2002, **409**, 138–146.

(3) S. M. George, *Chem. Rev.*, 2010, **110**, 111–131.

(4) H. R. Huff, A. Hou, C. Lim, Y. Kim, J. Barnett, G. Bersuker, G. A. Brown, C. D. Young, P. M. Zeitzoff, J. Gutt, P. Lysaght, M. I. Gardner and R. W. Murto, *Microelectron. Eng.*, 2003, **69**, 152–167.

(5) L. F. Edge, D. G. Schlom, R. T. Brewer, Y. J. Chabal, J. R. Williams, S. A. Chambers, C. Hinkle, G. Lucovsky, Y. Yang, S. Stemmer, M. Copel, B. Holländer and J. Schubert, *Appl. Phys. Lett.*, 2004, **84**, 4629.

(6) R. Chen, H. Kim, P. C. McIntyre and S. F. Bent, *Chem. Mater.*, 2005, **17**, 536–544.

(7) D.-G. Park, K.-Y. Lim, H.-J. Cho, T.-H. Cha, I.-S. Yeo, J.-S. Roh and J. W. Park, *Appl. Phys. Lett.*, 2002, **80**, 2514.

(8) O. Sneh, R. B. Clark-Phelps, A. R. Londergan, J. Winkler and T. E. Seidel, *Thin Solid Films*, 2002, **402**, 248–261.

(9) O. Seitz, M. Dai, F. S. Aguirre-Tostado, R. M. Wallace and Y. J. Chabal, *J. Am. Chem. Soc.*, 2009, **131**, 18159–18167.

(10) S. Hu, M. R. Shaner, J. A. Beardslee, M. Lichterman, B. S. Brunschwig and N. S. Lewis, *Science*, 2014, **344**, 1005–1009.

(11) M. Li, M. Dai and Y. J. Chabal, *Langmuir*, 2009, **25**, 1911–1914.

(12) B. Seger, A. B. Laursen, P. C. K. Vesborg, T. Pedersen, O. Hansen, S. Dahl and I. Chorkendorff, *Angew. Chem. Int. Ed.*, 2012, **51**, 9128–9131.

(13) D. Dusciac, V. Brizé, J.-N. Chazalviel, Y.-F. Lai, H. Roussel, S. Blonkowski, R. Schafranek, A. Klein, C. Henry de Villeneuve, P. Allongue, F. Ozanam and C. Dubourdieu, *Chem. Mater.*, 2012, **24**, 3135–3142.

(14) K. J. Hughes and J. R. Engstrom, *Journal of Vacuum Science and Technology A: Vacuum, Surfaces, and Films*, 2010, **28**, 1033.

(15) M. M. Frank, Y. J. Chabal and G. D. Wilk, *Appl. Phys. Lett.*, 2003, **82**, 4758.

(16) W. Peng, W. J. I. DeBenedetti, S. Kim, M. A. Hines and Y. J. Chabal, *Appl. Phys. Lett.*, 2014, **104**, 241601.

(17) L. J. Webb and N. S. Lewis, *The Journal of Physical Chemistry B*, 2003, **107**, 5404–5412.

(18) A. Bansal, X. Li, I. Lauermann, N. S. Lewis, S. I. Yi and W. H. Weinberg, *J. Am. Chem. Soc.*, 1996, **118**, 7225–7226.

(19) D. C. Gleason-Rohrer, B. S. Brunschwig and N. S. Lewis, *J. Phys. Chem. C*, 2013, **117**, 18031–18042.

(20) W. J. Royea, A. Juang and N. S. Lewis, *Appl. Phys. Lett.*, 2000, **77**, 1988.

(21) K. E. Plass, X. Liu, B. S. Brunschwig and N. S. Lewis, *Chem. Mater.*, 2008, **20**, 2228–2233.

(22) L. E. O'Leary, E. Johansson, B. S. Brunschwig and N. S. Lewis, *The Journal of Physical Chemistry B*, 2010, **114**, 14298–14302.

(23) J. W. Klaus, *Science*, 1997, **278**, 1934–1936.

(24) M. M. Frank, Y. J. Chabal, M. L. Green, A. Delabie, B. Brijs, G. D. Wilk, M.-Y. Ho, E. B. O. da Rosa, I. J. R. Baumvol and F. C. Stedile, *Appl. Phys. Lett.*, 2003, **83**, 740.

(25) M. T. Ho, Y. Wang, R. T. Brewer, L. S. Wielunski, Y. J. Chabal, N. Moumen and M. Boleslawski, *Appl. Phys. Lett.*, 2005, **87**, 133103.

(26) H. Yu, L. J. Webb, R. S. Ries, S. D. Solares, W. A. Goddard, J. R. Heath and N. S. Lewis, *The Journal of Physical Chemistry B*, 2005, **109**, 671–674.

(27) N. M. Terlinden, G. Dingemans, M. C. M. van de Sanden and W. M. M. Kessels, *Appl. Phys. Lett.*, 2010, **96**, 112101.

Appendix H

Supplementary Information for Use of Mixed CH_3 – /$HC(O)CH_2$ CH_2 – Si(111) Functionality to Control Interfacial Chemical and Electronic Properties During the Atomic Layer Deposition of Ultrathin Oxides on Si(111)

Reprinted with permission from L.E. O'Leary; N.C. Strandwitz; C.W. Roske; S. Pyo; B.S. Brunschwig; N.S. Lewis. *J. Phys. Chem. Lett.*, **2015**, *6*, 722-726.. Cpyright 2014 American Chemical Society.

H.1 Calculation of Surface Coverage from X-ray Photoelectron Spectra

The average oxide thickness was measured using quantitative XPS and AFM was not used for thickness measurements. The oxide coverage on the Si surfaces was calculated according to published methods using the following equations:[1]

$$\Phi_A = Q_{AB}\frac{I_A/I_A^{inf}}{I_B/I_B^{inf}}$$

$$Q_{AB}^X = \left[\frac{\lambda_A E_A \cos\theta}{a_A}\right],$$

where Φ_A is the fractional coverage of monolayer A over the substrate B. Q_{AB}^X is the monolayer matrix factor for XPS. I_A^{inf}/I_B^{inf} is an intensity ratio. λ_A is the inelastic mean free path in nm (IMFP). θ is the electron take-off angle from surface-normal. a_M is derive from $1000\rho N a_M^3 = A_M$ where, in turn, ρ is the density (in kilograms per cubic meter), N is Avogadro's Number and A_m is the mean atomic weight.

The full form of the equation is:

$$\Phi_A = \left[\frac{\lambda_A \cos\theta}{\sqrt[3]{\frac{A_A}{1000\rho N}}}\right]\left(\frac{I_B^{inf}}{I_A{}^{inf}}\right)\left(\frac{I_A}{I_B}\right).$$

λ_A can theoretically be obtained from multiple-angle XPS experiments. Elastic scattering effects are presumed negligible, so this is taken to be equal to the inelastic mean-free path. We know that this expression is incomplete because λ_{SiO_2} and $\lambda_{Al_2O_3}$ are not necessarily equal, however, we used $\lambda = 2.1$ nm following a published

procedure.[2]

On the Kratos we measured $(\frac{I^0_{Si}}{I_{SiO_2}}) = 1.3$ and $(\frac{I^0_{Si}}{I_{Al_2O_3}}) = 2.0$.

For aluminum oxide:

$$\sqrt[3]{\frac{A_A}{1000\rho N}} = \frac{101.9\,\mathrm{g\,mol^{-1}}}{(\frac{1000\,\mathrm{g}}{1\,\mathrm{kg}}) \times 6.023 \times 10^{23}\mathrm{mol^{-1}} \times 3950\frac{\mathrm{kg}}{\mathrm{m^3}}(\frac{1\,\mathrm{m}}{10\times10^9\,\mathrm{nm}})^3} = 3.5\,\mathrm{nm}.$$

On the Kratos $\theta = 0°$, $\cos 90 = 1$.

Using standard methods for propagation of errors, assumed errors on the relative sensitivity ratio to be 20 %. For a_A and λ_A the assumed the relative error is 30 %.

H.2 Microwave Conductivity Measurements

The SRV measurement was conducted in air, and the time taken to make the measurement prior to ALD deposition would have allowed for oxidation and a chemical change in the H – terminated Si(111) surface. A measurement of the recombination velocity for H – terminated Si surfaces prior to ALD is included in Table G.4 (0-cycle column).

H.3 Supporting Data

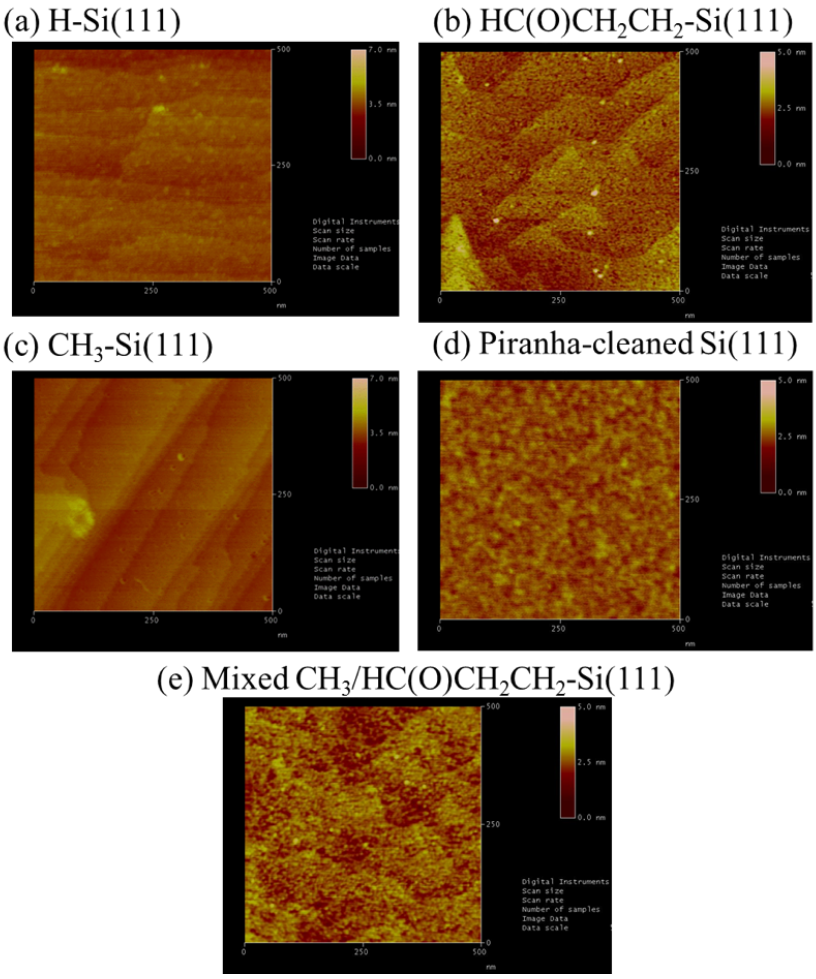

Figure H.1: Atomic-force microscopy images of various surfaces after five cycles of atomic-layer deposition using TMA and H_2O. The starting surfaces were (a) $H-Si(111)$, (b) aldehyde-functionalized Si(111), (c) methyl-functionalized Si(111), (d) piranha cleaned Si(111), and (e) Si(111) modified by a mixed monolayer containing aldehyde and methyl functional groups.

H.4 References

(1) D. C. Gleason-Rohrer, B. S. Brunschwig and N. S. Lewis, *J. Phys. Chem. C*, Sept. 2013, **117**, 18031–18042.

(2) K. J. Kim, J. S. Jang, J.-H. Lee, Y.-J. Jee and C.-S. Jun, *Anal. Chem.*, Oct. 2009, **81**, 8519–8522.

Appendix I

Complex Nanomineral Formation Utilizing Kinetic Control by PLAL

C.W. Roske, J.W. Lefler, A.M. Muller. (Submitted)

I.1 Abstract

We used pulsed-laser ablation in liquids (PLAL) of Cu or Zn foil targets in water or in aqueous Cu or Zn salt solutions. PLAL in neat water generated mixtures of metal and (thermodynamically preferred) metal oxide nanomaterials, whereas the availability of select dissolved anions predictably led to the fabrication of more complex phase-pure nanominerals. PLAL of Cu foil in aqueous $CuCl_2$ solution produced nanoparatacamite, $Cu_2Cl(OH)_3$, whereas nanorouaite, $Cu_2(NO_3)(OH)_3$, was formed in aqueous $Cu(NO_3)_2$ and NH_4OH solution. Likewise, we synthesized simonkolleite, $Zn_5(OH)_8Cl_2 \cdot H_2O$, or layered zinc hydroxide nitrate, $Zn_5(OH)_8(NO_3)_2 \cdot 2\,H_2O$, nanoparticles by PLAL of Zn targets in aqueous ablation liquids with added $ZnCl_2$ and NH_4OH or $Zn(NO_3)_2$, respectively. Bimetallic zincian paratacamite resulted from PLAL of Cu foil in aqueous Cu and Zn chloride solution. Our results show that kinetic control exceeded thermodynamic product formation during nanosecond ultraviolet PLAL.

I.2 Introduction

Pulsed laser ablation in liquids (PLAL) has emerged as an innovative technique for the fabrication of nanomaterials with tailored properties. Henglein and Fojtik pioneered the method when they prepared Au, Ni, and C colloids in the early 1990s .[1] Since then, PLAL has been successfully applied to the controlled generation of numerous metal, alloy, oxide, semiconductor, ceramics, and carbon nanoparticles .[2–4] Specifically, PLAL of Cu targets in water yielded crystalline particles of Cu and/or CuO with diameters ranging from 2 to 100 nm.[5–8] Other phases, such as Cu_2O, were accessible at high pulse energies .[9] Similarly, PLAL of Zn targets in water has been shown to produce crystalline Zn or ZnO particles with diameters ranging from 5 to 100 nm.[10–14] PLAL offers many tunable experimental parameters and is capable of producing nanomaterials with unique electronic and catalytic properties. Very high temperatures, pressures, and atom densities exist in the liquid confined plasma formed from precursors during PLAL, thus permitting exploration

of extreme regions of materials' phase diagrams. Control of nanoparticle size, polydispersity, and composition is achieved by choice of laser pulse energy and the chemical nature of the solid target or liquid medium. Nanoparticle catalysts exhibit maximum surface area and introduce additional benefits through the modulation of electronic properties as a result of quantum confinement. Another advantage of PLAL is the ease of handling and collecting the resulting nanoparticles, as they are suspended in the liquid upon synthesis. Analogous to the creation of geological minerals, the PLAL process involves high temperatures and pressures. Rapid cooling and injection of nanoparticles into the liquid that surrounds the plasma quench kinetic products. In nature, the entire periodic system is the toolkit for material formation.Therefore, natural minerals often have complex compositions. We show here that addition of select anions to the ablation solutions led to the fabrication of more complex phase-pure nanominerals (ergo the kinetic products) compared to PLAL of metals in water, which generated mixtures of metallic and (thermodynamically most stable) metal oxide nanomaterials.

I.3 Experimental Section

Materials and Methods

Pulsed laser ablation in liquids was performed in the Beckman Institute Laser Resource Center at California Institute of Technology, X-ray photoelectron spectroscopy in the Molecular Materials Research Center (Beckman Institute at California Institute of Technology), and energy-dispersive X-ray spectroscopy in the California Institute of Technology GPS Division Analytical Facility. Data analysis and graphing were performed with Igor Pro 6.37 (WaveMetrics). All chemicals were used as received. Deionized water was obtained from a Barnstead Diamond Nanopure system and had a resistivity of $\geq 16\,\mathrm{M\Omega - cm}$.

Syntheses

Nanomaterials were synthesized by PLAL. A 30 mm diameter metal disk was sonicated for 10 min in 10 % aqueous HCl to remove surface oxides and thoroughly washed with water. The clean disk was placed horizontally on a glass flange in a 30 mL glass beaker, which was filled with 10 mL liquid. All glassware was thoroughly cleaned with aqua regia before use. The disk moved between laser pulses, see next section. The metal disks consisted of Cu (0.15 mm thick, A.J. Oster) or Zn (0.25 mm thick, Alfa); all metal sheets had purities of >99.9 %. For preparation of monometallic materials, the liquid was water or aqueous solutions of

3.4 M $CuCl_2 \cdot 2\,H_2O$, 3.4 M $Cu(NO_3)_2 \cdot 3\,H_2O$, 3.3 M $Zn(NO_3)_2 \cdot 6\,H_2O$ (all Sigma-Aldrich), or saturated solutions of $Cu(NO_3)_2 \cdot 3\,H_2O$ or $ZnCl_2$ (EM Science) in 1.0 M aqueous NH_4OH (JT Baker). Cu or Zn foils were used in aqueous Cu or Zn solutions, respectively. Bimetallic nanoparticles were made from Cu foil in an aqueous solution of 2.1 M $CuCl_2 \cdot 2\,H_2O$ and 0.7 M $ZnCl_2$. Each sample was irradiated for 60 min by 150 mJ, 355 nm, 8 ns pulses, which were provided by a frequency-tripled 10 Hz Q-switched Nd:YAG laser (Spectra-Physics Quanta-Ray PRO-Series). The laser beam was focused with a 100 mm focal length plano-convex quartz lens 1.0 mm below the surface of the liquid, at the metal disk. The nanoparticle suspensions were transferred into glass vials after synthesis. Dry materials were obtained by centrifugation and washing with water until the supernatant did no longer show any salt absorption. The nanoparticles were dried under vacuum after washing twice with 3 mL acetone (EMD, OmniSolv(R)).

Characterization

X-ray photoelectron spectroscopy (XPS) data were taken with a Surface Science Instruments M-probe surface spectrometer, using monochromatic Al Kα radiation (1486.6 eV) and a vacuum chamber pressure of $< 5 \times 10^{-9}$ torr. Nanomineral samples were drop-cast from aqueous suspensions on clean Ti foil and dried in ambient air at room temperature. Survey scans were collected to identify the elements present in the materials. Depending on the elemental composition of the nanoparticles, high-resolution spectra were taken in the Cu 2p, Zn 2p, Cl 2s, N 1s, or O 1s regions. Binding energies and peak area quantifications were obtained from GaussianLorentzian peak fits after Shirley background subtraction,[15] using relative sensitivity factors, and were referenced to the C 1s peak arising from adventitious carbon, taken to have a binding energy of 284.8 eV.[16] XPS data analysis was performed with CasaXPS (Version 2.3.16 PR 1.6).

Powder X-ray diffraction (XRD) data were obtained with a Bruker D2 PHASER diffractometer, using monochromatic Cu Kα radiation (1.5418 Å; tube power 30 kV, 10 mA). The instrument resolution was 0.050° in 2θ, and the counting time was 3.0 s per step. Solid samples were mounted with Vaseline (X-Alliance GmbH) on a zero-diffraction silicon plate (MTI Corporation). Background subtraction and XRD pattern matching was performed with the Bruker DIFFRAC.SUITE software. Powder XRD peak assignment was carried out using the International Centre for Diffraction Data (ICDD, 2012) database; powder diffraction file (PDF) numbers are referenced throughout the Results and Discussion section.

Energy-dispersive X-ray spectroscopy (EDX) data were collected to determine the metal ratio in the PLAL-made bimetallic material. We used an Oxford X-Max SDD X-ray Energy Dispersive Spectrometer, which allowed quantitative elemental analysis with a relative accuracy of better than 5 % and detection limit of better than 0.5 %. A working distance of 8 mm was used to maximize X-ray counts, and analysis was performed with the AZtec software package.

Dynamic light scattering (DLS) data were acquired at room temperature with a Brookhaven ZetaPals instrument. Mean values and size distribution widths (σ) were calculated from the measured intensity histograms by the built-in software; they were obtained by averaging five 1 min sweeps and had an estimated relative error of ±4 %. An aqueous solution of 0.27 M cetyltrimethylammonium bromide (CTAB) and 0.1 M sodium chloride was passed through a 0.45 µm Millipore syringe filter three times into a freshly cleaned glass scintillation vial to remove all dust. Nanomaterials were suspended in this solution (5 µg mL^{-1}) and sonicated for 30 min.

I.4 Foil Target Setup

Large amounts of thermal energy are generated during PLAL. Efficient heat dissipation in the liquid is crucial to achieve reproducibility since bubble formation and thermal distortions of the laser beam interfere with the ablation process. Flow cell and magnetic stirring methods have been successfully employed in the synthesis of silver colloids from stationary solid targets at pulse energies below 13 mJ.[2] We previously reported PLAL preparations of transition metal oxide and hydroxide nanoparticles with 355 nm nanosecond pulses with energies ranging from 30 to 210 mJ.[17] The higher pulse energies necessitated moving the metal target. The simplest (oft-used) solution is target powder swirling in magnetically stirred ablation liquid.

We found that the target powder size mattered. Powder particles had to be small enough that gravity did not interfere with individual particles floating in the stirred liquid through the laser focus, which was located just below the liquid surface. Yet particles needed to be large enough that their surface appeared flat with respect to the focal beam waist, so that the main propagation vector of the shock wave was opposite to the incident light direction. A shock wave originating from a convex surface is less powerful than one from a flat surface, thereby leading to less rapid nanoparticle formation. As such, the optimal powder particle size depends on the density of the solid target, the viscosity of the ablation liquid, the stirring velocity,

and the focal beam waist. While some metals can easily be obtained commercially as powders in the desired size range, PLAL nanomaterial synthesis becomes more versatile if widely available metal foils can be used.

Both the foil target and ablation liquid must move at higher pulse energies, which were employed in the syntheses of metal oxide and hydroxide nanomaterials with 355 nm light. When we placed stationary Cu or Zn foil targets with thicknesses of $\geq$ 0.1 mm in magnetically stirred liquids we observed the appearance of holes within minutes after irradiation with focused 90 mJ, 355 nm, 8 ns, 10 Hz repetition rate laser pulses. Therefore, we designed and built a PLAL setup that allowed us to move the target foil within its plane between each laser pulse and to simultaneously agitate the liquid.

Moving the target instead of the laser focus is technologically easier. We placed a metal foil disk on a glass flange in a 30 mL beaker (Figure I.1a), which spun at 50 rpm and simultaneously moved back and forth horizontally; the travel distance was 23 mm so that the convergent vertical laser beam hit only the target and not the beaker walls. Two low-cost electrical motors powered both motions. The glass flange had an outside diameter of 30 mm at the bottom, 20 mm at the top, and its height was 10 mm. The disk was cut from commercially available metal foil such that it just fit horizontally into the beaker. A 4 mm diameter hole in the center of the disk facilitated convection of the liquid above and below the target disk. Two disposable, 4 mm diameter glass balls were placed under the metal foil disk to further agitate the liquid. We note that thin Cu foil (0.05 mm thickness) did not withstand the heat generated during PLAL and crumpled after a few minutes under our conditions. Therefore, we used foil targets of at least 0.1 mm thickness. We found that we succeeded in evenly ablating the metal target with our setup (Figure I.1b).

Our method offers a number of advantages: It is amenable to all target metals that are available as foils of at least 0.1 mm thickness. The glassware is low-cost and commercially available or easily made. All chemicals, including the resulting nanomaterials, come only into contact with thoroughly cleaned glass, preventing inadvertent contaminations. The method's simplicity allows for operation with any laser system of choice, as the target is moved with respect to the laser focus, eliminating the need for a laser scanner. Finally, the compactness of the setup permits its placement in inert gas atmosphere if desired.

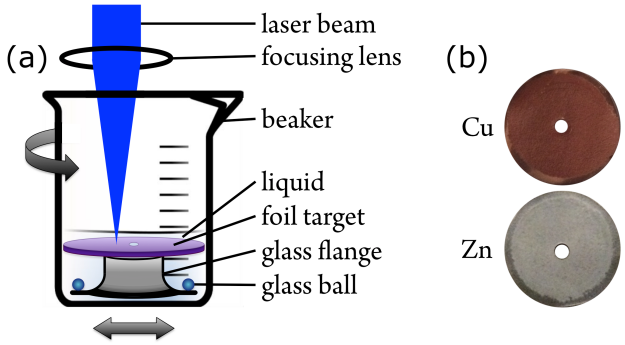

Figure I.1: (a) Schematic of PLAL setup (the arrows indicate motions); (b) Photos of foil targets after PLAL.

I.5 Results and Discussion

In PLAL, the generated plasma consists of chemical elements from the solid and the liquid. Our work on mixed metal hydroxide nanoparticles has shown that the relative proportion of metals in the generated materials was a function of the concentration of the metal ions that were dissolved in the ablation liquid. At high dissolved ion concentrations the metal composition of the resulting nanomaterials was predominantly governed by the ion species. For example, ferrous and ferric oxides were obtained from metallic Ni powder in aqueous $Fe(NO_3)_3$ solutions, whereas PLAL of Fe target powder in 3.0 M aqueous $Ni(NO_3)_2$ solution resulted in $[Ni_0 \cdot 78\, Fe_0 \cdot 22\,]$-layered double hydroxide nanosheets.[18]

We also found that nanomaterial yields were higher when metal ions were present in the ablation liquid, while all other experimental conditions were kept virtually identical. This was also true when the metal target and ion species were comprised of the same element. Syntheses with added metal ions typically yielded about 100 mg per batch, whereas we collected only < 10 mg per batch from PLAL in pure water. Select anions of the dissolved salts were incorporated into the prepared nanoparticles, thus forming more complex nanominerals utilizing kinetic control. Syntheses in neat water yielded simple metals or (thermodynamically preferred) metal (hydr)oxides. For a direct comparison of nanomaterial syntheses by PLAL, we used Cu or Zn foil in pure water or with added Cu or Zn salts, respectively. All materials were prepared at virtually the same physical conditions. We identified crystal phases of the PLAL-made nanomaterials by XRD. The bulk Cu/Zn ratio of the bimetallic material was determined by EDX. Surface compositions were probed by XPS. Note that the interrogation depths of XRD and EDX range from a few to a few hundred micrometers, whereas X-ray photoelectrons escape only

from the top few nanometers of solid surfaces. We also assessed nanoparticle size distributions by DLS. Characterization data in tabular form are available in the Supporting Information. Our approach allowed us to investigate if kinetic control transcended the generation of thermodynamic products. The synthesized nanomaterials are summarized in Table I.1 and described in more detail below.

Foil	Added salt	Obtained material (by XRD)
Cu	None	Cu, CuO
Cu	$CuCl_2 \cdot 2\,H_2O$	$Cu_2Cl(OH)_3$
Cu	$Cu(NO_3)_2 \cdot 3\,H_2O$, NH_4OH	$Cu_2(NO_3)(OH)_3$
Zn	None	Zn, ZnO
Zn	$ZnCl_2$, NH_4OH	$Zn_5(OH)_8 \cdot H_2O$
Zn	$Zn(NO_3)_2 \cdot 6\,H_2O$	$Zn_5(OH)_8(NO_3)_2 \cdot 2\,H_2O$
Cu	$CuCl_2 \cdot H_2O$, $ZnCl_2$	$Cu_3(Cu, Zn)Cl_2(OH)_6$

Table I.1: Nanomaterials synthesized by PLAL of metal foils in water or aqueous solutions.

Copper Materials

We used PLAL to synthesize Cu-containing nanomaterials from Cu foil targets in pure water, or equimolar aqueous solutions of copper chloride or nitrate. Because of its limited solubility in water, we could not use $Cu(OH)_2$ as a dissolved precursor. Depending on the ablation liquid, we obtained different materials.

PLAL of Cu in water generated a mixture of CuO and metallic Cu nanoparticles. Interestingly, we obtained a more complex nanomineral from PLAL of Cu foil in copper chloride solution: $Cu_2Cl(OH)_3$ in the paratacamite phase. In contrast, PLAL of Cu foil in an aqueous solution of copper nitrate and ammonium hydroxide led to the formation of rouaite nanoparticles. PLAL of Cu foil in $Cu(NO_3)_2$ solution without NH_4OH did not yield particles, presumably because a relatively high concentration of hydroxide ions was needed for solid-state material formation. Paratacamite and rouaite are not the thermodynamically most stable phases or compositions of oxidized copper .[19,20] The preparation of $Cu_2Cl(OH)_3$ and $Cu_2(NO_3)(OH)_3$ shows that our PLAL synthesis favored the formation of kinetic products if appropriate anions were present. A reddish-black solid was obtained by PLAL of Cu in water (Figure I.2). XRD data showed two phases consisting of metallic Cu (PDF 01-070-3038) and CuO (PDF 01-078-0428); no other crystal phases were detected. The XP spectra in the Cu 2p region exhibited a doublet with the expected branching ratio of 2:1 and corresponding satellite features. Central binding energies of Cu 2p3/2

peaks were 932.7 and 933.8 eV, consistent with assignment to metallic Cu[21] and divalent Cu – O[22], respectively. Relative peak quantitation revealed that the surface ratio of $Cu^{0/2+}$ was 4.0:1. We observed a single O 1s peak at 530.7 eV, attributable to CuO[23]. The nanoparticles had a monomodal size distribution and a hydrodynamic diameter of (225 ± 40) nm.

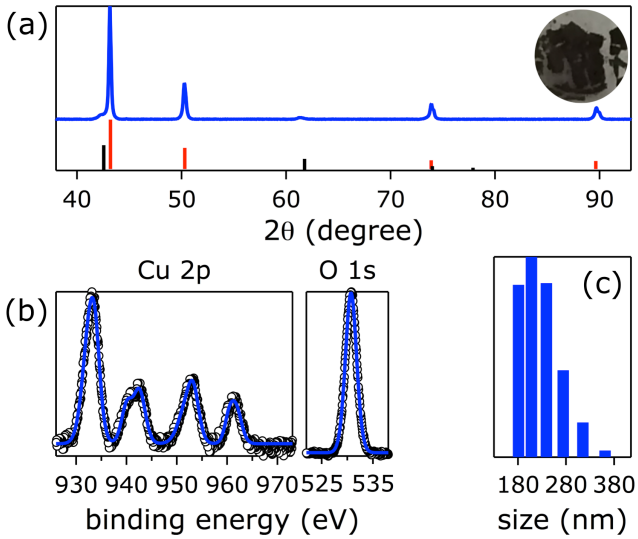

Figure I.2: (a) XRD data (blue), reported fixed-slit intensities of Cu (PDF 01-070-3038, red) and CuO (PDF 01-078-0428, black), inset: photo of the PLAL-made material; (b) XPS data in the Cu 2p and O 1s regions (open circles, data; lines, fits); (c) DLS particle size distribution.

Addition of $CuCl_2$ to the aqueous ablation liquid led to the formation of a green solid (Figure I.3). XRD data confirmed that it consisted of basic copper chloride, $Cu_2Cl(OH)_3$, in the paratacamite phase (PDF 01-070- 0821). The obtained diffraction pattern matched literature data very well [85] and showed no other crystal phases. XPS data in the Cu 2p region exhibited a doublet with a branching ratio of 2:1 and corresponding satellite features. The peaks with central binding energies of 933.4 and 935.4 eV were assigned to CuO and Cu – Cl $2p_{3/2}$ components, in accordance with reported data.[23,24] We detected single Cl 2s and O 1s core level peaks with binding energies of 270.0 and 531.5 eV, which we attributed to Cu – Cl and Cu – OH, respectively.[23] The nanoparticles exhibited a monomodal size distribution and a hydrodynamic diameter of (258 ± 43) nm.

Paratacamite is thermodynamically the most stable polymorph of $Cu_2Cl(OH)_3$.[25] The mineral crystallizes in the rhombohedral space group.[26] It occurs naturally as an oxidation product of other copper minerals under arid, saline conditions.

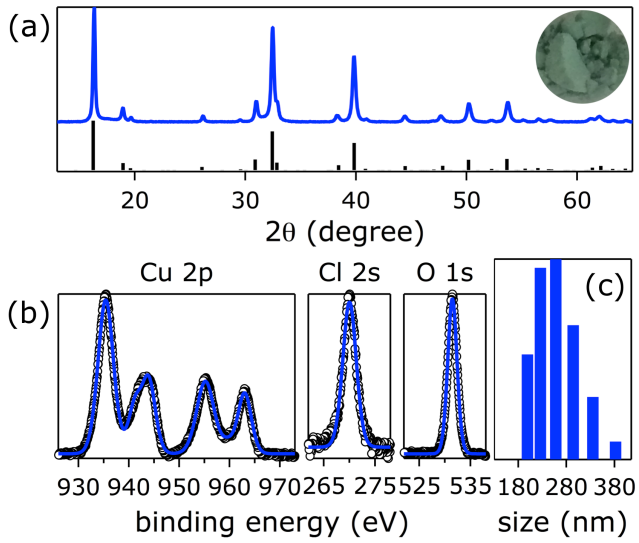

Figure I.3: (a) XRD data (blue), reported fixed-slit intensities of paratacamite (PDF 01-070-0821, black), inset: photo of the PLAL-made material; (b) XPS data in the Cu 2p, Cl 2s, and O 1s regions (open circles, data; lines, fits); (c) DLS particle size distribution.

Paratacamite is well studied in the context of archaeological objects and art, since it is a corrosion product of Cu-containing alloys; it is often called "bronze-disease".[27,28] We collected a green solid upon PLAL of Cu foil in an aqueous solution of $Cu(NO_3)_2$ and NH_4OH (Figure I.4). We deliberately chose NH_4OH as the hydroxide source, as to not introduce additional chemical elements to the ablation liquid. We identified the material as rouaite, $Cu_2(NO_3)(OH)_3$, by XRD; no other crystal phases were present. The XPS Cu 2p core level region exhibited a doublet with a branching ratio of 2:1 and corresponding satellite features, indicative of Cu^{2+} species. The peak with a central binding energy of 935.3 eV is consistent with Cu – OH and Cu – NO_3 $2p_{3/2}$ components [84]. We detected an N 1s core level peak with a binding energy of 407.3, which we attribute to Cu – NO_3.[23] A minor contribution of a component with a central binding energy of 403.6 eV was also present, consistent with a metal nitrite.[29] We assigned the two components in the O 1s region with binding energies of 531.5 eV and 532.5 eV to Cu – OH and Cu – NO_3, respectively.[30,31] The nanoparticles exhibited a monomodal size distribution and a hydrodynamic diameter of (156 ± 62) nm.

Rouaite is a rare mineral that was only described in 2001;[32] it was named after its locality of discovery at old Cu mines of Roua, Alpes-Maritimes, south-eastern France.[33] It is the thermodynamically least stable polymorph of $Cu_2(NO_3)(OH)_3$

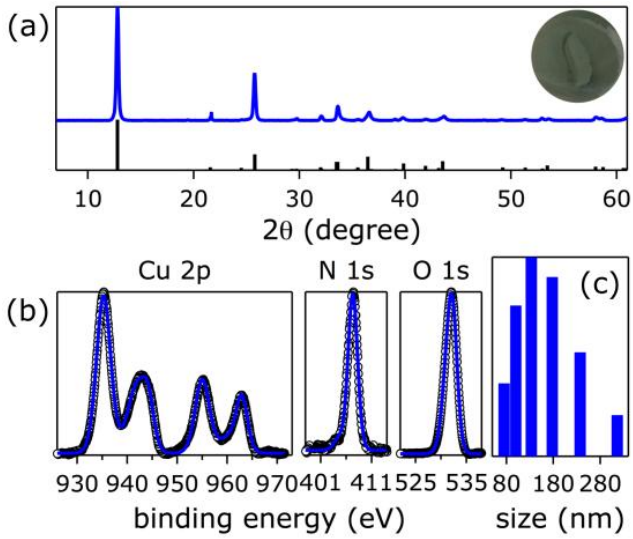

Figure I.4: (a) XRD data (blue), reported fixed-slit intensities of rouaite (PDF 01-075-1779, black), inset: photo of PLAL-made material; (b) XPS data in the Cu 2p, N 1s, and O 1s regions (open circles, data; lines, fits); (c) DLS particle size distribution.

minerals; decomposition to CuO occurs upon heating.[20] Copper hydroxide nitrates are well investigated as artificial patinas to restore archaeological copper and bronze surfaces.[34,35]

Zinc Materials

Analogous to our Cu-based materials, we used PLAL to prepare Zncontaining nanomaterials from Zn foil targets in pure water or in zinc chloride or nitrate aqueous solutions. Addition of $Zn(OH)_2$ as a precursor was not practical as its solubility in water is less than 0.01 g per 100 mL.[36] We obtained different materials from the three ablation liquids. PLAL of Zn in water produced a mixture of wurtzite ZnO and metallic Zn nanoparticles, as evidenced by XRD data (Figure I.5). Again, similar to our Cu materials, we generated more complex, but phase-pure nanominerals from PLAL of Zn foil in Zn salt solutions. We predicted that PLAL of $ZnCl_2$ in basic solution would produce the mineral simonkolleite. For maximum material yield, we prepared a saturated solution of $ZnCl_2$ in 1.0 M aqueous NH_4OH and indeed formed $Zn_5(OH)_8Cl_2 \cdot H_2O$ in the simonkolleite crystal phase. In contrast, the anionic clay $Zn_5(OH)_8(NO_3)_2 \cdot 2\,H_2O$ was the product of PLAL in aqueous $Zn(NO_3)_2$ solution. Both complex minerals exist in nature, but are not the thermodynamically most stable compositions or phases of oxidized Zn under standard conditions.[37–40] As

such, our results further substantiate that kinetic control exceeded thermodynamic product formation during PLAL under our conditions.

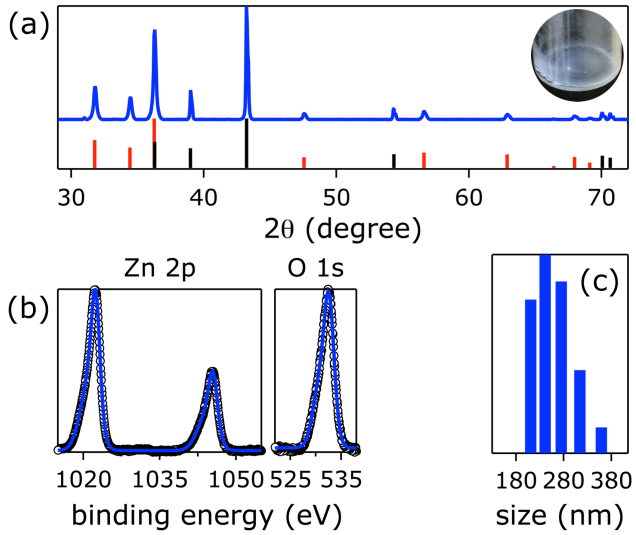

Figure I.5: (a) XRD data (blue), reported fixed-slit intensities of Zn (PDF 00-004-0831, black) and wurtzite ZnO (PDF 01-075-6445, red), inset: photo of PLAL-made material; (b) XPS data in the Zn 2p and O 1s regions (open circles, data; lines, fits); (c) DLS particle size distribution.

The powder diffraction pattern of the material made by PLAL of Zn in water (Figure I.5) was well matched by two crystalline phases, metallic Zn (PDF 00-004-0831) and wurtzite ZnO (zincite, PDF 01-075-6445). The XP spectra in the Zn 2p region confirmed the presence of metallic Zn and ZnO species at the surface (Figure I.5). The Zn 2p core level region consisted of a doublet with an expected branching ratio of 2:1. The Zn 2p3/2 peaks exhibited binding energies of 1021.2 and 1022.4 eV, allowing assignment to metallic Zn and ZnO,[41] with a surface $Zn^{0/2+}$ ratio of 1.1:1. The particles had a monomodal size distribution and a hydrodynamic diameter of (258 ± 40) nm. We obtained a white solid upon addition of $ZnCl_2$ and NH_4OH to the aqueous ablation liquid (Figure I.6). XRD data revealed that the mineral simonkolleite, $Zn_5(OH)_8Cl_2 \cdot H_2O$ (PDF 00-07-0155), was formed, as we had predicted. No other phases were detected. The XPS Zn 2p region showed a doublet with an expected branching ratio of 2:1; the Zn $2p_{3/2}$ component had a binding energy of 1022.8 eV, allowing assignment to Zn|–OH.[41] The O 1s core level peak consisted of two components at 530.5 and 531.9 eV, assignable to ZnO (presumably from surface oxidation) and Zn–OH, respectively.[41] We detected a single Cl 2s core level peak with a binding energy of 271.0 eV, consistent with Zn–Cl [84]. We measured a narrow monomodal size distribution and a hydrodynamic

diameter of (318 ± 14) nm. Simonkolleite is a layered hydroxide salt,[42] which occurs naturally as a weathering product of zinc-bearing slags.[40] It decomposes to ZnO upon heating.[39,43] The mineral has recently attracted interest for hydrogen gas sensing [107], supercapacitor [108], catalyst support [109], and photocatalysis applications [102]. It has also found use as a nutritional feed additive with high bioavailability and antimicrobial activity to supplement zinc in livestock.[44–47]

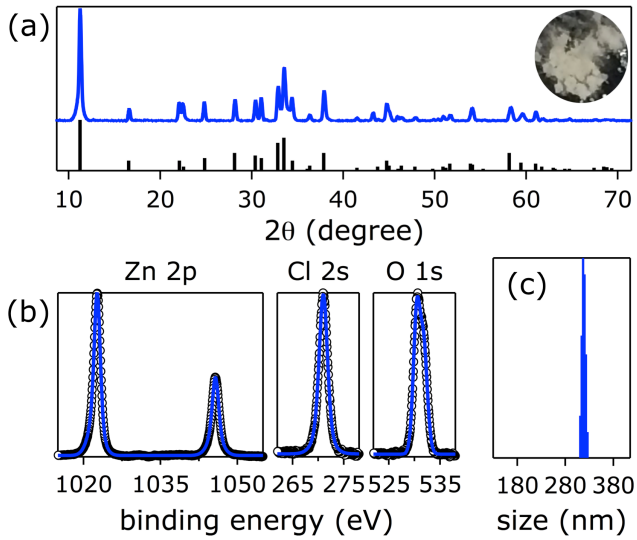

Figure I.6: (a) XRD data (blue), reported fixed-slit intensities of simonkolleite (PDF 00-07-0155, black), inset: photo of PLAL-made material; (b) XPS data in the Zn 2p, Cl 2s, and O 1s regions (open circles, data; lines, fits); (c) DLS particle size distribution.

A white solid formed by PLAL of Zn foil in aqueous $Zn(NO_3)_2$ solution (Figure I.7). XRD data revealed that the material consisted of the layered anionic clay zinc hydroxide nitrate, $Zn_5(OH)_8(NO_3)_2 \cdot 2\,H_2O$ (PDF 01-072- 0627); no other phase was detected. The XRD pattern exhibited a strong reflection at $2\theta = 9.09°$, attributable to the (200) diffraction of monoclinic $Zn_5(NO_3)_2(OH)_8 \cdot 2\,H_2O$.[48] The intensities of the basal $(00l)$ reflections decreased as l increased, which is characteristic for layered structures. Minor contributions from SiO_2 stemming from the silicon substrate were also present.

High-resolution XP spectra in the Zn 2p region showed a doublet with an expected branching ratio of 2:1. We observed two Zn $2p_{3/2}$ components with binding energies of 1021.4 and 1023.7 eV, consistent with Zn – OH in tetrahedral and octahedral coordination, respectively .[49] Monoclinic $Zn_5(OH)_8(NO_3)_2 \cdot 2\,H_2O$ has a hydrotalcite-like structure, which consists of slabs of edge-shared $Zn(OH)_6$ octa-

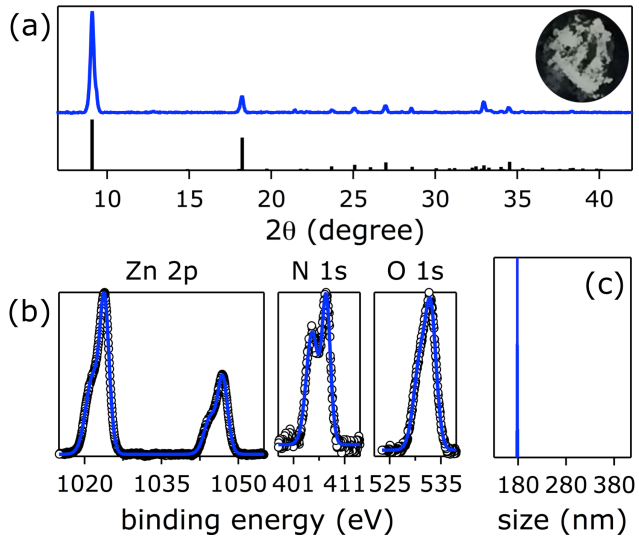

Figure I.7: (a) XRD data (blue), reported fixed-slit intensities of $Zn_5(OH)_8(NO_3)_2 \cdot 2\,H_2O$ (PDF 01-072-0627, black), inset: photo of PLAL-made material; (b) XPS data in the Zn 2p, N 1s, and O 1s regions (open circles, data; lines, fits); (c) DLS particle size distribution.

hedra and $Zn(OH)_4$ tetrahedra that are located above and below the plane of the octahedrally coordinated Zn ions. The bulk ratio of octahedral to tetrahedral sites is 3:2.[50] We detected a surface ratio of 2.9:2. The O 1s region exhibited two peaks with binding energies of 531.8 and 533.0 eV, attributable to $Zn-OH$ and $Zn-NO_3$, respectively.[41] We detected two components in the N 1s core level region, with binding energies of 404.9 and 407.4 eV. We tentatively assigned the lower binding energy peak to N-bound $Zn-NO_2$;[51] the higher binding energy peak is consistent with a transition metal nitrate.[23] We obtained a very narrow monomodal size distribution and a hydrodynamic diameter of (178 ± 0.5) nm. Zinc hydroxide nitrate is a layered anionic clay mineral, and consists of Zn^{2+} containing layers, whose net positive charge, stemming from the incorporation of tetrahedrally coordinated Zn^{2+} ions into the crystal structure of otherwise octahedrally coordinated metal ions, is balanced by intercalated nitrate anions [115].[48] Zinc hydroxide nitrate is an effective heterogeneous catalyst for the esterification of free fatty acids and the transesterification of vegetable oils.[52]

Bimetallic Nanoparticles

Finally, based on the insights we gained in our PLAL syntheses of monometallic materials, we aimed to prepare a mixed-metal nanomineral. We targeted a basic copper-zinc chloride material. Since we had synthesized paratacamite by PLAL of

Cu foil in aqueous $CuCl_2$ solution, we anticipated the formation of a similar mineral upon addition of $ZnCl_2$ to the $CuCl_2$-containing aqueous ablation liquid. A possible candidate was lightly Zn substituted basic copper chloride zincian paratacamite, also called herbertsmithite.

We collected a blue-green solid from PLAL of Cu foil in an aqueous solution of $CuCl_2$ and $ZnCl_2$ in a 3:1 molar ratio (Figure I.8). PLAL of Zn foil in the same ablation liquid was unsuccessful, as the Zn target dissolved during synthesis. XRD data confirmed that we synthesized zincian paratacamite (PDF 00-050-1558), as we had predicted. The material is a naturally occurring mineral with the formula $Cu_3(Cu,Zn)Cl_2(OH)_6$,[53] which forms rhombohedral, blue-green crystals.[54] Zincian paratacamite has recently gained attention for its quantum spin liquid properties due to its kagomé lattice structure.[**PLAL**, 55–57] We note that monometallic and zincian paratacamite crystals exhibit similar powder diffraction patterns, albeit with different reflection intensities. Differences are particularly pronounced in the region of $56° < 2\theta < 58°$ (inset in Figure. 8a). For a fair comparison of reflection intensities, we normalized measured XRD data of our mono- and bimetallic paratacamites to the strongest reflections. Clearly, the nanomaterial we synthesized by PLAL of Cu foil in an aqueous solution of $CuCl_2$ and $ZnCl_2$ was better matched by zincian paratacamite.

As with monometallic paratacamite, we observed in the XP spectra a doublet with a 2:1 branching ratio and corresponding satellite features in the Cu 2p region of XPS data. The Cu $2p_{3/2}$ peak consisted of two components with central binding energies of 933.3 and 935.4 eV, attributable to CuO and Cu – Cl, respectively.[23,24] We could not detect any peaks in the Zn 2p region, indicating a Cu-rich surface. EDX measurements showed that the bulk contained 0.1 atomic % Zn. We detected single Cl 2s and O 1s peaks at 270.1 and 531.6 eV, consistent with Cu – Cl and Cu – OH, respectively.[23] DLS data showed that our PLAL-made lightly doped zincian paratacamite had a monomodal size distribution and a hydrodynamic diameter of (208 ± 35) nm.

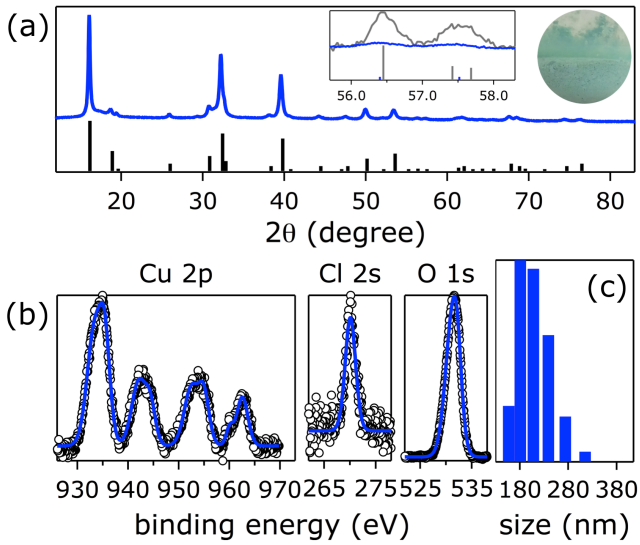

Figure I.8: (a) XRD data (blue), reported fixed-slit intensities of zincian paratacamite (PDF 00-050-1558, black), insets: left, expanded region in which reflections of mono- and bimetallic paratacamites differ most (blue, zincian paratacamite, PDF 00-050-1558; gray, monometallic paratacamite, PDF 01-070-0821); right, photo of the PLALmade material; (b) XPS data in the Cu 2p, Cl 2s, and O 1s regions (open circles, data; lines, fits); (c) DLS particle size distribution.

I.6 Conclusion

We synthesized mono- and lightly-doped bimetallic Cu and Zn nanomaterials by pulsed laser ablation in aqueous liquids, using 150 mJ, 355 nm, nanosecond pulses and a novel foil target setup. PLAL of Cu or Zn foil in pure water or with added Cu or Zn salts predictably produced different materials, depending on the chemical composition of the ablation liquid. Addition of select anions to the ablation solutions led to the fabrication of more complex phase-pure nanominerals. In contrast, PLAL of metals in neat water generated mixtures of metal and metal oxide nanomaterials. Our results demonstrate that kinetic control transcended thermodynamic product formation during nanosecond ultraviolet PLAL nanomaterials synthesis.

I.7 Acknowledgments

We thank George R. Rossman for helpful discussions. Research was performed in the Laser Resource Center and the Molecular Materials Research Center of the Beckman Institute of the California Institute of Technology. This work was supported by the NSF CCI Solar Fuels Program (CHE-1305124) and the Arnold and Mabel Beckman Foundation. C.W.R. thanks the National Science Foundation and Link Energy Foundation for graduate research fellowships.

I.8 References

(1) B. G. Ershov, E. Janata, A. Henglein and A. Fojtik, *The Journal of Physical Chemistry*, 1993, **97**, 4589–4594.

(2) T. Tsuji, K. Iryo, N. Watanabe and M. Tsuji, *Appl. Surf. Sci.*, 2002, **202**, 80–85.

(3) F. Mafuné, J.-y. Kohno, Y. Takeda and T. Kondow, *The Journal of Physical Chemistry B*, 2003, **107**, 4218–4223.

(4) S.-H. Tsai, Y.-H. Liu, P.-L. Wu and C.-S. Yeh, *J. Mater. Chem.*, 2003, **13**, 978–980.

(5) R. M. Tilaki, A. Iraji zad and S. M. Mahdavi, *Appl. Phys. A*, 2007, **88**, 415–419.

(6) K. S. Khashan, G. M. Sulaiman and F. A. Abdulameer, *Arab J Sci Eng*, 2015, **41**, 301–310.

(7) A. E. Tyurnina, V. Y. Shur, R. V. Kozin, D. K. Kuznetsov, V. I. Pryakhina and G. V. Burban, *Phys. Solid State*, 2014, **56**, 1431–1437.

(8) K. Amikura, T. Kimura, M. Hamada, N. Yokoyama, J. Miyazaki and Y. Yamada, *Appl. Surf. Sci.*, 2008, **254**, 6976–6982.

(9) J. M. J. Santillán, F. A. Videla, M. B. Fernández van Raap, D. C. Schinca and L. B. Scaffardi, *J. Appl. Phys.*, 2013, **113**, 134305.

(10) M. A. Gondal, Q. A. Drmosh, Z. H. Yamani and T. A. Saleh, *Appl. Surf. Sci.*, 2009, **256**, 298–304.

(11) S. C. Singh, *J. Nanopart. Res.*, 2011, **13**, 4143–4152.

(12) C. He, T. Sasaki, Y. Shimizu and N. Koshizaki, *Appl. Surf. Sci.*, 2008, **254**, 2196–2202.

(13) C. He, T. Sasaki, H. Usui, Y. Shimizu and N. Koshizaki, *J. Photochem. Photobiol., A*, 2007, **191**, 66–73.

(14) Y. Ishikawa, Y. Shimizu, T. Sasaki and N. Koshizaki, *J. Colloid Interface Sci.*, 2006, **300**, 612–615.

(15) D. A. Shirley, *Phys. Rev. B*, 1972, **5**, 4709–4714.

(16) T. L. Barr, *Journal of Vacuum Science and Technology A: Vacuum, Surfaces, and Films*, 1995, **13**, 1239.

(17) J. Bakemore, H. Gray, J. Winkler and A. Muller, *ACS Catal.*, 2013, **3**, 2497.

(18) B. M. Hunter, J. D. Blakemore, M. Deimund, H. B. Gray, J. R. Winkler and A. M. Müller, *J. Am. Chem. Soc.*, Sept. 2014, **136**, 13118–13121.

(19) T. L. Woods and R. M. Garrels, *Appl. Geochem.*, 1986, **1**, 181–187.

(20) C. H. Yoder, E. Bushong, X. Liu, V. Weidner, P. McWilliams, K. Martin, J. Lorgunpai, J. Haller and R. W. Schaeffer, *Mineral. Mag.*, 2010, **74**, 433–440.

(21) M. P. Seah, G. C. Smith and M. T. Anthony, *Surf. Interface Anal.*, 1990, **15**, 293–308.

(22) G. Ertl, R. Hierl, H. Knözinger, N. Thiele and H. P. Urbach, *Applications of Surface Science*, 1980, **5**, 49–64.

(23) C. D. Wagner, *NIST x-ray photoelectron spectroscopy (XPS) database*, Report, National Institute of Standards and Technology (NIST), 1990.

(24) S. Elzey, J. Baltrusaitis, S. Bian and V. H. Grassian, *J. Mater. Chem.*, 2011, **21**, 3162.

(25) A. M. Pollard, *Mineral. Mag.*, 1989, **53**, 557–563.

(26) M. E. Fleet, *Acta Crystallogr Sect B*, 1975, **31**, 183–187.

(27) R. L. Frost, W. Martens, J. T. Kloprogge and P. A. Williams, *J. Raman Spectrosc.*, 2002, **33**, 801–806.

(28) W. Martens, R. L. Frost and P. A. Williams, *n. jb. miner. abh.*, 2003, **178**, 197–215.

(29) J. Baltrusaitis, P. M. Jayaweera and V. H. Grassian, *Phys. Chem. Chem. Phys.*, 2009, **11**, 8295.

(30) N. S. McIntyre and M. G. Cook, *Anal. Chem.*, 1975, **47**, 2208–2213.

(31) C. E. Nanayakkara, P. M. Jayaweera, G. Rubasinghege, J. Baltrusaitis and V. H. Grassian, *J. Phys. Chem. A*, 2014, **118**, 158–166.

(32) H. Sarp, L. Cerny and Guenee, *Riviera Sci.*, 2001, **85**, 3.

(33) J. L. Jambor and A. C. Roberts, *Am. Mineral.*, 2005, **90**, 271–275.

(34) V. Hayez, T. Segato, A. Hubin and H. Terryn, *J. Raman Spectrosc.*, 2006, **37**, 1211–1220.

(35) R. d. P. Bendezú H, R. P. Gonçalves, A. C. Neiva and H. G. d. Melo, *J. Braz. Chem. Soc.*, 2007, **18**, 54–64.

(36) R. A. Reichle, K. G. McCurdy and L. G. Hepler, *Can. J. Chem.*, 1975, **53**, 3841–3845.

(37) S. J. Ahmadi, M. Hosseinpour, F. Javadi and R. Tayebee, *Ind. Eng. Chem. Res.*, 2013, **52**, 1448–1454.

(38) N. Nityashree and M. Rajamathi, *J. Phys. Chem. Solids*, 2013, **74**, 1164–1168.

(39) Y. Li, Y. Zou and Y. Hou, *Cryst. Res. Technol.*, 2011, **46**, 305–308.

(40) O. Medenbach and K. Schmetzer, *Die Naturwissenschaften*, 1976, **63**, 293–294.

(41) N. J. Nicholas, G. V. Franks and W. A. Ducker, *CrystEngComm*, 2012, **14**, 1232–1240.

(42) F. C. Hawthorne and E. Sokolova, *The Canadian Mineralogist*, 2002, **40**, 939–946.

(43) T. Kozawa, A. Onda, K. Yanagisawa, A. Kishi and Y. Masuda, *J. Solid State Chem.*, 2011, **184**, 589–596.

(44) J. Cao, P. R. Henry, C. B. Ammerman, R. D. Miles and R. C. Littell, *The Journal of Applied Poultry Research*, 2000, **9**, 513–517.

(45) H. M. Edwards and D. H. Baker, *J. Anim. Sci.*, 2000, **78**, 1017.

(46) A. B. Batal, T. M. Parr and D. H. Baker, *Poultr. Sci.*, 2001, **80**, 87–90.

(47) I. Mavromichalis, D. M. Webel, E. N. Parr and D. H. Baker, *Can. J. Anim. Sci.*, 2001, **81**, 387–391.

(48) W. Stählin and H. R. Oswald, *Acta Crystallogr Sect B*, 1970, **26**, 860–863.

(49) S. Bera, A. A. M. Prince, S. Velmurugan, P. S. Raghavan, R. Gopalan, G. Panneerselvam and S. V. Narasimhan, *J. Mater. Sci.*, 2001, **36**, 5379–5384.

(50) B. Schwenzer, K. M. Roth, J. R. Gomm, M. Murr and D. E. Morse, *J. Mater. Chem.*, 2006, **16**, 401–407.

(51) B. M. Hunter, W. Hieringer, J. R. Winkler, H. B. Gray and A. M. Müller, *Energy Environ. Sci.*, 2016, **9**, 1734–1743.

(52) C. Cordeiro, G. Arizaga, L. Ramos and F. Wypych, *Catal. Commun.*, 2008, **9**, 2140–2143.

(53) G. F. H. Smith, *Mineral. Mag.*, 1906, **14**, 170–177.

(54) R. S. W. Braithwaite, K. Mereiter, W. H. Paar and A. M. Clark, *Mineral. Mag.*, 2004, **68**, 527–539.

(55) J. S. Helton, K. Matan, M. P. Shores, E. A. Nytko, B. M. Bartlett, Y. Yoshida, Y. Takano, A. Suslov, Y. Qiu, J. H. Chung, D. G. Nocera and Y. S. Lee, *Phys. Rev. Lett.*, 2007, **98**, DOI: 10.1103/physrevlett.98.107204.

(56) G. Misguich and P. Sindzingre, *The European Physical Journal B*, 2007, **59**, 305–309.

(57) D. E. Freedman, T. H. Han, A. Prodi, P. Müller, Q.-Z. Huang, Y.-S. Chen, S. M. Webb, Y. S. Lee, T. M. McQueen and D. G. Nocera, *J. Am. Chem. Soc.*, 2010, **132**, 16185–16190.

Appendix J

Supplementary Information for Complex Nanomineral Formation Utilizing Kinetic Control by PLAL

Foil target	Added salt	Obtained material	PDF card
Cu	None	Cu, CuO	01-070-3038 (Cu), 01-078-0428 (CuO)
Cu	$CuCl_2 \cdot H_2O$	$Cu_2Cl(OH)_3$ (Paratacamite)	01-070-0821
Cu	$Cu(NO_3)_2 \cdot 3\,H_2O$, NH_4OH	$Cu_2(NO_3)(OH)_3$ (Rouaite)	01-075-1779
Zn	None	Zn, ZnO (Wurtzite)	00-004-0831 (Zn), 01-075-6445 (ZnO)
Zn	$ZnCl_2$, NH_4OH	$Zn_5(OH)_8Cl_2 \cdot H_2O$ (Simonkolleite)	00-07-0155
Zn	$Zn(NO_3)_2 \cdot 6\,H_2O$	$Zn_5(OH)_8(NO_3)_2 \cdot 2\,H_2O$	01-072-0627
Cu	$CuCl_2 \cdot H_2O$, $ZnCl_2$	$Cu_3(Cu,Zn)Cl_2(OH)_6$ (Zincian paratacamite)	00-050-1558

Table J.1: X-ray diffraction characterization of nanomaterials synthesized by PLAL of metal foils in neat water or aqueous solutions

Material	Cu $2p_{3/2}$ (eV)	Zn $2p_{3/2}$ (eV)	O 1s (eV)	Cl 2s (eV)	N 1s (eV)
Cu, CuO	932.7 (Cu), 933.8 (CuO)	–	530.7 (CuO)		
$Cu_2Cl(OH)_3$ (Paratacamite)	933.4 (CuO), 935.4 (Cu–Cl)	–	531.5 (Cu–OH)	270.0 (Cu–Cl)	
$Cu_2(NO_3)(OH)_3$ (Rouaite)	935.3 (Cu–OH & Cu–NO3)	–	531.5 (Cu–OH)		403.6 (Cu–NO_2)
Zn, ZnO (Wurtzite)	–	1021.2 (Zn), 1022.4 (ZnO)	530.5 (ZnO)	271.0 (Zn–Cl)	407.3 (Cu–NO_3)
$Zn_5(OH)_8Cl_2 \cdot H_2O$ (Simonkolleite)	–	1022.8 (Zn–OH)	530.5 (ZnO),531.9 (Zn–OH)		
$Zn_5(OH)_8(NO_3)_2 \cdot 2\,H_2O$	–	1021.4, 1023.7 (Zn–OH, tetrahedral and octahedral)	531.8 (Zn–OH), 533.0 (Zn–NO_3)		404.9, 407.4 (Zn–NO_3)
$Cu_3(Cu,Zn)Cl_2(OH)_6$ (Zincian paratacamite)	933.3 (CuO), 935.4 (Cu–Cl)	–	531.6 (Cu–OH)	270.1 (Cu–Cl)	

Table J.2: Central binding energies obtained from X-ray photoelectron spectra of nanomaterials synthesized by PLAL of metal foils in neat water or aqueous solutions. Assignments are in parentheses; details are in the main text.

Material	D_{hydr} (nm)	σ (nm)
Cu, CuO	225	40
$Cu_2Cl(OH)_3$ (Paratacamite)	258	43
$Cu_2(NO_3)(OH)_3$ (Rouaite)	xx	xx
Zn, ZnO (Wurtzite)	258	40
$Zn_5(OH)_8Cl_2 \cdot H_2O$ (Simonkolleite)	318	14
$Zn_5(OH)_8(NO_3)_2 \cdot 2\,H_2O$	178	0.5
$Cu_3(Cu,Zn)Cl_2(OH)_6$ (Zincian paratacamite)	208	35

Table J.3: Mean hydrodynamic particle diameters D_{hyd} with size distribution widths σ obtained from dynamic light scattering data of nanomaterials synthesized by PLAL of metal foils in neat water or aqueous solutions.

Appendix K

Synthesis, Characterization, and Properties of Metal Phosphide Catalysts for the Hydrogen-Evolution Reaction

Reprinted with permission from J. Callejas*; C.G. Read*; C.W. Roske; N.S. Lewis; R.E. Schaak. Accepted in *Chem. Mater.*, ASAP. Copyright 2016 American Chemical Society.

K.1 Abstract

Hydrogen gas obtained by the electrolysis of water has long been proposed as a clean and sustainable alternative to fossil fuels. Noble metals such as Pt are capable of splitting water at low overpotentials, but the implementation of inexpensive solar-driven water-splitting systems and electrolyzers could benefit from the development of robust, efficient, and abundant alternatives to noble metal catalysts. Transition metal phosphides (M_xP_y) have recently been identified as a promising family of Earth-abundant electrocatalysts for the hydrogen-evolution reaction (HER), and are capable of operating with low overpotentials at operationally relevant current densities while exhibiting stability under strongly acidic conditions. In this review, we highlight the progress that has been made in this field and provide insights into the synthesis, characterization and electrochemical behavior of transition metal phosphides as HER electrocatalysts. We also discuss strategies for the incorporation of metal phosphides into integrated solar-driven water-splitting systems and highlight key considerations involved in the testing and benchmarking of such devices.

K.2 Introduction

The development of clean, affordable and sustainable approaches to fuel generation and utilization is a critical global challenge. With a rapidly rising world population the global primary energy-consumption rate is expected to increase from 17 TW in 2010 to 27 TW by 2040.[1] Because of their high energy density and ease of combustion, fossil fuels have remained the primary global energy carriers for the past two centuries, and have played a pivotal role in worldwide industrial and technological development. Even though coal and natural gas could continue to meet the world's energy demand for the foreseeable future, environmental concerns over the extraction and inefficient combustion of non-renewable fossil fuels have

motivated the search for cleaner and more sustainable energy platforms.[1]

Solar, wind, and other renewable energy technologies have emerged as promising alternatives to conventional energy sources. These renewable resources are often intermittent and depend on the time of day and/or weather, requiring batteries and/or other storage technologies to compensate for the intermittency of the resource. The storage of energy as chemical bonds in molecules is a promising approach to facilitate long-term storage and additionally to serve the demands of transportation systems.[2] Molecular hydrogen, H_2, has a considerably higher specific energy than most hydrocarbons, and is a well-known zero-emission fuel that liberates only water upon combustion. The clean, scalable, and affordable production of hydrogen is also an important requirement for the implementation of fuel-cell technologies on a global scale.[3] Functional hydrogen-based fuel-cell modules are commercially available but are economically disfavored relative to traditional combustion engines and batteries because of high costs, storage issues, and limited access to H_2 fuel. The combination of fuel-cell technologies with the clean, widespread, and on-demand production of H_2 thus has the potential to significantly impact the transportation and industrial energy sectors.

Currently, most hydrogen is produced through industrial reforming methods.[3] For example, steam-methane reforming involves the reaction between steam (water vapor) and methane over a nickel-based catalyst at temperatures above 700 °C to yield H_2 and CO. The obtained CO is then further reacted with more steam to finally produce CO_2 and more H_2 through the water-gas shift reaction. In addition to high reaction temperatures, industrial reforming requires large amounts of natural gas and adds significantly to rising atmospheric CO_2 levels. Additionally, hydrogen produced by this method often carries sulfur-containing impurities that are of significant environmental concern and that can readily poison fuel-cell catalysts.[4] Devices that facilitate water electrolysis, including electrochemical and photoelectrochemical cells (PEC), are emerging technologies that have the potential to renewably generate clean hydrogen fuel from water without fossil fuels or harmful byproducts.

Overall water "splitting" is the electrochemical reaction that separates water into molecular hydrogen, $H_2(g)$, and molecular oxygen, $O_2(g)$. With $\Delta G = 237.2\,\mathrm{kJ\,mol^{-1}}$ under standard conditions, the water-splitting reaction is highly endothermic and requires 1.23 V per electron transferred. While water splitting can be facilitated in acidic, alkaline, or neutral aqueous solutions, each has unique advantages, disadvantages, and challenges.[5] Water splitting is favored in strong electrolytes because of

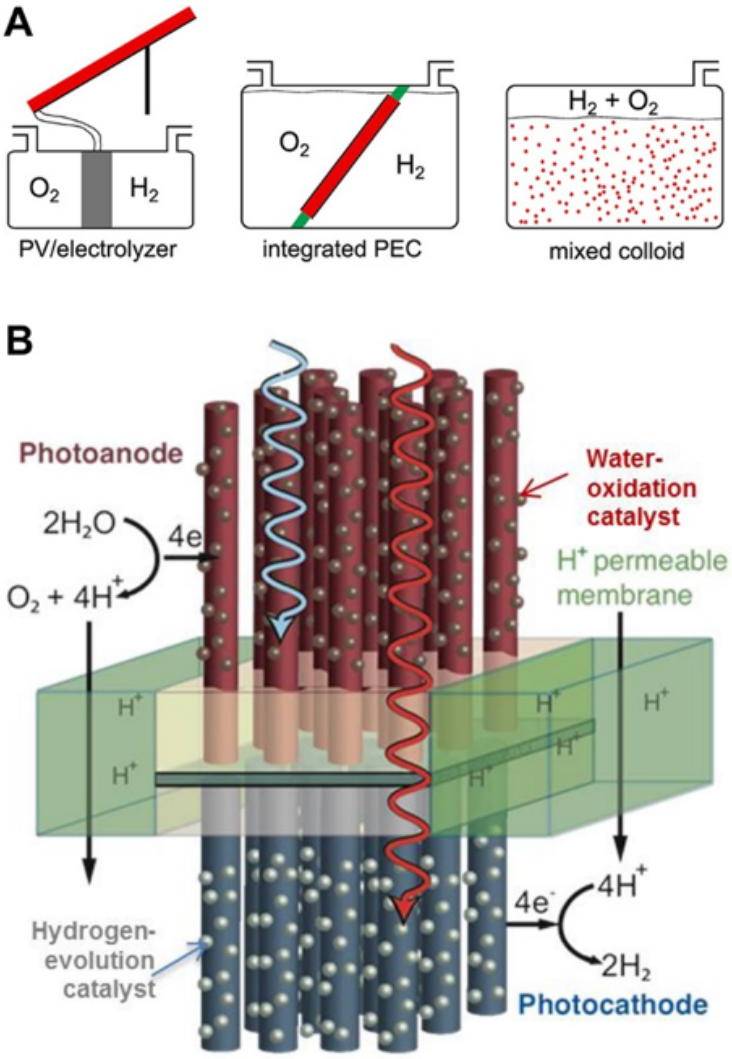

Figure K.1: (A) Design schemes for solar-driven electrochemical cells. Adapted with permission from ref.[5]. Copyright 2014 American Chemical Society. (B) Schematic of an integrated PEC water-splitting device, showing light-absorbing microwire semiconductor arrays with surface-anchored HER and OER catalysts. The anode (top) and cathode (bottom) compartments are connected by a proton-permeable membrane. Reproduced with permission from E. A. Santori.

their high ionic conductivities. Efficient, safe electrolyzers are constructed in either acidic or alkaline media so that either protons or hydroxide ions can be transferred between the anolyte and catholyte to avoid a substantial increase in pH gradients as a result of the electrolysis reaction.[6] Electrolysis under pH-neutral conditions is impacted by the formation of substantial pH gradients that can impede the water-splitting process.[7] The formation of pH gradients can be mitigated by use of a single compartment reactor with sufficient mixing, but such systems result in the formation

of explosive mixtures of O_2 and H_2 gases and/or are inefficient. Acidic electrolytes are particularly well suited for the HER, because the reduction of a positively charged proton is more energetically favorable than reduction of a neutral water molecule. Additionally, the extensive availability of highly efficient proton-exchange membranes favors a reactor design in acidic conditions. The water-splitting process can be described by two separate half-reactions: the hydrogen evolution reaction (HER), which involves proton reduction and occurs at the cathode, and the oxygen evolution reaction (OER), which involves water oxidation and occurs at the anode. Shown below are the HER and OER in acidic aqueous solutions, which is the primary emphasis of this review because it is relevant to the conditions under which polymer electrolyte membrane based water electrolysis devices operate.

Water Splitting	$2\,H_2O \longrightarrow 2\,H_2 + O_2$	$E^{\circ}_{cell} = 1.23\,V$ vs. NHE
OER	$2\,H_2O \longrightarrow O_2{}^{+}\,4\,H^{+} + 4\,e^{-}$	$E^{\circ} = 1.23\,V$ vs. NHE
HER	$2\,H^{+} + 2\,e^{-} \longrightarrow 2\,H_2 + O_2$	$E^{\circ} = 0.00\,V$ vs. NHE

Several different design schemes have been proposed for solar-driven electrochemical cells (Figure K.1).[5] The simplest, which consists of a photovoltaic cell or module connected to a water electrolyzer, indirectly converts solar energy into chemical fuel. Integrated photoelectrochemical cells are attractive options for direct solar fuel production because of their projected lower costs and potentially high efficiencies as compared to indirect schemes.[8] One possible configuration, in which several key components are integrated and work synergistically to facilitate overall sunlight-driven water electrolysis, is shown in Figure K.1.[9] The general layout includes two distinct arrays of semiconductor microwires that absorb different portions of the incoming solar spectrum, catalysts that decorate the microwire arrays to facilitate the OER and HER, and a membrane that separates the two compartments while allowing selective proton transport. High-energy photons ($> 1.8\,eV$) are absorbed at the photoanode (shown in red), and the OER catalysts attached to the photoanode's surface oxidize water and release O_2(g) and protons. Protons then move across a proton-permeable membrane toward the photocathode, where lower-energy ($< 1.2\,eV$) solar photons are absorbed. Catalysts that facilitate the HER are attached to the photocathode's surface where the protons combine with electrons to produce H_2(g). The membrane that separates the two compartments shuttles protons from the photoanode to the photocathode while keeping the H_2(g) and O_2(g) products in separate compartments. This avoids the formation of an explosive mixture of

H_2(g) and O_2(g) and also prevents the oxidation of H_2(g) at the anode and reduction of O_2(g) at the cathode, and recombination of products within the electrolyte. While effective integration of all of the components is required to achieve optimal solar water-splitting performance, the materials themselves are critical since they directly impact the overall efficiency, stability, scalability, and cost of the device. The widespread implementation of water-splitting technologies therefore requires the discovery, development, and integration of robust and Earth-abundant materials for each of these individual components. This review focuses specifically on catalytic materials for the HER, which is one of the key components of the cathode in a full solar-driven water-splitting device.

The HER can be facilitated by a diverse range of catalytic systems. In nature and under mild, benign, and pH-neutral operating conditions, the HER can be carried out by several biological catalysts, including the [FeFe],[10,11] [FeNi],[12,13] and [Fe]-only hydrogenases[14,15] as well as by the [FeMo] nitrogenase.[16,17] These enzymes often have metal-sulfur clusters as active sites embedded in a complex biological cavity that provides a suitable chemical environment for the HER. Substantial work has been directed towards developing molecular mimics of these enzyme active sites, as well as other homogeneous molecular catalysts that exhibit comparable or even higher rates for HER catalysis than the natural enzymes.[18] For example, several nickel phosphine complexes with proximal amine groups have been shown to facilitate the HER at very high rates, albeit in acetonitrile solutions.[19–22] Other examples of HER molecular catalysts include diiron,[23] iron diglyoxime[24] and cobalt diglyoxime[25] complexes, as well as thiomolybdate clusters.[26–28] Interestingly, model compounds of enzyme active sites often are inactive or are significantly less active than desired for catalytic hydrogen production. When inserted into the proper biological cavity, certain inactive synthetic complexes exhibit catalytic activities comparable to those of naturally occurring enzymes.[29] From a device perspective, biological and homogeneous systems with exceptional catalytic properties face challenges involving anchoring to and integrating with solid-state systems, as well as stability in chemically harsh, non-neutral electrolytic environments, including many of the proposed devices that require strongly acidic or basic conditions to function efficiently.[30] One key goal of HER-catalyst development is therefore finding heterogeneous systems that can combine the high activity of biological and molecular catalysts with the superior stability and integration capabilities of solid-state materials.

Platinum is the most widely used heterogeneous catalyst for the HER, due to the

high catalytic activity and durability of Pt under harsh operating conditions.[31] The low terrestrial abundance and cost of mining Pt has motivated the search for Earth-abundant alternatives.[5,9] Molybdenum-based materials have been at the forefront of Earth-abundant hydrogen-evolution catalysis for decades. NiMo alloys were reported by Fogarty and coworkers as highly active HER catalysts in alkaline aqueous solutions.[32] Other related alloys including CoMo,[33] FeMo,[33] and NiMoZn[34] have also been reported to be active catalysts for the HER. However, despite their high catalytic activity and stability under alkaline conditions, these alloys quickly corrode in acidic environments.[35] Other Mo-based HER catalysts, including Mo_2C,[36–38] MoB,[36] $Co_6Mo_{1.4}N_2$,[38] and $NiMoN_x$,[39] have been investigated, and many of these catalysts exhibit extended stability in acidic aqueous solutions.

Using theoretical and experimental methods, Hinnemann and coworkers showed that the edge sites of MoS_2, which are chemically and structurally distinct from the Mo-based alloys, have chemical environments that can facilitate the HER.[40] Accordingly, MoS_2 has been the leading Earth-abundant alternative to platinum for catalyzing the HER in acidic aqueous solutions. The HER-active edge sites of MoS_2 have structural commonalities with the active-site clusters in some hydrogenase and nitrogenase enzymes.[40] Extensive research efforts have been directed towards understanding and maximizing the number of exposed active sites in MoS_2, and this has led to the development of improved MoS_2-based HER catalysts that are highly active and acid stable.[41–43] Ooi[26] and Besenbacher[28] have developed $[Mo_3S_{13}]^{2-}$ and $[Mo_3S_4]^{4+}$ clusters, respectively, while Chang[27] has developed molecular-based systems, which all aim to mimic the HER-active MoS_2 edge sites. While such studies of molecular mimics of solid-state catalysts are important for active-site design and activity optimization, they also emphasize the structural and chemical interrelationships among heterogeneous, homogeneous, and biological catalytic systems.

The most highly studied molybdenum-based HER catalysts, including NiMo, Mo_2C, and MoS_2, are also well-known catalysts for hydrodesulfurization (HDS).[44] HDS is the catalytic process by which sulfur impurities are removed from hydrocarbon fuels and feedstocks. Despite being distinct chemical processes, both HDS and HER are regulated by the reversible and dissociative binding of hydrogen molecules on the surface of a catalyst. Computational studies have indicated that both HER and HDS catalysts have active sites that bind atomic hydrogen with intermediate strengths, such that the free energy of adsorbed hydrogen is closely matched to the free energy of the products, leading to $\Delta G^\circ_{H^*} \approx 0$.[45] Hydrogen adsorption energies that are too

high (e.g. strong hydrogen adsorption) would prevent the release of products, which include H_2 for the HER and H_2S for HDS. In contrast, hydrogen adsorption energies that are too low (e.g. weak hydrogen adsorption) will result in slow electron-transfer rates. Both strong and weak hydrogen adsorption, therefore, result in low catalytic rates. Because HDS catalysts have intermediate hydrogen adsorption energies, it has been proposed, by our group and others, that HDS catalyst systems may be fertile ground for the discovery and development of new Earth-abundant HER catalysts.

Among the most highly studied and active HDS catalysts are Ni_2P[46,47] and related transition metal phosphides, including CoP, Fe_2P, MoP, and WP.[48,49] Given the potential mechanistic analogy between the HDS and HER catalytic processes, we hypothesized that Ni_2P and other metal phosphides may indeed be active and Earth-abundant HER catalysts. Additionally, in 2005, Rodriquez and coworkers suggested, based on density functional theory (DFT) calculations, that the (001) surface of Ni_2P combines the favorable H binding present in hydrogenase systems with the thermostability of a heterogeneous catalyst, making it a very promising alternative to Pt for catalyzing the HER.[45] In 2013, we experimentally validated this prediction, showing that Ni_2P was indeed a highly active HER catalyst in acidic aqueous solution.[50] Since then, our group and others have demonstrated that the HDS-active metal phosphides comprise a new class of highly active and acid-stable HER catalysts. The field of metal phosphide HER catalysts has rapidly expanded to include a growing number of catalytic systems and preparation methods, demonstrations of integration into functional photocathode systems, mechanistic insights in the catalytic reactions, and guidelines for designing new catalysts and improving the performance of existing catalysts.

This Review article highlights recent developments in transition metal phosphides as an emerging family of highly active and Earth-abundant catalysts for the HER, primarily in acidic conditions that are relevant to proton-exchange-membrane electrolysis systems. The HER performance in pH-neutral and alkaline aqueous solutions is also highlighted due to potential relevance to alternative water-electrolysis systems. We include in this Review a survey of how transition metal phosphides are synthesized across multiple platforms such as bulk crystals, films, and nanoparticles, because collectively these techniques and the materials they produce are relevant for exploratory synthesis and catalyst discovery, optimization of catalytic performance through active-site exposure and surface area maximization, integration into devices, and understanding mechanistic details of the catalytic reactions. Addition-

ally, we discuss aspects of materials and electrochemical characterization that are crucial for fully understanding the materials being studied, accurately attributing catalytic activities to the correct materials features, and benchmarking performance metrics with related systems. We then provide an overview of the properties and performance metrics of transition metal phosphides for HER catalysis, including their integration with light-absorber materials as an important step toward building a practical solar-driven water-splitting device.

K.3 Overview of Metal Phosphides

Metal phosphides, represented by the general formula M_xP_y, are solid-state compounds formed from the combination of metallic or semimetallic elements with phosphorus. The crystal structures adopted by the large number of known binary, ternary, and higher-order metal phosphides are diverse (Figure K.2), spanning simple high-symmetry ionic structures such as NaCl-type LaP to more complex structures such as $ThCr_2Si_2$-type $LaRu_2P_2$ and skutterudite-type $LaRu_4P_{12}$. The bonding in metal phosphides is also diverse and, depending on the composition and constituent elements, can be described as ionic, covalent, or metallic. Metal-rich ($x > y$ in M_xP_y) or stoichiometric ($x = y = 1$ in M_xP_y) metal phosphides are often semiconducting and in some cases even metallic or superconducting due to the presence of significant metal-metal bonding. For instance, TiP and Fe_2P exhibit metallic behavior, whereas GaP and InP are well-known semiconductors. Superconducting properties have been observed in various metal-rich phases such as Mo_3P[51] and $LaRu_2P_2$[52].

The relatively strong M – P bonds can impart transition metal phosphides with high thermal stability and hardness, as well as resistance to oxidation and chemical attack. For example, the phosphides of various metals, such as Ti, Ta, Mo, and W, are of interest as oxidation-resistant coatings for high-temperature applications.[53,54] Importantly for applications such as HER electrocatalysis, many transition metal phosphides are impervious to dilute acids and bases, and some are unaffected even by strongly acidic or alkaline solutions. More ionic phosphides, such as Ca_3P_2 and Zn_3P_2, however, readily decompose in water to produce highly pyrophoric and toxic gases, such as phosphines and diphosphines.

In contrast to the metal-rich and stoichiometric phosphides, phosphorus-rich transition metal phosphides ($y > x$ in M_xP_y) exhibit significant phosphorus-phosphorus bonding, due to the ability of phosphorus to bond with itself to form various

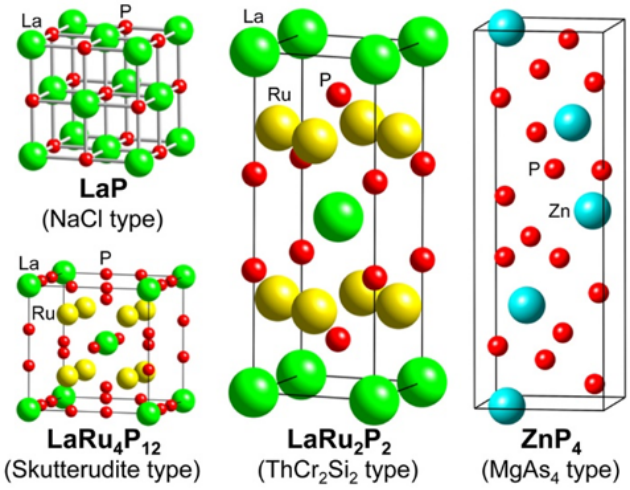

Figure K.2: Crystal structures of representative types of metal phosphides: NaCl-type LaP, skutterudite-type $LaRu_4P_{12}$, $ThCr_2Si_2$-type $LaRu_2P_2$, and $MgAs_4$-type ZnP_4.

oligomers and clusters. For example, a number of MP_2 compounds, such as NiP_2 and SiP_2, adopt the pyrite-type structure in which the phosphorus atoms are arranged in P–P dimers. Other polyphosphides contain various phosphorus oligomers, clusters, chains, and planes. These so-called polyphosphides exhibit characteristics that are markedly different from their metal-rich or stoichiometric counterparts, including lower thermal stabilities, higher reactivities, and softer materials properties that can be classified as significantly less refractory. As a result, many phosphorous-rich phosphides are thermally unstable, disproportioning at high temperatures to elemental phosphorus and more metal-rich phases.

K.4 Synthesis of Metal Phosphides

Metal phosphides can be synthesized using a variety of methods and in various forms, producing single crystals,[54–56] bulk polycrystalline powders,[57] films,[58,59] or nanostructured solids[60–66] (Figure K.3). Bulk metal phosphides can be prepared through traditional solid-state strategies by direct combination of the elements at high temperatures in an inert atmosphere or under vacuum. Using this approach, many phosphide phases can be routinely accessed in high purity and on a large scale. As is typical for bulk-scale solid-state reactions, high reaction temperatures ($> 900\,^{\circ}C$) and long reaction times (1-10 days) are generally required. For example, in a representative synthesis of bulk FeP,[67] stoichiometric amounts of iron metal and red phosphorus are sealed in an evacuated silica tube, which is then

heated to 900 °C for approximately 8 days. Red phosphorus is often used in these direct high-temperature solid-state reactions, although the more reactive white phosphorus allotrope can also be used, as can certain reactive metal phosphides. For example, various phosphide phases, including AlP[68] and NbP,[69] have been accessed by high-temperature reactions between a metal phosphide of a lower stability, such as Ca_3P_2 or Zn_3P_2, and the appropriate metal powder (> 1000 °C). Because the high-temperature solid-state reactions can produce highly reactive and pyrophoric byproducts, including P_4 and phosphine, properly trained personnel must work under rigorously air-free conditions to perform the reactions safely as well as to isolate the products.

To lower the temperatures required by direct reactions and to expand the palette of accessible phases, molten fluxes have been used extensively in the synthesis of metal phosphides.[55] In this approach, a nominally unreactive and low-melting metal, such as Sn or Pb, is mixed with the precursor elements and used as a high temperature solvent to enhance the diffusion rate of the solid reagents.[55] After the reaction, the metal matrix must be separated from the products either mechanically or by dissolution in acid. For example, in a representative flux synthesis of RuP_2,[70] stoichiometric amounts of ruthenium and red phosphorus powders are placed along with excess tin in an evacuated silica tube, which is sealed and heated to 1200 °C for approximately 3 days. After the reaction, the phosphide product is then recovered from the flux by dissolving the tin in hot concentrated HCl. In many instances, the flux method yields high-quality phosphide crystals (Figure K.3) and provides access to metastable and low-temperature phases that are inaccessible by the use of higher-temperature solid-state reactions, which tend to favor the formation of more thermodynamically stable products. Moreover, phosphide phases like CrP_4,[71] MnP_4[72,73] and Re_2P_5[74] are challenging to obtain through alternative methods without the use of high pressures.

Another approach that has been extensively used in the synthesis of metal phosphides is the phosphidation of metal oxides, hydroxides or other precursors by highly-active phosphorus species. The phosphidation can be obtained either through direct exposure to phosphine gas[75] or by exposure to related compounds generated in situ through the reduction of phosphate salts by hydrogen[48] or carbon.[76] For instance, several phosphide phases, such as Ni_2P, CoP, and FeP, can be readily obtained by the temperature-programmed reduction (TPR) of the corresponding metal phosphate.[48,49] In a representative TPR synthesis of CoP,[77] a stoichiometric mixture of cobalt nitrate and ammonium hydrogen phosphate is calcined in air at 500 °C for ap-

proximately 6 hours to produce a cobalt phosphate precursor, which is subsequently reduced by heating to 1000 °C for 2 h in a H_2-containing atmosphere. Originally developed to produce metal-oxide-supported phosphides for catalytic applications such as hydrodesulfurization or hydrodenitrogenation, the strategy has recently been extended to the production of phosphide materials directly on the surfaces of electroactive substrates, such as conductive carbon paper[78] and metal foams.[79] Electrochemical and electroless deposition methods have also been explored as a way to directly coat electrode surfaces with metal phosphides.[80–86] However, these approaches tend to yield amorphous Co–P and Ni–P alloys with a wide range of phosphorus contents.

The need for high-surface-area phosphide materials for catalytic and electrocatalytic applications has led to renewed interest in alternative synthetic strategies for the production of metal phosphides. For example, solvothermal reactions,[87] thermal decomposition of single-source organometallic precursors,[88] and the reaction of organometallic compounds or metallic nanoparticles with organophosphine reagents,[57,89] have been used to produce crystalline high-surface-area metal phosphides under reaction conditions that are frequently milder than those found in direct reactions or flux approaches. Furthermore, these methods typically produce metal phosphides in the form of dispersable nanocrystals that can be directly applied by drop-casting or spin-coating onto the surfaces of electrodes. Highly reactive reagents such as white phosphorus (P_4) or $P(SiMe_3)_3$ can be used as phosphorus sources, but milder reagents such as tri-n-octylphosphine (TOP) have been used as general phosphorus sources for the low-temperature conversion of metals into metal phosphides. Multiple phases such as Ni_2P, $Ni_{12}P_5$, Ni_5P_4, Cu_3P, Fe_2P, FeP, Co_2P, CoP, InP, PtP_2, PdP_2, RhP_2, Au_2P_3, Pd_5P_2, and MnP,[57,89,90] as well as mixed-metal solid solutions such as $(Ni_xFe_{1-x})_2P$[64], $(Ni_xCo_{1-x})_2P$[91] and $(Co_xFe_{1-x})_2P$,[92] have been synthesized as nanoparticles through these methods (Figure K.3). However, due to the use of solvents for such reactions, the temperature range is limited and generally cannot exceed 400 °C or the maximum reflux temperature of the highest-boiling solvents.

Several thin-film growth techniques have also been applied to the synthesis of transition metal phosphides, mainly for the fabrication of semiconducting or optoelectronic devices. Chemical vapor deposition (CVD) and metal-organic chemical vapor deposition (MOCVD) (Figure K.3) have been widely used to produce high-quality crystalline and amorphous thin films of several transition metal phosphides,

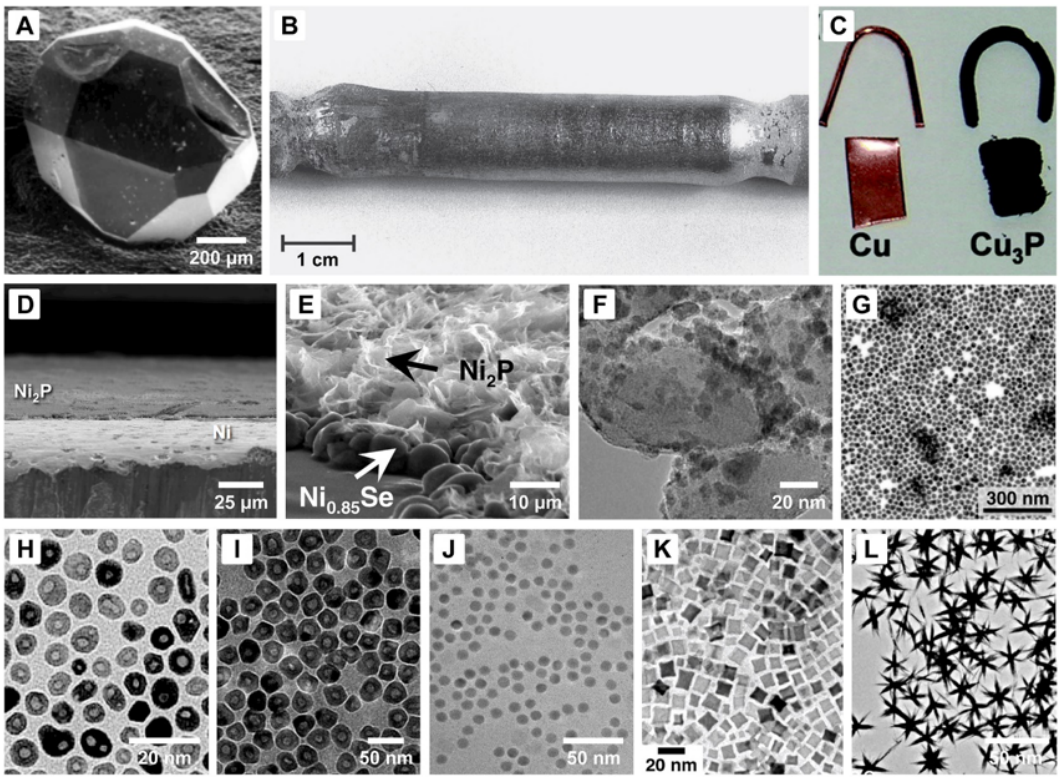

Figure K.3: Representative types of metal phosphide crystals, films, and nanoparticles. A) A crystal of $NdFe_4P_{12}$ with the cubic $LaFe_4P_{12}$-type structure grown from a tin flux. Adapted with permission from ref.[55]. Copyright 2005 WILEY-VCH Verlag GmbH & Co. KGaA, Weinheim B) Ni_2P single-crystal rod produced by the floating-zone method.Adapted with permission from ref.[56]. Copyright 2013 The Ceramic Society of Japan. C) Cu metal wire and foil and the wire and foil with a thick Cu_3P coating made by refluxing in trioctylphosphine. Adapted with permission from ref.[57]. Copyright 2007 American Chemical Society. D) SEM images of a Ni_2P film on Ni. Adapted with permission from ref.[58]. Copyright 2016 American Chemical Society. E) SEM image of a thin film showing a mixture of Ni_2P and $Ni_{0.85}Se$ deposited using CVD. Adapted with permission from ref.[59]. Copyright 2008 American Chemical Society. (F) TEM image of MoP nanoparticle catalysts supported on SiO_2. Adapted with permission from ref. 60. Copyright 2012 Elsevier B.V. (G) TEM image of Zn_3P_2 nanoparticles. Adapted with permission from ref.[61]. Copyright 2008 American Chemical Society. (H,I) TEM images of Ni_2P nanoparticles. Adapted with permission from refs.[62,63]. Copyright 2007 and 2009 American Chemical Society. (J) TEM image of $Fe_xNi_{2-x}P$ nanoparticles. Adapted with permission from ref.[64]. Copyright 2015 American Chemical Society. (K) TEM image of Rh_2P nanoparticles. Adapted with permission from ref.[65]. Copyright 2015 American Chemical Society. (L) TEM image of CoP nanoparticles. Adapted with permission from ref.[66]. Copyright 2011 American Chemical Society.

including InP,[93] GaP[94], Zn_3P_2,[95], Ni_2P,[96] and TiP,[97] among others. Typically in these processes, volatile gaseous precursors such as metal alkyls, metal halides, or in the case of MOCVD, single-source metal-organic compounds, are decomposed at high temperatures over an appropriate substrate. Similarly, physical vapor deposition (PVD) techniques, such as sputtering[98,99] and pulsed laser deposition (PLD),[100] have also been used to produce metal phosphide thin films on various substrates. However, in most cases the films obtained through these techniques are poorly crystalline or amorphous.

K.5 Characterization of Transition Metal Phosphides for the Hydrogen-Evolution Reaction

In this section we discuss methods for thorough and rigorous characterization of metal phosphides. Such methods allow the establishment of catalytic performance metrics using a common framework that permits both benchmarking and comparisons, and also enable accurate attribution of the observed catalytic properties to the key material features that define the systems of interest.

Characterization of Electrocatalytic Properties

Metal phosphide systems have emerged as highly active HER electrocatalysts and they are being increasingly investigated for this and other catalytic reactions. Accordingly, several recent articles have outlined and reviewed best practices for testing, reporting, and benchmarking such electrocatalytic materials as well as related photocatalyst systems.[5,30,101,102] Figure K.4 shows typical data for various types of benchmark Pt catalysts, which will be discussed in more detail below. Key considerations for appropriate electrocatalytic testing of the metal phosphide systems are briefly outlined below as well.

Materials for HER electrocatalysis are typically evaluated using a three-electrode setup, in which a reference electrode, a counter electrode, and a catalyst-modified working electrode are immersed in an aqueous electrolyte. The electrolyte must be continuously purged with high purity H_2 gas to establish standard conditions. When Pt is used as a counter electrode, a two-compartment cell, separated by a proton exchange membrane, must be utilized to separate the working and counter electrodes and thereby prevent cross-contamination by trace noble metal species, as well as undesired back reactions. When using a single compartment cell, only graphite rods or other inert materials should be used as counter electrodes.

Linear sweep voltammetry (LSV) and cyclic voltammetry (CV) are commonly used

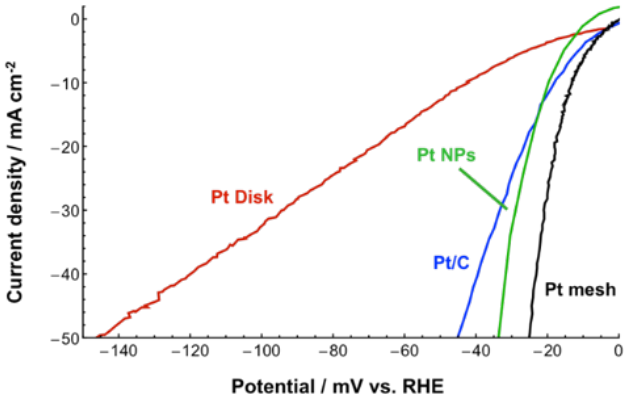

Figure K.4: Polarization Data for the HER in 0.5 M H_2SO_4 using Pt Electrodes.

to evaluate the HER performance by measurement of the catalytic current as a function of applied potential. The observed catalytic current is typically plotted as the experimentally observed current density, normalized to the geometric area of electrode, to facilitate comparisons among electrodes having different sizes. This approach however does not account for variations in catalyst loading or surface area. Methods to estimate the actual surface area of the catalyst include the use of bulk surface areas obtained through BET analysis or geometric estimates using mathematically-derived surface areas based on average particle sizes and shapes.[50,101] These estimates are limited by the realization that not all exposed surface sites are catalytically active. Electrochemical measurements of surface area most closely relate to HER operating conditions, but they have been predominately developed for noble metal systems and therefore may not be directly applicable to the metal phosphides. The exact determination of the true electrochemically active surface area may not be possible, so electrocatalytic testing on flat electrode substrates is preferable to best obtain the inherent electrochemical performance of a material. The use of flat substrates prevents artificial enhancement of electrochemical performance through increased surface area effects, thereby facilitating comparisons with other catalysts. Although the development of highly efficient 3D and porous electrodes is an important area of research for electrode design and optimization, such studies are most useful when the high surface area systems can be compared with the catalytic performance on a flat electrode.

When reporting the results of electrocatalytic testing, the overpotential required to reach a specific current density, which can be chosen depending on the target application, allows reliable comparison between catalysts tested under similar experimental

conditions. The "onset potential," which is the potential at which catalytic current first appears, is often reported in the literature. However, because the onset potential can be ascribed to the production of an arbitrarily defined current density, the "onset potential" is not a well-defined electrochemical property and hence is not a suitable metric for analytically evaluating or comparing different HER catalysts.[101] Other relevant metrics that are often reported for HER catalysts include Tafel slope, exchange-current density, and turnover frequency (TOF). These parameters in combination are also important for evaluating electrocatalytic performance and have been reviewed in detail in recent articles.[5,30,101,102]

Galvanostatic measurements and cyclic voltammetry are typically used to characterize the stability of a catalyst. Galvanostatic measurements maintain an application-relevant current density, such as $10\,\mathrm{mA/cm^2}$ for photoelectrochemical (PEC) cells, for a sufficiently long time to establish the desired degree of catalyst stability. Galvanostatic testing is particularly useful for evaluating the longevity of a catalyst under device-relevant operating conditions. For catalysts that dissolve slowly under operating conditions, high catalyst mass loadings may result in artificially prolonged stability. For this reason, galvanostatic stability measurements are most useful when performed at low mass loadings or when coupled with sensitive elemental analysis of the electrolyte, such as atomic absorption spectroscopy or inductively coupled plasma mass spectrometry (ICP-MS), to detect dissolution processes. An added benefit of galvanostatic testing is that the current density at which the experiment is conducted can be selected to investigate the HER stability for a wide range of applications and device designs, ranging from PEC's ($-10\,\mathrm{mA/cm^2}$ to $-20\,\mathrm{mA/cm^2}$) to electrolyzers ($-1\,\mathrm{A/cm^2}$ to $-2\,\mathrm{A/cm^2}$). Multiple cyclic voltammetry cycles over an appropriate potential window, such as between 0 V vs RHE and the potential required to reach or exceed a target operational current density, mimic the ramp-up and ramp-down cycles expected for solar-driven water-splitting systems. Additional useful studies include prolonged testing under the open-circuit potential (to simulate the system at rest), tests over longer periods of time (months to years), quartz-microbalance and electrolyte analysis studies to identify and understand slow dissolution processes, and impedance measurements to probe the electrical resistivity of the catalyst.

As mentioned above, catalyst benchmarking is important, and as a result, proper controls and reporting metrics are mandatory. For example, showing electrochemical data for standard Pt electrodes under the same conditions used to evaluate new

catalytic materials provides a necessary baseline for comparison. However, the availability of a wide range of different Pt standards having different surface areas and mass loadings, including flat Pt disks, Pt mesh electrodes, and supported Pt nanoparticles, complicates matters, as such systems exhibit very different catalytic performance (Figure K.4). Pt meshes are particularly desirable because they are commercially available, have high catalytic activity, and offer highly reproducible performance. Ultimately, the most active Pt standards should be used for comparison to new catalysts. The overpotentials for a clean Pt mesh are $\approx -15\,\mathrm{mV}$ to $-20\,\mathrm{mV}$ at a current density of $-10\,\mathrm{mA/cm^2}$. When reporting the results of electrocatalytic testing, the overpotential required to reach a specific current density (the operationally relevant benchmark current density) allows facile comparison between catalysts tested under similar experimental conditions. Reporting the electrode details is also important for characterizing and comparing catalysts. For example, differences in loading density and surface area can influence the reported metrics, and are important considerations.

Materials Characterization

Coupled with electrochemical characterization, it is important to fully characterize the key aspects of catalytic materials that contribute to their performance, including techniques that probe the bulk crystal structure, morphology, and chemical composition, as well as key surface chemistry details (Figure 5). This, coupled with the benchmarking efforts described in the preceding section, facilitates meaningful comparisons among catalytic systems, establishes the relevant parameters, and sets the stage for elucidating structure-property relationships. Ultimately, one should make deliberate and informed choices about which characterization tools will provide the necessary information for adequately evaluating a catalyst at each stage of discovery, development, and detailed understanding. Figure 5 shows conceptually how various materials and surface characterization tools can be used together to study catalytically active materials.

For metal phosphide HER catalysts in nanoparticle, bulk-powder, or thin-film form, powder X-ray diffraction (XRD) data enables the identification of all crystalline phases present in a sample, as well as an estimation of the size of crystalline domains through Scherrer analysis. Because phase diagrams of metal phosphides contain multiple crystalline compounds of different compositions and crystal structures, each of which can have different properties, high-quality XRD data is important for establishing phase formation and purity. Additionally, for particles that are found to

be highly anisotropic or films that contain highly oriented crystallites, the observation of preferred orientation by powder XRD data can confirm that the morphology is characteristic of the bulk sample. Powder XRD cannot, however, unambiguously confirm phase purity, nor can it exclude the possibility that catalytically relevant impurities are present or reveal the presence of amorphous components.

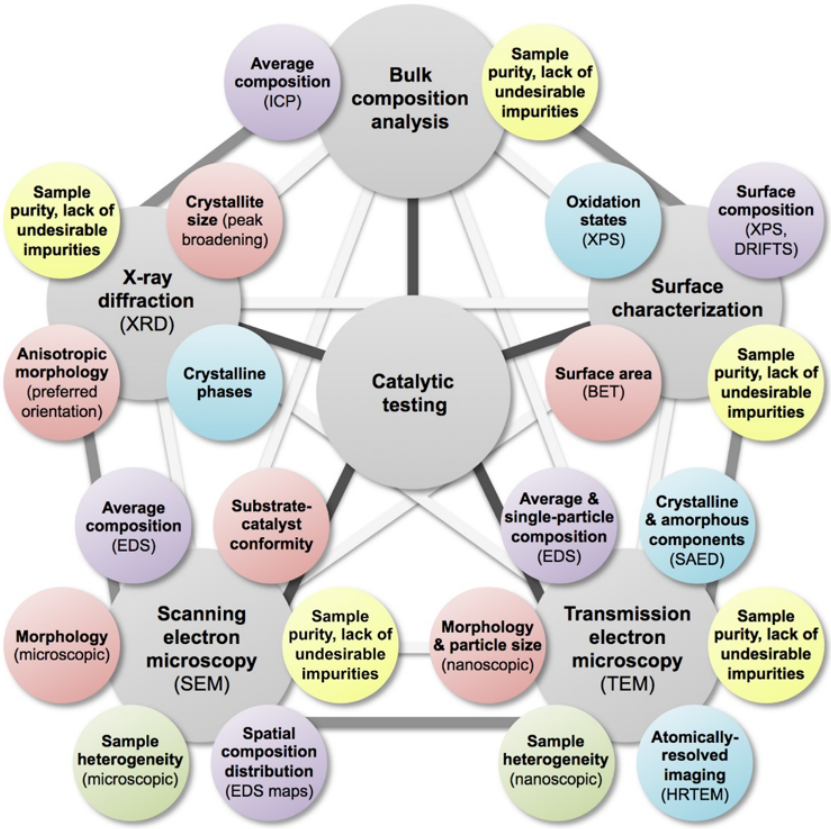

Figure K.5: Representative, non-exhaustive summary of materials-characterization data that can be used to understand the key characteristics that underpin the observed catalytic performance, including important aspects of surface and bulk structure, composition, and morphology. Color-coding shows complementary types of information that are provided by different characterization techniques.

Bulk elemental analysis can be used to compare the overall composition with the crystalline phase and thus to determine whether significant amorphous phases not detectable by powder XRD are present in a sample. For fully amorphous samples that have no long-range crystalline order, characterization can be more challenging. In these cases, rigorous analysis of composition, sample heterogeneity, and oxidation states can be especially important, along with any other microscopic or spectroscopic techniques that are appropriate and available. Because the structure and composition

at the surface of a catalyst may be quite different from that in the bulk, X-ray photoelectron spectroscopy (XPS) can be especially powerful. XPS can be utilized for identification of the oxidation states and chemical composition near the surface, both for crystalline and amorphous materials. However, for some systems, such as CoP and Co_2 P, differentiating oxidation states and quantifying their relative ratios is often not possible or straightforward. Synchrotron-based techniques such as X-ray absorption spectroscopy (XAS) and pair distribution function (PDF) analysis offer additional insights into the bulk and local structure of catalytic materials, and can be performed in situ and under operationally relevant conditions.[103]

Electron microscopy, particularly for nanoparticulate and thin-film metal phosphide catalysts, complements the bulk and surface analyses highlighted above. Both scanning electron microscopy (SEM) and transmission electron microscopy (TEM) can provide detailed information about the morphological aspects of a catalyst sample, including the distribution of shapes and sizes of the constituent particles or grains, as well as insights into sample heterogeneity. Beyond simply imaging the catalytic materials to characterize their morphological features, TEM data corroborate bulk structural and compositional information. For example, carefully and accurately analyzed lattice spacings, angles, and structural motifs observed by high-resolution TEM (HRTEM) can corroborate the assigned structure and provide knowledge about the facets that are exposed. Comparing the average particle or grain sizes observed by TEM to the grain sizes determined by Scherrer analysis of powder XRD data confirms that the bulk of the sample is comprised of same relative sizes as those observed microscopically. As with all microscopy techniques, only a small fraction of the sample is interrogated using SEM or TEM analysis, so care must be taken when formulating conclusions about the properties of a bulk sample from microscopic data alone.

Electron-diffraction data, both for individual particles and for large ensembles of particles, should match the bulk XRD data and, consequently, further confirm the structural assignment. Compositional analysis by energy-dispersive X-ray spectroscopy (EDS), again for both large ensembles of particles and also for individual particles as needed, can further validate the phase assignment. In conjunction with other types of materials-characterization data, such compositional analysis helps confirm that substantial amounts of amorphous or impurity phases are not present in a sample. SEM is particularly helpful because of the relatively large sample size (compared to TEM) that can be interrogated. For amorphous materials, high-

resolution EDS element maps obtained using TEM are particularly helpful because such maps can identify the presence, amounts, and distributions of the elements within the catalytic material, albeit for only a small region of the sample. For all materials, analysis before and after extended testing allows confirmation that the catalyst is stable under operating conditions. Materials characterization after electrochemical testing can be challenging because the catalyst is anchored directly to an electrode substrate, but surface analysis, as well as bulk analysis of the catalyst after physically detaching it from the electrode substrate, can still provide useful insights. These materials-characterization tools can provide valuable information when used separately, but can be even more powerful when used in a complementary fashion. Specifically, structural information from XRD should be in agreement with electron diffraction and with lattice spacings obtained from HRTEM. Similarly, grain sizes observed by TEM should be in agreement with Scherrer analysis from XRD. Elemental analyses from multiple techniques should match one another and should also match the stoichiometry expected for the assigned phase. Electrocatalysts can be examined both before and after electrocatalytic testing because several techniques can be performed directly on electrode substrates, including SEM, XPS, and XRD. Such analyses enable the identification of structural, compositional, and morphological changes during catalysis that provide important insights into both the true active form of the material and its stability.

K.6 Transistion Metal Phosphides for the HER

Despite being well-known catalysts for various hydrotreating processes, such as hydrodesulfurization and hydrodenitrogenation,[48,49] transition metal phosphides have only recently been explored as catalysts for the HER. Early work by Paseka[84,86] and Burchardt[82] demonstrated that amorphous alloys of Ni, Co, and Fe with small amounts of phosphorus (1 to 27 wt.%) were able to catalyze the HER at relatively low overpotentials in alkaline electrolytes. In 2005, based on density functional theory (DFT) calculations, Liu and Rodriguez predicted that Ni_2P may be a potential alternative to Pt, suggesting that synergistic effects between exposed proton-acceptor and hydride-acceptor centers on the (001) surface of Ni_2P could mimic features of the active sites of hydrogenase enzymes to facilitate efficient HER catalysis.[45] In 2013, we experimentally validated this prediction, showing that nanostructured Fe_2P-type Ni_2P was indeed a highly active HER electrocatalyst in acidic aqueous solutions.[50] Hu and co-workers similarly showed that Ni_2P nanopowders prepared through alternative solid-state approaches were also highly-active HER catalysts in

acidic aqueous solutions.[104] Since then, many groups worldwide have contributed extensively to the advancement of this field, including the discovery of other metal phosphide HER catalysts, the development of new and improved methods for the synthesis and processing of catalytic metal phosphide materials, the interrogation of their electrocatalytic and photocatalytic properties, investigations into the mechanisms by which they function, and demonstrations of their applicability in integrated systems and devices. While transition metal phosphides have also been shown to be active HER catalysts in pH-neutral and alkaline aqueous solutions, in this review we focus primarily on their behavior under acidic conditions that are relevant to proton-exchange-membrane electrolysis systems.

Nickel Phosphides

Table K.6 summarizes the performance of various nickel phosphide HER catalysts synthesized under different conditions and evaluated in 0.5 M H_2SO_4. The first Ni_2P materials studied experimentally as HER catalysts were nanoparticles synthesized by reacting trioctylphosphine (TOP) and nickel(II) acetylacetonate in 1-octadecene and oleylamine at 320 °C for 2 h.[50] Several synthetic routes to colloidal Ni_2P nanoparticles have been reported. For example, work by the groups of Brock,[47] Chiang,[62] Hyeon,[105] Robinson,[106] and Tracy,[62] along with our group,[57,89] demonstrated that high-quality Ni_2P nanocrystals could be readily obtained in solution by the co-reaction of organophosphine reagents such as TOP with nickel complexes or premade Ni nanopartices. The Ni_2P particles initially evaluated as HER catalysts were synthesized using the method reported by Tracy and co-workers because it produced a high yield of monodisperse, phase-pure Ni_2P nanocrystals through a simple one-pot reaction.[63] As shown in Figure 6, the as-synthesized Ni_2P particles were monodisperse, hollow, multi-faceted and single-crystalline, with an average diameter of 20 nm. The hollow morphology is the result of the nanoscale Kirkendall effect, which is caused by differences in the inward vs. outward diffusion rates of the constituent elements during the reaction. Kirkendall voids are commonly observed in metal phosphide nanoparticles synthesized by the decomposition of trioctylphosphine. Working electrodes of the Ni_2P material were prepared by applying the as-made nanoparticles to Ti foil substrates, followed by annealing at 450 °C in H_2(5 %)/N_2(95 %) to remove the organic ligands that capped the surface of the nanoparticles. The resulting nanoparticulate Ni_2P films required an overpotential of only −116 mV to produce an operationally relevant current density of $-10\,mA/cm^2$ ($\eta_{-10\,mA/cm^2} = -116\,mV$) in a strongly acidic electrolyte (0.50 M H_2SO_4), while

also demonstrating good stability and quantitative Faradaic efficiencies over 2 h of sustained hydrogen production.[50] Hu and co-workers similarly demonstrated that Ni_2P nanoparticles made using a bulk-scale reaction between NaH_2PO_2 and $NiCl_2 \cdot 6\,H_2O$ showed excellent activity and stability in both acidic and alkaline solutions, requiring overpotentials of approximately $\eta_{-10\,mA/cm^2} = -125$ mV and $\eta_{-10\,mA/cm^2} = -230$ mV in acidic and alkaline conditions, respectively.[104] The observed catalytic performance placed Ni_2P amongst the best non-noble-metal HER electrocatalysts in acidic aqueous solutions reported up to that point, including MoS_2,[40–42] NiMoN,[38] MoB,[35] and Mo_2C catalysts.[35,36]

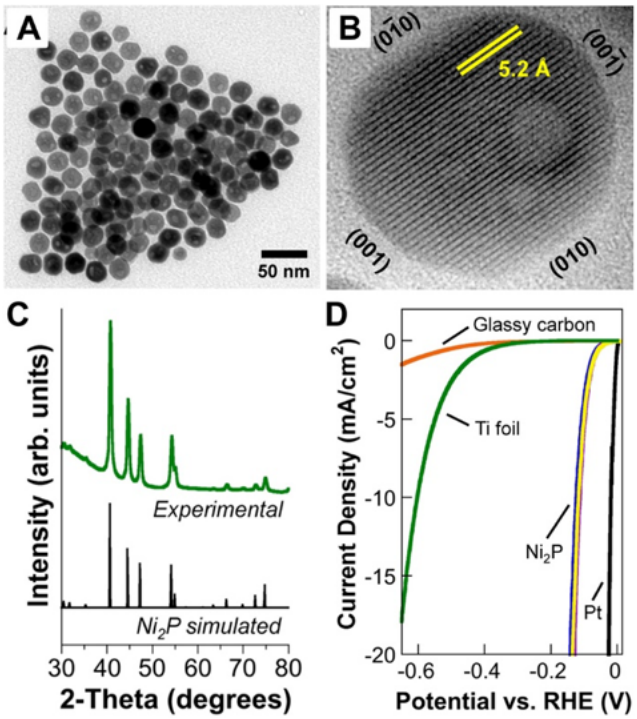

Figure K.6: A) TEM image of Ni_2P nanoparticles. B) HRTEM image of a representative Ni_2P nanoparticle highlighting the exposed Ni_2P(001) facet and the 5.2 Å lattice fringes that correspond to the (010) planes. C) Experimental powder XRD pattern for the Ni_2P nanoparticles, with the simulated pattern of Ni_2P shown for comparison. D) Polarization data for three individual Ni_2P electrodes in 0.5 M H_2SO_4, along with glassy carbon, Ti foil, and Pt in 0.5 M H_2SO_4, for comparison. Adapted with permission from ref.[50]. Copyright 2013 American Chemical Society.

Many other groups have described similar activities and stabilities for a wide portfolio of Ni_2P materials, including various nanostructures, films, and bulk powders (Figure 7). For example, Sun and coworkers reported Ni_2P nanoparticle films prepared via the low-temperature phosphidation of electrodeposited nickel hydroxide

precursors.[107] The resulting Ni_2P films displayed a HER performance comparable to those reported previously and made by other methods, requiring an overpotential of approximately $\eta_{-10\,mA/cm^2} = -130\,mV$ in 0.50 M H_2SO_4 and exhibiting stable hydrogen production for at least 15 h. Likewise, Liu and coworkers observed similar activities ($\eta_{-10\,mA/cm^2} \approx -124\,mV$) in samples of Ni_2P nanoparticles decorated on multiwalled carbon nanotubes (Ni_2P/CNT).[108] The Ni_2P/CNT material was synthesized in a one-pot reaction by the in-situ thermal decomposition of nickel acetylacetonate and TOP in an oleylamine solution of acid-treated CNTs, followed by deposition onto glassy carbon electrodes.

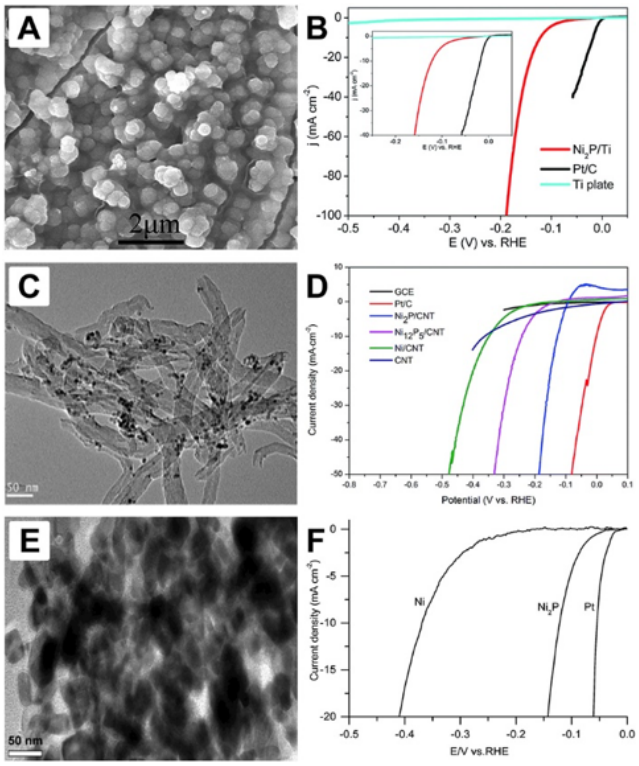

Figure K.7: A) SEM image of Ni_2P particles on a Ti plate and B) corresponding linear sweep voltammograms in 0.5 M H_2SO_4. Adapted with permission from ref.[107]. Copyright 2014 Royal Society of Chemistry. C) TEM image of Ni_2P particles decorating multiwalled carbon nanotubes and D) corresponding linear sweep voltammograms in 0.5 M H_2SO_4. Adapted with permission from ref.[108]. Copyright 2015 Royal Society of Chemistry. E) TEM image of bulk Ni_2P nanopowders and F) corresponding linear sweep voltammograms in 0.5 M H_2SO_4. Adapted with permission from ref.[104]. Copyright 2014 Royal Society of Chemistry.

Recently, our group also presented a general and scalable strategy for the synthesis of metal phosphide electrodes, including Ni_2P, based on the phosphidation of commercially available metal foils through the vapor-phase decomposition of

various organophosphine reagents (tributylphosphine and trioctylphosphine).[58] The resulting films exhibited excellent activities, with the Ni_2P electrodes requiring overpotentials for the HER of approximately $\eta_{-10\,mA/cm^2} = -128\,mV$ in 0.50 M H_2SO_4 and $\eta_{-10\,mA/cm^2} = -183\,mV$ in 1 M KOH. Additionally, we demonstrated that the same phosphidation strategy could be applied to evaporated metal thin films to form conformal metal phosphide coatings on a variety of substrates, including relevant photocathode materials such as highly-doped Si. Despite the low loadings and low surface areas of the samples, the Ni_2P thin-films on Si exhibited moderate activities for the HER, requiring an overpotential of $\eta_{-10\,mA/cm^2} = -240\,mV$ in 0.50 M H_2SO_4.

Significant enhancements to the HER activity of Ni_2P have been reported through the use of various phosphide-carbon composites and 3D electrode geometries. For instance, Wang and coworkers presented carbon-encapsulated Ni_2P nanoparticles (Ni_2P/C) prepared by the reduction of glucose-coated $NiNH_4PO_4 \cdot H_2O$ nanorods with H_2 at 700 °C.[109] These Ni_2P/C nanocomposites showed enhanced HER performance, requiring only $\eta_{-10\,mA/cm^2} = -87\,mV$ in 0.50 M H_2SO_4. The improved electrocatalytic activity of the Ni_2P/C composite was attributed to enriched nanoporosity and a more efficient use of the available active sites. Similarly, Du and coworkers reported a three-dimensional few-layer graphene/nickel foam (G@NF) electrode coated with nanostructured Ni_2P that displayed exceptional HER activity, requiring an overpotential of $\eta_{-10\,mA/cm^2} = -55\,mV$ in 0.50 M H_2SO_4.[110] Such high catalytic performance was attributed to the presence of more catalytically active sites provided by the larger surface area of the porous electrode, and to enhanced ion and electron transfer. However, the activity of the 3D Ni_2P–G@NF electrode was normalized to a flat geometric surface area despite being highly porous. Despite the wide diversity of synthetic preparations, sizes, morphologies, and supports that have been reported for Ni_2P-based HER catalysts, most results are in agreement, with an average reported overpotential for Ni_2P of $\eta_{-10\,mA/cm^2} = -125\,mV$ in 0.50 M H_2SO_4.

Other nickel phosphide phases with different compositions and structures have also been explored as HER electrocatalysts (Figure 8). Dismukes and coworkers reported micron-sized Ni_5P_4 particles prepared by the decomposition of nickel acetylacetonate, trioctylphosphine and trioctylphosphine oxide at $\approx$ 330 °C.[111] Electrodes of the material were fabricated by pressing 50 mg of dried Ni_5P_4 powders into 6 mm diameter pellets, and sealing all but one side with epoxy. The reported overpotential

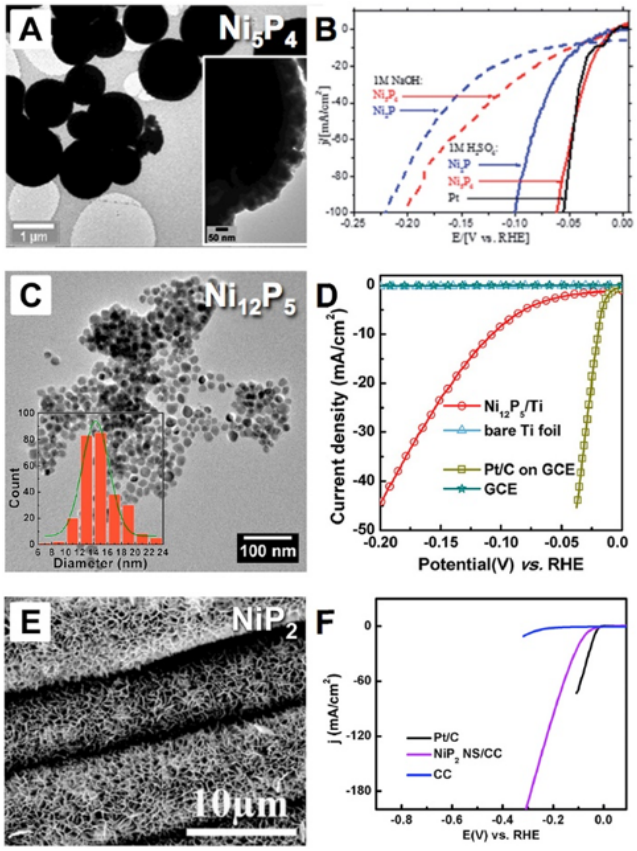

Figure K.8: A) TEM image of Ni_5P_4 particles and B) corresponding linear sweep voltammograms in 0.5 M H_2SO_4. Adapted with permission from ref.[111]. Copyright 2015 Royal Society of Chemistry. C) TEM image of $Ni_{12}P_5$ nanoparticles and D) corresponding linear sweep voltammograms in 0.5 M H_2SO_4. Adapted with permission from ref.[112]. Copyright 2014 American Chemical Society. E) TEM of NiP_2 nanosheets on carbon cloth and F) corresponding linear sweep voltammogram in 0.5 M H_2SO_4. Adapted with permission from ref.[113]. Copyright 2014 Royal Society of Chemistry.

required by the Ni_5P_4 electrodes in 0.50 M H_2SO_4 was an exceptionally small value of $\eta_{-10\,\mathrm{mA/cm^2}} = -23\,\mathrm{mV}$, which is almost identical to that of Pt. It is unclear why this Ni_5P_4 catalyst has such low overpotentials relative to all other reported metal phosphide HER catalysts. Ni_5P_4 nanoparticles prepared through similar methods and of comparable surface areas were reported by Liu and coworkers under similar testing conditions to require $\eta_{-10\,\mathrm{mA/cm^2}} = -118\,\mathrm{mV}$.[114] Likewise, Shalom and coworkers reported the growth of Ni5P4 nanoarchitectures directly on Ni foils by heating the metal with red phosphorus at 550 °C for 1 h under an inert atmosphere.[115] In this case, the reported overpotential for the Ni_5P_4 nanoarchitectures was $\eta_{-10\,\mathrm{mA/cm^2}} = -140\,\mathrm{mV}$, in close agreement with other reports.

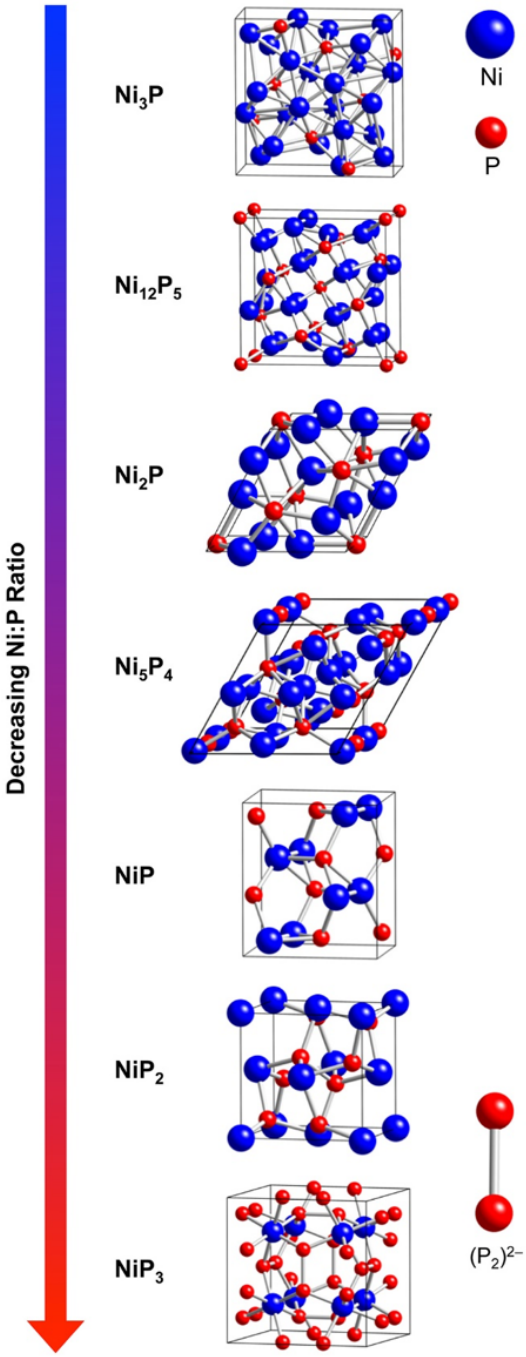

Figure K.9:]

Crystal structures of various nickel phosphides spanning a range of Ni:P ratios. The $(P_2)^{2-}$ dimer, which appears in the NiP_2 and NiP_3 polyphosphides, is also shown.

The $Ni_{12}P_5$ phase has also been identified as an active HER electrocatalyst (Figure 8). $Ni_{12}P_5$ nanoparticles on a titanium substrate[112] and $Ni_{12}P_5$/CNT nanohybrids[116] were reported to require overpotentials of approximately $\eta_{-10\,\mathrm{mA/cm^2}} = -105$ and

$\eta_{-10\,\mathrm{mA/cm^2}} = -129\,\mathrm{mV}$ in acid, respectively. In addition, the HER activity of NiP_2 nanosheet arrays supported on carbon cloth (NiP_2 NS/CC) has also been reported by Sun and coworkers.[113] The NiP_2 NS/CC material was obtained through a two-step synthetic strategy. First, $Ni(OH)_2$ nanosheets were grown on carbon cloth through hydrothermal methods, followed by phosphidation with NaH_2PO_2 at 300 °C for 2 h in an inert atmosphere. The NiP_2 NS/CC composites were highly active for the HER in acidic solutions and required an overpotential of $\eta_{-10\,\mathrm{mA/cm^2}} = -75\,\mathrm{mV}$. The NiP_2 NS/CC electrodes also maintained their catalytic activity for at least 57 h. However, it is worth noting again that 3D electrode geometries and other porous architectures can produce artificially enhanced performance if the reported activity is not normalized for exposed and/or active surface areas.

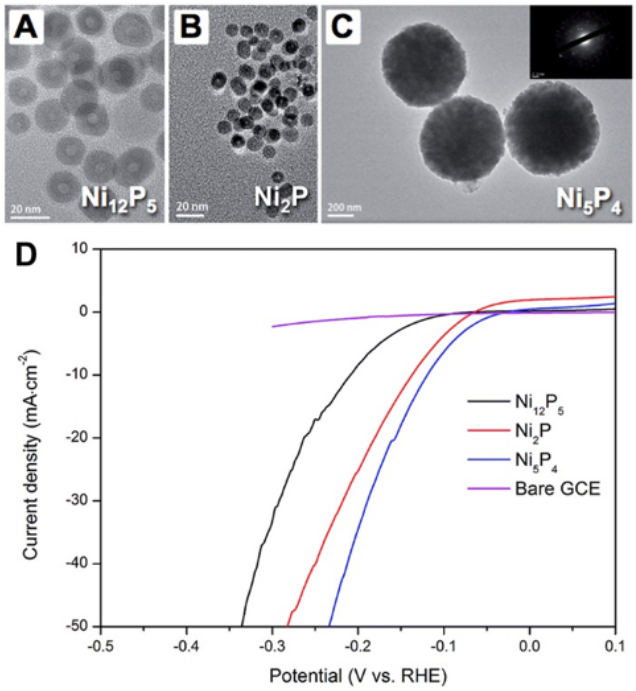

Figure K.10: TEM images of $Ni_{12}P_5$, Ni_2P, and Ni_5P_4 nanoparticles and their respective linear sweep voltammograms in 0.5 M H_2SO_4. Adapted with permission from ref.[114]. Copyright 2015 Royal Society of Chemistry.

Comparisons among the different nickel phosphides are particularly interesting and instructive (Figure 9). In face-centered cubic (fcc) Ni, each Ni atom is surrounded by and coordinated to 12 other Ni atoms. However, as phosphorus is incorporated and the P:Ni ratio in metal phosphides increases, the number of direct Ni – Ni interactions progressively decreases while the Ni – P coordination increases. In the case of pyrite-type NiP_2, no direct Ni – Ni interactions remain and phosphorus-phosphorus bonding

(P−P dimers, as mentioned previously) is observed. Additionally, the introduction of P into the structure significantly changes the geometry and arrangement of the Ni sites and leads to a gradual increase in the Ni−Ni bond distance from around 2.49 Å on the Ni(111) surface to 3.85 Å on the NiP_2 (001) surface (Figure 9). These differences in crystal structure and bonding may have a direct impact on the catalytic properties of the various metal phosphides. Liu and coworkers prepared different nanostructured nickel phosphide phases ($Ni_{12}P_5$, Ni_2P, Ni_5P_4) and compared their activities for the HER under similar conditions (Figure K.10).[114] The Ni_5P_4 phase exhibited superior electrocatalytic performance relative to $Ni_{12}P_5$ and Ni_2P, with the behavior attributed to a higher positive charge on the Ni and a stronger ensemble effect from P in Ni_5P_4. However, as can be seen in Figure K.10, variations in the particle sizes, morphologies, and surface areas of the samples could account for some of the observed differences in HER activity. Along with similar studies by Kucernak and Sundaram comparing $Ni_{12}P_5$ and Ni_2P[117] and by Dismukes and coworkers comparing Ni_5P_4 and Ni_2P,[111] these results suggest that the metal-to-phosphorus ratio in metal phosphides might play an important role in affecting the HER performance, with more phosphorus-rich phases tending to exhibit higher HER activities. While comparing the intrinsic activities of HER catalysts tested using different electrode fabrication methods and loadings poses significant challenges, reports on the HER activity of NiP_2 nanosheets ($\eta_{-10\,mA/cm^2} = -75\,mV$) also seems to support these conclusions.[113] The observed trends are consistent with the putative mechanism for the HER on Ni_2P(001), which invokes an ensemble effect involving cooperativity of the P and Ni atoms that implies a dependence on the P:Ni ratio.

Material	$\eta_{-10\,mA/cm^2}$	$\eta_{-20\,mA/cm^2}$	Tafel slope (mV dec^{-1})	Exchange Current Density (A/cm^2)	Loading density (mg/cm^2)	Reference
Ni_2P NPs/Ti	≈-116	-130	-46	3.3×10^{-5}	1	[50]
Ni_2P/Ni	-128	-153	66	-	-	[58]
Ni_2P NS/Ni foam	≈-115	≈-140	68	-	-	[79]
Polydispersed Ni_2P/GCE	≈-125	-140	≈87	-	0.38	[104]
Nanoparticle films Ni_2P/Ti	≈-130	-138	60	-	2	[107]
Ni_2P/CNT	-124	-	53	5.37×10^{-5}	-	[108]
Peapod-like Ni_2P/C	-87	-115	54	-	0.36	[109]
Ni_2P-G@NF	≈-150	-	≈30		-	[110]
Ni_5P_4 MP pellet	-23	-	33	-	177	[111]
Ni_2P MP pellet	-42	-	38	-	177	[111]
$Ni_{12}P_5$/Ti	-107	-141	63	-	3	[112]
NiP_2 NS/CC	-75	-	51	2.60×10^{-4}	4.3	[113]
Ni_2P NPs	-137	-	49	-	1.99	[114]
Ni_5P_4 NPs	-118	-	42	-	1.99	[114]
$Ni_{12}P_5$ NPs	-208	-	75	-	1.99	[114]
Ni_5P_4/Ni	-140	-	40	-	-	[115]
$Ni_{12}P_5$/CNT	-129	-	56	7.10×10^{-5}	0.75	[116]
Ni_2P/GCE	-	-	84	2.90×10^{-6}	0.15	[117]
$Ni_{12}P_5$/GCE	-	-	108	3.70×10^{-7}	0.15	[117]
MOF-derived Ni_2P	≈-200	-	62	7.10×10^{-5}	0.35	[118]
MOF-derived $Ni_{12}P_5$	≈-650	-	270	4.50×10^{-5}	0.35	[118]
Ni_2P/CNSs	-92	-108	47	4.90×10^{-4}	-	[119]
Ni_2P NPs/Ni foam	-136	-	-	-	0.14	[120]
Ni-P films	-93	-	33 and 98	-	0.35	[121]
Ni_2P-NRs/Ni	-131	-163	106.1	8.62×10^{-5}	-	[122]
Ni_5P_4	-	-62	46.1	2.75×10^{-4}	0.15	[123]
Ni_2P	-	-228	83.3	2.10×10^{-4}	-	[124]
Ni_2P/NRGO	-102	-122	59	4.90×10^{-5}	-	[125]
Ni_2P-G/NF	-75	-	51	-	-	[126]
(Ni_2P)@graphitized carbon	-45	-	46	-	0.38	[127]

Table K.1: Compilation of HER performance metrics for various nickel phosphide catalysts synthesized under different conditions and evaluated in 0.5 M H_2SO_4

Cobalt Phosphides

Following the initial studies of Ni_2P as an Earth-abundant HER catalyst, cobalt phosphide (CoP) was also identified as an active and acid-stable HER catalyst.[128] Like Ni_2P, CoP is a structurally and compositionally distinct but active HDS catalyst. CoP nanoparticles, which were prepared by reacting Co nanoparticles with TOP at ≈ 320 °C, were quasi-spherical, multi-faceted, highly uniform, and hollow, with an average diameter of 13 ± 2 nm (Figure K.11), similar to those of Ni_2P mentioned previously. Electrodes comprised of CoP nanoparticles on a Ti support outperformed Ni_2P and other nickel-containing phosphides in both activity and stability in 0.50 M H_2SO_4, requiring an overpotential of $\eta_{-10\,mA/cm^2} = -75$ mV and remaining stable for over 24 h while exhibiting 100 % Faradaic efficiency.

Several groups have since corroborated these results for a wide variety of CoP morphologies and supports (Figure K.12). For example, Sun and coworkers have reported similar HER activities in 0.50 M H_2SO_4 for a number of different CoP-based electrodes obtained via the low-temperature phosphidation of various cobalt

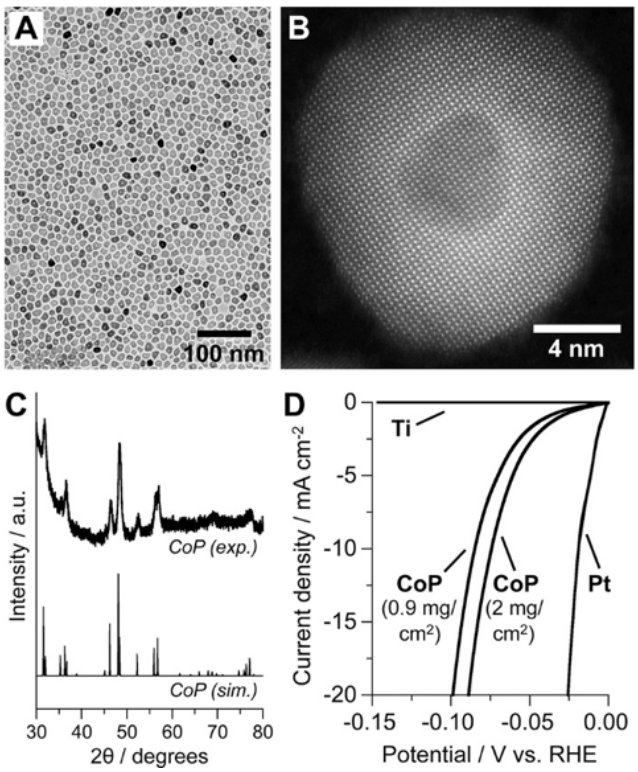

Figure K.11: (A) TEM image, (B) high-angle annular dark field (HAADF) scanning transmission electron microscopy (STEM) image, and (C) powder XRD data for CoP nanoparticles. (D) Polarization data for CoP/Ti electrodes in 0.50 M H_2SO_4, along with Ti foil and Pt mesh for comparison. Panels (A), (C), and (D) adapted with permission from ref.[128]. Copyright 2014 WILEY-VCH Verlag GmbH & Co. KGaA, Weinheim.

precursors with NaH_2PO_2. These reports include carbon nanotubes decorated with CoP nanocrystals ($\eta_{-10\,\mathrm{mA/cm^2}} = -122\,\mathrm{mV}$),[129] CoP nanosheet arrays supported on Ti plates ($\eta_{-10\,\mathrm{mA/cm^2}} = -90\,\mathrm{mV}$),[128] self-supported nanoporous cobalt phosphide nanowire arrays on carbon cloth ($\eta_{-10\,\mathrm{mA/cm^2}} = -67\,\mathrm{mV}$),[127] CoP nanotubes ($\eta_{-10\,\mathrm{mA/cm^2}} = -72\,\mathrm{mV}$),[128] three-dimensional interconnected networks of porous CoP nanowires ($\eta_{-10\,\mathrm{mA/cm^2}} = -100\,\mathrm{mV}$),[130] and CoP nanoparticle films on carbon cloth ($\eta_{-10\,\mathrm{mA/cm^2}} = -48\,\mathrm{mV}$).[131] It is worth noting that the increased activity observed in a few of these instances could be attributed to the use of highly porous 3D electrodes without normalization to exposed or active surface areas. Many other reports, too numerous to include as an exhaustive list, describe related iterations and comparable HER activities for various CoP materials.

Interestingly, Lewis, Soriaga, and coworkers have demonstrated that electrodeposited amorphous Co–P films exhibit HER activities comparable to those of crys-

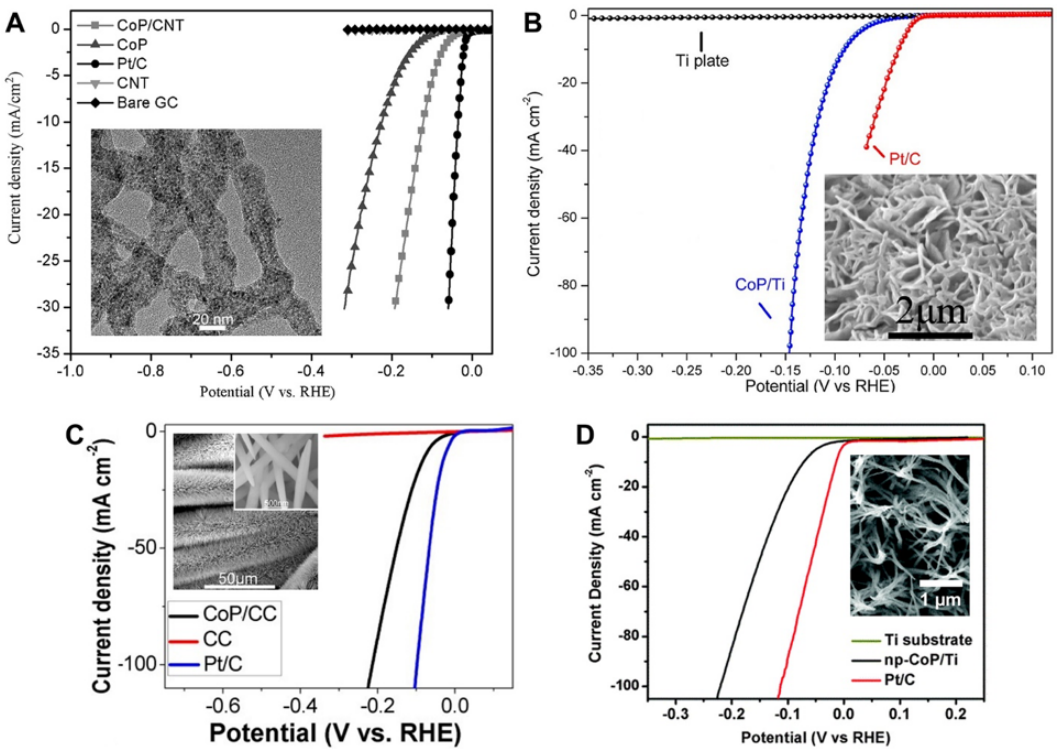

Figure K.12: Polarization data in 0.5 M H_2SO_4, and corresponding TEM or SEM images (in the insets) for various nanostructured CoP HER catalysts. A) CoP nanocrystals on carbon nanotubes. Adapted with permission from ref.[132]. Copyright 2014 WILEY-VCH Verlag GmbH & Co. KGaA, Weinheim. B) CoP nanosheets on a Ti plate. Adapted with permission from ref.[133]. Copyright 2014 American Chemical Society. C) Self-supported CoP nanowires on carbon cloth. Adapted with permission from ref.[129]. Copyright 2014 American Chemical Society. D) CoP nanosheets on a Ti plate. Adapted with permission from ref.[130]. Copyright 2014 Royal Society of Chemistry.

talline CoP phases (Figure K.13).[81] The Co–P films were synthesized by cathodic deposition from a boric acid solution of Co^{2+} and $H_2PO_2^-$ on Cu foils, followed by operando purification to produce an electrocatalyst with a Co:P atomic ratio of 1:1. The electrodeposited CoP catalysts showed high activities with an overpotential of $\eta_{-10\,\mathrm{mA/cm^2}} = -85\,\mathrm{mV}$ needed in highly acidic solutions (0.50 M H_2SO_4). In agreement with this report, Sun and coworkers later observed comparable activities using electrodeposited amorphous Co–P films prepared under similar experimental conditions ($\eta_{-10\,\mathrm{mA/cm^2}} = -98\,\mathrm{mV}$).

As in the case of Ni_2P, despite the wide diversity of synthetic preparations, sizes, morphologies, and supports that have been reported, most results are in agreement, reporting an average overpotential for CoP of $\eta_{-10\,\mathrm{mA/cm^2}} = -80\,\mathrm{mV}$ in 0.50 M

H_2SO_4. Table K.6 summarizes the performance of various cobalt phosphide HER catalysts synthesized under various conditions and evaluated in 0.5 M H_2SO_4.

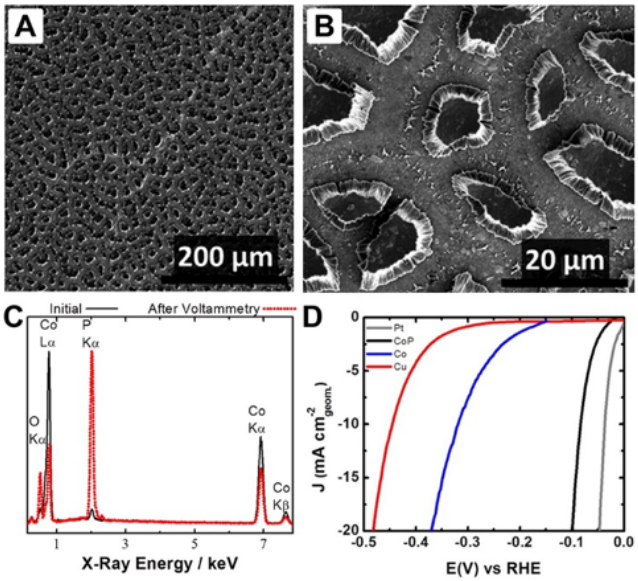

Figure K.13: (A) Low-magnification and (B) high-magnification SEM images of electrodeposited amorphous Co-P films. (C) XPS spectrum of Co-P films before and after voltammetry. (D) Linear sweep voltammograms in 0.5 M H_2SO_4, along with Pt, Co, and Cu controls. Adapted with permission from ref.[81]. Copyright 2014 American Chemical Society.

Comparisons among electrocatalysts with different structures, but identical constituent elements and morphologies, are important for identifying key structural characteristics that could lead to higher HER activities. With this in mind, we recently studied nanostructures of Co_2P, a cobalt phosphide phase that is compositionally and structurally distinct from CoP, by synthesizing by morphologically equivalent Co_2P and CoP nanoparticles and evaluating their catalytic activity for the HER in 0.50 M H_2SO_4 (Figure K.14).[134] The Co_2P phase displayed slightly higher overpotentials ($\eta_{-10\,mA/cm^2} = -95$ mV) than CoP ($\eta_{-10\,mA/cm^2} = -75$ mV). This behavior correlates with the different Co/P ratio of the phases, and suggests that the increased Co – P character of CoP may provide a higher density of proximal cobalt and phosphorus surface atoms, which are hypothesized to be active sites for the HER. Liu and coworkers further explored the influence of phase, structure, and support effects on the HER activity by synthesizing a series of cobalt phosphide-based electrocatalysts, including Co_2P, CoP, Co_2P/CNTs, CoP/CNTs, Co_2P/nitrogen-doped carbon nanotubes (NCNTs) and CoP/NCNTs, through the solution-based decomposition of various organophosphine reagents.[135] Their results indicated that catalytic activity

Material	$\eta_{-10\,mA/cm^2}$	$\eta_{-20\,mA/cm^2}$	Tafel slope (mV dec^{-1})	Exchange Current Density (A/cm^2)	Loading density (mg/cm^2)	Reference
Co_2P/Co	-174	-	60	-		[58]
CoP/CC	-49	-59	30.1	-	13.6	[78]
Co-P films	-85	-	50	2.00×10^{-4}	-	[81]
CoP NPs/Ti	-75	-85	50	1.40×10^{-4}	2	[128]
CoP/CC	-67	-100	51	2.88×10^{-4}	0.92	[129]
CoP NTs	-	-129	60	-	-	[137]
CoP NPs	-	-297	82	-	-	[137]
CoP NWs/Ti	-	-95	65	-	0.8	[130]
CoP NPs/CC	-48	-	70	-	4	[131]
CoP/CNT	-122	-	54	1.30×10^{-4}	0.28	[132]
CoP/Ti	-90	-	43	-	2	[133]
Co_2P NPs/Ti	-95	-109	45	-	1	[134]
Co_2P	-406		101	3.20×10^{-3}	-	[135]
CoP	-383		90	1.70×10^{-2}	-	[135]
Co_2P/CNTs	-195	-219	74	3.90×10^{-2}	-	[135]
CoP/CNTs	-165	-198	68	6.80×10^{-2}	-	[135]
Co_2P/NCNTs	-	-171	62	1.02×10^{-1}	-	[135]
CoP/NCNTs	-79	-99	49	3.20×10^{-1}	-	[135]
Branched CoP	-	-117	48	-	1	[136]
CoP NWs	-110	-142	54	1.60×10^{-4}	0.35	[138]
CoP NPs	-221	-	61	5.40×10^{-5}	0.35	[138]
CoP NSs	-164	-	87	3.20×10^{-5}	0.35	[138]
Co_2P NRs/Ti	-134	-167	51.7	-	1	[139]
Co-P films	-94	-	42	-	2.6	[140]
CoP/RGO	≈250	-	104.8	4.00×10^{-5}	0.29	[141]
CoP/C	-130	-	-	-	-	[142]
Urchin-like CoP NCs	≈100	-	46	-	0.28	[143]
CoP NBAs/Ti	-203	-	40	-	1.96	[144]
CoP@C Nanocables	-170	-	61	-	0.35	[145]
Co_2P NW	≈100	-	45	-	2	[146]
CoP NW	≈100	-	41	-	2	[146]
CoP_2/RGO	-88	-106	50	-	0.28	[147]
CoP hollow polyhedron	-159	-	59	3.70×10^{-2}	0.10	[148]
CoP particles	-355	-	77	5.00×10^{-3}	0.10	[148]
CoP NPAs	-393		105	-	-	[149]
CoP NRAs	-181		69	-	-	[149]
Co_2P/GCE	-	-160	53	2.10×10^{-4}	-	[150]

Table K.2: Compilation of HER performance metrics for various cobalt phosphide catalysts synthesized under different conditions and evaluated in 0.5 M H_2SO_4

followed the order CoP/NCNTs > Co_2P/NCNTs > CoP/CNTs > Co_2P/CNTs > CoP > Co_2P, with the more phosphorus-rich CoP phase outperforming the corresponding Co_2P counterparts in each case. The highest activity of the series was obtained by the CoP/NCNTs catalysts, which required $\eta_{-10\,mA/cm^2} = -85\,mV$. While preliminary, these reports are in agreement with observations on the nickel phosphide system, indicating that more phosphorus-rich phases exhibit higher HER activities. Furthermore, direct comparisons by our group of multifaceted CoP nanoparticles with highly branched CoP nanostructures that exposed a high density of (111) facets suggested that the high HER activity of CoP is intrinsic to the system, and that shape control may not play a significant role in defining the magnitude of the overpotentials required to produce operationally relevant cathodic current densities.[136]

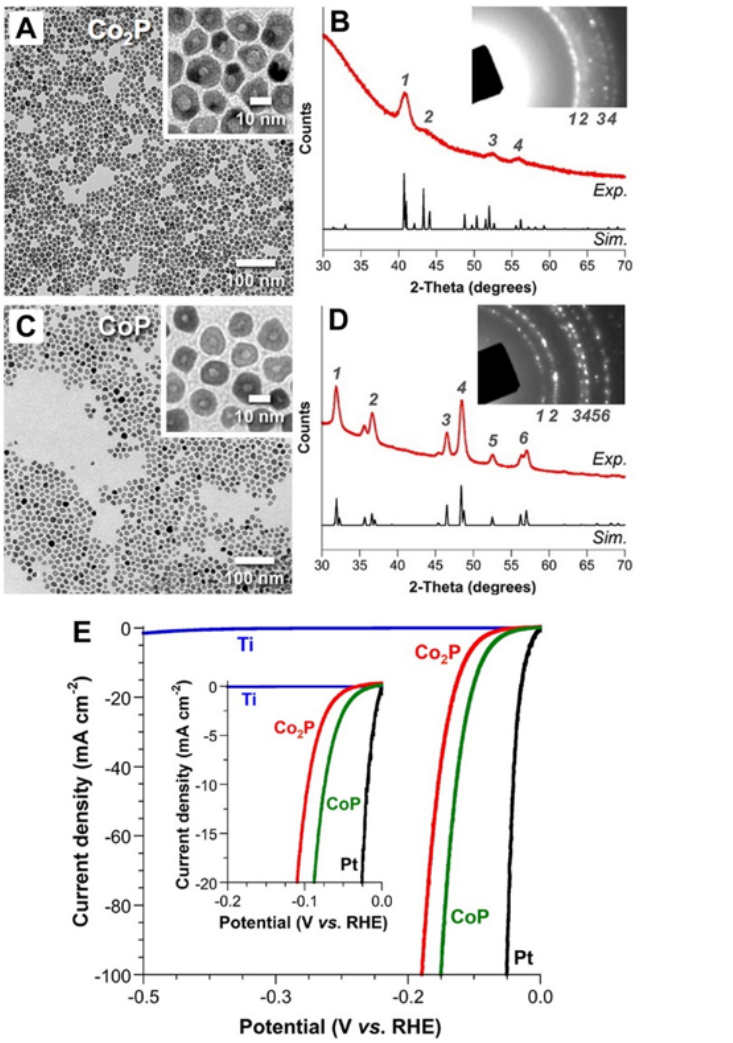

Figure K.14: (A) TEM image of Co_2P nanoparticles and (B) corresponding XRD and SAED patterns. (C) TEM image of CoP nanoparticles and (D) corresponding XRD and SAED patterns. (E) Polarization data of CoP/Ti and Co_2P/Ti electrodes in 0.5 M H_2SO_4 along with Pt mesh and bare Ti foil for comparison. Adapted with permission from ref.[134]. Copyright 2015 American Chemical Society.

Iron Phosphides

As the cheapest and most terrestrially abundant transition metal, iron is a particularly interesting target for incorporation into metal phosphide HER catalysts. Iron-containing clusters have been found in the active sites of various enzymes including [FeFe] and [Fe]-only hydrogenases, which have been demonstrated to be highly active and efficient HER catalysts in biological systems. Interestingly, iron phosphides such as FeP and Fe_2P are also known hydrodesulfurization catalysts, yet with significantly lower activities than other transition metal phosphides

such as Ni_2P.[48,49,135,151] Both our group and the Sun group independently identified MnP-type FeP as an exceptionally active HER electrocatalyst in acidic, basic and neutral-pH conditions (Figure K.15),[152,153] that outperforms other comparable metal phosphide systems including CoP and Ni_2P. Table 3 summarizes the performance of various iron phosphide HER catalysts synthesized under various conditions and evaluated in 0.5 M H_2SO_4.

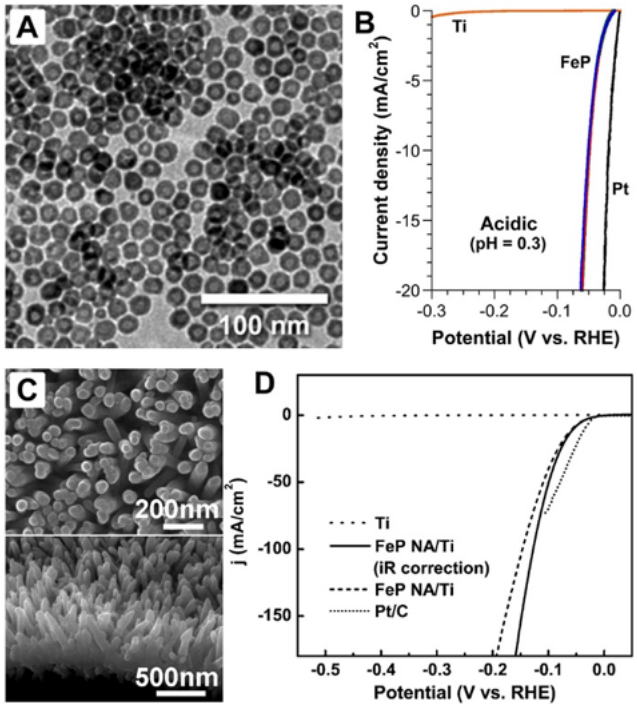

Figure K.15: (A) TEM image of FeP nanoparticles and B) polarization data for FeP/Ti electrodes. Adapted with permission from ref.[152]. Copyright 2014 American Chemical Society. (C) SEM image of self-supported FeP nanowires on Ti and (D) corresponding polarization data in 0.5 M H_2SO_4. Adapted with permission from ref.[153]. Copyright 2014 WILEY-VCH Verlag GmbH & Co. KGaA, Weinheim.

Similar to our CoP system, we synthesized colloidal FeP nanoparticles by reacting premade Fe nanocrystals with TOP at elevated temperatures.[152] The resulting FeP nanoparticles were spherical and hollow, with an average diameter of 13 ± 2 nm (Figure K.15), and were morphologically comparable to the Ni_2P and CoP nanoparticles that had been synthesized previously. Working electrodes (FePNP/Ti) with FeP nanoparticles were prepared by drop-casting appropriate amounts to obtain mass loadings of 1 mg/cm^2 of an FeP nanoparticle suspension onto Ti substrates, followed by treatment at 450 °C in a reducing atmosphere to remove any remaining surface ligands. Linear sweep voltammetry measurements for the FeP NP/Ti

electrodes in acidic solutions (0.5 M H_2SO_4) demonstrated exceptionally high HER activities, with overpotentials of only $\eta_{-10\,mA/cm^2} = -50\,mV$ required. Sun and coworkers studied FeP nanowire arrays supported on conductive Ti plates (FeP-NA/Ti) (Figure K.15).[132] These arrays were synthesized chemically by converting FeOOH nanowire arrays, which were hydrothermally grown directly onto Ti plates, into FePNA/Ti by a low-temperature phosphidation reaction with NaH_2PO_2 . The resulting FePNA/Ti system required an overpotential of $\eta_{-10\,mA/cm^2} = -55\,mV$ in 0.5 M H_2SO_4, comparable to the behavior of the FePNP/Ti system. While both FeP electrodes exhibited HER activities that were significantly higher than comparable electrodes of Ni_2P and CoP, long-term stability measurements indicated decreases in activity of the Fe-based systems after more than 15 h of sustained hydrogen production. In the case of the FePNP/Ti sample, the required overpotential increased by approximately 52 mV, compared to an increase of 11 mV for comparable CoP nanoparticles after 24 h of sustained operation at $-20\,mA/cm^2$. While activity is an important metric for HER performance, a practical catalyst clearly requires a balance between activity and long-term stability. As such, CoP might be a more robust candidate for further development and testing efforts, such as integration with light absorbers and use in solar-driven water-splitting devices.

Other phases in the iron phosphide system have also been studied as HER catalysts. For example, Yang and coworkers reported phosphorus-rich FeP_2/C nanohybrids prepared by the pyrolysis of ferrocene and red phosphorus in an evacuated and sealed quartz tube at 500 °C.[154] The resulting material was investigated for the HER in 0.50 M H_2SO_4 and showed very low HER activities, requiring an overpotential of −500 mV to achieve a current density of $-5\,mA/cm^2$. In addition, Fe_2P nanoparticles encapsulated in a sandwichlike graphited carbon envelope were reported by Wang and coworkers, with an observed overpotential for the HER of $\eta_{-10\,mA/cm^2} = -88\,mV$.[155] While still preliminary, the lower HER activity of Fe_2P relative to FeP is in agreement with previously established general trends that phosphide phases having a higher phosphorus content show improved activities for the HER. However, it is possible that this activity trend may not extend to phosphorus-rich phases, such as FeP_2, because their different structures and bonding (e.g. P−P bonds) may impact their relative activities and stabilities. While still preliminary, the lower HER activity of Fe_2 P relative to FeP is in agreement with previously established general trends that phosphide phases having a higher phosphorus content show improved activities for the HER. However, it is possible that this activity trend may not extend to phosphorus-rich phases, such as FeP_2, because their different

Material	$\eta_{-10\,mA/cm^2}$	$\eta_{-20\,mA/cm^2}$	Tafel slope (mV dec^{-1})	Exchange Current Density (A/cm^2)	Loading density (mg/cm^2)	Reference
Fe_{2P}/Fe	-191	-	55	-	-	[58]
FeP NPs/Ti	-50	-	37	4.30×10^{-4}	1	[152]
FeP NA/Ti	-55	-72	38	4.20×10^{-4}	0.28	[153]
FeP2/C	-	-	66	1.75×10^{-6}	0.42	[154]
Fe_2P/GCS	≈100	-	49	-	0.36	[155]
FeP/CC	-34	-43	29.2	6.80×10^{-4}	4.9	[156]
HMFeP@C	-115	-	56	1.91×10^{-4}	-	[157]
FeP NWs	-96	-	39	1.70×10^{-4}	-	[158]
FeP_2 NWs	-61	-	37	5.50×10^{-4}	-	[158]
FeP/GS	-123	-	50	1.20×10^{-4}	0.28	[159]
FeP NAs/CC	-58	-	45	5.00×10^{-4}	1.5	[160]
FeP NAs/Ti	-85	-	60	-	-	[161]
FeP NSs	≈240	-	67	-	-	[162]
FeP/CC	-	-54	32	5.90×10^{-4}	4.2	[163]
FeP-CS	-112	-	58	2.20×10^{-4}	0.28	[164]

Table K.3: Compilation of HER performance metrics for various iron phosphide catalysts synthesized under different conditions and evaluated in 0.5 M H_2SO_4

Material	$\eta_{-10\,mA/cm^2}$	$\eta_{-20\,mA/cm^2}$	Tafel slope (mV dec^{-1})	Exchange Current Density (A/cm^2)	Loading density (mg/cm^2)	Reference
MoP	≈ -130	-	54	3.40×10^{-5}	-	[165]
Mo_3P	≈ -500	-	147	-	-	[165]
WP/Ti	-120	-140	54	4.50×10^{-5}	1	[166]
WP NAs/CC	-130	-	69	2.90×10^{-4}	2	[167]
WP_2 SMPs	-161	-	65	1.70×10^{-5}	0.5	[168]
MoP NPs	-125	-	54	8.60×10^{-5}	0.36	[169]
MoP/GCE	-246	-	60	4.15 x 10-6	7.1×10^{-2}	[170]
MoP/CF	-200	-	56.4	-	0.36	[171]
MoP MPs	-150	-	50	1×10^{-5}	0.1	[172]
MoP flakes	-	-155	71.77	-	1.425	[173]
MoP_2 NPs/Mo	-143	-	57	6.00×10^{-5}	-	[174]
WP_2 nanorods	-148	-	52	1.30×10^{-5}	-	[175]

Table K.4: Compilation of HER performance metrics for various molybdenum and tungsten phosphide catalysts synthesized under different conditions and evaluated in 0.5 M H_2SO_4

structures and bonding (e.g. P−P bonds) may impact their relative activities and stabilities.

Molybdenum and Tungsten Phosphides

Molybdenum and tungsten phosphides are among some of the most active HDS catalysts reported to date, making them attractive targets as catalysts for the HER.[48,49] Table 4 summarizes the performance of various molybdenum phosphide and tungsten phosphide HER catalysts synthesized and evaluated under various conditions. Wang and coworkers reported the HER activity of crystalline Mo_3P and MoP prepared through bulk solid-state approaches.[165] The metal-rich Mo_3P phase dis-

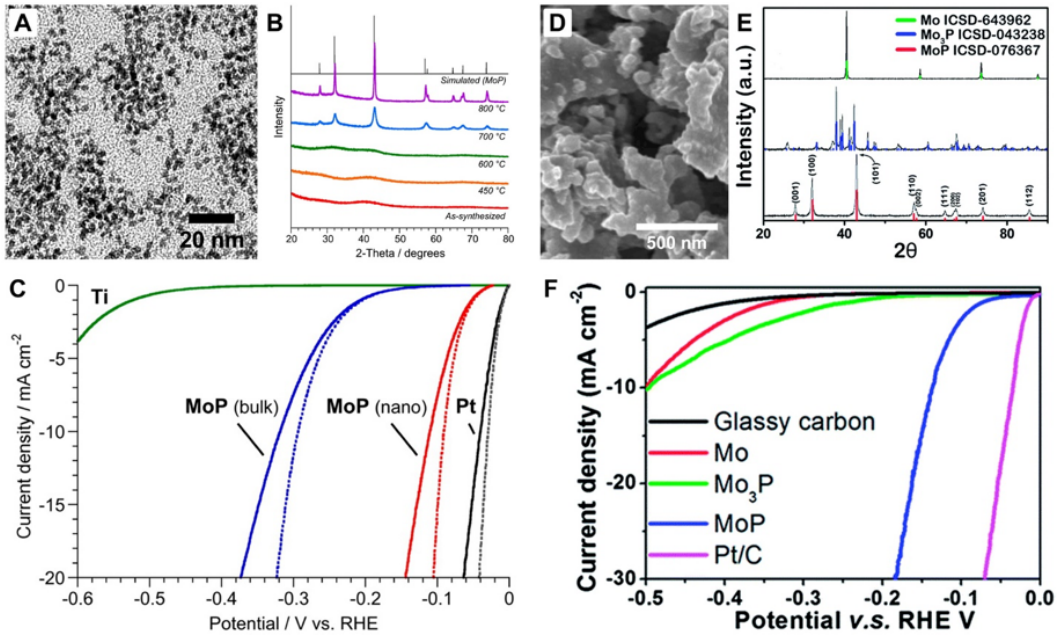

Figure K.16: (A) TEM image of amorphous MoP nanoparticles, (B) corresponding XRD patterns at different annealing temperatures, and (C) polarization data of bulk and nano MoP in 0.5 M H_2SO_4, along with a Pt control. Adapted with permission from ref.[176]. Copyright 2014 American Chemical Society. (D) SEM image of crystalline MoP particles, (E) corresponding XRD patterns, and (F) polarization data of MoP and Mo_3P in 0 0.5 M H_2SO_4, along with a Pt control. Adapted from ref.[165]. Copyright 2014 Royal Society of Chemistry.

played low HER activity, requiring an overpotential of $\eta_{-10\,\mathrm{mA/cm^2}} = -500\,\mathrm{mV}$ in 0.50 M H_2SO_4. However, the stoichiometric MoP phase exhibited much improved performance even in bulk form, exhibiting an overpotential of approximately $\eta_{-10\,\mathrm{mA/cm^2}} = -125\,\mathrm{mV}$ under the same conditions (Figure K.16). Our group reported on the synthesis and HER performance of amorphous molybdenum phosphide (MoP) nanoparticles having diameters of $\approx 3\,\mathrm{nm}$ prepared through the decomposition of $Mo(CO)_6$ and TOP in squalane at 320 °C (Figure K.16).[176] The MoP nanoparticles remained amorphous even after annealing to 450 °C to remove the organic surface ligands. Working electrodes of the MoP nanoparticles on Ti foil (MoP/Ti) exhibited overpotentials of $\eta_{-10\,\mathrm{mA/cm^2}} = -90\,\mathrm{mV}$ in 0.50 M H_2SO_4. These potentials remained constant after 18 h of galvanostatic testing and after over 500 cyclic voltammetric sweeps, indicating substantial stability under operating conditions. Amorphous tungsten phosphide (WP) nanoparticles of comparable morphology and size were also obtained using similar synthetic methods (Figure K.17).[166] When tested for the HER, WP/Ti electrodes displayed slightly lower ac-

tivities than MoP, producing a current density of $-10\,\mathrm{mA/cm^2}$ at an overpotential of $-120\,\mathrm{mV}$ in $0.50\,\mathrm{M}\ H_2SO_4$. Crystalline WP nanorod arrays on carbon cloth (WP NAs/CC) reported by Sun and coworkers displayed similar activity, requiring an overpotential of $\eta_{-10\,\mathrm{mA/cm^2}} = -130\,\mathrm{mV}$ in $0.50\,\mathrm{M}\ H_2SO_4$ (Figure K.17).[167] Under the same conditions, crystalline, submicron WP_2 particles reported by the same group required a slightly higher overpotential of $\eta_{-10\,\mathrm{mA/cm^2}} = -161\,\mathrm{mV}$.[168]

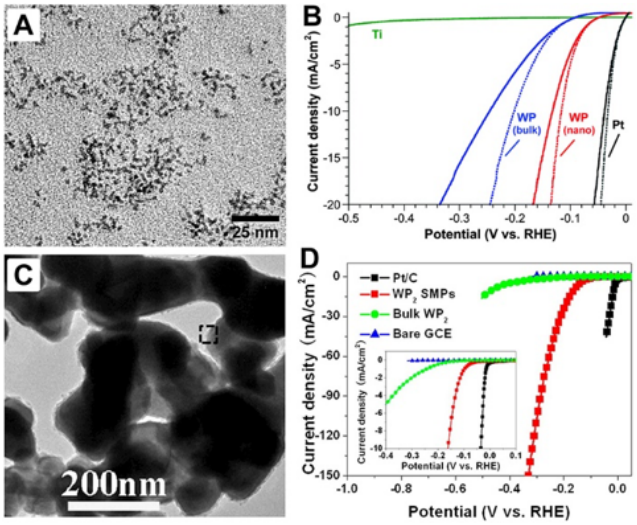

Figure K.17: (A) TEM image of amorphous WP nanoparticles and (B) corresponding polarization data in $0.5\,\mathrm{M}\ H_2SO_4$, along with a Pt control. Adapted with permission from ref.[166]. Copyright 2014 Royal Society of Chemistry. (C) TEM image of crystalline WP_2 nanoparticles and (D) corresponding polarization data in in $0.5\,\mathrm{M}\ H_2SO_4$, along with a Pt control. Adapted with permission from ref.[168]. Copyright 2015 American Chemical Society.

Copper Phosphides

Compared to the phosphides of the iron group elements (Fe, Co, Ni), copper phosphides have attracted significantly less attention as HER electrocatalysts, and only a few studies on Cu_3P have been reported to date. An initial study by Sun and coworkers on self-supported Cu_3P nanowire arrays grown on commercial porous copper foams (Cu_3P NW/CF) reported catalytic current densities at an overpotential of $\eta_{-10\,\mathrm{mA/cm^2}} = -143\,\mathrm{mV}$, with only minor degradation after continuous hydrogen production for 25 h (Figure K.18).[177] Likewise, Kong and coworkers described the phosphidation of $Cu(OH)_2$ precursors to form Cu_3P nanocubes, which exhibited moderate activities for the HER ($\eta_{-10\,\mathrm{mA/cm^2}} = -320\,\mathrm{mV}$) when tested on glassy carbon electrodes (GCE) (Figure K.18).[178] Recently, our group reported the synthesis of phase-pure Cu_3P films grown directly onto Cu foils through the

vapor-phase phosphidation of commercially available metal foils with organophosphine reagents.[58] The Cu_3P films appeared to be very unstable under the operating conditions, perhaps due to rapid degradation at the Cu_3P/Cu interface. The previous report on Cu_3P nanowire arrays presumably was performed on a more robust catalyst/substrate interface. Cu_3P therefore shows some evidence of moderate HER activity, but overall is not as stable at this point as the Fe, Co, and Ni phosphide systems.

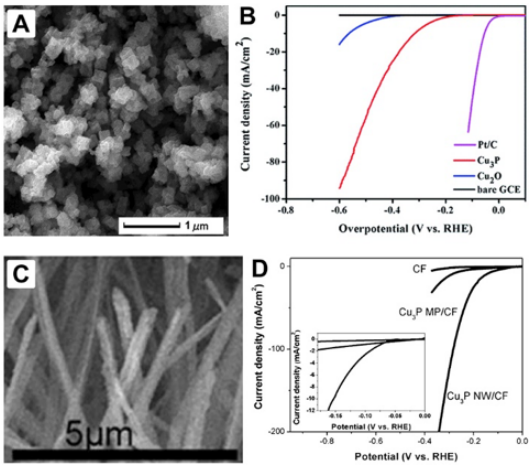

Figure K.18: (A) SEM image of Cu_3P nanocubes and (B) corresponding polarization data in 0.5 M H_2SO_4, along with a Pt control. Adapted with permission from ref.[177]. Copyright 2014 WILEY-VCH Verlag GmbH & Co. KGaA, Weinheim. (C) SEM image of self-supported Cu_3P nanowires on carbon cloth and (D) corresponding polarization data in 0.5 M H_2SO_4. Adapted with permission from ref.[178]. Copyright 2016 Royal Society of Chemistry.

Cation and Anion Substituted Metal Phosphides

Mixed-metal transition metal phosphides have recently been explored as electrocatalysts for the HER through a combined experimental and theoretical approach. Jaramillo and coworkers utilized density functional theory calculations to predict the hydrogen adsorption free energies, ΔG_H, for a series of mixed-metal transition metal phosphides, and compared these results to experimentally determined HER activities to identify optimized metal phosphide catalysts for the HER (Figure K.19).[149] Applying this methodology, a $Fe_{0.5}Co_{0.5}P$ alloy was found to be the most active of all the studied systems, with a near-zero theoretical ΔG_H of 0.004 eV and an experimental TOF_{avg} of 0.19 ± 0.01 H_2 s^{-1}. Nevertheless, the study also indicated that monometallic CoP exhibits a comparable HER activity, with a theoretical $\Delta G_H = -0.09$ eV and an experimental TOF_{avg} of $\approx 0.18 H_2$ s^{-1}, suggesting that

strategies based exclusively on cation solid solutions might not lead to significant improvements in HER activity. A different study by Wang and coworkers also explored the use of mixed-metal phosphides for the HER, in particular Fe-substituted Ni_2P sandwich nanocomposites.[179] These $(Fe, Ni)_2P$ nanocomposites were prepared by soaking $NiNH_4PO_4 \cdot H_2O$ nanosheets synthesized by a hydrothermal approach in an aqueous $FeCl_2$ solution, followed by a second hydrothermal process to carbon-coat the nanostructures, followed by reduction in a H_2 atmosphere at 680 °C. The polarization data for the Fe-substituted Ni_2P composites and Ni_2P controls indicated enhanced activity for $(Fe, Ni)_2$ P system, which required an overpotential of approximately $\eta_{-10\,mA/cm^2} = -75$ mV compared to the $\eta_{-10\,mA/cm^2} = -150$ mV required by Ni_2P to reach the same current density. However, iron phosphide controls were not included for comparison.

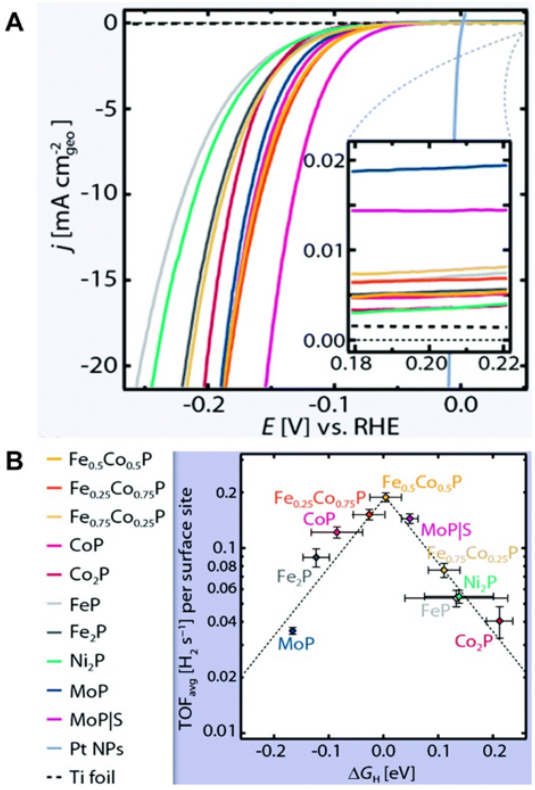

Figure K.19: (A) Polarization data for several transition metal phosphides in 0.5 M H_2SO_4, along with a Pt control. (B) Volcano plot showing the TOF of several transition metal phosphides as a function of hydrogen adsorption free energies. The color-coded key for both panels is shown in (B). Adapted with permission from ref.[149]. Copyright 2015 Royal Society of Chemistry.

Anion substitution has also been explored as an approach for improving the HER activity of metal phosphides. Based on the mechanistic commonalities shared

by many HER and HDS catalysts, Jaramillo and coworkers hypothesized that the introduction of sulfur onto metal phosphides might lead to enhancements in their catalytic activity and stability for the HER, as surface phosphosulfides are considered to be the sites of enhanced activity during HDS catalysis by both Ni_2P and MoP.[180] To explore this possibility, sulfur was introduced into the surface region of MoP films by post-sulfidation in a quartz tube furnace at 400 °C under a mixture of 10 % H_2S in H_2. The introduction of sulfur led to significant improvements in the electrocatalytic HER activity of the MoP films, with the MoP|S catalyst requiring an overpotential of only $\eta_{-10\,\mathrm{mA/cm^2}} = -64\,\mathrm{mV}$ compared to the required $\eta_{-10\,\mathrm{mA/cm^2}} = -117\,\mathrm{mV}$ of the unmodified MoP films (Figure K.20). Similarly, Jin and coworkers developed a nanostructured pyrite-type cobalt phosphosulfide (CoPS) catalyst for the HER (Figure K.21).[181] The CoPS electrodes were prepared by reacting a series of cobalt-based precursors at 500 °C with sulfur and phosphorus vapors produced by the evaporation of the elemental powders in an inert atmosphere. High-surface-area CoPS nanoplates grown on carbon paper displayed the highest HER performance of the studied samples, achieving a geometric current density of $-10\,\mathrm{mA/cm^2}$ at an overpotential of only $\eta_{-10\,\mathrm{mA/cm^2}} = -48\,\mathrm{mV}$ in 0.50 M H_2SO_4. This activity places CoPS among the best Earth-abundant HER electrocatalysts reported to date, and perhaps more importantly demonstrates that tuning the electronic structure and reactivity of catalysts by substituting non-metallic atoms can serve as a powerful strategy to enhance the activity of transition metal compounds.

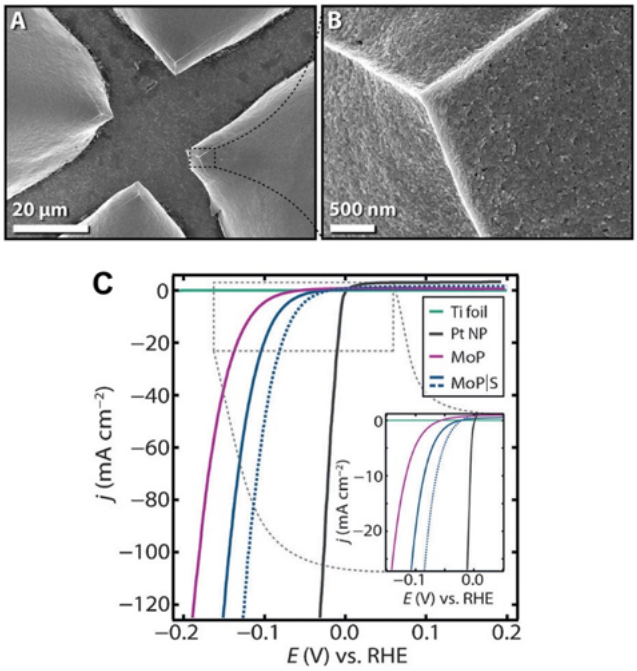

Figure K.20: (A) Low-magnification and (B) high-magnification SEM images of MoP|S. (C) Polarization data for MoP and MoP|S in 0.5 M H_2SO_4, along with a Pt control. Adapted with permission from ref.[180]. Copyright 2014 WILEY-VCH Verlag GmbH & Co. KGaA, Weinheim.

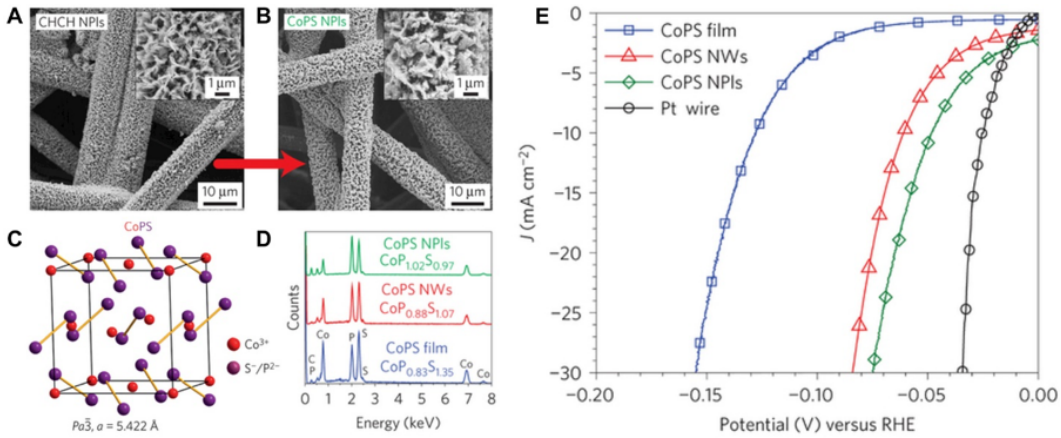

Figure K.21: (A) SEM images of cobalt hydroxide carbonate hydrate precursor. (B) SEM images of CoPS nanoplate product after reaction in a thiophosphate atmosphere. (C) Crystal structure of CoPS. (D) EDS spectra for CoPS films, CoPS nanowires on graphite, and CoPS nanoplates on carbon fiber paper. (E) Polarization data in 0.5 M H_2SO_4 for CoPS films, nanowires and nanoplates, along with a Pt control. Adapted with permission from ref.[181]. Copyright 2015 Macmillan Publishers Limited.

Mechanistic and Surface Studies of Metal Phosphides

Despite great interest in the use of metal phosphides as catalysts for the HER, to date only a few mechanistic and surface studies have been reported. The surface structure of the catalysts under operating conditions, the identity of the catalytically active sites, and key details of the HER mechanism on metal phosphide surfaces remain largely unknown. The existing studies have focused mainly on density functional theory (DFT) calculations of the hydrogen absorption energies on various metal phosphide surfaces. Based on such calculations, Liu and Rodriguez associated the HER behavior of Ni_2P to an ensemble effect, in which the presence of P atoms dilutes the number of highly active Ni sites on the surface, potentially leading to more moderate binding of the products and intermediates (Figure K.22).[45] Importantly, they also identified the P sites as active, suggesting that the presence of both proton-acceptor and hydride-acceptor centers on the surface could be playing a role in facilitating the HER. Based on DFT calculations, Hu and coworkers suggested that phosphorus-stabilized Ni-bridge sites on Ni_2P could also serve as active sites and provide moderate binding to hydrogen atoms.[182] Further studies by Jaramillo[27] and Wang[165] indicated that several metal phosphide surfaces have hydrogen absorption energies that are close to thermo-neutral, but specific structural or mechanistic characteristics that could lead to better catalyst design have not been explicitly identified. Additionally, several experimental surface studies by Asakura and coworkers on nickel phosphide crystals, including low-energy electron diffraction (LEED), scanning tunneling microscopy (STM), and photoemission electron microscopy (PEEM), indicate the presence of reconstructed surface structures, implying that the bulk terminated structures of metal phosphides may not be stable.[183,184] However, these and similar experiments are carried out in environments that are very different from those used during actual HER operating conditions. In situ and ex situ characterization studies of transition metal phosphide materials under HER conditions could thus provide insights into the origin of the high catalytic activity, and ultimately the mechanism by which the HER occurs.

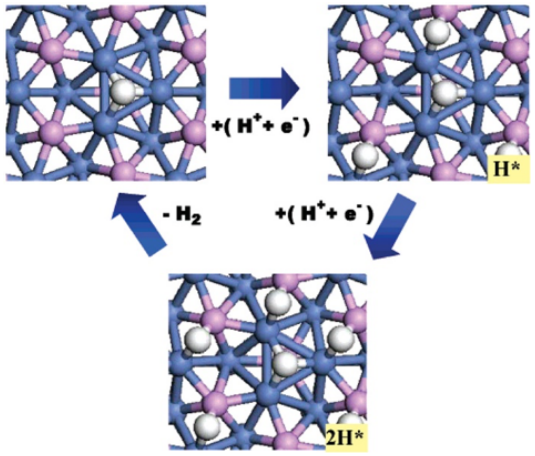

Figure K.22: Optimized structures for the (001) surface of Ni_2P, during different steps in hydrogen evolution reaction. Hydrogen atoms shown in white, nickel in blue, and phosphorus in purple. Reproduced with permission from ref.[45]. Copyright 2005 American Chemical Society.

K.7 Integration with Light Absorbers

Integration of kinetically competent catalysts with light absorbers remains challenging because of the delicate interplay between light absorption, carrier collection, charge transfer at interfaces, and catalysis. For the HER, most studies involving the integration of catalysts with light-absorbing materials have focused on Pt and MoS_2, but recently have expanded to metal phosphide systems. In this section we discuss key metrics, experimental conditions, specific challenges, and recent highlights involving the coupling of metal phosphide electrocatalysts to photocathodes.

Background, Considerations, and Metrics

Solar-powered hydrogen production depends critically on the judicious choice of materials to maximize the overall system solar-to-hydrogen efficiency,η_{STH} . This quantity represents the ratio of useful power out (H_2 and O_2) to the total power of sunlight illuminating the system. A single light absorber can potentially reach a maximum efficiency of 11 % while a stacked configuration consisting of two light absorbers may yield in excess of 22 % (Figure K.23).[185] As such, on the path toward economic viability, considerable efforts have been invested in achieving high efficiencies by developing photoelectrosynthetic cells driven by tandem photoabsorbers, with the highest achieved η_{STH} of 18 % reported by Licht and coworkers in 2000 using Pt black and RuO_2 as electrocatalysts for the hydrogen- and oxygen-evolution reactions, respectively.[186] While η_{STH} remains the key figure of merit for an entire

cell, optimization occurs by understanding the behavior of the individual components comprising the whole system. An important metric for a single component is the ideal regenerative cell efficiency, η_{IRC}, which represents the ratio of the total electrical power output relative to the input solar power for each half reaction.[187] This differs from η_{STH} because only electrical power is generated while measuring instead of a net chemical reaction only driven by solar energy for η_{STH}. Ideally, the photoelectrode performance should be determined without a coupled catalyst, with an electrochemically reversible one-electron redox couple such as methyl viologen ($MV^{2+/+}$), to establish the maximum performance obtainable from the absorber. This measurement aids in distinguishing issues intrinsic to the semiconductor from those due to the coupling of a catalyst with the electrode surface.

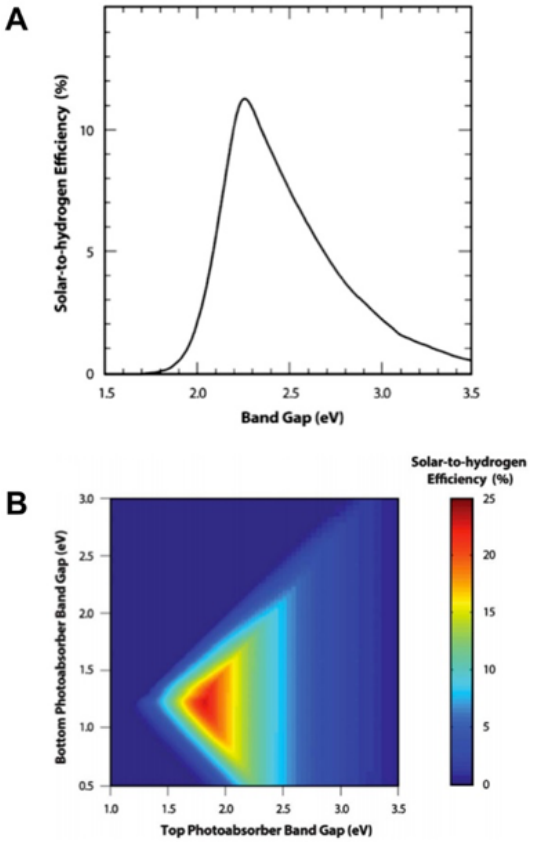

Figure K.23: Solar-to-hydrogen efficiency for (A) single and (B) double light-absorber water splitting systems. Adapted with permission from ref.[185]. Copyright 2013 Royal Society of Chemistry.

Fundamental electrode characteristics can be determined using three-electrode measurements to probe the current density as a function of applied potential on each photoelectrode. Additionally, experiments should not be limited by mass trans-

port (i.e. should be performed with rapid stirring of the solution), uncompensated resistance overpotentials (by correcting for the iR drop whenever possible), cell geometry, the nature of the counter electrode (by avoiding precious metals which could contaminate the cell) or the reference electrode (by using a well-defined Nernstian potential with a known pH and maintaining 1 atm of H_2), or the nature of the illumination source (by using an artificial light that matches well with the solar spectrum). For example, for metal working electrodes, the solution resistance can be electronically compensated using a current-interrupt method. In contrast, for a photoelectrode the uncompensated resistance of the setup should be determined with a glassy carbon electrode in place of the semiconductor. Instead of electronic compensation, a Luggin capillary reference electrode can be used to minimize solution resistance for either metal or semiconducting electrodes. Pt contamination is a common pitfall in the evaluation of HER catalysts, because even sub-monolayer deposits of Pt can result in high HER activities and therefore produce apparent enhancements in activity and/or stability.[188,189] When possible, it is best to avoid the use of Pt counter electrodes, by using high-purity carbon rods or other Pt-free electrodes instead. The catalyst and synthesis preparation should additionally be performed with precautions taken to minimize the possibility of noble metal contamination, e.g. all glassware should be carefully cleaned using aqua regia. The possibility of trace surface contamination underscores the importance of utilizing XPS to check for trace metal impurities. Together the open-circuit voltage (V_{oc}), short-circuit photocurrent density (J_{sc}), and fill factor (ff) form the basis set of metrics for evaluating the characteristics of a given photoelectrode. The open-circuit potential is the potential measured at zero current with a high-quality multimeter. The magnitude of the photovoltage is governed by the band gap of the material, practically reaching approximately two-thirds of the band gap in well-engineered systems. Photovoltages are lower in practice due to recombination.

In contrast to the short-circuit current density, which is the current measured with a high-resistivity multimeter at zero voltage and generally depends linearly on the photon flux reaching the semiconductor, the open-circuit voltage depends logarithmically on the illumination intensity. The actual photocurrent depends on the rate at which the current approaches the limiting photocurrent, with the potential dependence of the current called the fill factor, reflecting the "squareness" of the J–V characteristic of the photoelectrode. Hence J–V measurements obtained with a potentiostat yield information about the light absorption and photocarrier collection. The Faradaic yield for H_2 production should also be determined. The ultimate test

is to measure all of these parameters after prolonged operation, which ultimately must be stable on the order of 10 years for a commercially viable electrode with η_{STH} > 10 %, but more tractably on the bench by measuring η_{IRC} after accelerated degradation with an appropriate benchmarking protocol.[190]

Structuring of Photoelectrodes

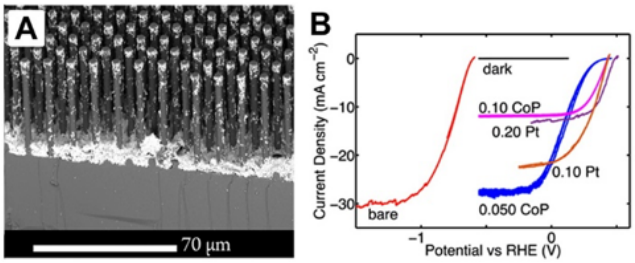

Figure K.24: (A) SEM image of CoP nanoparticles on n^+p-Si microwire (MW) arrays. (B) Effect of catalyst loading on the current density vs potential behavior of n^+p-Si planar photocathodes in contact with H_2(g)-saturated 0.50 M H_2SO_4(aq) and under 100 mW/cm^2 of AM1.5G simulated solar illumination. Adapted with permission from ref.[191]. Copyright 2015 American Chemical Society.

One guiding principle to produce high η_{IRC} for a photocathode relies on maximizing simultaneously the photovoltage and short-circuit current density, while accommodating thick catalyst overlayers. In a semiconducting device, both the voltage and current intimately depend on the generation rate of electron-hole pairs. This rate, in turn, depends on the flux of photons with energies greater than the bandgap. Illumination can occur on either the backside or front side of a solar cell, so the absorbance and reflectivity of a catalyst are important properties. For frontside exposure to the sun, it is critical for the catalyst film to have low light absorption, but for backside illumination, light absorption by the catalyst is not crucial.[192] Micro- and nano-structured photoelectrodes may offer an alternative approach for decoupling light absorption of a catalyst film from the light absorption necessary to produce photogenerated carriers within the semiconductor. High-aspect-ratio microwire or nanowire devices, for example, can utilize catalysts with lower TOFs by enabling higher mass loadings of the catalytic materials without compromising necessary light absorption by the semiconductor. For example, when CoP nanoparticle HER catalysts were coupled with n^+p-Si microwires, high catalyst mass loadings were easily accommodated on the microwires (Figure K.24). The resulting performance (of 2 %) was limited by parasitic resistance, presumably due to poor contact,[191] rather than by light absorption, as would have occurred with a planar geometry. Likewise,

Jin and coworkers used a structured photoelectrode with a catalytically active metal phosphide film that had intimate contact between the catalyst and the light absorber. Integration of CoPS with micropyramid n^+-p silicon substrates was achieved first by electron-beam deposition of cobalt, followed by heating in a furnace in the presence of 1:1 sulphur: phosphorous powder. Using this approach, η_{IRC} was nearly 5 % (Figure K.25).[181]

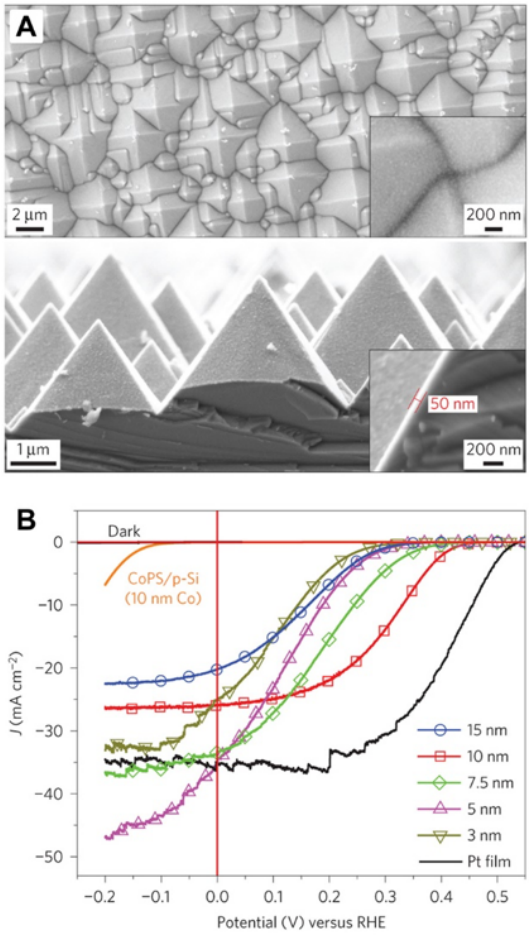

Figure K.25: (A) SEM images of micropyramid-structured silicon photocathodes coated with 10 nm CoPS showing top and cross-section views. (B) *J*–*V* curves in 0.5 M H_2SO_4 and under one sun illumination of microstructured n^+p-Si electrodes coated with 3, 5, 7.5, 10, and 15 nm of CoPS and 5 nm of Pt. A planar CoPS/p-Si electrode is shown for comparison. Adapted with permission from ref.[181]. Copyright 2015 Macmillan Publishers Limited.

Maintaining Charge Separation

Various strategies have been developed for enhancing the separation of charge carriers, including judicious selection of materials with optimal properties and careful

engineering of the junction between the catalyst and light absorber. Considering the coupling of metal phosphide HER catalysts to light-absorbing semiconductors, a large barrier height and a correspondingly high photovoltage – in an ideal Schottky contact – could be obtainable with a low work function catalyst contacting the p-type semiconductor. The work functions of metal phosphide HER catalysts have not yet been determined. However, Liu and coworkers reported that a heterostructure of CoSe and p-type Si exhibited η_{IRC} of 0.6 %.[193] Zhang and coworkers anchored $Ni_{12}P_5$ nanoparticles onto p-type silicon nanowires and illuminated for 2.8 h with = 3 %.[112] Liu observed an initial η_{IRC} of 2 % upon coupling CoP nanoparticles with p-type silicon nanowire-array photocathodes.[194] This system was fabricated by first electrodepositing Co and then using phosphidation at 500 °C to produce crystalline CoP particles. Significant enhancement of catalytic activity (compared with a bare surface) was observed over the course of an hour. However a loss in activity occurred shortly thereafter, and this decline in performance was attributed to passivation by silicon oxide. Zang obtained $\eta_{IRC} \approx 3$ % without using a p-n junction by dipping p-type silicon nanowires into a solution of iron nitrate and then heating in the presence of NaH_2PO_2, to yield FeP. The photoelectrode remained active for over 1 h of operation.[195]

Another approach for enhancing the separation of charge carriers relies on forming a metallurgical junction created by diffusing dopants that create an appropriate built-in electric field necessary for photocarrier collection. The built-in potential in this strategy does not depend on the work function of the catalyst; however, the formation of well-behaved buried junctions remains an unsolved challenge for many semiconductor systems. Both approaches potentially face challenges associated with colloidially synthesized nanoparticle catalysts capped by organic ligands, which require high temperatures to expose the catalytically active sites. Interstitial defects introduced by diffusion of a foreign material into the bulk of the semiconductor can lead to trap-assisted recombination, thereby lowering the performance of the photoelectrode. Low-temperature processing is therefore desirable for integrating materials with many photocathodes. For example, preliminarily results suggest that extension of an electrodeposition procedure[81] for growing amorphous CoP onto planar p-WSe_2 or n^+p-Si appears tenable.

Charge Transfer Between Catalyst and Light Absorber

The charge transfer of electrons from the absorber to the catalyst depends on the electrical and mechanical contact. Poor contact could result in parasitic series re-

sistances, thereby detrimentally affecting the device performance. Charge transfer within the bulk of the catalyst could also result in a parasitic resistance. As such, a thin layer or low-resistivity catalyst film is desirable. The resistivities of metal phosphides have not yet been reported. Ensuring intimate electrical and mechanical contact between nanoparticles and substrates remains an open challenge. Appropriate binding agents could result in improved adhesion and electron transport. An alternative strategy is to deposit the materials directly by vacuum deposition, potentially resulting in thin, conformal, highly active electrodes. Jaramillo and coworkers demonstrated that Co metal deposited by electron-beam evaporation onto n^+p-Si, followed by phosphidation, yielded highly active CoP on planar silicon (Figure K.26).[196] The TOF values were nearly ten times those reported previously, allowing for thinner films and suggesting a more intrinsically active material than the nanoparticles, and/or better interfacial contact between the substrate and catalyst film. The resulting photocathode exhibited $\eta_{\mathrm{IRC}} = 5$ % while showing stability for 24 h of operation.

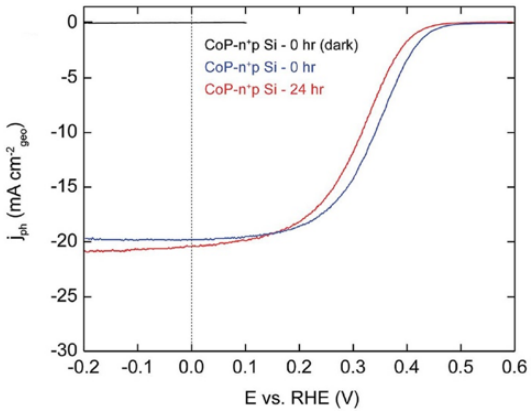

Figure K.26: Linear sweep voltammograms of a CoP thin film on n^+p-Si photocathodes under one sun illumination before and after 24 hours of operation in 0.5 M H_2SO_4. Adapted with permission from ref.[196]. Copyright 2012 Macmillan Publishers Limited.

Particle-Based Absorbers

One technoeconomic analysis suggests that H_2 generation systems using multijunction semiconductors have an undesirably high calculated H_2 cost ($ 6 per kg of H_2), which is driven primarily by the expected cost of cell packaging. In contrast, water splitting using colloidal systems that function in inexpensive plastic bags could potentially result in a system that has a very low cost of H_2 ($ 1.49 per kg of H_2).[197] Thus, a particle-bed PEC device in bags is an attractive option for an economically

scalable hydrogen generation platform, provided that an intrinsically safe system can be designed such that H_2 and O_2 are not evolved in the same bag at the same time. Along these lines, FeP nanoparticles anchored onto TiO_2 under UV illumination produced H_2 for 16 h at nearly the same rate as Pt.[152] Fu and coworkers coupled CoP, Ni_2P, and Cu_3P to CdS particles and produced H_2 for over 10 h, obtaining a maximum H_2 production rate of 251 μmol h^{-1} with CoP.[198]

Outlook

Metal phosphides demonstrate promising photocatalytic activity when coupled to light absorbers. Future efforts should also include longer stability windows, which will be important for evaluating commercially viable photocathode systems. The design of an efficient water-splitting system will be aided by reporting the intrinsic resistivities of these catalyst films, and including absorption and reflection spectra of the films. An expanded suite of deposition techniques that ensures intimate contact between the semiconductor and catalyst film, in addition to more complete characterization, will be useful for integrating these materials into devices.

A challenge facing the construction of a functional, inexpensive water-splitting device operating in acidic regimes is the lack of Earth-abundant oxygen-evolving catalysts. As the search continues for compatible families of anode materials, another approach relies on the incorporation of a bipolar membrane situated in between an acidic catholyte and an alkaline anolyte. The membrane simultaneously maintains a steady-state pH difference between each compartment and prevents gaseous product crossover, thereby allowing the use of an optimized acid-compatible photocathode and base-compatible photoanode. Sun demonstrated solar-driven water-spitting with an η_{STH} of 10 % for > 100 h using a GaAs/InGaP tandem stack immersed in an anolyte compartment (pH 9.3) driving the OER with a NiO_x coating and a back contact wired to a Ti mesh coated with CoP carrying out the HER in the catholyte compartment.[199] In addition to the overpotential losses from catalysis, the bipolar membrane operating at a current density of 10 mA/cm^2 results in an additional 400 mV to 500 mV resistive loss. Luo similarly reported a device using a pervoskite light harvester located outside of the solutions wired to a $NiFeO_x$ electrode in the anolyte (pH 13.9) and a CoP on Ti foil electrode in the catholyte (pH 0.4) giving η_{STH} of 12 % for nearly 100 h.[200] Future work may result in completely wireless devices.

K.8 Conclusions

Transition metal phosphides have emerged as a robust family of Earth-abundant catalysts for the HER. The high catalytic activity and stability displayed by these materials, including in strongly acidic aqueous electrolytes, has motivated extensive efforts in synthesis, characterization, catalytic testing, and device integration. Currently, several phosphides of Ni, Co, Fe, Mo, and W are considered to be highly promising HER catalysts, and anion substitution appears to be a particularly useful approach for further improving their catalytic performance. Despite these discoveries and ongoing improvements as more systems are being interrogated, mechanistic studies remain scarce. In situ studies, coupled with computational investigations, will be especially useful for furthering our understanding of how the HER proceeds on transition metal phosphide surfaces under operational conditions. Such studies will also help to reveal design guidelines for producing catalytic materials that expose the highest possible density of surface active sites. Finally, the integration of metal phosphides with light absorbers is still at an early stage. Nonetheless, the development of methods capable of producing favorable interfaces between catalysts and light absorbers, as well as novel photocathode architectures, may be key steps towards realizing integrated water-splitting systems comprised entirely of inexpensive and Earth-abundant materials.

K.9 Acknowledgments

This work was supported by the National Science Foundation (NSF) Center for Chemical Innovation in Solar Fuels (CHE-1305124). C.W.R. thanks the Link Energy Foundation for a graduate research fellowship.

K.10 References

(1) N. S. Lewis and D. G. Nocera, *Proceedings of the National Academy of Sciences*, 2006, **103**, 15729–15735.

(2) B. M. Hunter, J. D. Blakemore, M. Deimund, H. B. Gray, J. R. Winkler and A. M. Müller, *J. Am. Chem. Soc.*, 2014, **136**, 13118–13121.

(3) DOE, *A National Vision of America's Transistion to a Hydrogen Economy-To 2030 and Beyond. 2001*, 2, 2007, pp. 739–756.

(4) X. Cheng, Z. Shi, N. Glass, L. Zhang, J. Zhang, D. Song, Z.-S. Liu, H. Wang and J. Shen, *J. Power Sources*, 2007, **165**, 739–756.

(5) J. R. McKone, N. S. Lewis and H. B. Gray, *Chem. Mater.*, 2014, **26**, 407–414.

(6) C. Xiang, K. M. Papadantonakis and N. S. Lewis, *Mater. Horiz.*, 2016, **3**, 169–173.

(7) E. A. Hernández-Pagán, N. M. Vargas-Barbosa, T. Wang, Y. Zhao, E. S. Smotkin and T. E. Mallouk, *Energy and Environmental Science*, 2012, **5**, 7582.

(8) N. S. Lewis, *Science*, 2016, **351**, aad1920–aad1920.

(9) H. B. Gray, *Nat. Chem.*, 2009, **1**, 112–112.

(10) A. Parkin, C. Cavazza, J. C. Fontecilla-Camps and F. A. Armstrong, *J. Am. Chem. Soc.*, 2006, **128**, 16808–16815.

(11) C. Madden, M. D. Vaughn, I. Dı/ez-Pérez, K. A. Brown, P. W. King, D. Gust, A. L. Moore and T. A. Moore, *J. Am. Chem. Soc.*, 2012, **134**, 1577–1582.

(12) A. Volbeda et al., *Nature*, 1995, **373**, 580–587.

(13) C. L. McIntosh, F. Germer, R. Schulz, J. Appel and A. K. Jones, *J. Am. Chem. Soc.*, 2011, **133**, 11308–11319.

(14) C. Tard, X. Liu, S. K. Ibrahim, M. Bruschi, L. D. Gioia, S. C. Davies, X. Yang, L.-S. Wang, G. Sawers and C. J. Pickett, *Nature*, 2005, **433**, 610–613.

(15) S. Shima, O. Pilak, S. Vogt, M. Schick, M. S. Stagni, W. Meyer-Klaucke, E. Warkentin, R. K. Thauer and U. Ermler, *Science*, 2008, **321**, 572–575.

(16) B. K. Burgess and D. J. Lowe, *Chem. Rev.*, 1996, **96**, 2983–3012.

(17) T. L. Gall, S. K. Ibrahim, C. A. Gormal, B. E. Smith and C. J. Pickett, *Chem. Commun.*, 1999, 773–774.

(18) M. Y. Darensbourg and R. D. Bethel, *Nat. Chem.*, 2011, **4**, 11–13.

(19) R. Mejia-Rodriguez, D. Chong, J. H. Reibenspies, M. P. Soriaga and M. Y. Darensbourg, *J. Am. Chem. Soc.*, 2004, **126**, 12004–12014.

(20) A. Le Goff, V. Artero, B. Jousselme, P. D. Tran, N. Guillet, R. Metaye, A. Fihri, S. Palacin and M. Fontecave, *Science*, 2009, **326**, 1384–1387.

(21) M. L. Helm, M. P. Stewart, R. M. Bullock, M. R. DuBois and D. L. DuBois, *Science*, 2011, **333**, 863–866.

(22) T. Liu, D. L. DuBois and R. M. Bullock, *Nat. Chem.*, 2013, **5**, 228–233.

(23) T. Liu and M. Y. Darensbourg, *J. Am. Chem. Soc.*, 2007, **129**, 7008–7009.

(24) M. J. Rose, H. B. Gray and J. R. Winkler, *J. Am. Chem. Soc.*, 2012, **134**, 8310–8313.

(25) X. Hu, B. S. Brunschwig and J. C. Peters, *J. Am. Chem. Soc.*, 2007, **129**, 8988–8998.

(26) J. Kristensen, J. Zhang, I. Chorkendorff, J. Ulstrup and B. L. Ooi, *Dalton Trans.*, 2006, 3985.

(27) H. I. Karunadasa, E. Montalvo, Y. Sun, M. Majda, J. R. Long and C. J. Chang, *Science*, 2012, **335**, 698–702.

(28) J. Kibsgaard, T. F. Jaramillo and F. Besenbacher, *Nat. Chem.*, 2014, **6**, 248–253.

(29) R. D. Bethel and M. Y. Darensbourg, *Nature*, 2013, **499**, 40–41.

(30) J. R. McKone, S. C. Marinescu, B. S. Brunschwig, J. R. Winkler and H. B. Gray, *Chem. Sci.*, 2014, **5**, 865–878.

(31) M. G. Walter, E. L. Warren, J. R. McKone, S. W. Boettcher, Q. Mi, E. A. Santori and N. S. Lewis, *Chem. Rev.*, 2010, **110**, 6446–6473.

(32) D. Brown, M. Mahmood, A. Turner, S. Hall and P. Fogarty, *Int. J. Hydrogen Energy*, 1982, **7**, 405–410.

(33) D. E. Brown, M. N. Mahmood, M. C. M. Man and A. K. Turner, *Electrochim. Acta*, 1984, **29**, 1551–1556.

(34) D. G. Nocera, *Acc. Chem. Res.*, 2012, **45**, 767–776.

(35) J. R. McKone, B. F. Sadtler, C. A. Werlang, N. S. Lewis and H. B. Gray, *ACS Catal.*, 2013, **3**, 166–169.

(36) H. Vrubel and X. Hu, *Angew. Chem. Int. Ed.*, 2012, **51**, 12703–12706.

(37) W. F. Chen, C. H. Wang, K. Sasaki, N. Marinkovic, W. Xu, J. T. Muckerman, Y. Zhu and R. R. Adzic, *Energy and Environmental Science*, 2013, **6**, 943.

(38) B. Cao, G. M. Veith, J. C. Neuefeind, R. R. Adzic and P. G. Khalifah, *J. Am. Chem. Soc.*, 2013, **135**, 19186–19192.

(39) W.-F. Chen, K. Sasaki, C. Ma, A. I. Frenkel, N. Marinkovic, J. T. Muckerman, Y. Zhu and R. R. Adzic, *Angew. Chem. Int. Ed.*, 2012, **51**, 6131–6135.

(40) B. Hinnemann, P. G. Moses, J. Bonde, K. P. Jørgensen, J. H. Nielsen, S. Horch, I. Chorkendorff and J. K. Nørskov, *J. Am. Chem. Soc.*, 2005, **127**, 5308–5309.

(41) T. F. Jaramillo, K. P. Jorgensen, J. Bonde, J. H. Nielsen, S. Horch and I. Chorkendorff, *Science*, 2007, **317**, 100–102.

(42) Y. Li, H. Wang, L. Xie, Y. Liang, G. Hong and H. Dai, *J. Am. Chem. Soc.*, 2011, **133**, 7296–7299.

(43) J. Kibsgaard, Z. Chen, B. N. Reinecke and T. F. Jaramillo, *Nat. Mater.*, 2012, **11**, 963–969.

(44) C. G. Morales-Guio, L.-A. Stern and X. Hu, *Chem. Soc. Rev.*, 2014, **43**, 6555.

(45) P. Liu and J. A. Rodriguez, *J. Am. Chem. Soc.*, 2005, **127**, 14871–14878.

(46) S. T. Oyama, X. Wang, Y. K. Lee and W. J. Chun, *J. Catal.*, 2004, **221**, 263–273.

(47) K. Senevirathne, A. W. Burns, M. E. Bussell and S. L. Brock, *Adv. Funct. Mater.*, 2007, **17**, 3933–3939.

(48) S. Oyama, *J. Catal.*, 2003, **216**, 343–352.

(49) S. T. Oyama, T. Gott, H. Zhao and Y.-K. Lee, *Catal. Today*, 2009, **143**, 94–107.

(50) E. J. Popczun, J. R. McKone, C. G. Read, A. J. Biacchi, A. M. Wiltrout, N. S. Lewis and R. E. Schaak, *J. Am. Chem. Soc.*, 2013, **135**, 9267–9270.

(51) R. D. Blaugher, J. K. Hulm and P. N. Yocom, *J. Phys. Chem. Solids*, 1965, **26**, 2037–2039.

(52) W. Jeitschko, R. Glaum and L. Boonk, *J. Solid State Chem.*, 1987, **69**, 93–100.

(53) *Ames Research Report*, 1964, **204**, 966–966.

(54) S. Motojima, T. Wakamatsu and K. Sugiyama, *Journal of the Less Common Metals*, 1981, **82**, 379–383.

(55) M. G. Kanatzidis, R. Pöttgen and W. Jeitschko, *Angew. Chem. Int. Ed.*, 2005, **44**, 6996–7023.

(56) S. Otani and N. Ohashi, *J. Ceram. Soc. Jpn.*, 2013, **121**, 331–332.

(57) A. E. Henkes and R. E. Schaak, *Chem. Mater.*, 2007, **19**, 4234–4242.

(58) C. G. Read, J. F. Callejas, C. F. Holder and R. E. Schaak, *ACS Appl. Mater. Interfaces*, 2016, **8**, 12798–12803.

(59) A. Panneerselvam, M. A. Malik, M. Afzaal, P. O'Brien and M. Helliwell, *J. Am. Chem. Soc.*, 2008, **130**, 2420–2421.

(60) A. Infantes-Molina et al., *Appl. Catal., B*, 2012, **113-114**, 87–99.

(61) M. H. Mobarok, E. J. Luber, G. M. Bernard, L. Peng, R. E. Wasylishen and J. M. Buriak, *Chem. Mater.*, 2014, **26**, 1925–1935.

(62) R.-K. Chiang and R.-T. Chiang, *Inorg. Chem.*, 2007, **46**, 369–371.

(63) J. Wang, A. C. Johnston-Peck and J. B. Tracy, *Chem. Mater.*, 2009, **21**, 4462–4467.

(64) A. Hitihami-Mudiyanselage, M. P. Arachchige, T. Seda, G. Lawes and S. L. Brock, *Chem. of Mater.*, 2015, **27**, 6592–6600.

(65) S. E. Habas, F. G. Baddour, D. A. Ruddy, C. P. Nash, J. Wang, M. Pan, J. E. Hensley and J. A. Schaidle, *Chem. Mater.*, 2015, **27**, 7580–7592.

(66) H. Zhang, D.-H. Ha, R. Hovden, L. F. Kourkoutis and R. D. Robinson, *Nano Lett.*, 2011, **11**, 188–197.

(67) B. F. Stein and R. H. Walmsley, *Phys. Rev.*, 1966, **148**, 933–939.

(68) A. Addamiano, *J. Am. Chem. Soc.*, 1960, **82**, 1537–1540.

(69) R. L. Ripley, *Journal of the Less Common Metals*, 1962, **4**, 496–503.

(70) R. Kaner, C. A. Castro, R. P. Gruska and A. Wold, *Mater. Res. Bull.*, 1977, **12**, 1143–1147.

(71) D. J. Braun and W. Jeitschko, *Z. Anorg. Allg. Chem.*, 1978, **445**, 157–166.

(72) W. Jeitschko, R. Rühl, U. Krieger and C. Heiden, *Mater. Res. Bull.*, 1980, **15**, 1755–1762.

(73) R. Rühl and W. Jeitschko, *Acta Crystallogr Sect B*, 1981, **37**, 39–44.

(74) R. Ruehl and W. Jeitschko, *Inorg. Chem.*, 1982, **21**, 1886–1891.

(75) S. Yang, C. Liang and R. Prins, *J. Catal.*, 2006, **237**, 118–130.

(76) Z. W. Yao, *J. Alloys Compd.*, 2009, **475**, L38–L41.

(77) I. Abu and K. Smith, *J. Catal.*, 2006, **241**, 356–366.

(78) X. Yang, A.-Y. Lu, Y. Zhu, M. N. Hedhili, S. Min, K.-W. Huang, Y. Han and L.-J. Li, *Nano Energy*, 2015, **15**, 634–641.

(79) Y. Shi, Y. Xu, S. Zhuo, J. Zhang and B. Zhang, *ACS Appl. Mater. Interfaces*, 2015, **7**, 2376–2384.

(80) Y. Yu, Z. Song, H. Ge and G. Wei, *Progress in Natural Science: Materials International*, 2014, **24**, 232–238.

(81) F. H. Saadi, A. I. Carim, E. Verlage, J. C. Hemminger, N. S. Lewis and M. P. Soriaga, *J. Phys. Chem. C*, 2014, **118**, 29294–29300.

(82) T. Burchardt, *Int. J. Hydrogen Energy*, 2000, **25**, 627–634.

(83) E. Rudnik, K. Kokoszka and J. Łapsa, *Surf. Coat. Technol.*, 2008, **202**, 2584–2590.

(84) I. Paseka and J. Velicka, *Electrochim. Acta*, 1997, **42**, 237–242.

(85) T. Morikawa, T. Nakade, M. Yokoi, Y. Fukumoto and C. Iwakura, *Electrochim. Acta*, 1997, **42**, 115–118.

(86) I. Paseka, *Electrochim. Acta*, 1995, **40**, 1633–1640.

(87) Y. Xie, H. L. Su, X. F. Qian, X. M. Liu and Y. T. Qian, *J. Solid State Chem.*, 2000, **149**, 88–91.

(88) C. M. Lukehart, S. B. Milne and S. R. Stock, *ChemInform*, 2010, **29**, no–no.

(89) A. E. Henkes, Y. Vasquez and R. E. Schaak, *J. Am. Chem. Soc.*, 2007, **129**, 1896–1897.

(90) S. C. Perera, G. Tsoi, L. E. Wenger and S. L. Brock, *J. Am. Chem. Soc.*, 2003, **125**, 13960–13961.

(91) D. R. Liyanage, S. J. Danforth, Y. Liu, M. E. Bussell and S. L. Brock, *Chem. Mater.*, 2015, **27**, 4349–4357.

(92) D. Li, M. P. Arachchige, B. Kulikowski, G. Lawes, T. Seda and S. L. Brock, *Chem. Mater.*, 2016, **28**, 3920–3927.

(93) M. Razeghi, M. A. Poisson, J. P. Larivain and J. P. Duchemin, *JEM*, 1983, **12**, 371–395.

(94) R. M. Biefeld, *J. Cryst. Growth*, 1982, **56**, 382–388.

(95) J. Long, *J. Electrochem. Soc.*, 1983, **130**, 725.

(96) S. Motojima, K. Haguri, Y. Takahashi and K. Sugiyama, *Journal of the Less Common Metals*, 1979, **64**, 101–106.

(97) T. S. Lewkebandara, J. W. Proscia and C. H. Winter, *Chem. Mater.*, 1995, **7**, 1053–1054.

(98) F. Schrey, T. Boone, S. Nakahara, M. Robbins and A. Appelbaum, *Thin Solid Films*, 1987, **149**, 303–311.

(99) J. S. Yoon, *J. Electrochem. Soc.*, 1989, **136**, 3513.

(100) A. Iribarren, R. Castro-Rodrı/guez, L. Ponce-Cabrera and J. L. Peña, *Thin Solid Films*, 2006, **510**, 134–137.

(101) J. D. Benck, T. R. Hellstern, J. Kibsgaard, P. Chakthranont and T. F. Jaramillo, *ACS Catal.*, 2014, **4**, 3957–3971.

(102) C. C. L. McCrory, S. Jung, I. M. Ferrer, S. M. Chatman, J. C. Peters and T. F. Jaramillo, *J. Am. Chem. Soc.*, 2015, **137**, 4347–4357.

(103) D.-H. Ha, L. M. Moreau, C. R. Bealing, H. Zhang, R. G. Hennig and R. D. Robinson, *J. Mater. Chem.*, 2011, **21**, 11498.

(104) L. Feng, H. Vrubel, M. Bensimon and X. Hu, *Phys. Chem. Chem. Phys.*, 2014, **16**, 5917.

(105) J. Park, B. Koo, K. Y. Yoon, Y. Hwang, M. Kang, J.-G. Park and T. Hyeon, *J. Am. Chem. Soc.*, 2005, **127**, 8433–8440.

(106) L. M. Moreau, D.-H. Ha, H. Zhang, R. Hovden, D. A. Muller and R. D. Robinson, *Chem. Mater.*, 2013, **25**, 2394–2403.

(107) Z. Pu, Q. Liu, C. Tang, A. M. Asiri and X. Sun, *Nanoscale*, 2014, **6**, 11031–11034.

(108) Y. Pan, W. Hu, D. Liu, Y. Liu and C. Liu, *J. Mater. Chem. A*, 2015, **3**, 13087–13094.

(109) Y. Bai, H. Zhang, X. Li, L. Liu, H. Xu, H. Qiu and Y. Wang, *Nanoscale*, 2015, **7**, 1446–1453.

(110) A. Han, S. Jin, H. Chen, H. Ji, Z. Sun and P. Du, *J. Mater. Chem. A*, 2015, **3**, 1941–1946.

(111) A. B. Laursen, K. R. Patraju, M. J. Whitaker, M. Retuerto, T. Sarkar, N. Yao, K. V. Ramanujachary, M. Greenblatt and G. C. Dismukes, *Energy Environ. Sci.*, 2015, **8**, 1027–1034.

(112) Z. Huang, Z. Chen, Z. Chen, C. Lv, H. Meng and C. Zhang, *ACS Nano*, 2014, **8**, 8121–8129.

(113) P. Jiang, Q. Liu and X. Sun, *Nanoscale*, 2014, **6**, 13440–13445.

(114) Y. Pan, Y. Liu, J. Zhao, K. Yang, J. Liang, D. Liu, W. Hu, D. Liu, Y. Liu and C. Liu, *J. Mater. Chem. A*, 2015, **3**, 1656–1665.

(115) M. Ledendecker, S. Krick Calderón, C. Papp, H.-P. Steinrück, M. Antonietti and M. Shalom, *Angew. Chem. Int. Ed.*, 2015, **54**, 12361–12365.

(116) C. Wang, T. Ding, Y. Sun, X. Zhou, Y. Liu and Q. Yang, *Nanoscale*, 2015, **7**, 19241–19249.

(117) A. R. J. Kucernak and V. N. Naranammalpuram Sundaram, *J. Mater. Chem. A*, 2014, **2**, 17435–17445.

(118) T. Tian, L. Ai and J. Jiang, *RSC Adv.*, 2015, **5**, 10290–10295.

(119) Y. Pan, Y. Liu and C. Liu, *J. Power Sources*, 2015, **285**, 169–177.

(120) L.-A. Stern, L. Feng, F. Song and X. Hu, *Energy Environ. Sci.*, 2015, **8**, 2347–2351.

(121) N. Jiang, B. You, M. Sheng and Y. Sun, *ChemCatChem*, 2016, **8**, 277–277.

(122) X. Wang, Y. V. Kolen'ko and L. Liu, *Chem. Commun.*, 2015, **51**, 6738–6741.

(123) J. Li, J. Li, X. Zhou, Z. Xia, W. Gao, Y. Ma and Y. Qu, *ACS Appl. Mater. Interfaces*, 2016, **8**, 10826–10834.

(124) Y. Pan, Y. Lin, Y. Liu and C. Liu, *Appl. Surf. Sci.*, 2016, **366**, 439–447.

(125) Y. Pan, N. Yang, Y. Chen, Y. Lin, Y. Li, Y. Liu and C. Liu, *J. Power Sources*, 2015, **297**, 45–52.

(126) Z.-x. Cai, X.-h. Song, Y.-r. Wang and X. Chen, *ChemElectroChem*, 2015, **2**, 1665–1671.

(127) Y. Bai, H. Zhang, L. Fang, L. Liu, H. Qiu and Y. Wang, *J. Mater. Chem. A*, 2015, **3**, 5434–5441.

(128) E. J. Popczun, C. G. Read, C. W. Roske, N. S. Lewis and R. E. Schaak, *Angew. Chem. Int. Ed.*, 2014, **53**, 5427–5430.

(129) J. Tian, Q. Liu, A. M. Asiri and X. Sun, *J. Am. Chem. Soc.*, 2014, **136**, 7587–7590.

(130) S. Gu, H. Du, A. M. Asiri, X. Sun and C. M. Li, *Phys. Chem. Chem. Phys.*, 2014, **16**, 16909.

(131) Q. Li, Z. Xing, A. M. Asiri, P. Jiang and X. Sun, *Int. J. Hydrogen Energy*, 2014, **39**, 16806–16811.

(132) Q. Liu, J. Tian, W. Cui, P. Jiang, N. Cheng, A. M. Asiri and X. Sun, *Angew. Chem. Int. Ed.*, 2014, **53**, 6710–6714.

(133) Z. Pu, Q. Liu, P. Jiang, A. M. Asiri, A. Y. Obaid and X. Sun, *Chem. Mater.*, 2014, **26**, 4326–4329.

(134) J. F. Callejas, C. G. Read, E. J. Popczun, J. M. McEnaney and R. E. Schaak, *Chem. Mater.*, 2015, **27**, 3769–3774.

(135) Y. Pan, Y. Lin, Y. Chen, Y. Liu and C. Liu, *J. Mater. Chem. A*, 2016, **4**, 4745–4754.

(136) E. J. Popczun, C. W. Roske, C. G. Read, J. C. Crompton, J. M. McEnaney, J. F. Callejas, N. S. Lewis and R. E. Schaak, *J. Mater. Chem. A*, 2015, **3**, 5420–5425.

(137) H. Du, Q. Liu, N. Cheng, A. M. Asiri, X. Sun and C. M. Li, *J. Mater. Chem. A*, 2014, **2**, 14812.

(138) P. Jiang, Q. Liu, C. Ge, W. Cui, Z. Pu, A. M. Asiri and X. Sun, *J. Mater. Chem. A*, 2014, **2**, 14634.

(139) Z. Huang, Z. Chen, Z. Chen, C. Lv, M. G. Humphrey and C. Zhang, *Nano Energy*, 2014, **9**, 373–382.

(140) N. Jiang, B. You, M. Sheng and Y. Sun, *Angew. Chem. Int. Ed.*, 2015, **54**, 6251–6254.

(141) L. Ma, X. Shen, H. Zhou, G. Zhu, Z. Ji and K. Chen, *J. Mater. Chem. A*, 2015, **3**, 5337–5343.

(142) J. Ryu, N. Jung, J. H. Jang, H.-J. Kim and S. J. Yoo, *ACS Catal.*, 2015, **5**, 4066–4074.

(143) H. Yang, Y. Zhang, F. Hu and Q. Wang, *Nano Lett.*, 2015, **15**, 7616–7620.

(144) Z. Niu, J. Jiang and L. Ai, *Electrochem. Commun.*, 2015, **56**, 56–60.

(145) C. Wang, J. Jiang, X. Zhou, W. Wang, J. Zuo and Q. Yang, *J. Power Sources*, 2015, **286**, 464–469.

(146) Z. Jin, P. Li and D. Xiao, *Green Chem.*, 2016, **18**, 1459–1464.

(147) J. Wang, W. Yang and J. Liu, *J. Mater. Chem. A*, 2016, **4**, 4686–4690.

(148) M. Liu and J. Li, *ACS Appl. Mater. Interfaces*, 2016, **8**, 2158–2165.

(149) J. Kibsgaard, C. Tsai, K. Chan, J. D. Benck, J. K. Nørskov, F. Abild-Pedersen and T. F. Jaramillo, *Energy Environ. Sci.*, 2015, **8**, 3022–3029.

(150) A. Lu, Y. Chen, H. Li, A. Dowd, M. B. Cortie, Q. Xie, H. Guo, Q. Qi and D.-L. Peng, *Int. J. Hydrogen Energy*, 2014, **39**, 18919–18928.

(151) X. Wang, P. Clark and S. T. Oyama, *J. Catal.*, 2002, **208**, 321–331.

(152) J. F. Callejas, J. M. McEnaney, C. G. Read, J. C. Crompton, A. J. Biacchi, E. J. Popczun, T. R. Gordon, N. S. Lewis and R. E. Schaak, *ACS Nano*, 2014, **8**, 11101–11107.

(153) P. Jiang, Q. Liu, Y. Liang, J. Tian, A. M. Asiri and X. Sun, *Angewandte Chemie*, 2014, **126**, 13069–13073.

(154) J. Jiang, C. Wang, J. Zhang, W. Wang, X. Zhou, B. Pan, K. Tang, J. Zuo and Q. Yang, *J. Mater. Chem. A*, 2015, **3**, 499–503.

(155) Y. Zhang, H. Zhang, Y. Feng, L. Liu and Y. Wang, *ACS Appl. Mater. Interfaces*, 2015, **7**, 26684–26690.

(156) X. Yang, A.-Y. Lu, Y. Zhu, S. Min, M. N. Hedhili, Y. Han, K.-W. Huang and L.-J. Li, *Nanoscale*, 2015, **7**, 10974–10981.

(157) X. Zhu, M. Liu, Y. Liu, R. Chen, Z. Nie, J. Li and S. Yao, *J. Mater. Chem. A*, 2016, **4**, 8974–8977.

(158) C. Y. Son, I. H. Kwak, Y. R. Lim and J. Park, *Chem. Commun.*, 2016, **52**, 2819–2822.

(159) Z. Zhang, B. Lu, J. Hao, W. Yang and J. Tang, *Chem. Commun.*, 2014, **50**, 11554–11557.

(160) Y. Liang, Q. Liu, A. M. Asiri, X. Sun and Y. Luo, *ACS Catal.*, 2014, **4**, 4065–4069.

(161) R. Liu, S. Gu, H. Du and C. M. Li, *J. Mater. Chem. A*, 2014, **2**, 17263–17267.

(162) Y. Xu, R. Wu, J. Zhang, Y. Shi and B. Zhang, *Chem. Commun.*, 2013, **49**, 6656.

(163) J. Tian, Q. Liu, Y. Liang, Z. Xing, A. M. Asiri and X. Sun, *ACS Appl. Mater. Interfaces*, 2014, **6**, 20579–20584.

(164) Z. Zhang, J. Hao, W. Yang, B. Lu and J. Tang, *Nanoscale*, 2015, **7**, 4400–4405.

(165) P. Xiao, M. A. Sk, L. Thia, X. Ge, R. J. Lim, J.-Y. Wang, K. H. Lim and X. Wang, *Energy Environ. Sci.*, 2014, **7**, 2624–2629.

(166) J. M. McEnaney, J. Chance Crompton, J. F. Callejas, E. J. Popczun, C. G. Read, N. S. Lewis and R. E. Schaak, *Chem. Commun.*, 2014, **50**, 11026.

(167) Z. Pu, Q. Liu, A. M. Asiri and X. Sun, *ACS Appl. Mater. Interfaces*, 2014, **6**, 21874–21879.

(168) Z. Xing, Q. Liu, A. M. Asiri and X. Sun, *ACS Catal.*, 2015, **5**, 145–149.

(169) Z. Xing, Q. Liu, A. M. Asiri and X. Sun, *Adv. Mater.*, 2014, **26**, 5702–5707.

(170) X. Chen, D. Wang, Z. Wang, P. Zhou, Z. Wu and F. Jiang, *Chem. Commun.*, 2014, **50**, 11683–11685.

(171) W. Cui, Q. Liu, Z. Xing, A. M. Asiri, K. A. Alamry and X. Sun, *Appl. Catal., B*, 2015, **164**, 144–150.

(172) T. Wang, K. Du, W. Liu, Z. Zhu, Y. Shao and M. Li, *J. Mater. Chem. A*, 2015, **3**, 4368–4373.

(173) Z. Chen, C. Lv, Z. Chen, L. Jin, J. Wang and Z. Huang, *American Journal of Analytical Chemistry*, 2014, **05**, 1200–1213.

(174) Z. Pu, I. Saana Amiinu, M. Wang, Y. Yang and S. Mu, *Nanoscale*, 2016, **8**, 8500–8504.

(175) H. Du, S. Gu, R. Liu and C. M. Li, *J. Power Sources*, 2015, **278**, 540–545.

(176) J. M. McEnaney, J. C. Crompton, J. F. Callejas, E. J. Popczun, A. J. Biacchi, N. S. Lewis and R. E. Schaak, *Chem. Mater.*, 2014, **26**, 4826–4831.

(177) J. Tian, Q. Liu, N. Cheng, A. M. Asiri and X. Sun, *Angew. Chem. Int. Ed.*, 2014, **53**, 9577–9581.

(178) L. Ma, X. Shen, H. Zhou, J. Zhu, C. Xi, Z. Ji and L. Kong, *RSC Adv.*, 2016, **6**, 9672–9677.

(179) Y. Feng, Y. OuYang, L. Peng, H. Qiu, H. Wang and Y. Wang, *J. Mater. Chem. A*, 2015, **3**, 9587–9594.

(180) J. Kibsgaard and T. F. Jaramillo, *Angew. Chem. Int. Ed.*, 2014, **53**, 14433–14437.

(181) M. Caban-Acevedo et al., *Nat. Mater.*, 2015, **14**, 1245–1251.

(182) M. H. Hansen, L.-A. Stern, L. Feng, J. Rossmeisl and X. Hu, *Phys. Chem. Chem. Phys.*, 2015, **17**, 10823–10829.

(183) S. Suzuki, G. M. Moula, T. Miyamoto, Y. Nakagawa, K. Kinosthita, K. Asakura, S. T. Oyama and S. Otani, *J. Nanosci. Nanotechnol.*, 2009, **9**, 195–201.

(184) A. B. Hernandez, H. Ariga, S. Takakusagi, K. Kinoshita, S. Suzuki, S. Otani, S. T. Oyama and K. Asakura, *Chem. Phys. Lett.*, 2011, **513**, 48–52.

(185) B. A. Pinaud, J. D. Benck, L. C. Seitz, A. J. Forman, Z. Chen, T. G. Deutsch, B. D. James, K. N. Baum, G. N. Baum, S. Ardo, H. Wang, E. Miller and T. F. Jaramillo, *Energy and Environmental Science*, 2013, **6**, 1983.

(186) S. Licht, B. Wang, S. Mukerji, T. Soga, M. Umeno and H. Tributsch, *The Journal of Physical Chemistry B*, 2000, **104**, 8920–8924.

(187) R. H. Coridan, A. C. Nielander, S. A. Francis, M. T. McDowell, V. Dix, S. M. Chatman and N. S. Lewis, *Energy Environ. Sci.*, 2015, **8**, 2886–2901.

(188) D. V. Esposito, S. T. Hunt, A. L. Stottlemyer, K. D. Dobson, B. E. McCandless, R. W. Birkmire and J. G. Chen, *Angewandte Chemie*, 2010, **122**, 10055–10058.

(189) I. E. L. Stephens and I. Chorkendorff, *Angew. Chem. Int. Ed.*, 2011, **50**, 1476–1477.

(190) A. J. Bard and M. A. Fox, *Acc. Chem. Res.*, 1995, **28**, 141–145.

(191) C. W. Roske, E. J. Popczun, B. Seger, C. G. Read, T. Pedersen, O. Hansen, P. C. K. Vesborg, B. S. Brunschwig, R. E. Schaak, I. Chorkendorff, H. B. Gray and N. S. Lewis, *J. Phys. Chem. Lett.*, 2015, **6**, 1679–1683.

(192) D. Bae, T. Pedersen, B. Seger, M. Malizia, A. Kuznetsov, O. Hansen, I. Chorkendorff and P. C. K. Vesborg, *Energy Environ. Sci.*, 2015, **8**, 650–660.

(193) M. Basu, Z.-W. Zhang, C.-J. Chen, P.-T. Chen, K.-C. Yang, C.-G. Ma, C. C. Lin, S.-F. Hu and R.-S. Liu, *Angew. Chem. Int. Ed.*, 2015, **54**, 6211–6216.

(194) X.-Q. Bao, M. Fatima Cerqueira, P. Alpuim and L. Liu, *Chem. Commun.*, 2015, **51**, 10742–10745.

(195) C. Lv, Z. Chen, Z. Chen, B. Zhang, Y. Qin, Z. Huang and C. Zhang, *J. Mater. Chem. A*, 2015, **3**, 17669–17675.

(196) T. R. Hellstern, J. D. Benck, J. Kibsgaard, C. Hahn and T. F. Jaramillo, *Adv. Energy Mater.*, 2015, **6**, 1501758.

(197) B. D. James, G. N. Baum, J. Perez and K. N. Baum, 2009, DOI: 10.2172/1218403.

(198) S. Cao, Y. Chen, C.-J. Wang, X.-J. Lv and W.-F. Fu, *Chem. Commun.*, 2015, **51**, 8708–8711.

(199) K. Sun, R. Liu, Y. Chen, E. Verlage, N. S. Lewis and C. Xiang, *Adv. Energy Mater.*, 2016, **6**, DOI: 10.1002/aenm.201670077.

(200) J. Luo, J. H. Im, M. T. Mayer, M. Schreier, M. K. Nazeeruddin, N. G. Park, S. D. Tilley, H. J. Fan and M. Gratzel, *Science*, 2014, **345**, 1593–1596.